
Theses and Dissertations

Spring 2012

High throughput patient-specific orthopaedic analysis: development of interactive tools and application to graft placement in anterior cruciate ligament reconstruction

Austin Jedidiah Ramme
University of Iowa

Copyright 2012 Austin Jedidiah Ramme

This dissertation is available at Iowa Research Online: <http://ir.uiowa.edu/etd/2966>

Recommended Citation

Ramme, Austin Jedidiah. "High throughput patient-specific orthopaedic analysis: development of interactive tools and application to graft placement in anterior cruciate ligament reconstruction." PhD (Doctor of Philosophy) thesis, University of Iowa, 2012.
<http://ir.uiowa.edu/etd/2966>.

Follow this and additional works at: <http://ir.uiowa.edu/etd>



Part of the [Biomedical Engineering and Bioengineering Commons](#)

HIGH THROUGHPUT PATIENT-SPECIFIC ORTHOPAEDIC ANALYSIS:
DEVELOPMENT OF INTERACTIVE TOOLS
AND
APPLICATION TO GRAFT PLACEMENT IN ANTERIOR CRUCIATE LIGAMENT
RECONSTRUCTION

by
Austin Jedidiah Ramme

An Abstract

Of a thesis submitted in partial fulfillment
of the requirements for the Doctor of
Philosophy degree in Biomedical Engineering
in the Graduate College of
The University of Iowa

May 2012

Thesis Supervisors: Associate Professor Nicole M. Grosland
Associate Professor Vincent A. Magnotta

ABSTRACT

Medical imaging technologies have allowed for in vivo evaluation of the human musculoskeletal system. With advances in both medical imaging and computing, patient-specific model development of anatomic structures is becoming a reality. Three-dimensional surface models are useful for patient-specific measurements and finite element studies. Orthopaedics is closely tied to engineering in the analysis of injury mechanisms, design of implantable medical devices, and potentially in the prediction of injury. However, a disconnection exists between medical imaging and orthopaedic analysis; whereby, the ability to generate three-dimensional models from an imaging dataset is difficult, which has restricted its application to large patient populations. We have compiled image processing, image segmentation, and surface generation tools in a single software package catered specifically to image-based orthopaedic analysis. We have also optimized an automated segmentation technique to allow for high-throughput bone segmentation and developed algorithms that help to automate the cumbersome process of mesh generation in finite element analysis. We apply these tools to evaluate graft placement in anterior cruciate ligament reconstruction in a multicenter study that aims to improve the patient outcomes of those that undergo this procedure.

Abstract Approved: _____
 Thesis Supervisor

Title and Department

Date

Thesis Supervisor

Title and Department

Date

HIGH THROUGHPUT PATIENT-SPECIFIC ORTHOPAEDIC ANALYSIS:
DEVELOPMENT OF INTERACTIVE TOOLS
AND
APPLICATION TO GRAFT PLACEMENT IN ANTERIOR CRUCIATE LIGAMENT
RECONSTRUCTION

by
Austin Jedidiah Ramme

A thesis submitted in partial fulfillment
of the requirements for the Doctor of
Philosophy degree in Biomedical Engineering
in the Graduate College of
The University of Iowa

May 2012

Thesis Supervisors: Associate Professor Nicole M. Grosland
Associate Professor Vincent A. Magnotta

Copyright by
AUSTIN JEDIDIAH RAMME
2012
All Rights Reserved

Graduate College
The University of Iowa
Iowa City, Iowa

CERTIFICATE OF APPROVAL

PH.D. THESIS

This is to certify that the Ph.D. thesis of

Austin Jedidiah Ramme

has been approved by the Examining Committee
for the thesis requirement for the Doctor of Philosophy
degree in Biomedical Engineering at the May 2012 graduation.

Thesis Committee: _____
Nicole M. Grosland, Thesis Supervisor

Vincent A. Magnotta, Thesis Supervisor

Punam K. Saha

Joseph D. Smucker

David G. Wilder

Brian W. Wolf

ACKNOWLEDGMENTS

Biomedical engineering is truly multidisciplinary and requires collaboration for success. This thesis would not have been possible without the participation, flexibility, and support of many individuals. I would like to thank my advisors Dr. Nicole Grosland and Dr. Vincent Magnotta for the opportunity to work with them during the past several years and I am grateful for their funding of my graduate studies. Their unwavering support of my interest to present and publish this work was very much appreciated. I would like to thank my committee members Drs. Saha, Smucker, Wilder, and Wolf for their support and suggestions regarding my thesis work. Each has impacted my graduate education uniquely and I am thankful for it.

I'd like to extend my appreciation to Dr. Kiran Shivanna for his assistance in programming and constructive feedback on multiple aspects of this work, to Dr. Carla Britton for assistance in statistical analysis and organizing the acquisition of the CT images in the ACL study, to Dr. Warne and Dr. Willey for their welcoming attitudes, knot tying sessions, and help in understanding the clinical aspects of the ACL study, and to Dr. Luca Antiga and Dr. Killian Pohl for their assistance in utilizing their respective open source software packages. I'd like to thank Joe Ekdahl, Marla Kleingartner, Jeff Yager, and Dan Thedens for their friendship, humor, and encouragement and also Kent Williams and Steven Dunn for their individual contributions to my programming education. Finally, I want to express my appreciation to the MRRF and MIMX lab members for their companionship over the past several years.

ABSTRACT

Medical imaging technologies have allowed for in vivo evaluation of the human musculoskeletal system. With advances in both medical imaging and computing, patient-specific model development of anatomic structures is becoming a reality. Three-dimensional surface models are useful for patient-specific measurements and finite element studies. Orthopaedics is closely tied to engineering in the analysis of injury mechanisms, design of implantable medical devices, and potentially in the prediction of injury. However, a disconnection exists between medical imaging and orthopaedic analysis; whereby, the ability to generate three-dimensional models from an imaging dataset is difficult, which has restricted its application to large patient populations. We have compiled image processing, image segmentation, and surface generation tools in a single software package catered specifically to image-based orthopaedic analysis. We have also optimized an automated segmentation technique to allow for high-throughput bone segmentation and developed algorithms that help to automate the cumbersome process of mesh generation in finite element analysis. We apply these tools to evaluate graft placement in anterior cruciate ligament reconstruction in a multicenter study that aims to improve the patient outcomes of those that undergo this procedure.

TABLE OF CONTENTS

LIST OF TABLES	viii
LIST OF FIGURES	xi
CHAPTER 1 OVERVIEW	1
CHAPTER 2 UNDERSTANDING MODELING IN MEDICINE	4
2.1 Introduction.....	4
2.1.1 What is Modeling?	4
2.1.2 Vital Factors in Modeling.....	4
2.1.3 Patient-Specific Musculoskeletal Modeling.....	6
2.2 Generating Patient-Specific Biomedical Models.....	7
2.2.1 Generation of Models with Accurate Mass and Force Parameters	7
2.2.2 Generation of Geometrically Accurate Models.....	10
2.2.3 Generation of Models with Accurate Material Properties.....	18
2.3 Musculoskeletal Analysis Methods	19
2.3.1 Static and Dynamic Analysis.....	20
2.3.2 Structural Analysis	24
2.3.3 Continuum Mechanics.....	25
2.4 Applications of Biomedical Modeling.....	38
2.4.1 Rapid Prototyping.....	39
2.4.2 Applications of Computational Models.....	42
CHAPTER 3 AUTOMATED BUILDING BLOCK PLACEMENT IN MULTIBLOCK FINITE ELEMENT MESHING.....	51
3.1 Overview.....	51
3.2 Human Bone Surface Library	51
3.3 Automated Building Block Algorithm	55
3.3.1 Abstract.....	55
3.3.2 Introduction	55
3.3.3 Methods	61
3.3.4 Results	73
3.3.5 Discussion.....	79
3.4 Building Block Growing Algorithm.....	80
3.4.1 Abstract.....	80
3.4.2 Introduction	81
3.4.3 Materials and Methods: The Algorithm	81
3.4.4 Evaluation Methods.....	90
3.4.5 Results and Discussion	92
3.4.6 Conclusions	105
CHAPTER 4 MUSCULOSKELETAL IMAGE ANALYSIS.....	106
4.1 Overview.....	106
4.2 IA-Image Processing Toolkit.....	107
4.3 EM Segmentation of the Phalanx Bones of the Hand	110
4.3.1 Abstract.....	110

4.3.2	Introduction	110
4.3.3	Methods	114
4.3.4	Results	119
4.3.5	Discussion.....	123
4.4	EM Segmentation of the Femur and Tibia	127
4.4.1	Abstract.....	127
4.4.2	Introduction	128
4.4.3	Materials and Methods	130
4.4.4	Results	139
4.4.5	Discussion.....	143
4.4.6	Conclusion.....	145
CHAPTER 5 THE ANTERIOR CRUCIATE LIGAMENT		146
5.1	Anatomy	146
5.2	Injury.....	149
5.2.1	Epidemiology	149
5.2.2	Mechanism	150
5.2.3	Associated Injuries	150
5.2.4	Functional Testing.....	151
5.3	Reconstruction	154
5.3.1	Indications	154
5.3.2	Techniques.....	155
5.3.3	Grafts	159
5.3.4	Rehabilitation	161
5.3.5	Outcomes.....	162
5.3.6	Reconstruction Complications.....	163
5.4	Evaluation of Tunnel Placement.....	164
5.4.1	Overview	164
5.4.2	The Tibial ACL Tunnel Aperture.....	166
5.4.3	The Femoral ACL Tunnel Aperture	169
5.5	Finite Element Studies.....	174
CHAPTER 6 THREE-DIMENSIONAL EVALUATION OF GRAFT PLACEMENT IN ANTERIOR CRUCIATE LIGAMENT RECONSTRUCTION		176
6.1	Overview.....	176
6.2	Surgeon Oriented 3D Measurement System.....	177
6.2.1	Abstract.....	177
6.2.2	Introduction	178
6.2.3	Materials and Methods	179
6.2.4	Results	191
6.2.5	Discussion.....	193
6.3	Automatic Virtual Drill Bit Alignment.....	196
6.3.1	Abstract.....	196
6.3.2	Introduction	197
6.3.3	Materials and Methods	198
6.3.4	Results	201
6.3.5	Discussion.....	205
6.3.6	Conclusions	206
6.4	Visualization Techniques.....	207
6.4.1	Overview	207
6.4.2	Discrete ACL Aperture Centroid Mapping.....	207

6.4.3 ACL Tunnel Aperture Overlap Mapping	208
6.4.4 Conclusions	210
6.5 Multicenter Orthopaedic Outcomes Network Datasets	211
6.6 Analysis of the MOON Datasets	216
6.6.1 Moon Dataset Goals	216
6.6.2 Analysis Methods	216
6.6.3 Surgical Technique Results	218
6.6.4 Level of Surgical Experience Results.....	228
6.6.5 Surgeon Variability Results.....	239
6.6.6 Discussion and Conclusions	250
6.7 The Estimated Anatomic Footprint	253
6.7.1 Introduction	253
6.7.2 Materials and Methods	256
6.7.3 Results	258
6.7.4 Discussion and Conclusions	264
6.8 ACL Revision Cases.....	265
 CHAPTER 7 CONCLUDING REMARKS.....	 268
7.1 Overview.....	268
7.2 Limitations and Future Work.....	270
7.3 Closing.....	273
 APPENDIX A AUTOMATED MULTIBLOCK DEFINITIONS	 274
 APPENDIX B IA-IMAGE PROCESSING TOOLKIT.....	 276
B.1 Pre-Processing Tools.....	276
B.1.1 Resampling Tool.....	276
B.1.2 Mirror Tool	277
B.1.3 Threshold Tool.....	277
B.1.4 Cropping Tool.....	278
B.1.5 Image Math Tool	279
B.1.6 Island Removal and Gap Filling Tool.....	279
B.1.7 Gaussian Smoothing Tool.....	280
B.2 Orthopaedic Segmentation Tools.....	281
B.2.1 Simple Thresholding.....	281
B.2.2 Region Growing.....	281
B.2.3 Manual Contour-Based Segmentation	283
B.3 Surface Tools	287
B.3.1 Surface Generation, Smoothing, and Decimation	287
B.3.2 Surface Registration Tool	288
B.4 Graphical User Interface	289
B.4.1 Overview.....	289
B.4.2 Cropping Widget.....	290
B.4.3 Landmark Widget	291
B.4.4 Contour Widget.....	292
B.5 Record Keeping.....	293
 APPENDIX C ANTERIOR CRUCIATE LIGAMENT GRAFT PLACEMENT	 294
C.1 Standard Descriptive Statistics.....	294
C.2 Graphical Data Representations.....	302
C.3 Discrete ACL Aperture Centroid Maps	313

C.4 ACL Tunnel Aperture Overlap Maps	318
REFERENCES	326

LIST OF TABLES

Table 3.1 The Automated Building Block Algorithm was applied to 29 bones from various locations in the body and the resulting mesh quality metrics.	75
Table 3.2 The parameters used to generate the building blocks for 4 bones.	76
Table 3.3 The parameters used to generate the building blocks for an additional 4 bones.	76
Table 3.4 The 47 bones that the Building Block Growing Algorithm was applied where only a trunk multiblock structure was used.	92
Table 3.5 Detailed results from the Building Block Growing Algorithm for a subset of bones that was analyzed.	93
Table 3.6 Detailed results from the Building Block Growing Algorithm for a subset of bones that was analyzed.	94
Table 3.7 Results from the Building Block Growing Algorithm applied to the femur an aorta.	94
Table 3.8 The parameters used to generate the building blocks for four bones.	95
Table 3.9 The parameters used to generate the building blocks for an additional three bones and one vascular structure.	95
Table 3.10 Detailed results from a subset of bones for the BBGA, ABBA, manual definitions by a beginning IA-FEMesh user, and manual definitions by an expert IA-FEMesh.	101
Table 3.11 Detailed results from a subset of bones for the BBGA, ABBA, manual definitions by a beginning IA-FEMesh user, and manual definitions by an expert IA-FEMesh.	102
Table 4.1 Average relative overlap metric and average similarity index values with standard deviations for the phalanx bones of the hand.	121
Table 4.2 Average Euclidean distance and standard deviation between the Expectation Maximization segmented surfaces and the physical surface scans. ...	123
Table 4.3 Parameters used for segmenting the distal femur and proximal tibia using the EM segmentation algorithm.	137
Table 4.4 Segmentation evaluation metrics comparing the EM segmentations to the manual segmentations for the 72 femurs.	141
Table 4.5 Segmentation evaluation metrics comparing the EM segmentations to the manual segmentations for the 72 tibias.	141
Table 4.6 Union overlap (Jaccard coefficient) segmentation evaluation metrics comparing the EM segmentations to each of the manual raters.	142

Table 4.7 Breakdown of times required for the semi-automated segmentation process.	143
Table 6.1 Femoral tunnel and aperture location measurements from 10 CT datasets.	191
Table 6.2 Tibial tunnel and aperture location measurements from 10 CT datasets.	192
Table 6.3 Intraclass correlation coefficients for 4 trained users for each measurement.	192
Table 6.4 The average angular measures (α , β , γ) from 4 manual drill bit placements of each of the ten subjects.	202
Table 6.5 The absolute difference between the average manually aligned drill bits and the automated alignment methods for the femur where 'X' _M represents the manual alignment, 'X' _A represents the AutoBit alignment, and 'X' _I represents the ICP alignment.	203
Table 6.6 The absolute difference between the average manually aligned drill bits and the automated alignment methods for the tibia where 'X' _M represents the manual alignment, 'X' _A represents the AutoBit alignment, and 'X' _I represents the ICP alignment.	204
Table 6.7 A summary of the variables from the cadaver study organized by surgeon.	212
Table 6.8 A summary of the variables from the patient study organized by surgeon.	212
Table 6.9 Standard descriptive statistics for the cadaver study describing the distance from the tunnel aperture centroid to the AM bundle center for the tibia and the femur organized by surgical technique.	262
Table 6.10 Standard descriptive statistics for the cadaver study describing the distance from the tunnel aperture centroid to the PL bundle center for the tibia and the femur organized by surgical technique.	262
Table 6.11 Standard descriptive statistics for the cadaver study describing the distance from the tunnel aperture centroid to the center point between the bundle centers for the tibia and the femur organized by surgical technique.	263
Table 6.12 Standard descriptive statistics for the patient study describing the distance from the tunnel aperture centroid to the AM bundle center for the tibia and the femur organized by surgical technique.	263
Table 6.13 Standard descriptive statistics for the patient study describing the distance from the tunnel aperture centroid to the PL bundle center for the tibia and the femur organized by surgical technique.	264
Table 6.14 Standard descriptive statistics for the patient study describing the distance from the tunnel aperture centroid to the center point between the bundle centers for the tibia and the femur organized by surgical technique.	264
Table C.1 Descriptive statistics for the femoral and tibial tunnel angular measurements for the cadaver dataset.	294

Table C.2 Descriptive statistics for the femoral and tibial tunnel spatial measurements for the cadaver dataset.	294
Table C.3 Descriptive statistics for the femoral and tibial tunnel angular measurements for the cadaver dataset organized by surgical technique.	295
Table C.4 Descriptive statistics for the femoral and tibial tunnel spatial measurements for the cadaver dataset organized by surgical technique.	295
Table C.5 Descriptive statistics for the femoral and tibial tunnel angular measurements for the cadaver dataset organized level of surgeon experience.....	296
Table C.6 Descriptive statistics for the femoral and tibial tunnel spatial measurements for the cadaver dataset organized by surgical technique and level of surgeon experience.	296
Table C.7 Descriptive statistics for the femoral and tibial tunnel angular measurements for the cadaver dataset organized by surgical technique and level of surgeon experience.	297
Table C.8 Descriptive statistics for the femoral and tibial tunnel spatial measurements for the cadaver dataset organized by surgical technique and level of surgeon xperience.	298
Table C.9 Descriptive statistics for the femoral and tibial tunnel angular measurements for the patient dataset.	299
Table C.10 Descriptive statistics for the femoral and tibial tunnel spatial measurements for the patient dataset.	299
Table C.11 Descriptive statistics for the femoral and tibial tunnel angular measurements for the patient dataset organized by surgeon.....	300
Table C.12 Descriptive statistics for the femoral and tibial tunnel spatial measurements for the patient dataset organized by surgeon.....	301

LIST OF FIGURES

Figure 1.1 A flow diagram demonstrating the full patient-specific modeling process including the contributions in this document.....	3
Figure 2.1 Average anatomic relationships. A) A diagram showing average length relationships useful in static and dynamic analyses. B) An example of a model using simple shapes to estimate human body segments for simplified analysis.....	9
Figure 2.2 Virtual surface representations. A) A point cloud distribution of a patient-specific model of the patella. B) A triangulated surface mesh of a patient-specific model of the patella.....	18
Figure 2.3 Mechanical representations of the musculoskeletal system. A) A rigid body mechanics representation of a muscle composed of a contractile element (CE), serial elastic element (SE), parallel elastic element (PE), and a viscous element (DE). B) A simple free body diagram representing the forces and torques represented in the lower extremity.....	21
Figure 2.4 The finite difference method. A) An example of a finite difference mesh and its node structure. B) A section of a finite difference mesh with associated variables assigned to demonstrate the finite difference variables.	28
Figure 2.5 An example of a boundary element mesh demonstrating the boundary segments/elements as the operator for the mesh.....	31
Figure 2.6 An example of a finite element mesh demonstrating the finite element node structure as the operator for the mesh.	34
Figure 2.7 Applications of rapid prototyping. A) A three-dimensional model used for the development of sawing and drilling patient-specific maxillofacial surgical guides. B) The manufactured patient-specific maxillofacial surgical guide. C) Another three-dimensional model used for development of a patient-specific drilling guide for cervical spine laminar screw placement in posterior occipitocervical fusion. D) The manufactured patient-specific surgical guide placed on a model of a cervical vertebra.....	41
Figure 2.8 Applications of virtual models. A) A three-dimensional scaphoid model depicting the “safe zone” for screw placement. B) A representation of the “safe zone” and potential screw placement trajectories. C) Image depicting the placement of pedicle screws in the T6 vertebra. D) A compilation of CT slices and pedicle screw trajectory estimates based on an automated method for optimizing this surgical procedure.	44
Figure 2.9 An application of finite element simulation. A) Facial muscle actions that were simulated in the finite element model for various facial expressions. B) A section of the finite element model that demonstrates how properties of different tissues were associated with the finite element model. C) The generic facial finite element model that was registered to fit various other patient geometries. D) An example of a mandible and maxillary repositioning surgical procedure on the finite element model.....	45

Figure 2.10 The Vascular Modeling Toolkit. A) An MRA dataset used to develop three-dimensional patient-specific vascular models. B) An example demonstrating a finite element tetrahedral mesh of the abdominal aorta. C) An example demonstrating a finite element tetrahedral mesh of an internal carotid aneurysm.....	48
Figure 2.11 An example of finite element analysis. A) A finite element model representing the tibial component of a total knee replacement. Colors indicate different regions that were specifically investigated with the darkest region representing the tibial post. B) A color coded representation (blue = 2 MPa and yellow = 32 MPa) of the von Mises stresses for the tibial plateau of high flexion implant at 155° of flexion.....	50
Figure 3.1 Three-dimensional model generation process. A) A sample human scapula from a human skeletal collection. B) A CT scan of the bone was performed. C) A label map for the region of interest was generated using a simple region growing segmentation technique that involves the placement of a single seed(orange asterisk) in 3D Slicer. D) After segmentation, manual editing of label map was performed in the BRAINS2 software suite to ensure accurate label map assignments. E) 3D Slicer was used to generate a triangulated surface representation of the label map. F) Laplacian smoothing was applied.	53
Figure 3.2 Sample smoothed three-dimensional surface models generated using the described process in Figure 3.1. A) Ilium. B) Scapula. C) Patella. D) Ulna. E) Rib. F) Calcaneus. and G) Clavicle.	54
Figure 3.3 The steps used in the multiblock meshing process used in the IA-FEMesh software. A) The multiblock meshing process begins by choosing a surface to mesh (e.g. proximal phalanx of the finger). B) Individual blocks are manually placed around the surface to establish a block structure. C) A hexahedral mesh is assigned to the blocks. D) Closest point projection is used to project the mesh from the blocks onto the surface; internal elements are calculated to form a volumetric mesh. E) The resulting hexahedral mesh can be used for finite element analysis.	59
Figure 3.4 Example building block structures of different complexity. A) A manually defined block structure for a proximal phalanx bone of the hand composed of two building blocks. B) The corresponding hexahedral mesh for the proximal phalanx bone generated using IA-FEMesh. C) A manually defined block structure for the posterior elements of the third cervical vertebra composed of 117 building blocks. D) The corresponding hexahedral mesh for the posterior elements of the third cervical vertebra generated using IA-FEMesh.	60
Figure 3.5 The Automated Building Block Algorithm. A) A flow diagram depicting the steps of the Automated Building Block Algorithm. B) Incremental results corresponding to the steps described in (A) demonstrated using a model of the proximal phalanx bone of the index finger.....	62

Figure 3.6 Gaussian curvature analysis. A) The first step in the point selection filter involves removing segmentation artifacts that typically have a Gaussian curvature value greater or less than three standard deviations from the mean. B) Two regions identified as being between two and three standard deviations from the mean Gaussian curvature value.....	65
Figure 3.7 A visual depiction of the 9 cases of block overlap demonstrated in one dimension for simplification. The dashed line represents an edge of one block while the solid line represents the edge of another block. The distance between the lines should be ignored, and only the position of the lines considered.	67
Figure 3.8 A simple case of combinatorial building block rectification. A) Two building blocks overlapping in space. B) The resulting building blocks after rectification of overlap. In this case, one block has maintained its original volume, while the other original block has been modified to remove the region of overlap. Three additional blocks have been added to compensate for volume loss caused by the modification of the second original block.....	68
Figure 3.9 The PRMF is used to remove small differences between overlapping blocks. A) Two overlapping blocks that differ by a small amount (in this case <20% of the overall length of the block edge) along one axis. B) Here, a PRMF value of 5 will remove this small difference and result in two overlapping blocks without a small step off.	71
Figure 3.10 The merge blocks parameter can simplify a block structure by merging blocks that share faces with identical coordinates. Here we demonstrate a simple block structure A) composed of eight blocks and the resulting structures after the merge blocks parameter is applied to the B) x-axis, C) y-axis, D) z-axis, E) x- and y-axes, F) x- and z-axes, G) y- and z-axes, and H) the x-, y-, and z-axes.....	71
Figure 3.11 The band factor is used to remove narrow bands of blocks within a structure. A) A block structure containing a centrally located narrow band of blocks. B) The resulting block structure after a band factor of 0.2 is applied, which incorporates the narrow blocks into the neighboring blocks.	72
Figure 3.12 From left to right, the objects are the original surface, building block structure generated using the automated algorithm, an overlap view of the building block structure and the surface, and a hexahedral finite element mesh generated using the automatically generated building block structure. The Automated Building Block Algorithm was applied to the A) scaphoid, B) the trapezium, C) the twelfth rib, and D) the sternum.	77
Figure 3.13 From left to right, the objects are the original surface, building block structure generated using the automated algorithm, an overlap view of the building block structure and the surface, and a hexahedral finite element mesh generated using the automatically generated building block structure. The Automated Building Block Algorithm was applied to the A) third cuneiform, B) the cuboid, C) the metatarsal of the second toe, and D) the patella.....	78
Figure 3.14 A flow diagram describing the steps of the Building Block Growing Algorithm. The dotted set of arrows demonstrates the path used to generate the building block structure in Figure 3.15.....	83

Figure 3.15 Incremental results corresponding to the dotted path described in Figure 3.14 demonstrated using a surface of the third rib. A) Surface point selection by user. B) Reorientation of the selected surface. C) Trunk centerline generation. D) Trunk centerline angular analysis. E) Incremental additions of building blocks along third rib. F) Finalized block structure reoriented back to the original position.	84
Figure 3.16 A comparison of different outputs from the Building Block Growing Algorithm demonstrating different multiblock structures. A) A surface of the human femur used as an input to the semi-automated algorithm. B) A trunk centerline representation of the femur. C) A multiblock structure of the femur including a trunk structure without branches. D) A hexahedral finite element mesh of the femur generated using the semi-automatically generated building block trunk structure. E) A trunk and 3 branches centerline representation of the femur. F) A multiblock structure of the femur including three branches representing the greater trochanter(1), lateral condyle(2), and medial condyle(3). G) A hexahedral finite element mesh of the femur generated using the semi-automatically generated building block trunk and branch structure.	89
Figure 3.17 From left to right, the objects are the original surface, building block structure generated using the semi-automated algorithm, and a hexahedral finite element mesh generated using the semi-automatically generated building block structure. The Building Block Growing Algorithm was applied to A) the ulna, B) the cuboid, C) the sternum, and D) the second metacarpal.	96
Figure 3.18 A comparison of the run times for six representative cases in the generation of multiblock structures using BBGA, ABBA, manual definitions by a beginning IA-FEMesh user, and manual definitions by an expert IA-FEMesh user. The * indicates a case where the ABBA did not create a building block structure.	98
Figure 3.19 A comparison of the number of building blocks for a multiblock structure for six representative cases using BBGA, ABBA, manual definitions by a beginning IA-FEMesh user, and manual definitions by an expert IA-FEMesh user. The * indicates a case where the ABBA did not create a building block structure.	99
Figure 3.20 From left to right, the objects are the original surface, BBGA building block structure, ABBA building block structure, beginner building block structure, and expert building block structure. The two cases are the A) second metacarpal and B) the cuboid.	100
Figure 3.21 The Building Block Growing Algorithm applied to the human abdominal aorta. A) A surface of the human abdominal aorta with four smaller branching vessels. B) Centerlines used to represent the branching vasculature. C) A multiblock structure generated using the BBGA. D) A manually edited multiblock structure that allowed for hexahedral meshing. Regions that were edited are indicated by arrows in (C). E) A hexahedral mesh generated from the multiblock structure in (D).	103

Figure 4.1 The workflow for bone surface generation starts with imaging the region of interest. It proceeds with image processing and segmentation. Finally, a triangulated surface can be generated from the segmented image.	107
Figure 4.2 A screenshot from the <i>IA-Image Processing</i> Graphical User Interface. This application allows access to image processing functionalities in a user-friendly interface.....	109
Figure 4.3 The generation of a surface representation of the patella. A) A DICOM image is loaded. B) Hardware beam hardening artifact is thresholded away. C/D) A mirror operation is applied. E) The image is isotropically resampled. F) The image is cropped to isolate the patella. G) Seed points are placed for region growing segmentation. H) The output from the region growing segmentation. I) A surface representation of the patella. J) The surface overlapped with the original image.	109
Figure 4.4 Sample landmark identification at various locations on CT images of the hand.....	116
Figure 4.5 The Expectation Maximization algorithm used to segment the phalanx bones from a CT image of the hand. A) Surface models of the anterior aspects of the twelve phalanx bones. B) The posterior aspects of the bone models pictured alone.....	120
Figure 4.6 Euclidean distance map comparison between the physical surface scans and the Expectation Maximization algorithm based segmentation of a CT hand image. The three phalanx bones of the index finger (distal, medial, and proximal) are pictured from left to right. Distances are presented in mm.....	122
Figure 4.7 Thirion Demon's registration demonstrated on two images. A) The Thirion Demon's registration applied to a CT image of the knee with soft tissues present. The axial images represent the atlas (left), the registered atlas (center), and the subject (right). B) The Thirion Demon's registration applied to a binary CT image of the knee with soft tissues thresholded away. The axial images represent the atlas (left), the registered atlas (center), and the subject (right).....	133
Figure 4.8 The patient-specific probability map generation process. A) A sagittal CT slice of a human knee. B) A thresholded sagittal CT slice of the knee demonstrated in Figure 4.8A. C) The Gaussian ($\sigma=1.5$ and kernel width = 5) smoothed sagittal slice applied to Figure 4.8B. D) The resulting image after thresholding Figure 4.8C. E) The resulting image after removing islands using a connectivity filter from Figure 4.8D. F) The finalized patient-specific probability map after atlas to subject registration to map the probability images onto the subject CT scan.....	135
Figure 4.9 The calculated threshold value used by the patient-specific probability map generation procedure on 72 CT datasets of the knee.	136
Figure 4.10 The Expectation Maximization algorithm applied to CT images of the human knee. A) Surface models of the posterior aspect of the distal femur and proximal tibia. B) The anterior aspect of the bone models pictured alone.....	140

Figure 4.11 The Dice coefficient comparing the EM segmentation to a manual segmentation for 72 CT datasets of the knee.....	140
Figure 5.1 The anatomy of the human knee including bones, menisci, ligaments, and cartilage.....	147
Figure 5.2 The clock method for defining the ACL insertion on the lateral femoral condyle.....	148
Figure 5.3 The anterior drawer test.....	152
Figure 5.4 The Lachman test.	153
Figure 5.5 The pivot-shift test.....	153
Figure 5.6 Diagrams of the ACL and ACL reconstruction. A) A proton density weighted MRI image highlighting an intact ACL. B) An ACL reconstructed knee demonstrating the tibial and femoral tunnels and initial graft placement. C) A CT image demonstrating portions of the tibial and femoral tunnels.	154
Figure 5.7 The two-incision single bundle ACL reconstruction technique.....	156
Figure 5.8 The transtibial single bundle ACL reconstruction technique.....	157
Figure 5.9 The medial portal single bundle ACL reconstruction technique.....	157
Figure 5.10 Drill tunnels resulting from a double bundle ACL reconstruction.....	158
Figure 5.11 Different methods of evaluating ACL reconstructions. A) An example of a lateral radiograph based tunnel measurement system using Blumensaat’s line and the medial tibial plateau. B) An example of a CT based tunnel measurement system using a single CT slice. C) A CT reconstructed femur based measurement system using straight-line measurements. D) A CT reconstructed femur based tunnel measurement system using a grid oriented with plain lateral radiographic landmarks.	165
Figure 5.12 Suggested measurements for the tibia. The suggested measurement criteria from the ESSKA for the tibia demonstrated using a A) lateral radiographic view and B) anterior-posterior radiographic view.....	167
Figure 5.13 A tibial measurement system established from the “bird’s eye view” of the tibial plateau using similar measurements as those recommended from the ESSKA.....	168
Figure 5.14 Forsythe’s method of describing the tibial attachment of the ACL using surface reconstructions.	169
Figure 5.15 Watanabe’s method of describing the femoral attachment of the ACL.	170
Figure 5.16 The quadrant method of describing the femoral attachment of the ACL.....	171
Figure 5.17 Takahashi’s method of describing the femoral attachment of the ACL.....	172
Figure 5.18 Mochizuki’s method of describing the femoral attachment of the ACL.....	173

Figure 5.19 Forsythe’s method of describing the femoral attachment of the ACL on surface reconstructions.	174
Figure 6.1 A flow diagram describing the process to determine positional and angular information for the femoral and tibial tunnels using a virtual drill bit.	181
Figure 6.2 Standardized bone orientations. A) Femur. B) Tibia.	182
Figure 6.3 A cylinder with a diameter of 10mm was used to simulate the drill bit used to create the ACL tunnels. The cylinders were manually aligned in the tunnels of the A) femur and B) tibia.	182
Figure 6.4 Tibial tunnel angles (α , β , γ) were measured based on the tunnel centerline’s deviation from the A) surgically oriented coordinate system as demonstrated B) looking down the y-axis and C) looking down the x-axis.....	184
Figure 6.5 Femoral tunnel angles (α , β , γ) were measured based on the tunnel centerline’s deviation from the A) surgically oriented coordinate system as demonstrated B) looking down the y-axis and C) looking down the x-axis.....	185
Figure 6.6 The drill bit centerline identification process. A) A virtual drill bit aligned in a femoral tunnel. B) The end caps of the drill bit are isolated. C) The end cap centroids are calculated and define the centerline of the drill bit.....	186
Figure 6.7 The virtual drill bits were cropped to match the tunnel aperture. A) Femur. B) Tibia.....	187
Figure 6.8 Measurements of the tibial plateau. A) A measurement (a/A) of the tunnel aperture centroid based on the anterior-posterior distance of the tibial plateau. B) A measurement (m/M) of the tunnel aperture centroid based on the medial-lateral distance of the tibial plateau.	187
Figure 6.9 Measurements of the lateral femoral condyle. A) A measurement (c/C) of the tunnel aperture centroid based on the diameter of the lateral femoral condyle. B) A measurement (n/N) of the tunnel aperture centroid based on the height of the intercondylar notch.	188
Figure 6.10 Evaluation using digital phantoms. A) Nine virtual drill bits used to test the angular measurements. B) Three virtual drill bits used to test the aperture localization measurements.	188
Figure 6.11 Mapping of subjects onto an oriented surface. A) Original bone orientations prior to iterative closest point (ICP) registration. B) Aligned surfaces after ICP registration.....	190
Figure 6.12 Two examples of grossly misplaced tunnels. A) A case where the femoral drill tunnel penetrated the cortex. B) A case where the femoral drill tunnel missed the lateral condyle.....	193
Figure 6.13 Ten surface representations of drill tunnels. A) Femur. B) Tibia.	199

Figure 6.14 The automated drill bit alignment process. This process is demonstrated using a A) femoral tunnel and a B) tibial tunnel. From left to right, the objects are the bone surface, the bone surface highlighting the drill tunnel, the oriented bounding box and major axis (represented by two spheres) for the bone tunnel, the AutoBit aligned drill bit with the tunnel surface, the AutoBit aligned drill bit within the bone surface, and another view of the AutoBit aligned drill bit within the bone surface.	200
Figure 6.15 A comparison between the AutoBit alignment (red) and the average manually aligned drill bit (green). This is demonstrated for a A) femoral tunnel and a B) tibial tunnel. From left to right, the objects are the AutoBit aligned drill bit within the bone surface, a view of both the AutoBit aligned drill bit and manually aligned drill bit and the bone tunnel surface, and finally the automatically aligned drill bit and the manually aligned drill bit visualized within the bone surface.	205
Figure 6.16 The process used for Discrete ACL Aperture Centroid Mapping. A) A native bone surface is selected: the femur. B) The atlas surface is selected. C) The native bone surface is aligned to the atlas. D) A sphere is generated to represent the tunnel aperture centroid that was previously calculated. E) A closest-point projection is used to map the sphere onto the native bone surface. F) The sphere can be visualized on the native bone surface.	208
Figure 6.17 The process used for ACL Tunnel Aperture Overlap Mapping. A) A small sphere from the Discrete ACL Aperture Centroid Mapping visualization method. B) The sphere bound to the native surface is enlarged on a subject specific basis to match the size of the drill bit used for the ACL reconstruction. C) Multiple large spheres represented simultaneously are difficult to visualize. D) The number of times a bone surface point is encapsulated in a sphere can be used to color code the surface. E) The color scale is normalized by dividing the point “count” data by the total number of spheres considered to give a 0 to 1 scale.	209
Figure 6.18 The 72 cadaveric knee surface representations generated from CT datasets.	213
Figure 6.19 The 78 patient knee surface representations generated from CT datasets.	215
Figure 6.20 A color coded discrete sphere representation of the A) femur and B) tibia for the cadaver dataset organized by surgical technique: medial portal (green), transtibial (red), and two incision (blue).	219
Figure 6.21 Discrete sphere representations of the femur (3 views) and the tibia for the cadaver dataset organized by the technique used for the ACL reconstruction.	220
Figure 6.22 A box and whisker representation of the cadaver dataset’s femoral tunnel angle α organized by ACL reconstruction technique.	221
Figure 6.23 A box and whisker representation of the cadaver dataset’s femoral tunnel angle β organized by ACL reconstruction technique.	222

Figure 6.24 A box and whisker representation of the cadaver dataset's femoral tunnel angle γ organized by ACL reconstruction technique.....	223
Figure 6.25 A box and whisker representation of the cadaver dataset's femoral tunnel aperture position measure c/C organized by ACL reconstruction technique.....	224
Figure 6.26 A box and whisker representation of the cadaver dataset's tibial tunnel angle α organized by ACL reconstruction technique.	226
Figure 6.27 A box and whisker representation of the cadaver dataset's tibial tunnel aperture position measure a/A organized by ACL reconstruction technique.	228
Figure 6.28 A color coded discrete sphere representation of the A) femur and B) tibia for the transtibial surgical technique from cadaver dataset organized by level of surgical experience: experienced (red) and new to practice (green).	230
Figure 6.29 A color coded discrete sphere representation of the A) femur and B) tibia for the medial portal surgical technique from cadaver dataset organized by level of surgical experience: experienced (red) and new to practice (green). ...	230
Figure 6.30 A color coded discrete sphere representation of the A) femur and B) tibia for the two incision surgical technique from cadaver dataset organized by level of surgical experience: experienced (red) and new to practice (green). ...	231
Figure 6.31 A box and whisker representation of the cadaver dataset's femoral tunnel aperture position measure c/C organized by level of surgeon experience and ACL reconstruction surgical technique (MP = medial portal, TT = transtibial, TI = two incision).	234
Figure 6.32 A box and whisker representation of the cadaver dataset's tibial tunnel angle α organized by level of surgeon experience and ACL reconstruction surgical technique (MP = medial portal, TT = transtibial, TI = two incision).	236
Figure 6.33 Discrete sphere representations of the femur (3 views) and the tibia for the patient dataset organized by surgeon. Four surgeons are depicted.....	240
Figure 6.34 Discrete sphere representations of the femur (3 views) and the tibia for the patient dataset organized by surgeon. Four more surgeons are depicted.....	241
Figure 6.35 A box and whisker representation of the patient dataset's femoral tunnel angle α organized by surgeon. Eight surgeons are depicted.....	243
Figure 6.36 A box and whisker representation of the patient dataset's femoral tunnel angle β organized by surgeon. Eight surgeons are depicted.....	244
Figure 6.37 A box and whisker representation of the patient dataset's femoral tunnel angle γ organized by surgeon. Eight surgeons are depicted.	244
Figure 6.38 A box and whisker representation of the patient dataset's femoral tunnel aperture position measure c/C organized by surgeon. Eight surgeons are depicted.	245

Figure 6.39 A box and whisker representation of the patient dataset's femoral tunnel aperture position measure n/N organized by surgeon. Eight surgeons are depicted.	245
Figure 6.40 A box and whisker representation of the patient dataset's tibial tunnel angle α organized by surgeon. Eight surgeons are depicted.	247
Figure 6.41 A box and whisker representation of the patient dataset's tibial tunnel angle β organized by surgeon. Eight surgeons are depicted.	248
Figure 6.42 A box and whisker representation of the patient dataset's tibial tunnel angle γ organized by surgeon. Eight surgeons are depicted.	248
Figure 6.43 A box and whisker representation of the patient dataset's tibial tunnel aperture position measure a/A organized by surgeon. Eight surgeons are depicted.	249
Figure 6.44 A box and whisker representation of the patient dataset's tibial tunnel aperture position measure m/M organized by surgeon. Eight surgeons are depicted.	249
Figure 6.45 The estimated positions of the ACL bundle centers (AM and PL) positioned on the A) femur and the B) tibia using published measurements.	257
Figure 6.46 The estimated ACL footprint overlapped on the femur. A) An estimation of the ACL footprint on the femur using 3D CT measurements. B) A discrete sphere representation of the femur from the cadaver dataset overlapped with an estimated ACL footprint (white outline); three techniques are demonstrated: medial portal (green), two incision (blue), and transtibial (red). C) A discrete sphere representation of the femur from the patient dataset overlapped with an estimated ACL footprint (white outline); three techniques are demonstrated: medial portal (green), two incision (blue), and transtibial (red).	258
Figure 6.47 The estimated ACL footprint overlapped on the tibial plateau. A) An estimation of the ACL footprint on the tibia using 3D CT measurements. B) A discrete sphere representation of the tibia from the cadaver dataset overlapped with an estimated ACL footprint (white outline); three techniques are demonstrated: medial portal (green), two incision (blue), and transtibial (red). C) A discrete sphere representation of the tibia from the patient dataset overlapped with an estimated ACL footprint (white outline); three techniques are demonstrated: medial portal (green), two incision (blue), and transtibial (red).	259
Figure 6.48 Femoral and tibial ACL Tunnel Aperture Overlap Maps for the cadaver dataset representing three ACL reconstruction techniques. Two discrete spheres corresponding to the estimated locations of the AM and PL bundles of the ACL have been placed on both the femur and the tibia.	260
Figure 6.49 Femoral and tibial ACL Tunnel Aperture Overlap Maps for the patient dataset representing three ACL reconstruction techniques. Two discrete spheres corresponding to the estimated locations of the AM and PL bundles of the ACL have been placed on both the femur and the tibia.	261

Figure 6.50 Discrete sphere representation of the A) femur (two views) and the B) tibia demonstrating the 3 revisions at The University of Iowa to date from the MOON patient dataset. The red, blue, and green spheres represent the 3 different patients, while the smaller yellow spheres represent the AM and PL bundles of the estimated ACL location.....	267
Figure 7.1 Sample results from various sections of this thesis. A) The ABBA applied to the sternum. B) The BBGA applied to a human aorta. C) EM segmentation of the phalanx bones of the hand. D) Patient-specific probability map generation for use with EM segmentation. E) The <i>IA-Image Processing</i> toolkit. F) The novel 3D ACL drill tunnel measurement system for the femur. G) Discrete sphere representation from the cadaver study. H) ACL Aperture Overlap Maps from the cadaver study.....	269
Figure 7.2 A case of bilateral ACL reconstructions performed by the same surgeon on the same day demonstrated on the A) femur and B) tibia. Both left and right ACL tunnel aperture centroids are represented: left (blue) and right (red).....	271
Figure A.1 An example of how loads and boundary conditions were assigned to a hexahedral mesh. A) A load of 30N is distributed to the nodes corresponding to one side of the hexahedral mesh. B) A zero displacement boundary condition for all three primary axes is applied to the nodes opposing the loaded nodes of the hexahedral mesh.	274
Figure A.2 A volume mesh quality metric for the phalanx bones of the index finger demonstrating positive volume elements.....	275
Figure B.1 A resample operation example demonstrated on a human knee CT imaging study. The figure depicts the A) original image and the B) isotropically resampled image. This functionality can be used to reduce the file size of an image to allow for automated segmentation. It can also be used to create an isotropic image to allow for easier error estimation.....	276
Figure B.2 A mirror operation example demonstrated on a human knee imaging study. This functionality can be used to simplify large-scale studies by transforming all knees to either right or left representations. A) A right knee is transformed to a B) left knee.....	277
Figure B.3 A thresholding operation used to remove hardware artifacts from an ACL reconstruction CT image. A) The image containing hardware artifact and B) the image after the artifact has been removed.....	278
Figure B.4 The cropping tool. A) A CT image containing two knees. B) The cropping tool applied to generate two separate image sets, each containing a single knee.	278
Figure B.5 The image math tool. A) Image addition demonstrated using two mask files: femur and tibia. B) Image subtraction demonstrated using two mask files: tibia and tibial drill tunnel.....	279

Figure B.6 The island removal and gap filling tool. A) The raw results of automated segmentation can result in mask representations of the region of interest (e.g. distal femur) containing gaps and islands. B) After application of the island removal and gap filling tool, the resulting mask representation contains no islands or gaps.	280
Figure B.7 A Gaussian smoothing operation demonstrated on a A) binary representation of the distal end of a femur and B) the resulting image. This operation is useful in developing probability maps that are required by some statistical image segmentation procedures (e.g. EM segmentation).	280
Figure B.8 A thresholding operation demonstrated on A) cortical bone with two possible outputs: B) gray scale or C) binary. This can be useful as a simple method of bone segmentation.	281
Figure B.9 Region growing segmentation examples. A) Selection of seed points for the connected threshold region growing algorithm. B) An example result from the seed points chosen in (A) for the connected threshold region growing algorithm. C) Selection of seed points for the confidence connected region growing algorithm. D) An example result from the seed points chosen in (C) for the confidence connected region growing algorithm.	282
Figure B.10 Addition of a second contour to an axial CT slice.	284
Figure B.11 Contour deletion functionality. A) Two contours for an axial CT slice. B) Deletion of a single contour by a user on an axial CT slice.	284
Figure B.12 Contour deletion functionality for all slice contours. A) Two contours assigned to an axial CT slice. B) Deletion of all of a slice's contours from an axial CT slice.	285
Figure B.13 The copy operation can copy a B) given contour to the A) previous slice and to the C) next slice.	285
Figure B.14 The contour modification process. A) Two contours for an axial CT slice. B) Modification of a contour after placement.	285
Figure B.15 The contour to mask conversion tool. A) Two contours for an axial CT slice. B) Creation of a binary representation from the contours.	286
Figure B.16 The mask to contour conversion tool. A) A binary representation of a tibial diaphysis. B) Contour extracted from the binary representation. C) Visualization of all contours that have been extracted from a binary representation of a tibia.	286
Figure B.17 The surface from mask generation tool. A) One slice from a three-dimensional binary representation of a cervical vertebra. B) A three-dimensional surface generated using the surface generation feature.	287
Figure B.18 The surface smoothing tool. A) A three-dimensional surface representation of a femur demonstrating a stair-step appearance artifact. B) A three-dimensional surface of a femur after surface smoothing.	288

Figure B.19 The surface registration tool. A) Three-dimensional representations of 72 distal femurs demonstrating different positions and orientations of the surfaces. B) An atlas femur (red) and a subject femur (blue) that are not aligned in space. C) The subject femur (blue) aligned with atlas femur (red) using the ICP transform.	288
Figure B.20 A screenshot from the <i>IA-Image Processing</i> Graphical User Interface. This application allows access to image processing functionalities in a user-friendly interface.	289
Figure B.21 A screenshot of the interactive cropping widget including a box with moveable faces and slider bars for control over the cropping operations.	290
Figure B.22 A screenshot of the landmark widget applied to an image for seed selection used for region growing segmentation. This widget could also be used for landmark selection on a surface for the Building Block Growing Algorithm.	291
Figure B.23 Demonstration of the contour widget. A) The contour widget allows for point selection (green dots) with interpolated splines between the points. B) After a contour is finalized, it is represented as a red line.	292
Figure B.24 A sample step record to allow the user to trace operations they have used in the past.	293
Figure C.1 A scatter plot describing the femoral ACL tunnel angles of the cadaver dataset for the three angular measures (α , β , and γ).	302
Figure C.2 A scatter plot describing the femoral ACL tunnel aperture's proportional position of the cadaver dataset for the two spatial measures (c/C and n/N).	303
Figure C.3 A scatter plot describing the tibial ACL tunnel angles of the cadaver dataset for the three angular measures (α , β , and γ).	303
Figure C.4 A scatter plot describing the tibial ACL tunnel aperture's proportional position of the cadaver dataset for the two spatial measures (a/A and m/M).	304
Figure C.5 A box and whisker representation of the cadaver dataset's femoral tunnel aperture position measure n/N organized by ACL reconstruction technique.	304
Figure C.6 A box and whisker representation of the cadaver dataset's tibial tunnel angle β organized by ACL reconstruction technique.	305
Figure C.7 A box and whisker representation of the cadaver dataset's tibial tunnel angle γ organized by ACL reconstruction technique.	305
Figure C.8 A box and whisker representation of the cadaver dataset's tibial tunnel aperture position measure m/M organized by ACL reconstruction technique.	306

Figure C.9 A box and whisker representation of the cadaver dataset's femoral tunnel angle α organized by level of surgeon experience and ACL reconstruction surgical technique (MP = medial portal, TT = transtibial, TI = two incision).	306
Figure C.10 A box and whisker representation of the cadaver dataset's femoral tunnel angle β organized by level of surgeon experience and ACL reconstruction surgical technique (MP = medial portal, TT = transtibial, TI = two incision).	307
Figure C.11 A box and whisker representation of the cadaver dataset's femoral tunnel angle γ organized by level of surgeon experience and ACL reconstruction surgical technique (MP = medial portal, TT = transtibial, TI = two incision).	307
Figure C.12 A box and whisker representation of the cadaver dataset's femoral tunnel aperture position measure n/N organized by level of surgeon experience and ACL reconstruction surgical technique (MP = medial portal, TT = transtibial, TI = two incision).	308
Figure C.13 A box and whisker representation of the cadaver dataset's tibial tunnel angle β organized by level of surgeon experience and ACL reconstruction surgical technique (MP = medial portal, TT = transtibial, TI = two incision).	308
Figure C.14 A box and whisker representation of the cadaver dataset's tibial tunnel angle γ organized by level of surgeon experience and ACL reconstruction surgical technique (MP = medial portal, TT = transtibial, TI = two incision).	309
Figure C.15 A box and whisker representation of the cadaver dataset's tibial tunnel aperture position measure a/A organized by level of surgeon experience and ACL reconstruction surgical technique (MP = medial portal, TT = transtibial, TI = two incision).	309
Figure C.16 A box and whisker representation of the cadaver dataset's tibial tunnel aperture position measure m/M organized by level of surgeon experience and ACL reconstruction surgical technique (MP = medial portal, TT = transtibial, TI = two incision).	310
Figure C.17 A scatter plot describing the femoral ACL tunnel angles of the patient dataset for the three angular measures (α , β , and γ).....	310
Figure C.18 A scatter plot describing the femoral ACL tunnel aperture's proportional position of the patient dataset for the two spatial measures (c/C and n/N).	311
Figure C.19 A scatter plot describing the tibial ACL tunnel angles of the patient dataset for the three angular measures (α , β , and γ).....	311
Figure C.20 A scatter plot describing the tibial ACL tunnel aperture's proportional position of the patient dataset for the two spatial measures (a/A and m/M).	312
Figure C.21 The MOON cadaver dataset. A) Three views of the native femur with sphere representations of the tunnel aperture centroids. B) A view of the tibia with sphere representations of the tunnel aperture centroids.....	313

Figure C.22 Discrete sphere representations of the femur (3 views) and the tibia for the cadaver dataset organized by the level of surgeon experience for the transtibial technique for ACL reconstruction.	314
Figure C.23 Discrete sphere representations of the femur (3 views) and the tibia for the cadaver dataset organized by the level of surgeon experience for the medial portal technique for ACL reconstruction.	315
Figure C.24 Discrete sphere representations of the femur (3 views) and the tibia for the cadaver dataset organized by the level of surgeon experience for the two incision technique for ACL reconstruction.	316
Figure C.25 The MOON patient dataset. A) Three views of the native femur with sphere representations of the tunnel aperture centroids for the patient dataset. B) A view of the tibia with sphere representations of the tunnel aperture centroids for the patient dataset.	317
Figure C.26 ACL Tunnel Aperture Overlap Maps for the femur (left) and tibia (right) for the cadaver dataset depicting the likelihood of ACL tunnel placement on a native bone surface.	318
Figure C.27 ACL Tunnel Aperture Overlap Maps for the femur (left) and tibia (right) for the cadaver dataset depicting the likelihood of ACL tunnel placement on a native bone surface organized by surgical technique.	319
Figure C.28 ACL Tunnel Aperture Overlap Maps for the femur (left) and tibia (right) for the cadaver dataset depicting the likelihood of ACL tunnel placement on a native bone surface for the medial portal technique organized by level of surgeon experience.	320
Figure C.29 ACL Tunnel Aperture Overlap Maps for the femur (left) and tibia (right) for the cadaver dataset depicting the likelihood of ACL tunnel placement on a native bone surface for the transtibial technique organized by level of surgeon experience.	321
Figure C.30 ACL Tunnel Aperture Overlap Maps for the femur (left) and tibia (right) for the cadaver dataset depicting the likelihood of ACL tunnel placement on a native bone surface for the two incision technique organized by level of surgeon experience.	322
Figure C.31 ACL Tunnel Aperture Overlap Maps for the femur (left) and tibia (right) for the patient dataset depicting the likelihood of ACL tunnel placement on a native bone surface.	323
Figure C.32 ACL Tunnel Aperture Overlap Maps for the patient dataset depicting the likelihood of ACL tunnel placement on a native femur bone surface organized by surgeon. Eight surgeons are depicted.	324
Figure C.33 ACL Tunnel Aperture Overlap Maps for the patient dataset depicting the likelihood of ACL tunnel placement on a native tibia bone surface organized by surgeon. Eight surgeons are depicted.	325

CHAPTER 1

OVERVIEW

Medical imaging technologies have allowed for *in vivo* exploration and evaluation of the human musculoskeletal system. The utility of these technologies has exponentially grown as the time required for data collection has decreased and the image resolution has increased. Medical imaging obviously has diagnostic value, but the amount of information contained within each image set is useful in other applications including the modeling and analysis of anatomic structures. With advances in both medical imaging and computing, patient-specific model development is becoming a reality. Three-dimensional models are useful for making measurements on a patient-specific basis, and also for finite element analysis, which has traditionally provided insight into orthopaedic implant design.

Orthopaedics is closely tied to the engineering discipline in the analysis of injury mechanisms, design of medical devices used in surgical reconstructions, and potentially in the prediction of injury and clinical outcomes. However, a disconnection exists between medical imaging and orthopaedic analysis; whereby, the ability to generate three-dimensional surface models from a medical imaging dataset is difficult without the proper programming background and knowledge base. This has restricted three-dimensional orthopaedic modeling on large patient populations.

A flexible, high-throughput system is needed to guide the orthopaedic researcher and clinician through the stages of image processing, surface model development, and analysis with the ultimate goal of improving patient care. The ability to model patient-specific anatomy and perform analysis within a single clinic visit could improve surgical outcomes by providing the clinician with quantitative data to support a surgical option prior to operating. Some commercial software packages exist; however, they have restricted functionality and an associated high cost, which is far from ideal in a research

environment. We have compiled image processing, segmentation, and surface generation tools into a single software package to foster image-based orthopaedic analysis at The University of Iowa. This toolkit is connected to the existing IA-FEMesh and Surgical Suite framework in the MIMX Laboratory at The University of Iowa. We have also optimized an automated segmentation technique to allow for high-throughput bone segmentation and developed algorithms that help to automate the cumbersome process of mesh generation in finite element analysis. A flow diagram describing how the tools described in this document fit into the larger workflow are available in Figure 1.1.

In addition to developing tools to foster high-throughput orthopaedic analysis, we have applied these tools to a clinical investigation regarding the variability of graft placement in arthroscopic anterior cruciate ligament (ACL) reconstruction. Over 150 postoperative CT datasets of human knee ACL reconstructions (cadaveric and live subjects) were collected by the Multicenter Orthopaedic Outcomes Network (MOON). We have utilized our image processing, segmentation, and surface generation tools to develop surface models of this dataset. In addition, we have developed a novel measurement system to evaluate ACL drill tunnels by simulating the placement of surgical drill bits. This measurement system has been applied to the 150 CT surface models from the MOON study. Statistical analysis of the 3D measurements based on a number of different study variables was performed to identify factors that could improve patient outcomes. We also describe two 3D visualization methods for aiding in representing the results from large-scale ACL graft placement studies in a single geometric representation.

This document is organized into six sections: Understanding Modeling in Medicine, Automated Building Block Placement in Multiblock Finite Element Meshing, Musculoskeletal Image Analysis, The Anterior Cruciate Ligament, Three-Dimensional Evaluation of Tunnel Placement in Anterior Cruciate Ligament Reconstruction, and Concluding Remarks.

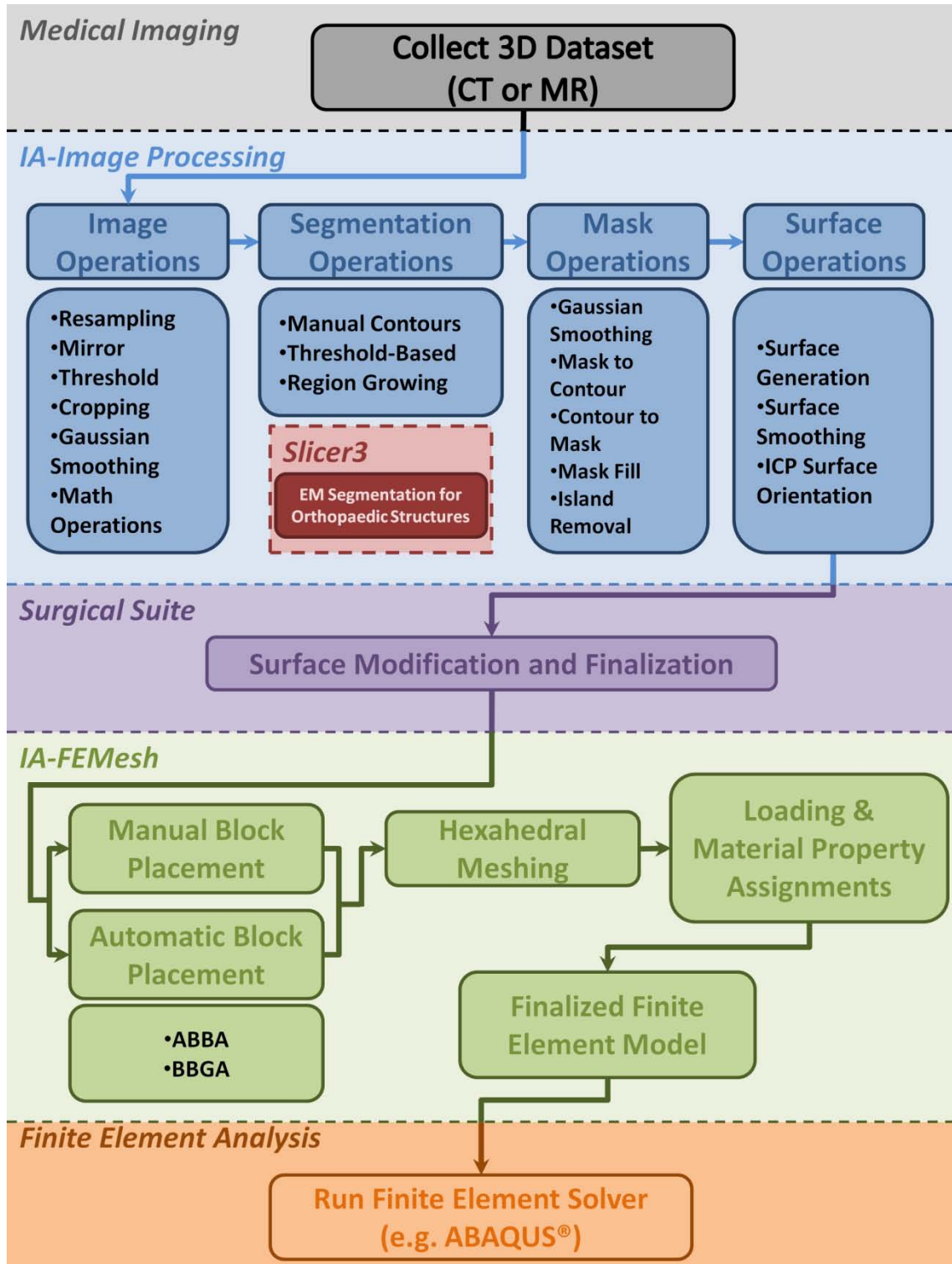


Figure 1.1 A flow diagram demonstrating the full patient-specific modeling process including the contributions in this document.

CHAPTER 2

UNDERSTANDING MODELING IN MEDICINE

2.1 Introduction

2.1.1 What is Modeling?

Experimentation and modeling are two methods of scientific research that are often intertwined. Experimentation uses physical testing to develop a better understanding of how certain parameters affect a system as a whole. Modeling applies quantitative analysis to scientific observation in hopes of enhancing understanding of a given system[1]. By aiming to understand the theoretical aspects of a given problem, modeling brings a specific toolset to scientific investigation including computer simulation and advanced statistical techniques. Establishing a useful model can be difficult since models tend to be simplifications of a system based on governing relationships. The ability to determine what should be included and what should be omitted from a model is challenging and is usually learned from experience. A good model allows a researcher to question accepted theories, critique experimental design, and discover information about a system that otherwise may have remained hidden[1]. Modelers must thoroughly understand the theoretical aspects of a system and the underlying assumptions for their model. They must be capable of interpreting whether or not the results of a model reflect reality and identify discrepancies between the theoretical and experimental. In medicine, modeling is applied in a variety of ways ranging from anatomic models to mouse models of human disease. In many ways, modeling has shaped the methods for diagnosis and treatment of many medical conditions.

2.1.2 Vital Factors in Modeling

The importance of modeling in medicine cannot be overemphasized; however, its application is by no means a trivial task. Vague descriptions and undefined goals can

often act as major roadblocks to this type of research. The first step in medical modeling can be one of the most difficult; it entails finding a system that is worth modeling. “Good” systems are found in a variety of forms, but often involve addressing a specific disease process or traumatic incident. Collaboration with medical professionals is essential to finding a problem that is timely in the research community and the clinic. The goals of medical modeling should be to provide a better understanding of a system, lead to innovations useful in medicine, or open the door for additional research. Without an application, a medical model will remain unused and the effort put into it will have been wasted. Once a system worth modeling has been identified, a specific component of the system must be identified for further analysis. For example, if diabetes was chosen as a system, then the skeletal changes associated with Charcot foot maybe an issue worth modeling. A better understanding of the development of Charcot foot could help to improve treatment and prevention of this disease process. In this example, we have identified a clinically relevant problem and a system component where modeling could be beneficial.

Once a system and a modeling objective have been identified, only then is a discussion of model type and complexity appropriate. Many different types of models exist ranging from whole body representations for dynamic analysis to bone micro-architecture models for finite element studies to hemodynamic investigations in the vascular system. The advantages and disadvantages of modeling methods must be evaluated to choose the best method for a given problem.

Once a method of modeling has been selected, the governing equations for the given model must be investigated and derived for the specific situation. Assumptions for the method of analysis must be investigated to best understand the meaning of the model’s result. The physical scale of the model must be determined, geometry and materials of the region of interest must be defined, and forces acting on the system identified. In patient-specific modeling, many of these factors are catered specifically to

an individual using various means of technology. The question becomes what level of patient-specificity is required for a given study, since the level of patient specificity also increases the level of model complexity. In some cases, highly complicated models result in unsolvable systems of equations. Many generic studies use average and standardized values from previous studies to simplify a system. Most modern patient-specific studies include at least some simplifying assumptions. For example, it is theoretically possible to estimate the forces exerted on the hip from every muscle involved in motion of the lower extremity. Whether or not this is essential for a given investigation must be determined by the investigator. If unnecessary, a model may only apply a composite force at a certain location. Recognizing the simplifications incorporated in a model is vital to understanding a model's level of applicability. For the purposes of this chapter, we will focus on musculoskeletal modeling.

2.1.3 Patient-Specific Musculoskeletal Modeling

Modeling the musculoskeletal system has been accomplished using a multitude of methods for a variety of purposes. Traditionally, experimentally measured average parameters of the musculoskeletal system have been used for research. For example, in the case of modeling a femur, geometry may be defined using anatomic properties from a single femur and material properties may be assigned based on the results of past experimental studies. Forces and loads may be assigned based on a test's design specifications. With innovations in computing and imaging technology, the ability to generate patient-specific models on a clinical basis has been a priority in recent years. Though frequently used, the term "patient-specific" seems to rarely be clearly defined, perhaps due to its intuitive undertones. However, it would seem that "patient-specific" often has a unique meaning. For example, if a study were looking at the stress imposed on the cranium of a specific baseball player after the impact of a hardball, then patient-specific may refer to the geometry and material properties of the skull. If we were

instead interested in bone remodeling as a result of the fracture, patient-specific may refer to the micro-architecture of the bone as it changes in a given patient. Instead, if we were interested in full body dynamics resulting from the impact, patient-specific may refer to the weight and geometry of the ballplayer as a whole. From a single situation, we have developed multiple definitions of “patient-specific” based on geometry, material properties, and scale. What are we really suggesting by “patient-specific” and why does it seem to have so many unique definitions?

Patient-specific modeling aims to best replicate a patient or component of a patient in terms of their response to some stimuli via means of a model. This model may be virtual, physical, computational, or defined in many other ways. Geometry, material properties, and force representation are three areas that can be made patient-specific using various techniques, but can also be simplified depending on whether or not a model requires it. The conditions and goals of a given study determine the individual meaning of “patient-specific” for a research project. Overall, patient-specific musculoskeletal modeling offers the potential to apply engineering analysis to better understand individualized orthopaedic mechanics.

2.2 Generating Patient-Specific Biomedical Models

To achieve patient-specific analysis, accurate measurements must be obtained to represent a given patient. This section is dedicated to understanding modern methods of generating patient-specific medical models. Mass and force parameters, geometry, and material properties are considered in this section; however, the final level of patient-specificity is decided upon by the investigator and is dependent on the goals of the study.

2.2.1 Generation of Models with Accurate Mass and Force

Parameters

The diversity of weight and body shape evident in the population cannot be ignored, especially in patient-specific modeling. Patient measurements can be

determined using physical measuring devices, but it is often impractical due to time constraints and funding. For these reasons, much anatomic research has focused on deriving relationships to represent average properties of body segments[2]. Using these average relationships, properties like spatial measurements, mass centers, mass distributions, and mass moments of inertia can be determined using standardized tables. Figure 2.1A shows relationships for average body segment length measured from different locations. It should be recognized that using estimated values adds a degree of uncertainty to a given study, but allows a better approximation than simply guessing. Another approach uses known simple shapes to represent body segments as seen in Figure 2.1B. Anatomic measurements and densities derived from other studies can be applied to these shapes for modeling. To track the body components in three dimensions, motion tracking systems have been developed to record the locations of specifically placed markers on the patient's body. These measurements can be used to develop velocity and acceleration data for each of the body segments during movement, which can be useful in solving whole body dynamics problems.

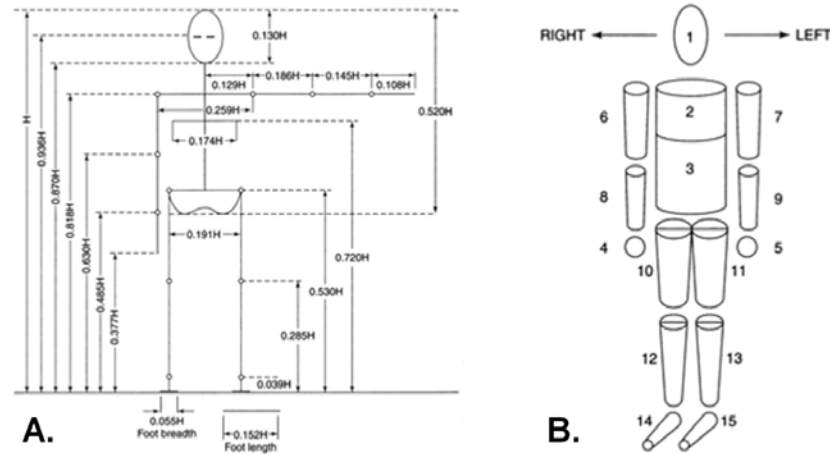


Figure 2.1 Average anatomic relationships. A) A diagram showing average length relationships useful in static and dynamic analyses. B) An example of a model using simple shapes to estimate human body segments for simplified analysis.

(Source: Bartel DL, et al.[2])

In addition to dimensional and mass properties, muscle and ligament forces can be also be estimated for modeling[2]. In mechanical representations, muscles are defined by lines of action; medical imaging and cadaveric studies have helped to define the origins and insertions of muscles to define their lines of action. In addition, electromyogram (EMG) analysis has allowed for the determination of muscle activation based on recorded voltages from specific movements. It has been found that regardless of size and shape, most skeletal muscles reach a maximum stress of 0.2MPa when fully activated[2]. If it is assumed that all skeletal muscles are maximally active, a relationship between muscle force and cross-sectional areas can be used to estimate individual forces. Since skeletal muscles are not maximally active for all movements, the EMG data can be used to scale the level of forces generated by specific muscles. Force deformation curves are available for ligaments from cadaveric studies. Ligaments do not create forces within a system, but instead deform based on the amount of force to which they are exposed. By

measuring the deformation on a patient-specific basis, we are able to estimate the amount of force within a ligament.

2.2.2 Generation of Geometrically Accurate Models

Establishing geometry that is representative of a specific patient can be vital to understanding how a particular patient may respond to a variety of factors. It can also pave the way for patient-specific implant design and surgical optimization. To generate geometric surface models with features matching those of a given patient, multiple techniques have been demonstrated including contact imaging, non-contact scanning, computed tomography, and magnetic resonance[3].

2.2.2.1 Direct Modeling

Direct modeling is the ability to generate a surface model directly from a discrete collection of points using either contact imaging or non-contact scanning. Contact imaging involves the use of touch probe digitizers, which feature a pressure sensitive tip that can be used to record three-dimensional positional information for an object[3]. If performed correctly, this method can generate an extremely accurate three dimensional point cloud representation of an object. The resolution of the generated surface model directly corresponds to the amount of time spent tracking the surface, which can prove to be slow and laborious. The resolution has an upper limit corresponding to the size of the touch probe tip. Typically, this method is limited to model generation of objects that are directly palpable. For example, model generation is limited to the surface of the skin in live patients, while deeper tissues could be represented with dissection of cadaveric specimens.

Non-contact scanning is another direct method of surface model generation. Laser-based scanning systems are used to establish a point cloud representation of the external topology of an object in three dimensions[3]. Scanning times vary based on the size of the region of interest and the desired resolution. Models of the skin surface in a

living patient or dissected components of a cadaver can be modeled using this method. However, the resolution and accuracy of the models are limited by several factors inherent to the design. The beam width sets a limit to the resolution that can be obtained using a laser scanning procedure. In addition, the line of sight for the laser is very important in collecting points. If an object has features that are not directly visible based on a line of sight, then these features will not appear on the surface model. Performing several scans and overlapping the results can reveal hidden features. Movement while the procedure is performed will also affect the accuracy of the model. In live patients, breath holding can be used to avoid motion artifact if the scan length is accommodating to a single breath hold. The composition of the material being scanned may also affect the resolution of the final surface model; transparent and highly reflective materials give poor results. In live patients, greasy or moist skin can decrease model resolution, but this can be minimized by adding talcum powder to the skin surface prior to scanning. Watery eyes and hair can also cause absorption and scattering of light that may lead to decreased surface model resolution. Smoothing filters have been developed to remove grossly outlying points from the point cloud and to improve the overall resolution of the scan.

2.2.2.2 Indirect Modeling

Medical imaging modalities have been shown to be useful in the development of three-dimensional anatomic surface models[3]. Unlike the direct surface model generation methods, these imaging modalities are capable of visualizing both external and internal structures in both cadavers and living patients. We will refer to these methods as indirect methods since additional data processing is required prior to model generation, namely, image segmentation. Magnetic resonance and computed tomography are the two most common modalities used to generate three-dimensional anatomic surface models.

2.2.2.2.1 Medical Imaging

Computed tomography (CT) imaging is a three-dimensional imaging technology that measures levels of x-ray absorption at many angles for a narrow slice of a patient[3]. By translating the patient axially through the scanner, a compilation of slices can be reconstructed to generate a three-dimensional image set, which can be used to create anatomically accurate surface models. The amount of measured x-ray absorption for a slice thickness is proportional to the density of the underlying tissues. The collection of x-ray absorption measurements can be compiled into a gray scale image with individual voxels assigned a specific value representing the x-ray absorption properties. For example, black voxels represent air (-1000 voxel value), white voxels represent dense tissues like bone (400-1000 voxel value), and intermediate gray voxels represent materials with density properties between air and bone such as fat (-40 - -80 voxel value) or soft tissues (40-80 voxel value)[4, 5]. CT imaging is a fast method of gathering anatomical information, but it does expose the patient to x-ray radiation. Due to high contrast on CT, it is the modality of choice when bones are considered the region of interest for an imaging study.

The resolution of surface models generated from CT imaging is dependent on the resolution of the medical images themselves. Partial pixel effect, anatomical coverage, slice thickness, gantry tilt, and artifacts all affect the final resolution of CT images[3]. Each resulting slice from a CT scanner is traditionally divided into a 512 by 512 pixel grid. If boundaries of different tissues intersect within a slice pixel, the boundaries between the two structures will be blurred and the pixel will have an intermediate density value. This is known as the partial pixel effect, and it has a direct effect on the ability to discern very thin or very closely spaced objects within a CT image. Since a given image is typically broken into a 512 by 512 pixel grid, limiting the field of view for a given region can increase the resolution of the image. Slice thickness refers to the distance between images of a CT imaging dataset with a typical value being 0.5mm[3]. If slice

thickness is an order of magnitude greater than the in-plane pixel size, then the resulting images and surface models may have a stair-step appearance. Collimation width refers to the width of the x-ray beam used to create the image slice. A method to generate more accurate images is to use a slice distance smaller than the collimation value; this results in image overlap, which allows for more accurate imaging of very thin structures.

The x-rays used in CT imaging can be directed at an angle to avoid radiation-sensitive organs; this angle is termed gantry tilt[3]. Large gantry tilt (approximately 90°) is easily noted on images and can be easily corrected. Small gantry tilt can be overlooked or incorrectly compensated due to difficulties in measuring the angle by which the image is rotated. Failing to correctly compensate for gantry tilt can lead to shear distortion of the image due to improperly aligned slices. Artifacts on CT images result from multiple factors. Research subjects must remain motionless during a CT scan to prevent image distortion and blurring; faster scan times have reduced this problem. Very dense bone and metallic objects within soft tissues cause scattering, streaked appearances, and false shadows. Noise within CT images can cause discrepancies at interfaces between tissues of differing density values, which can result in rough, porous surface models. Optimizing scan parameters at the front end of image collection tends to be the best way to ensure that images are of the highest quality.

Magnetic resonance imaging (MRI) is another medical imaging modality capable of producing anatomically accurate surface models[3, 6]. Unlike CT imaging, this technique does not expose a patient to x-ray radiation; however, requisite scan times are typically much longer. In very general terms, MRI takes advantage of the polarity of hydrogen nuclei in water molecules in the human body. By placing a research subject in a high field magnet, some of the water molecules can be aligned in the same direction. Radiofrequency (RF) pulses are used to temporarily alter the alignment of the molecules in a single slice (usually approximately 1mm in thickness) of the research subject[3]. After completion of the RF pulse, energy is released from the individual atoms as they

return to their former alignment. The scanner computes the precise locations of the water molecules by detecting the resulting discharged energy. Each slice is represented as a gray scale image with each level of gray being proportional to the strength of the detected discharged energy. Areas with high levels of water (blood, CSF) appear white or light gray, while areas with low levels of water (air, bone) appear black or dark gray on the images. Various MRI sequences have been designed to optimize the visualization of specific tissues based on a multitude of potential scanning parameters. Typically, MRI is the modality of choice for imaging soft tissues like the brain, muscles, and cartilage as they often have higher concentrations of hydrogen nuclei than bone. The scanner collects a multitude of slices from a given patient and these slices can be reconstructed to form a three-dimensional image set useful for generating surface models.

Multiple factors affect the resolution of MR images including scan parameters, movement, and metallic objects[3]. Slice thickness has a large impact on image quality and surface model accuracy. Like CT imaging, stair-step effect will occur if slice thickness is an order of magnitude greater than the in-plane pixel size. However, thinner slices allow for better accuracy, but also require longer scan times. Very small slice thicknesses can lead to loss of some image information if thin sections of tissue are missed between slices. Like CT scanners, motion and metallic objects cause artifacts on MR images. However, since scan times are longer for MRI, motion artifact can become an issue for image quality during breathing and swallowing. Flowing fluids within the body are not ideal for the MR scanning process. Partial pixel effect can blur boundaries between tissues as seen in CT imaging. Magnetic field variations can cause intensity nonuniformity throughout an image[7, 8]. Finally, positioning artifact can also hamper model reconstruction. For example, if a patient is lying directly on the region of interest, then soft tissues will likely deform and not accurately represent the geometry of these tissues.

Other medical imaging modalities have been used to generate patient-specific geometric models. Ultrasound and three-dimensional fluoroscopy have been used to generate surface models in some cases[9-11]. Micro-CT has been shown to be useful in developing models of trabecular bone and other structures beyond the capabilities of standard CT imaging[12]. The advantages and disadvantages of each imaging modality must be weighed to determine the best technique for a study.

2.2.2.2.2 Image Processing

After completing a medical imaging study, the images must be processed to make the anatomical information useful for model generation. Various filters have been designed to improve image quality depending on the needs of the researcher[3, 13]. Sharpening filters help to increase the ability to discern edges with the disadvantage of increasing noise, while smoothing filters help to decrease noise with the disadvantage of blurring edges. After the raw image set has been filtered, a segmentation process must be performed. Image segmentation involves the identification and isolation of regions of interest within an image set. Separating bone and muscle from musculoskeletal image sets can be challenging. Low resolution, noise, and spatial variability often make segmentation of muscle difficult[14]. The inhomogeneous composition of bone can make it difficult to separate from surrounding tissues[15]. Degenerative diseases like osteoarthritis add to the complexity by reducing the intensity difference between bones and surrounding tissues[16]. Close articulations also make it difficult to identify borders between musculoskeletal components[15].

Manual segmentation by means of tracing every slice of an image set remains the gold-standard for segmentation. However, many semi-automated and automated methods have been developed including thresholding and region-based techniques[8, 17]. Many of these methods expedite the often laborious manual segmentation but still rely on manual editing after their implementation to ensure segmentation accuracy. Typically,

these processes are divided into two parts: recognition and delineation. Recognition is the ability to identify an object in an image, while delineation is the ability to account for an object's spatial extent[18]. Thresholding segmentation techniques remove a region of interest from the background of an image simply based on voxel intensity value. Simple thresholding involves selecting a voxel value corresponding to a tissue of interest and simply extracting all voxels with that voxel value from the image[3, 6, 8, 17]. It can be performed below or above a certain voxel value or it can be performed between two values. Improvements to simple thresholding include histogram analysis and application of the expectation-maximization algorithm. Thresholding operations have traditionally worked well for segmenting regions that uniformly differ in density from their surroundings such as bone.

Region-based techniques group voxels based on a certain criteria such as texture or intensity value[8, 17]. Region growing is a technique that begins with a user-selected voxel and proceeds by checking neighboring voxels to see if they fit the selected criteria. If the neighboring voxels match the given criteria, then they are marked as being part of the region of interest. This proceeds until no neighboring voxels remain that fit the given criteria[3, 6, 17]. The final result is a connected region corresponding to the region of interest. Another region-based technique has been termed region splitting and merging[8]. This technique continuously breaks an image into quadrants and checks whether or not a given quadrant meets the selected criteria. The process continues to create sub-images until all regions have been identified and uniquely labeled. At this point, the labeled regions are compared to each other and merged if they share consistent properties. Region-based techniques can be very useful if multiple regions of an image contain identical voxel values and only a single region is desired. Problems arise if structures are within close proximity or contact, whereby region-based segmentation may include additional information than simply the single region of interest. A priori knowledge of the shape or expected location of certain anatomical features can be

included to improve most segmentation results. Additional methods have been developed that utilize the power of statistics[10, 19-21], positional information[22], neural networks[23], shape information[19], and combinations of multiple techniques[17, 24-26].

2.2.2.3 Surface Representations

Either the resulting point set or segmented image from image processing can be useful for generating three-dimensional surface representations[8]. Through additional image processing procedures, a segmented image can be transformed into a collection of points like those obtained from direct imaging methods. A point set can be used to represent a surface as seen in Figure 2.2A; however, area and volume calculations are not directly available. A more standard surface representation is a triangular mesh which is composed of vertices and triangles as seen in Figure 2.2B. Several triangulation methods have been developed including Marching Cubes and Delaunay[24, 26]. The Marching Cubes algorithm uses the look-up table approach to evaluate a 2 by 2 by 2 voxel grid to identify point patterns and develop a triangulation scheme. Delaunay triangulation produces a maximally equilateral triangle mesh for a given point set using Voronoi and Delaunay diagrams. Triangulation software using these techniques is freely available to generate a triangular mesh from either a segmented image or a point set. The resulting triangular surface mesh allows for easy visualization and analysis of the region of interest. These virtual representations are often directly used for diagnosis and patient education in cases of complicated geometry such as in comminuted fracture visualization[11].

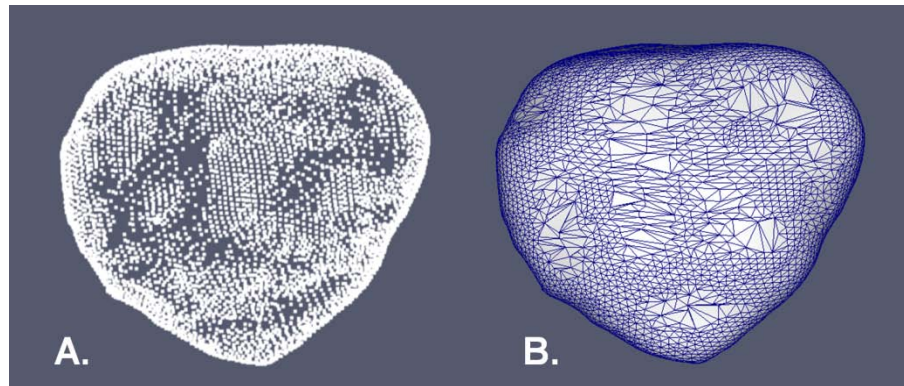


Figure 2.2 Virtual surface representations. A) A point cloud distribution of a patient-specific model of the patella. B) A triangulated surface mesh of a patient-specific model of the patella.

2.2.2.4 Physical Models

Once surface representations have been generated of a patient-specific region of interest, the goals of a study direct whether the analysis is purely virtual or if a physical model will be necessary. Physical models have the advantage of allowing direct contact and interaction with a three-dimensional object. Testing or product finishing may come as a next step for the physical model. Section 2.4.1 will briefly investigate the production and potential applications of physical models. If a virtual model is desired, various computational methods for this technique have been developed. The applications of virtual models will be the concentration of Section 2.4.2.

2.2.3 Generation of Models with Accurate Material

Properties

Material properties are often important in the analysis of musculoskeletal structures and can be an important factor in attempting to tailor analysis to a specific patient. Musculoskeletal elements (e.g. bone, muscle) have a hierarchical structure that may be important to a given analysis. The level of detail required is determined by the scale (e.g. whole bone versus microstructure of bone) required by the study[2].

Anisotropy, non-homogeneity, elasticity, plasticity, fatigue, and creep are properties that are shared amongst many of these materials that can make them difficult to model. However, material properties can be assumed to be a continuum if the study has the correct physical scale. In general, material properties have been determined for the musculoskeletal system based on traditional testing procedures, but these estimated values must be compared to regions with similar microstructures. Calibration curves for these materials have been used widely in biomedical research; however, it has been noted that age, disease, and inter-patient variability must be viewed as a limitation. If available, material testing can be performed for the specific tissues of interest to obtain patient-specific values; however, this is not necessarily practical for live patients. In the development of patient-specific models using medical imaging, bone density and spatial properties determined from voxel intensity values can be correlated back to obtain specific values for material properties[27, 28]. In particular, this information is useful for finite element analysis where it is often necessary to assign material properties to individual pieces of a structure.

2.3 Musculoskeletal Analysis Methods

Analysis of the musculoskeletal system is performed on a variety of levels depending on the goals of a given study. By utilizing patient-specific factors, these analysis techniques can be performed on a patient-specific basis. Static and dynamic analyses are often utilized to obtain a general understanding of a system and to derive equations for more complex analysis techniques. Using mechanics of materials theory, structural analysis can be performed using simple model representations. Continuum mechanics is often thought of as the “gold-standard” of analysis of components of the musculoskeletal system. In this section, the abilities and assumptions associated with these analysis techniques are investigated.

2.3.1 Static and Dynamic Analysis

To perform rigid body engineering analysis on the musculoskeletal system, the system can be viewed as a series of rigid links, actuators, and constraints[2]. Newton's laws can be used to determine resulting forces within a structure. Typically, rigid body mechanics has three components: a description of the system in mechanical terms, a description of the external forces and constraints on the system, and application of the laws of motion to the system[2]. Rigid body model elements can be assigned to individual components of the musculoskeletal system. Bones and limb segments are typically modeled as rigid links with assigned mass and dimensional properties. A rigid link system assumes that bone is a rigid structure, which is a limitation to this method as bone is a deformable structure. Joints are modeled as rigid or deformable contact regions that add kinematic constraints on a system. Different joint types (e.g., hinge versus ball and socket) require different constraining conditions. Joints are typically assumed to be frictionless and ignore cartilage deformation. Muscles and tendons are often represented as simple actuators, but can be modeled as a more complicated system of viscoelastic components as seen in Figure 2.3A.

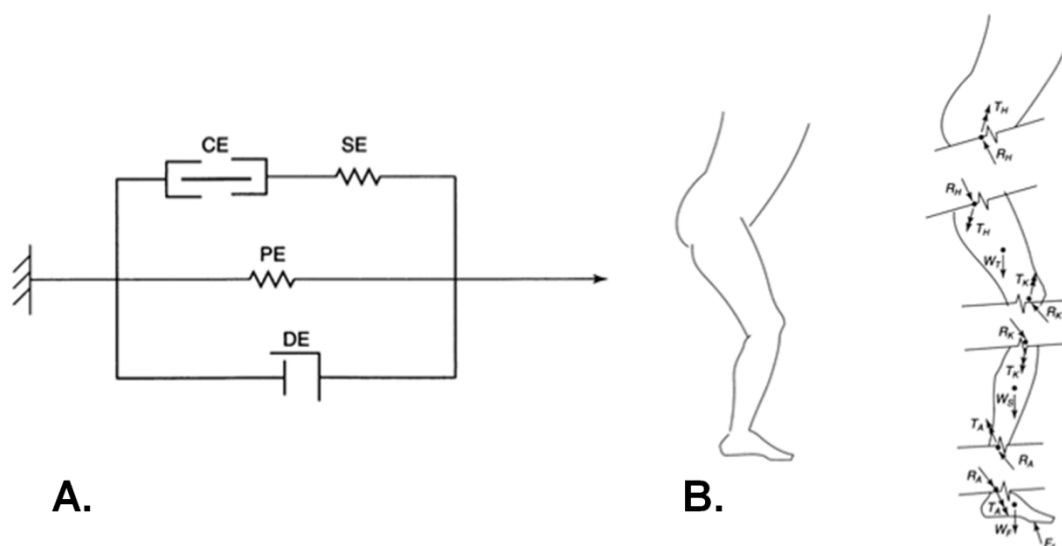


Figure 2.3 Mechanical representations of the musculoskeletal system. A) A rigid body mechanics representation of a muscle composed of a contractile element (CE), serial elastic element (SE), parallel elastic element (PE), and a viscous element (DE). B) A simple free body diagram representing the forces and torques represented in the lower extremity.

(Source: Bartel DL, et al.[2])

Rigid body models assume that muscles act along a straight line of action from origin to insertion and ignore any complex interaction with the surrounding tissues. Ligaments and joint capsule components can be incorporated as elastic or viscoelastic springs in the system with properties derived from experimental force-deformation curves. The goals of a study determine the design of a rigid body model for a segment of the body. If motion is absent, a static analysis can be performed; otherwise, a dynamic analysis is performed. Either way, Newton's laws of motion can be applied to the system to solve for the system's internal forces. Free body diagrams are often used to define unknown forces and moments within a system. Figure 2.3B demonstrates the generation

of a simple free body diagram of the lower extremity that can be used to determine resulting forces (R_i) and moments (T_i) based on knowledge of system weights and forces. To determine forces within individual elements of the system such as specific muscles, additional techniques are required to compensate for the system's indeterminacy.

Static analysis is appropriate for determining internal system forces when external loads are applied and motion is absent. In these cases, the system is defined by a system of rigid links, each having force (F) and moment (M) equilibrium equations assigned to them (Eq. 2.1-2.2)[2].

$$\sum(F_i)_{int} = - \sum(F_i)_{ext} \quad (\text{Eq. 2.1})$$

$$\sum(M_i)_{int} = - \sum(M_i)_{ext} \quad (\text{Eq. 2.2})$$

In three dimensions, we will have $6n$ equations for the system with 'n' being the number of links in the system. Internal forces in the system are considered to include joint contact forces, muscle forces, ligament forces, and soft tissue forces. External forces acting on the system include gravity and loads applied to the system.

Dynamic analysis incorporates accelerations into static analysis using Newton's laws of motion to determine the resultant forces and moments acting across a joint. In these cases, mass (m), acceleration (\ddot{r}), and angular accelerations (\dot{H}) are incorporated (Eq. 2.3-2.4)[2].

$$\sum(F_i)_{int} + \sum(F_i)_{ext} = m_i \ddot{r}_i \quad (\text{Eq. 2.3})$$

$$\sum(M_i)_{int} + \sum(M_i)_{ext} = \dot{H}_i \quad (\text{Eq. 2.4})$$

In three dimensions, we will also have $6n$ equations for the system with 'n' being the number of links in the system. Two methods of dynamic analysis have been developed: direct dynamics and inverse dynamics. Direct dynamics determines resulting

motions of a system based on known forces of a system. This requires the number of unknown forces to be equal to the number of known equilibrium equations. This is not commonly used since it is rare that all forces are known before the analysis, but it is solvable using iterative methods. Inverse dynamics determines the forces of a system based on known motions and a loading history. Here as well, the number of unknowns exceeds the number of available equations. However, this is often preferred since incorporation of motion tracking systems can reduce the number of unknowns to match the number of system equations.

Static and dynamic analyses are useful in investigating the forces across joints and between adjacent segments, but are incapable alone of determining the forces present in individual components of the system. Muscle redundancy is an example of this principle since the inclusion of individual muscles in most systems renders an indeterminate system of equations[2]. To avoid this, two tactics can be applied: include auxiliary information or utilize engineering optimization. Auxiliary information aims to increase the number of system constraints to reduce the number of unknown variables. This can be accomplished by force reduction, muscle scaling, and soft tissue inclusion. Force reduction uses EMG data and prior knowledge to identify forces that can be eliminated from the system of equations to allow for a determinate system. Muscle scaling uses EMG data to determine the proportionality of muscle involvement based on underlying assumptions that we have previously discussed. Determining muscle force proportionality relationships reduces the number of system unknowns. Soft tissue deformation based on experimental force-deformation curves can also reduce the number of system unknowns. Optimization, the second technique, is a method used in engineering that aims to maximize or minimize a specific criterion for the system. In the case of muscle activation, it has been theorized that the nervous system determines the mechanically optimal combination of muscles to reach a certain configuration of the

body. Optimization finds the best combination of muscles to perform a certain body motion amongst a large number of possibilities.

2.3.2 Structural Analysis

Structural analysis of musculoskeletal system components can be performed on a variety of levels ranging from simple to complex[2]. The ability to select the simplest method of analysis for a study should be the goal when determining the most appropriate modeling method. Equations derived from mechanics of materials offer a computational means to determine values of interest (e.g. stress and strain) in geometrically simplified but representative systems. In simplified systems, isolated components of an overall system are typically modeled to obtain rudimentary information or to validate more complex models. Several techniques have been shown to be useful in orthopaedic applications including beam and contact analysis.

Composite beam theory has been shown to be useful in investigating load sharing between bones and implant systems[2]. This is performed with the assumption that the area of investigation is far from abrupt changes in geometry, material properties, and loading. It is also assumed that the material is elastic and the plane sections of a material remain in-plane after bending. Using equilibrium equations, Hooke's law, and the definitions of stress and strain, the equations necessary to determine the stress and strain values are derived for the cases of axial loading and bending. After deriving the equations for a beam composed of one material, it can easily be extended to include beams with multiple materials to represent bone-implant systems if necessary. In the case of an unsymmetrical cross section such as in bones, the equations can be modified to represent this type of system to avoid errors in magnitude and location of maximum bending stresses. This type of analysis has been used to estimate the likelihood of developing vertebral compression fractures and hip fractures as well as to act as a method to verify the results from finite element analysis.

If it is necessary to determine load distributions, then beam on elastic foundation analysis is useful[2]. In this analysis, differential equations are derived to associate displacement of the beam and foundation due to the load. This type of analysis has been used to investigate the stresses involved in bone-cement-implant systems. To investigate the interface between two objects, contact analysis is typically used to investigate the stresses and deformations. Hertz theory is utilized when the two materials have similar elastic modulus values, while elastic contact analysis is performed when the elastic modulus differs significantly. In contact analysis, loading increases result in increasing pressure and contact area, an inherent nonlinearity. This type of analysis assumes that the contact area is much smaller than the whole object and that the contact is frictionless. Equations have been derived using simplified shapes for both Hertz Theory and elastic contact analysis, and have been useful in evaluating the contact between the acetabulum and femoral head in total hip arthroplasty systems. Overall, structural analysis techniques offer a means to evaluate simplified versions of a system to obtain rudimentary information or to allow for validation of more complex analysis types.

2.3.3 Continuum Mechanics

Continuum mechanics is a third method of analysis commonly applied to biomedical models[29-31]. Solid, fluid, and thermal mechanics have all been mathematically described by systems of differential equations limited to applications involving a small number of simple geometries and specified loading conditions. The guiding principle of continuum mechanics is that it is possible to derive equations and relationships that describe small pieces of an often geometrically complex system. In this type of analysis, a model is broken into a large number of smaller pieces, an element mesh, which allow for the determination of a solution to an otherwise unmanageable problem. Equilibrium and material equations are used to link the many small pieces together and enable the approximation of stress and strain values, heat transfer, or fluid

flow within a given system. A large number of elements with small element volumes results in an increased accuracy of the approximation; however, increased accuracy comes with the cost of increased computational time.

Continuum mechanics analysis is typically broken into three stages: pre-processing, solving, and post-processing. In the preprocessing stage, the geometry of interest is defined and an element mesh is assigned to this geometry. In the solving stage, systems of equations are generated and solved; multiple formulations have been developed to address the solver stage. Finally, post-processing allows for easy visualization of the results. Traditionally, three numerical methods have been associated with the solving stage of continuum mechanics; they include the finite difference, finite element, and the boundary element methods. All three methods typically involve three steps in their analysis including replacement of calculus with algebraic expressions, generation of a mesh or grid to represent the geometry of an object of interest, and finally a solution set of algebraic equations to describe an unknown system response for a variable determined by the user. Finite element and boundary element are well established in the analysis of solid mechanics, while finite difference has been most useful in heat transfer and fluid flow analysis. Combinations of these methods also exist for various applications, but our concentration will be on the three traditional methods[29].

Accuracy of the results from continuum mechanics is dependent on the information that is put into the model to be analyzed. Mesh geometry, boundary conditions, and initial conditions are required for analysis; these three areas must be defined with care to ensure an accurate solution. If the element mesh does not accurately represent the geometry of interest, then analysis of the model will also not represent the model of interest. If elements within the mesh are distorted, then the results of the analysis can also be skewed. Boundary and initial conditions must be carefully selected to ensure they accurately represent joint, ligament, and muscle forces[32, 33].

2.3.3.1 Governing Equations

In addition to the equations from statics and dynamics, equations relating to material properties are also available to handle indeterminate systems. Continuum mechanics relies on these equations in establishing a determinate system of equations. In three dimensions, there are six strain-displacement equations (Eq. 2.5-2.10) that are defined as follows with ϵ representing strain and u representing displacement.

$$\epsilon_{xx} = \frac{\partial u_x}{\partial x} \quad (\text{Eq. 2.5})$$

$$\epsilon_{yy} = \frac{\partial u_y}{\partial y} \quad (\text{Eq. 2.6})$$

$$\epsilon_{zz} = \frac{\partial u_z}{\partial z} \quad (\text{Eq. 2.7})$$

$$\epsilon_{xy} = \frac{1}{2} \left(\frac{\partial u_x}{\partial y} + \frac{\partial u_y}{\partial x} \right) \quad (\text{Eq. 2.8})$$

$$\epsilon_{xz} = \frac{1}{2} \left(\frac{\partial u_x}{\partial z} + \frac{\partial u_z}{\partial x} \right) \quad (\text{Eq. 2.9})$$

$$\epsilon_{yz} = \frac{1}{2} \left(\frac{\partial u_y}{\partial z} + \frac{\partial u_z}{\partial y} \right) \quad (\text{Eq. 2.10})$$

In three dimensions, Hooke's law allows us to define six stress-strain relationships (Eq. 2.11-2.16) as follows where μ represents the shear modulus, ΔT represents temperature change, ν represents Poisson's ratio, E represents Young's modulus, and α represents the coefficient of thermal expansion.

$$\epsilon_{xx} = \frac{1}{E} [\sigma_{xx} - \nu(\sigma_{yy} + \sigma_{zz})] + \alpha(\Delta T) \quad (\text{Eq. 2.11})$$

$$\epsilon_{yy} = \frac{1}{E} [\sigma_{yy} - \nu(\sigma_{xx} + \sigma_{zz})] + \alpha(\Delta T) \quad (\text{Eq. 2.12})$$

$$\epsilon_{zz} = \frac{1}{E} [\sigma_{zz} - \nu(\sigma_{xx} + \sigma_{yy})] + \alpha(\Delta T) \quad (\text{Eq. 2.13})$$

$$\epsilon_{xy} = \frac{1}{2\mu} \sigma_{xy} \quad (\text{Eq. 2.14})$$

$$\varepsilon_{xz} = \frac{1}{2\mu} \sigma_{xz} \quad (\text{Eq. 2.15})$$

$$\varepsilon_{yz} = \frac{1}{2\mu} \sigma_{yz} \quad (\text{Eq. 2.16})$$

2.3.3.2 Finite Difference Method

The finite difference method divides a system or object into a structured grid of cells (finite difference mesh) and generates algebraic approximations of a system's governing differential equations[30, 31]. Figure 2.4 shows a sample mesh and the variables associated with the algebraic approximations.

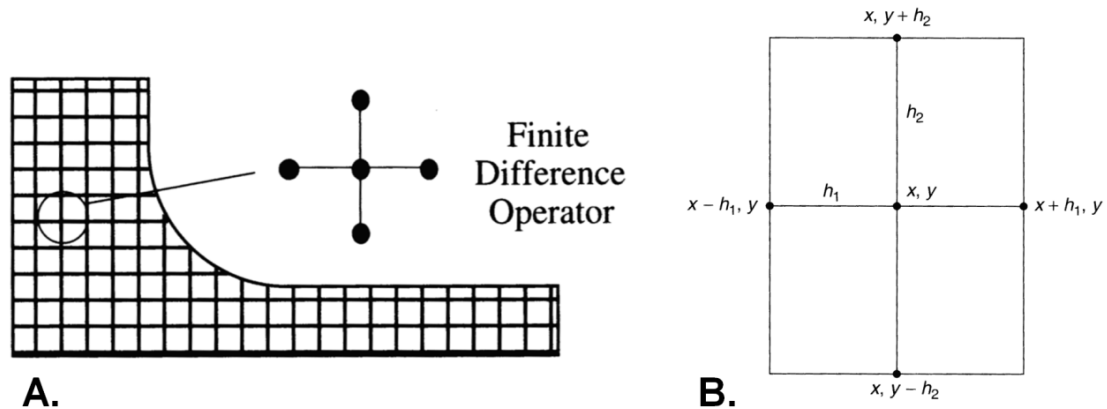


Figure 2.4 The finite difference method. A) An example of a finite difference mesh and its node structure. B) A section of a finite difference mesh with associated variables assigned to demonstrate the finite difference variables.

(Source: A) Kane JH, et al.[31] B) *Encyclopedia of Computational Mechanics: Fundamentals*[29])

Formally, the derivative of a function can be expressed as a Newtonian Quotient (Eq. 2.17), which describes the difference between two points (x and $x+h$) on a function (u) with an infinitesimally small step (h)[29].

$$u'(x) = \lim_{h \rightarrow 0} \frac{u(x+h) - u(x)}{h} \quad (\text{Eq. 2.17})$$

Assuming that the step size is measurable, algebraic equations can be used to approximate the derivative of the function with regards to the two points. This approximation can be substituted into a system's governing differential equations to allow for numerical approximation. Each node of the finite difference mesh can be calculated using this relationship applied to three equations: forward, backward, and central. The forward difference equation (moving a step, h , in the positive direction on a given axis) is given by two points, x and $x+h$ [29] as shown in Eq. 2.18.

$$u'(x) \approx \frac{u(x+h) - u(x)}{h} \quad (\text{Eq. 2.18})$$

The backward difference equation (moving a step, h , in the negative direction on a given axis) is given by two points, x and $x-h$ [29] as shown in Eq. 2.19.

$$u'(x) \approx \frac{u(x) - u(x-h)}{h} \quad (\text{Eq. 2.19})$$

The central difference equation (moving a step, $h/2$, in both the positive and negative directions from a central point, x) is given by two points, $x+h/2$ and $x-h/2$ [29] as shown in Eq. 2.20.

$$u'(x) \approx \frac{u(x+h/2) - u(x-h/2)}{2h} \quad (\text{Eq. 2.20})$$

The above equations are given only in a single direction for simplicity, but they can easily be expanded in three dimensions. By being able to represent a differential equation algebraically, we can reduce a problem requiring calculus to a manageable algebraic expression. Finite difference approximations are calculated for each node to

approximate values for the entire finite difference mesh. The calculation structure shows that the displacement of a node is related to the displacement of surrounding nodes connected by the grid structure. Boundary and loading conditions for a given problem are necessary to find a unique solution to the system of algebraic equations. The number of nodes within the finite difference mesh directly corresponds to the number of unknown variables and the computational time required in solving the entire system.

Two types of error are inherent to the finite difference method[29]. Rounding error is always present and simply deals with rounding numbers during a calculation. The second type of error, truncation error, deals with the difference of an estimated result and the actual system. This can be estimated using a Taylor series derivation and shown to be proportional to the step size, h [29]. An advantage of this method is its ability to easily transform calculus into an algebraic approximation with little effort. A disadvantage of the finite difference method is that it is not ideal for objects with complicated geometries due to the structured nature of its mesh[29, 31]. In addition, it is difficult to vary the mesh density, which can hamper analysis of regions with rapidly changing variables. Typically, finite difference methods are most useful for heat transfer and fluid flow problems[30].

2.3.3.3 Boundary Element Method

The boundary element method divides a system into a collection of boundary segments or surface elements as shown in Figure 2.5[29-31]. Unlike the finite difference method, the governing differential equations are not directly used in the boundary element method; instead, they are transformed into equivalent integral equations. Based on specific geometries, boundary conditions, and the Gauss-Green and Divergence Theorems, the integral equations are transformed from a combination of volume and surface integrals to only a collection of surface integral equations. The system of equations can be solved given appropriate boundary and initial conditions, and

polynomial interpolation allows for extension of the solution to all locations within the system. The calculation of internal points is optional for the boundary element method, and is dependent on the goals of the analysis[29].

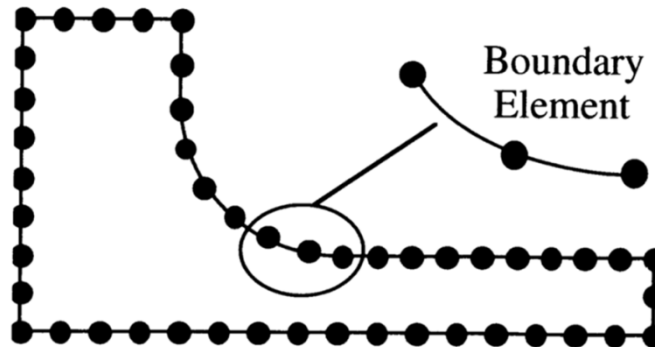


Figure 2.5 An example of a boundary element mesh demonstrating the boundary segments/elements as the operator for the mesh.

(Source: Kane JH, et al.[31])

To understand how the boundary element method works, an understanding of the Gauss-Green Theorem, Divergence Theorem, and Green's Second Identity is best described elsewhere[31]. The final result is an equation (Eq. 2.21) that relates a volume integral to a surface integral seen as follows with b as a scalar function, a as a gradient function, and 'n' as vector normal to the surface.

$$\int_V (b \nabla^2 a - a \nabla^2 b) dV = \int_S (b \nabla a \cdot \mathbf{n} - a \nabla b \cdot \mathbf{n}) dS \quad (\text{Eq. 2.21})$$

The Gauss-Green Theorem, Divergence Theorem, and Green's Second Identity demonstrate the methods by which the governing differential equations can be manipulated in such a way to find a form that can be manageably solved.

The governing equations are manipulated to form the boundary integral equations for the system using the aforementioned methods[31]. To approximate the solution for the entire system, we estimate the integrals at each of the nodes within the boundary element mesh by polynomial interpolation. Using boundary conditions and loading conditions, we can simplify the complicated integration procedure to that of a simple integration of an algebraic expression. Various computerized integration techniques are available that sum the area under the curve including the equal interval and Gauss methods. By performing this procedure at each of the nodal points, we are able to match the number of unknowns with the number of equations available. Typically, the equations are organized into a matrix format with the rows corresponding to the nodes and the columns corresponding to the individual boundary elements. Various matrix solving procedures are available with Gauss elimination being one of the most common. Once the solution has been determined for the nodes of the boundary element mesh, interior values can also be determined using alternative methods.

Since this method is based on analysis of the boundary, modeling the boundary and incorporating boundary conditions is relatively easily[30, 31]. Different derivations have allowed for inclusion of elastic and nonlinear material behavior in the analysis. Unlike the other methods, only surface grids are required for this analysis type, which can be easier to develop than volumetric meshes. Boundary element analysis is not limited to a single area of application; it is applicable to solid, fluid, and thermal analysis. This method can easily model regions of complicated geometry and since calculations are restricted to the surface, it can account for regions of rapidly changing variables. However, boundary element analysis can require numerical integration of complex functions which is computationally expensive and time consuming. A boundary element analysis with 'n' nodes, will have 'n' independent equations generated from integrating the boundary integration equations over the original 'n' nodes. Thus larger numbers of nodes leads to additional unknowns and additional computational time. Typically, this

method is reserved for certain applications that are not easier accomplished using finite difference and finite element methods.

2.3.3.4 Finite Element Method

Finite element methods have been considered a cornerstone for solid mechanics for many years. The first finite element model of a human organ was performed on the spine in 1973[33]. Today's literature is saturated with studies that have applied this method for a variety of applications within engineering including solid, fluid, and thermal mechanics. Like the finite difference and boundary element methods, the finite element method also requires a mesh as shown in Figure 2.6[30, 31]. The mesh is unstructured which allows elements to fit a wide variety of geometries. The method is based on transforming a system's governing differential equations into volume integral equation representations, which are adapted to each node of the finite element mesh. Between the nodes, polynomial interpolation is used to determine unknown quantities. In solid mechanics, displacement is used to describe the system, and with appropriate boundary and loading conditions, a unique solution for the system can be determined. Finite element meshes address the issues of complex geometry and also allow for accurate representation of regions with rapidly changing variables. However, the accuracy of finite element analysis is dependent on a variety of factors including how accurately a finite element mesh represents the geometry of interest.

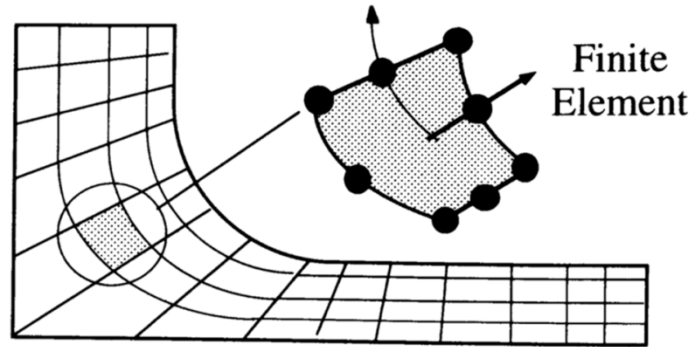


Figure 2.6 An example of a finite element mesh demonstrating the finite element node structure as the operator for the mesh.

(Source: Kane JH, et al.[31])

Mesh generation can prove to be a time-consuming and challenging task, which has spurred the development of automated meshing software both commercially and academically. Prior to mesh generation, the best element type for the analysis at hand must be determined. Two categories of elements have been developed: structural and continuum. Structural elements include beam, plate, and shell elements, while continuum elements include line, 2D plane stress, 2D plane strain, axisymmetric, and 3D elements.

Structural elements are reserved for situations where one dimension of an object is significantly smaller than the other dimensions, and mechanics of materials approximations are used to account for the smaller dimension. They are less computationally expensive than continuum elements, and include rotational degrees of freedom in addition to displacement degrees of freedom. Structural elements require rotational degrees of freedom to satisfy boundary conditions associated with bending behavior typical of this element type.

Structural elements are used for specific purposes and have certain assumptions associated with them. Beam elements are used to analyze rigid joints of frames, plate

elements are used to analyze transversely loaded flat thin structures, and shell elements are used to model curved objects with a small thickness. Beam and shell elements have six degrees of freedom corresponding to three displacements and three in-plane rotations. Plate elements have three degrees of freedom corresponding to transverse displacement and two in-plane rotations normal to the surface. All three types assume that shear deformation is negligible if the elements are thin, and that plane sections remain unchanged after deformation. Also, shell elements ignore stress differences across the thickness of the element.

Continuum elements, the other element class, are also used to approximate the element displacements[30]. A one-dimensional line element is the simplest form of continuum elements. In this case, an axial load is applied and only a single displacement degree of freedom is calculated. In two-dimensional problems, a three-noded triangle is the simplest element that can be used and two degrees of freedom are investigated. Two dimensional elements can be used to approximate three-dimensional elements by assigning a given thickness to the elements. In the case of very thin geometries, a plane stress element is used and this assumes that the stress in the direction of the thickness can be neglected in the analysis. In the case of very thick geometries, a plane strain element is used and this assumes that strain in the direction of the thickness can be neglected in the analysis. Axisymmetric elements utilize geometric symmetry to simplify a three-dimensional analysis into a two-dimensional problem that is rotated 360 degrees about an axis. Three-dimensional continuum elements are widely used with tetrahedron and hexahedron shapes being the element shapes with three degrees of freedom[33]. Tetrahedrons are more commonly used for representation of complex geometries. Hexahedrons fill a given volume with fewer elements than tetrahedrons, and thus have a faster computation time. Three-dimensional analysis is more computationally expensive than two-dimensional analysis, but avoids many of the assumptions that are otherwise required.

After element type and shape have been defined, we must determine the interpolation function for the elements[30]. Linear interpolation is often used to model the displacement over each element. Strain-displacement and stress-strain relationships are used to help match the number of unknown variables with the number of equations. After the equations have been defined for the system, the next step involves developing the element stiffness matrix, k_e . This matrix helps tie together the interpolation, strain-displacement, and stress-strain equations and is better described elsewhere. Two options are available for developing the element stiffness matrix including the Direct Equilibrium Approach and the Energy Approach. Typically, the Energy Approach is used due to its applicability to a wide variety of problems and element shapes. In the Energy Approach, the goal is to reach equilibrium; equilibrium is defined as the state where potential energy is at its minimum, this is also known as the principle of minimal potential energy. In a system, total potential energy is defined as the difference between strain energy (U) and work (W) performed by the system. A detailed explanation of this is better described elsewhere, but it is summarized in Eq. 2.22 where $dv = A_e dx$, 'A' is the cross sectional area, u is displacement, and F is force.

$$TPE = U - W = \int_v \frac{1}{2} [\sigma]^T [\epsilon] dv - [u_e]^T [F_e] \quad (\text{Eq. 2.22})$$

After numerical integration of the volume integral, the resulting equations are used to assemble the global system of equations for the elements including the element stiffness matrix. This system of equations can be represented as shown in Eq. 2.23.

$$[F]_{external} = \sum_{elements} [F_e] = \sum_{elements} [k_e] [u_e] \quad (\text{Eq. 2.23})$$

Boundary conditions help to fill aspects of the displacement matrix, u , and external loads are used to fill the force matrix, F . To solve the equations, standard

equation solvers are implemented to find the unknown displacement and force variables. The unknown values can then be used to solve for stresses and strains in the system.

Finite element model accuracy is dependent on a variety of factors that can easily lead to error. Boundary conditions must be carefully selected to ensure that it accurately represents joint, ligament, and muscle forces[32, 33]. The equations and material properties used to represent model mechanics may not exactly represent the behavior. Mesh generation for finite element analysis can be challenging and a source of error. Also, if elements within the mesh are distorted then the results of the analysis can also be skewed. Displacement based FE techniques typically overestimate the stiffness of individual elements[30]. Since stiffness is used to determine the unknown displacements, the displacements are underestimated, which also leads to an underestimation of stresses. After analysis, stress and displacement values should always be checked for accuracy.

One method of improving the accuracy of finite element models is incorporating higher order interpolation functions for approximating displacements within elements. Linear approximations assume a constant displacement over all elements, which results in a constant strain value in each element. Refining the mesh to account for regions where variables change rapidly can ensure accuracy; however, quadratic or higher order functions can also approximate displacements without increasing the number of elements. These higher order equations do come with additional computational complexity. Nonlinear behavior can be represented in finite element analysis to better represent materials that have a response that is not linear[30]. Nonlinearity is a property related to material, geometry, and boundary behaviors. These nonlinear properties can be accounted for by applying loads in small increments which allows a representative behavior at each increment. Care must be taken when incorporating nonlinear properties in a finite element analysis to ensure that the model is demonstrating the expected results.

2.3.3.5 General Guidelines for Continuum Mechanics

Solutions from continuum mechanics are approximations to the exact solution and should always be carefully checked for accuracy[30]. Prior to performing an analysis on a given system, a problem with a known solution should be performed to test the capabilities, usability, and accuracy of the software. This is sometimes called a benchmark study. Once the method of solving (e.g. hand calculation or computer solver) has been verified, additional steps should be taken to ensure that the final results are as accurate as possible. Constraining conditions must accurately represent the desired conditions and prevent rigid body motion. Additionally, the mesh representation of the object must accurately represent the object's geometry. Using the correct size and shapes of elements is essential to performing an accurate analysis. Ensuring that element size does not abruptly change and is evenly distributed across the mesh will help to allow an accurate approximation. Very long and thin elements should be avoided, while increasing the element density in regions of rapidly changing stress will allow for the best accuracy. Ideally, a convergence study is performed to determine the minimum number of elements required to obtain an accurate solution in the minimum amount of time. After the analysis has completed, several factors should be checked to ensure accuracy. As a first check, final stress and strain values should be roughly checked to ensure that their values are consistent with experimental or expected values. As a second check of the analysis, external forces should be checked against the calculated reaction forces. Finally, round off error and error associated with numerical integration must be accounted for as they are inherent to continuum mechanics analysis methods.

2.4 Applications of Biomedical Modeling

The development and analysis of biomedical models, both computer representations and physical objects, has spurred research and development of new technologies[3]. Modeling is not limited to a single role; instead, it has provided a means

to improve many aspects of medicine. The ability to visualize virtual models of complex anatomy allows direct interaction with otherwise “hidden” anatomical features. During patient counseling, this enhanced ability to visualize a given problem can improve patient understanding and aid in establishing a treatment plan. From a surgeon’s perspective, modeling allows improved diagnostic ability especially in cases that are difficult to visualize from an image set alone. By better understanding the underlying anatomy through visualization, surgical simulations can be performed to practice and test surgical approaches. Analysis of biomedical models improves surgical planning by allowing for mathematical optimization of a given procedure prior to its actual implementation. From a technical perspective, modeling provides a means to prepare surgical templates prior to surgery, aid in orientation during surgery, and produce surgical implants that will ideally function appropriately for the remainder of a patient’s lifespan. This section is dedicated to presenting a small sample of medical modeling examples with a concentration on surgical and orthopaedic applications.

2.4.1 Rapid Prototyping

Rapid prototyping uses three-dimensional computer representations to generate physical models in a matter of hours[3]. The technique has its roots in the automotive and aerospace industry where models are generated with geometric regularity. Human anatomy is geometrically irregular, which leads to a variety of challenges in generating physical models. A variety of rapid prototyping techniques have been developed for physical model generation including stereolithography, digital light processing, fused deposition modeling, selective laser sintering, three-dimensional printing, jetting head technology, and laminated object manufacture. These methods are cumulatively referred to as layer prototyping methods as each involves the generation of a model from a series of layers built in succession, but each method uses a different material or process to achieve the final physical model. Stereolithography, one example, involves curing thin

layers of liquid resin by UV light using a very accurate laser[4, 5]. A stage is lowered as each layer is cured to eventually generate a complete physical model. Typically, the x and y-axes correspond to the plane in which the layers are formed, while the z-axis corresponds to the layering direction. Most techniques are accurate to fractions of a millimeter in the xy plane, and typically the layer thickness is between 0.05mm and 0.3mm. Layering can cause a step-effect in the z-axis, thus the model is typically oriented such that details are most represented in the x- and y-axes. The resolution in the x- and y-axes is limited by the diameter of the laser beam.

A variety of factors must be considered when generating physical models using rapid prototyping[3]. Model orientation is crucial to the build process for many reasons some of which have already been addressed. Orientation can greatly affect the cost of a given prototype by reducing the number of layers necessary for a build, which also reduces the time necessary to develop a physical model. However, reducing the number of layers can also cause a stair-step artifact which means that a balance between model smoothness and cost must be determined. Depending on the shape of the structures being developed, supporting structures may be necessary during the build phase for the model. These are typically removed after the model is completed, but optimizing orientation to reduce the number of supporting structures necessary is important to reduce cost. Orienting the object so that the widest section is built first is vital to avoid the risk of build failure. Sectioning, another factor, refers to splitting an object into multiple pieces to ensure that internal cavities are correctly modeled; it can also be used to build multiple components simultaneously thereby reducing production time. Optimizing the build process takes a great deal of experience and planning to ensure accurate and cost-effective physical model generation.

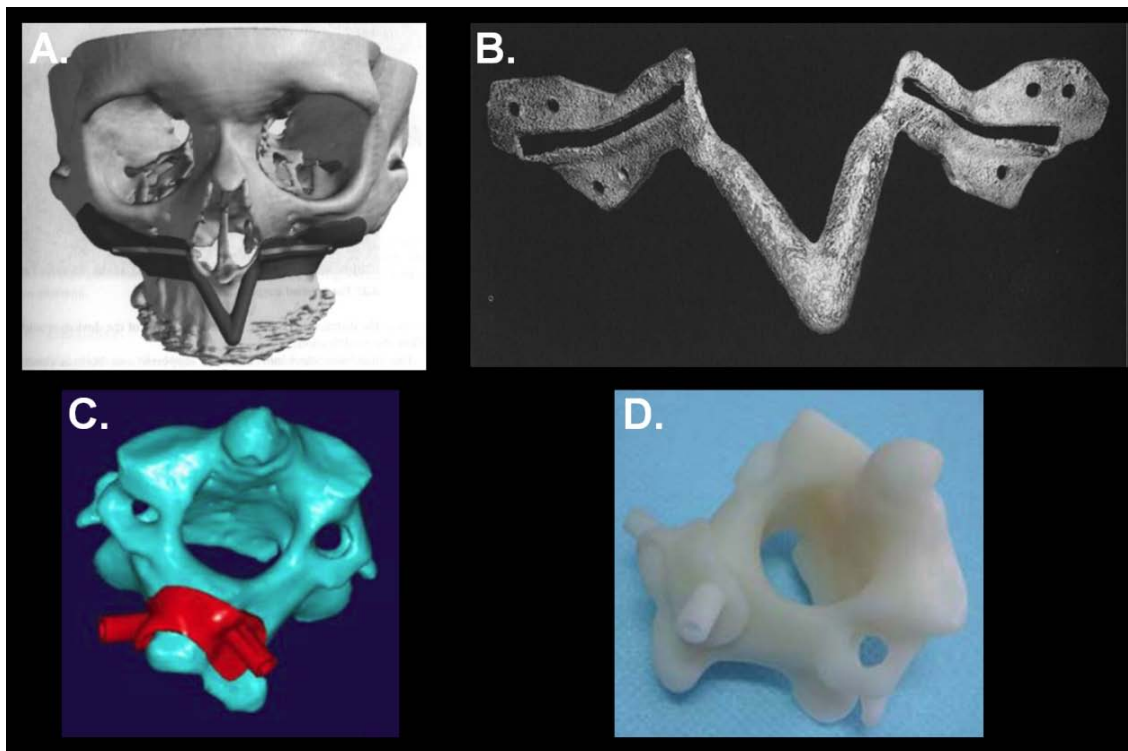


Figure 2.7 Applications of rapid prototyping. A) A three-dimensional model used for the development of sawing and drilling patient-specific maxillofacial surgical guides. B) The manufactured patient-specific maxillofacial surgical guide. C) Another three-dimensional model used for development of a patient-specific drilling guide for cervical spine laminar screw placement in posterior occipitocervical fusion. D) The manufactured patient-specific surgical guide placed on a model of a cervical vertebra.

(Source: A/B)Bibb R.[3] C/D) Lu S, et al.[34])

Applications of rapid prototyping technology are diverse and include surgical, rehabilitative, and research applications[3]. Often times in the surgical setting it is important to evaluate the depth and quality of bone prior to altering the patient's natural bone structure. In total knee arthroplasty, prior knowledge of bone quality can be important in developing a plan for optimal bone cuts. Physical models can be useful in simulating cuts and in generating a patient-specific replacement implant. Bone quality

can also be important for determining the optimal sites of drilling locations for osseointegrated implants. Screws anchored to skeletal bone may be used to attach dentures, hearing aids, and physical feature prosthesis(e.g. ear, nose). Bone quality can be important for ensuring long lasting attachment points for prosthesis, and physical models are helpful in determining optimal drilling locations. In addition, using anatomical landmarks and computer model extrusion techniques, patient-specific guides can be developed to ensure that optimal drilling locations are transferred from the physical model to the patient's anatomy in the operating room as seen in Figure 2.7[3, 34]. These custom fitting guides can also be helpful in planned osteotomy procedures where ideal locations for saw cuts are established by guide slots in the surgical guide. Overall, these guides can save substantial time in the operating room and offer an additional safety factor when dealing with sensitive anatomical components. Physical models allow for deformity visualization, surgical simulation, and development of patient-specific surgical tools.

The design of patient-specific prosthetics for rehabilitation is another application of rapid prototyping[3]. Patient-specific removable dental frameworks and cranioplasty plates are two examples of prosthetics generated using rapid prototyping and modeling. Surface scans of the skin can be used to generate burn therapy masks to prevent excessive scarring during treatment[3]. These surface scans can also be used to generate silicone facial prosthesis for cosmetic and corrective purposes. Rapid prototyping is also widely used in research. Physical cancellous bone models have been developed to validate computational FE models and to study the effect of osteoporosis on bone structure. Others have used rapid prototyping techniques to investigate skin texture.

2.4.2 Applications of Computational Models

Aside from physical model generation, computational analysis can be performed directly from virtual representations. The power of modern computing has drastically

improved the efficiency of this analysis type. A wide variety of applications in medicine have utilized these analysis methods. In surgical planning, anatomic models have been shown to be useful in optimizing the alignment and orientation of total knee implants thereby reducing operating times and ensuring long implant lifespan[35]. In disease and complication prevention, patient-specific finite element models have been used to investigate stress shielding effects from implants and also to estimate the compressive strength of vertebral bodies in the aging population[27, 36, 37]. Outside orthopaedics, patient-specific computational hemodynamic models have been found to be useful in assessing the risk of aneurysm rupture[38]. The scientific literature is flooded with papers related to medical computational analysis; a subset of these papers is presented with a concentration on orthopaedic applications and their clinical significance.

2.4.2.1 Surgical Planning

Surgical planning is one of the most directly applicable areas of computational modeling to clinical medicine. The ability to optimize procedures prior to actually performing them results in a better outcome than simply a “best guess” in the operating room. The old carpentry adage, “Measure twice, cut once” is very applicable to computational planning of surgical procedures. Levanthal, et. al presents a computational approach to determinate the optimal screw orientation for minimally invasive surgical repair of acute scaphoid fractures[39]. In the past, this procedure required an open operation and the potential of a long cast immobilization, which can now be avoided. In the minimally invasive procedure, increased screw length and central placement within the scaphoid are mechanically preferred and are correlated with better healing rates and decreased chances of nonunion. Risks of inappropriately aligned screw placement include penetration of the joint space, cartilage damage, delayed union, nonunion, and additional fracture. Using a patient’s CT image set, three-dimensional models are generated for screw placement simulation. Following parameters related to the scaphoid

“safe zone” for screw placement, a maximal screw length is determined as seen in Figure 2.8A/B. This model system will allow for actual to optimal screw orientation comparison studies, and it paves the way for computer-guided screw placement in acute scaphoid fracture repair.

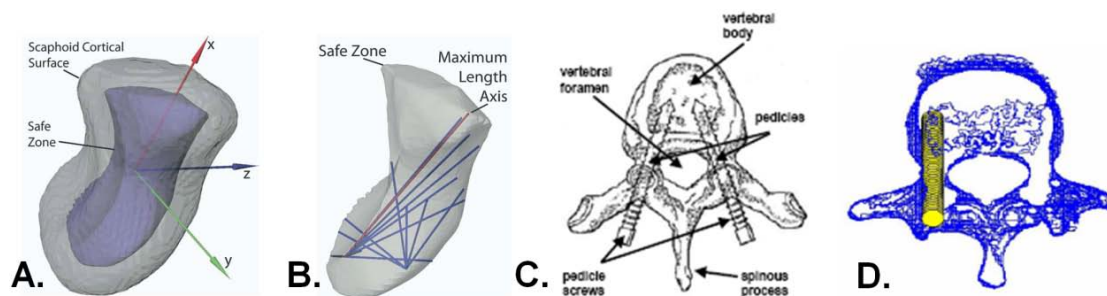


Figure 2.8 Applications of virtual models. A) A three-dimensional scaphoid model depicting the “safe zone” for screw placement. B) A representation of the “safe zone” and potential screw placement trajectories. C) Image depicting the placement of pedicle screws in the T6 vertebra. D) A compilation of CT slices and pedicle screw trajectory estimates based on an automated method for optimizing this surgical procedure.

(Source: A/B)Levanthal EL, et al.[39] C/D)Wicker R, et al.[40])

Wicker, et. al describes another automated protocol for optimizing multiple factors in pedicle screw insertion for spinal fusion procedures[40]. Spinal fusion is performed for a variety of medical conditions with a goal of ensuring structural stability within a certain segment of the spine. In this procedure, surgical screws are placed into the bodies of the pedicles and anchor stabilization devices to the vertebrae as shown in Figure 2.8C. Typically, the surgeon will select the size, length, and trajectory of the pedicle screws based on experience and patient-specific image set measurements. If a pedicle screw is placed incorrectly, there is potential of damaging surrounding tissues

like the spinal cord. With the abilities of current medical imaging technologies, automated methods are available for determining optimal size, length, and trajectory for the pedicle screws to remove the “guess work” that can be involved. After imaging and segmentation, pedicle identification procedures select this region from each of the slices of a CT image. Simple calculations can be used to determine the optimal route of the screw as shown in Figure 2.8D. Based on the optimal route, the screw size and insertion distance can be automatically determined to simplify this challenging procedure.

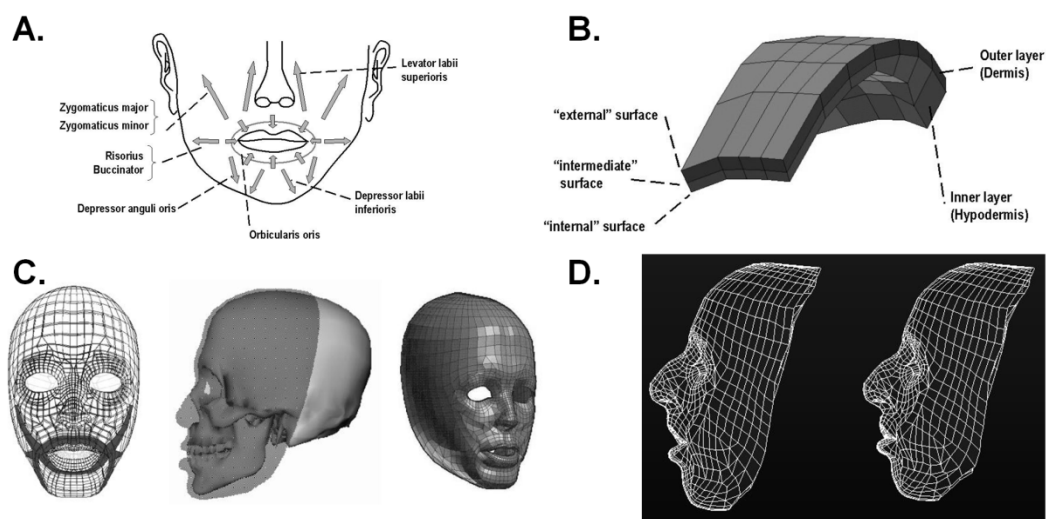


Figure 2.9 An application of finite element simulation. A) Facial muscle actions that were simulated in the finite element model for various facial expressions. B) A section of the finite element model that demonstrates how properties of different tissues were associated with the finite element model. C) The generic facial finite element model that was registered to fit various other patient geometries. D) An example of a mandible and maxillary repositioning surgical procedure on the finite element model.

(Source: Chabanas M, et al.[41])

Aside from determining optimal surgical conditions, very complicated surgeries that aim to improve both function and cosmetics have also utilized the capabilities of biomedical modeling. Chabanas, et al. demonstrated the use of a finite element model for planning patient-specific maxillofacial surgeries[41]. In dysmorphism of the face, it is often desirable for surgical modification to improve facial function and cosmetics. The human face is a complicated system of fat, muscles, bone, and soft tissue, and the interactions between all of these components allow for facial expression, speech, and mastication. A finite element model of the face incorporating these features was generated for a “generic” face, and a registration procedure was developed to morph the generic finite element mesh to a patient-specific surface model generated from a CT image set. Surgical procedures were simulated by modifying the finite element mesh node structure to reposition facial bones. Soft tissue changes caused by modifying the bone structure were observed and rated for accuracy by surgeons. Though a large-step forward in maxillofacial surgical planning, this model still requires improvements in a variety of areas including the eyes, throat, and neck. Four images in Figure 2.9 describe components of this system.

2.4.2.2 Biomechanical Simulation

The ability to simulate the movement of the human body is helpful in understanding the forces and stresses involved in normal human motion, and also the effects that injury can have on the body. Cervical spinal cord injuries can severely limit the abilities of a patient’s upper extremity; current rehabilitative options include neuroprosthesis using functional electrical stimulation[42]. This type of system requires testing and validation to allow for patient-specific applications and rehabilitation. Blana, et al. developed a three-dimensional upper extremity model to allow for simulation, testing, and validation of neuroprosthesis designs. This model was developed using commercial dynamic analysis software and parameters were assigned based on previous

cadaveric studies. It was comprised of six bones, five joints, and 29 muscles of the upper extremity, and allowed the user to define the extent of muscle paralysis and system constraints. The software accounts for the governing biomechanical computations and allows for both forward and inverse dynamic simulations. Forward dynamics takes muscle activation and external loads as inputs and outputs the expected motion from the arm. Inverse dynamics takes motion and external loads as inputs and outputs expected muscle activations. The model was validated using EMG measurements, and has shown promising results. In the future, this model will allow for patient-specific neuroprosthetic systems to increase the quality of life for those who suffer from spinal cord injury.

Performing finite element analysis on a patient-specific basis has long been a challenge for a variety of reasons. Antiga, et al. released an open-source software package, the Vascular Modeling Toolkit, meant for finite element analysis of human vasculature[43]. This software package addresses the specific concerns of generating patient-specific finite element models by guiding image segmentation, medial axis analysis, surface mesh generation, and tetrahedral mesh generation in a user-friendly format. The final tetrahedral mesh can be used for finite element analysis. By streamlining this process in a single software package, various computational hemodynamic studies are now feasible for individual researchers with limited programming experience. The advantage of patient-specific hemodynamic studies is the potential ability to investigate different variables and their relationship to human disease to aid in prediction, diagnosis, and treatment of a variety of disorders. As in structural finite element models, the governing equations are derived and applied to perform hemodynamic analysis. The novelty of this software is its ability to promote patient-specific analysis in a field that had been previously inhibited on a large-scale. Figure 2.10 demonstrates the functionality of this toolset.

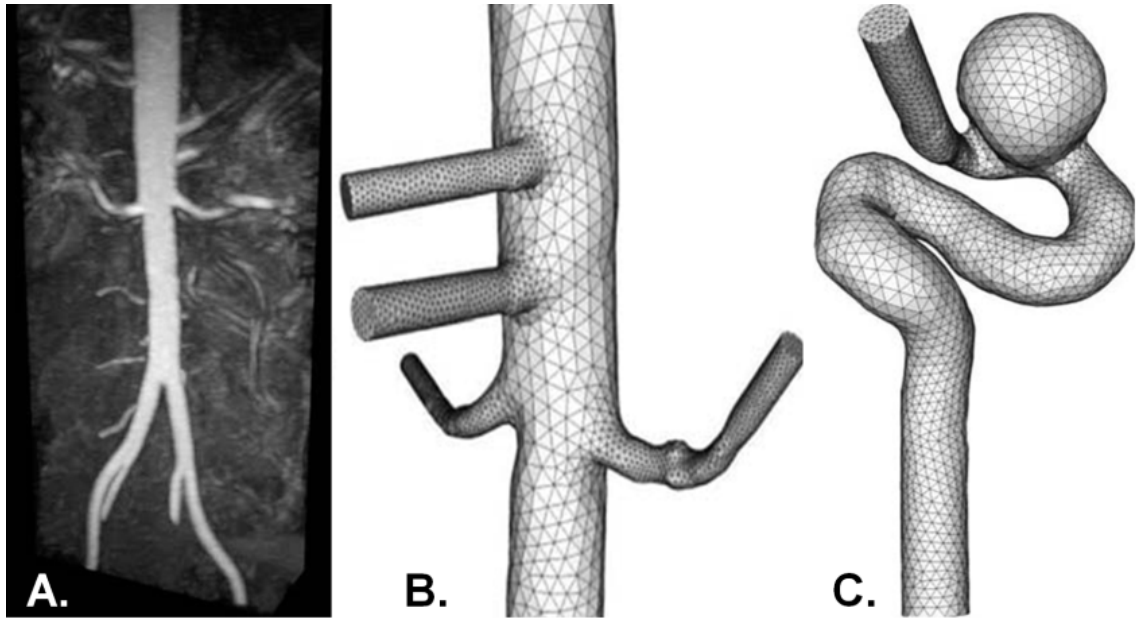


Figure 2.10 The Vascular Modeling Toolkit. A) An MRA dataset used to develop three-dimensional patient-specific vascular models. B) An example demonstrating a finite element tetrahedral mesh of the abdominal aorta. C) An example demonstrating a finite element tetrahedral mesh of an internal carotid aneurysm.

(Source: Antiga L, et al.[43])

2.4.2.3 Implant Performance Evaluation

Multiple methods have been used for implant performance analysis including beam on elastic foundation analysis. Femoral shaft fractures are often repaired using an intermedullary femoral nail and interlocking screws[44]. The positioning of the intermedullary nail influences the stresses distributed to the interlocking screws, which are often the sites of implant failure. Lin et al. describes a mathematical model based on radiographs that was used to develop the relations necessary for analysis of this implant system including beam on elastic foundation theory to represent the nail-cortical bone contact. Using the governing equations for displacement and the patient-specific geometry measured from the radiograph, equations representative of the system were

derived. Parametric analysis was applied to the system of equations to investigate the effects of multiple variables, and it was found that the distance between the locking screws and the fracture site, the number of locking screws, and the locking screw length greatly impacts the stresses placed on the locking screws. These results offer optimization procedures for future femoral shaft fracture repairs including: ensuring a long distance between locking screws and fracture site, decreasing the clearance between the screw and screw hole, and selecting a screw material with a high elastic modulus. Overall, it was found that the best method to reduce stresses on the locking screws was to ensure firm intermedullary nail-cortical bone contact. By performing this analysis on a given implant system, various factors were tested and optimal conditions were determined. In the future, automated systems to plan and apply these optimization procedures will help to reduce failure of femoral shaft fracture repairs.

Once a patient-specific model and mesh is generated, finite element analysis can be used in a number of ways including implant performance analysis. Barink, et al. compared two total knee implants with a goal of developing an implant capable of operating at high flexion degrees[45]. In the Asian total knee replacement market, it is very desirable to allow for flexion angles between 110-165° to allow for kneeling, squatting, and crossed-leg sitting common in their culture. Standard implants are not designed to reach these degrees of flexion, thus another total knee implant was designed to address these design challenges. Using dynamic finite element contact analysis, simulations were performed to compare the contact stresses at high degree flexion angles between the two implant types. It was determined that both implants performed well at normal degrees of flexion, and the high flexion implant reduced stresses and deformations at high flexion angles. However, elevated stresses were still present at the tibial post in the high flexion implant, which could decrease the longevity of the implant. Figure 2.11 demonstrates the finite element model and a resulting simulation. By simulating this situation, limitations of the design were determined prior to implantation

and failure in a patient. Finite element analysis is a very useful tool in evaluating implants which can decrease morbidity in patient populations. Patient-specific models could have been used to investigate the effects of different implants on different patient properties. This type of investigation could be useful in determining the optimal implant for a given patient.

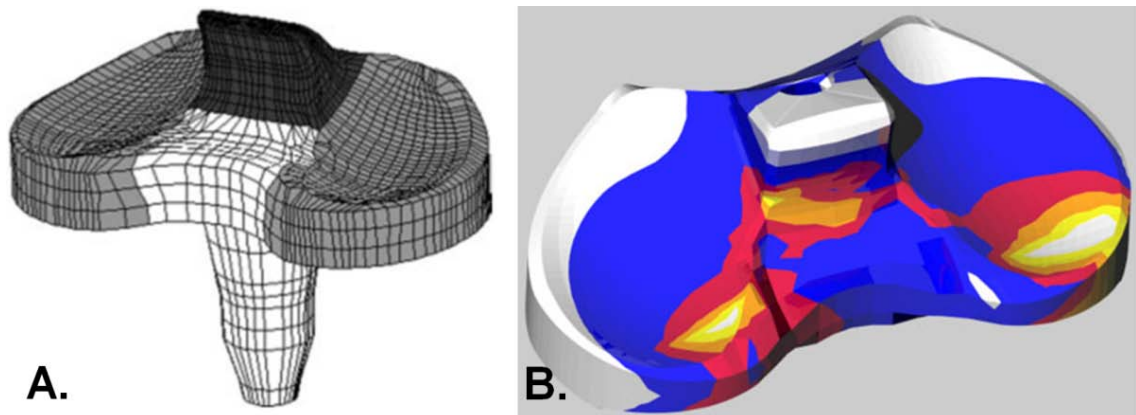


Figure 2.11 An example of finite element analysis. A) A finite element model representing the tibial component of a total knee replacement. Colors indicate different regions that were specifically investigated with the darkest region representing the tibial post. B) A color coded representation (blue = 2 MPa and yellow = 32 MPa) of the von Mises stresses for the tibial plateau of high flexion implant at 155° of flexion.

(Source: Barink M, et al.[45])

CHAPTER 3

AUTOMATED BUILDING BLOCK PLACEMENT IN MULTIBLOCK FINITE ELEMENT MESHING

3.1 Overview

Musculoskeletal finite element analysis has been essential to research in orthopaedic biomechanics. The generation of a volumetric mesh is often the most challenging step in a finite element analysis. Hexahedral meshing tools that are based on a multiblock approach rely on the manual placement of building blocks for their mesh generation scheme. Here we present two algorithms for automated placement of building blocks for multiblock meshing: the Automated Building Block Algorithm and the Building Block Growing Algorithm. We also present the development of a bone surface library that allowed for the evaluation of both of the algorithms over a wide range of geometries.

3.2 Human Bone Surface Library

As an initial step towards developing a flexible tool for automatic block placement for multiblock hexahedral meshing, a library of human bone surfaces was required to allow for testing of our algorithms with a wide range of geometries. Unfortunately, anatomic surfaces of the human skeleton are not easily and freely available. To address this issue, we have generated a library of surfaces of the human skeleton using open source software, a human skeleton, and a CT scanner.

A human skeleton was borrowed from the University of Iowa Department of Anatomy and Cell Biology. The collection of bones was obtained from a single donor and had previously been cleaned and disarticulated. All major human skeletal bones were represented except the bones of the middle ear and the hyoid bone. Also, only a unilateral upper extremity, lower extremity, and set of ribs were available as a part of this bone collection.

Due to bone's high contrast on CT images and the lack of surrounding tissues, CT imaging fostered a straight forward post-imaging analysis. Also, several blankets were used to separate the bones from the surface of the scanner table to ensure easy distinction of the bones from the scanner table during image processing. The bones were scanned at the University of Iowa Hospitals and Clinics using a Siemens 64-slice helical scan.

An overview of our image processing technique is found in Figure 3.1. Image processing started with organizing the images to find each of the respective bones in the dataset. Next, a simple region growing technique available in the 3D Slicer was employed. Region growing segmentation proved to be a viable initial segmentation step, but manual editing was required to fill gaps and ensure segmentation accuracy. Manual editing was performed in BRAINS2[46]. After a label map was ensured to be an accurate representation of the CT images, 3D Slicer was used to generate three-dimensional triangulated surface representations of each bone. Laplacian smoothing was applied to the three-dimensional surface models to remove stair-step artifact from the raw image dataset. Sample surface models of various bones of the human skeleton are available in Figure 3.2.

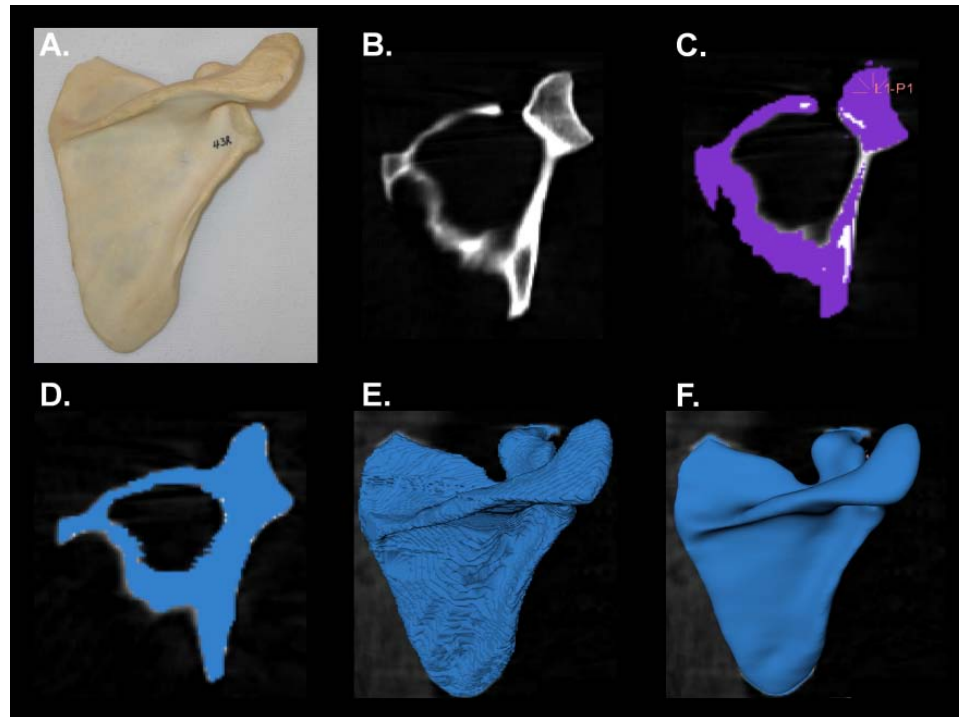


Figure 3.1 Three-dimensional model generation process. A) A sample human scapula from a human skeletal collection. B) A CT scan of the bone was performed. C) A label map for the region of interest was generated using a simple region growing segmentation technique that involves the placement of a single seed (orange asterisk) in 3D Slicer. D) After segmentation, manual editing of label map was performed in the BRAINS2 software suite to ensure accurate label map assignments. E) 3D Slicer was used to generate a triangulated surface representation of the label map. F) Laplacian smoothing was applied.

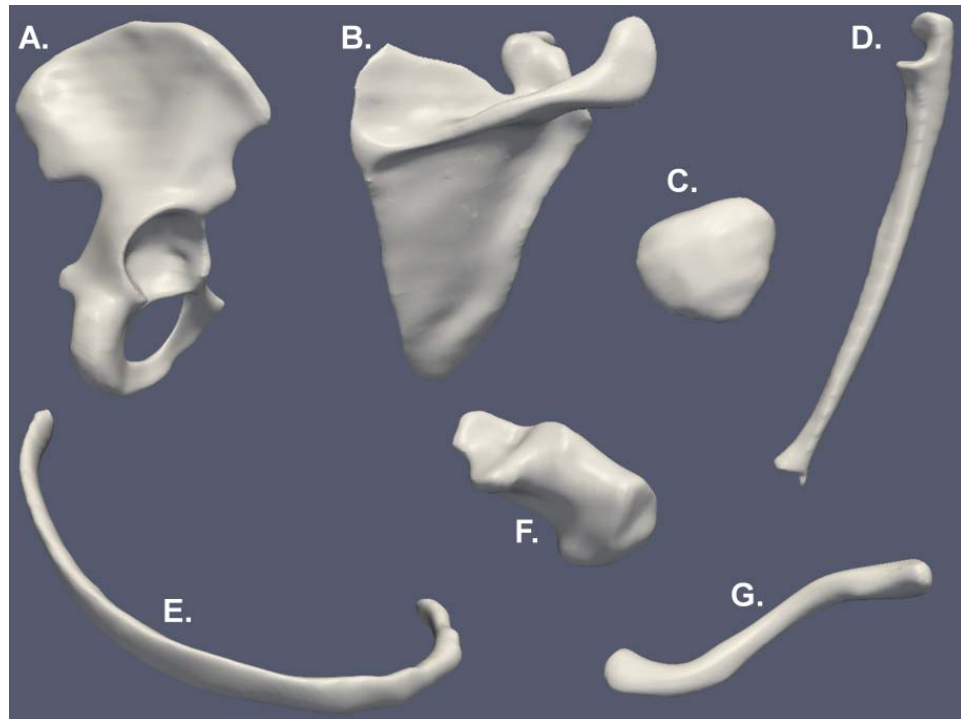


Figure 3.2 Sample smoothed three-dimensional surface models generated using the described process in Figure 3.1. A) Ilium. B) Scapula. C) Patella. D) Ulna. E) Rib. F) Calcaneus. and G) Clavicle.

3.3 Automated Building Block Algorithm

3.3.1 Abstract

Musculoskeletal finite element analysis has been essential to research in orthopaedic biomechanics. The generation of a volumetric mesh is often the most challenging step in a finite element analysis. Hexahedral meshing tools that are based on a multiblock approach rely on the manual placement of building blocks for their mesh generation scheme. We hypothesize that Gaussian curvature analysis could be used to automatically develop a building block structure for multiblock hexahedral mesh generation. The Automated Building Block Algorithm incorporates principles from differential geometry, combinatorics, statistical analysis, and computer science to automatically generate a building block structure to represent a given surface without prior information. We have applied this algorithm to 29 bones of varying geometries, and successfully generated a usable mesh in all cases. This work represents a significant advancement in automating the definition of building blocks.

3.3.2 Introduction

3.3.2.1 Finite Element Analysis

Finite element analysis (FEA) is a method of continuum mechanics that has been vital to the biomechanics community due to its ability to evaluate structures with complicated geometries. In orthopaedic biomechanics, it has allowed for engineering analyses of bones, joint articulations, and implant systems [47, 48]. The amount of literature pertaining to biomechanical finite element studies is extensive with a great deal of recent work being dedicated to implant performance and evaluations of injuries in the musculoskeletal system [49-55].

Implant performance evaluation is a key area where FEA has been extremely useful. Helgason et al. used FEA to investigate the rate of bone failure in an evaluation

of osseointegrated femoral attachments for transfemoral amputees [56]. In an attempt to improve on conventional implants, Harrysson et al. presented a method of patient-specific total knee replacement femoral component design and utilized FEA to demonstrate that a patient-specific implant more evenly distributes stresses to the underlying bone [57]. Furmanski et al. applied FEA to predict crack propagation from stress concentrations in four UHMWPE acetabular cup designs and used the results to suggest design improvements for future implant systems [58].

Evaluations of the musculoskeletal system are also an area where FEA has increased our understanding of orthopaedic biomechanics. In an attempt to better understand joint mechanics using FEA, Shirazi et al. investigated stress distributions associated with common osteochondral defects and their effects on articular cartilage [59]. Varga et al. developed a finite element model to simulate a simplified version of Colles' fracture common in early stages of osteoporosis [60]. Zeinali et al. reports a patient-specific approach to predicting compressive vertebral fractures using FEA in an effort to noninvasively evaluate vertebral body strength [61].

The ability to perform clinically relevant finite element studies is dependent on the ability of the researcher to accurately model the biomechanical system. Medical imaging technologies and image processing techniques have allowed for the generation of patient-specific surface representations using a variety of semi-automated approaches [15, 17, 62-66]. Generation of finite element models from medical imaging data requires a series of steps including image segmentation, mesh generation, and assignment of material properties, loading and boundary conditions. Each of these steps can be challenging and time-consuming. The goal of this work is to address the challenge of automating mesh generation for hexahedral meshes.

3.3.2.2 Finite Element Mesh Generation

In the past, finite element mesh development was performed manually, which proved to be laborious and time consuming. Commercial software packages have been developed to perform volumetric finite element meshing including Mimics[®], TrueGrid[®], ABAQUS[®], and ANSYS[®] to name just a few. Volumetric meshing typically involves one of two element shapes: tetrahedrons or hexahedrons. Tetrahedral elements offer the advantage of more easily representing complicated geometries than hexahedral elements. However, hexahedral elements are less stiff than tetrahedral elements and thus will often give more accurate results. Higher order tetrahedral elements have been shown to give similar results to hexahedral elements; however, some researchers still prefer hexahedral elements [67]. Another advantage of hexahedral meshes is they typically require fewer elements to fill a given volume when compared to tetrahedral meshes; this often results in a reduced computational time for the FEA.

Finite element mesh generation techniques are classified as either involving unstructured or structured grids. Unstructured grids rely on explicit node location and connectivity definitions with respect to neighboring nodes. Many methods have been developed including plastering, the Whisker Weaving method, advancing fronts, and medial axis analysis [68-75]. Structured grids have a regular ordering of nodes such that unknown locations can be determined from neighboring nodes. A common method within structured grid techniques is the multiblock approach, which has been shown to be useful in meshing complex geometries. In this approach, the overall domain is subdivided into interconnecting blocks that are individually assigned a structured grid [76-82]. This method combines the efficiency of traditional structured grid techniques with the geometric flexibility of unstructured methods.

3.3.2.3 IA-FEMesh

The methods for automatic hexahedral meshing of geometrically complicated structures remain an active area of research. IA-FEMesh (<http://www.ccad.uiowa.edu/mimx>), an open-source hexahedral meshing tool was developed to facilitate the generation of hexahedral meshes for anatomic structures, which is a functionality that few finite element pre-processing packages are designed to address [64]. The software uses a multiblock structured grid meshing technique, and a variety of tools have been developed to enable the user to manually place and manipulate building blocks around a given surface for finite element mesh generation. Figure 3.3 details the steps of the multiblock hexahedral meshing process used in IA-FEMesh including block placement, mesh assignment, and mesh projection onto the surface of interest. As the complexity of the surface increases (e.g. phalanx bones versus cervical vertebrae), the number of required building blocks increases and the placement thereof becomes more challenging and time consuming (Figure 3.4). Automation of building block definitions/placement would ultimately decrease the time required to generate a finite element mesh; however, it poses the challenge of determining optimal size and locations for building blocks to produce high quality hexahedral meshes. To our knowledge, a three-dimensional technique to automatically define block structures does not currently exist in either commercial or open-source multiblock meshing software packages.

Based on experience using the multiblock meshing procedure, the user typically concentrates building block placement around regions of complex geometry on a surface. These regions of complex geometry often display Gaussian curvature values that significantly differ from surrounding values. Surface regions containing features with very large positive values (peaks) and regions with very large negative values (valleys) often correspond to locations that a user would typically surround with a building block. Others have used Gaussian curvature calculations to automatically identify anatomical

landmarks on bone models [83, 84]. We hypothesize that Gaussian curvature analysis can be used to automatically define the building blocks for hexahedral mesh generation.

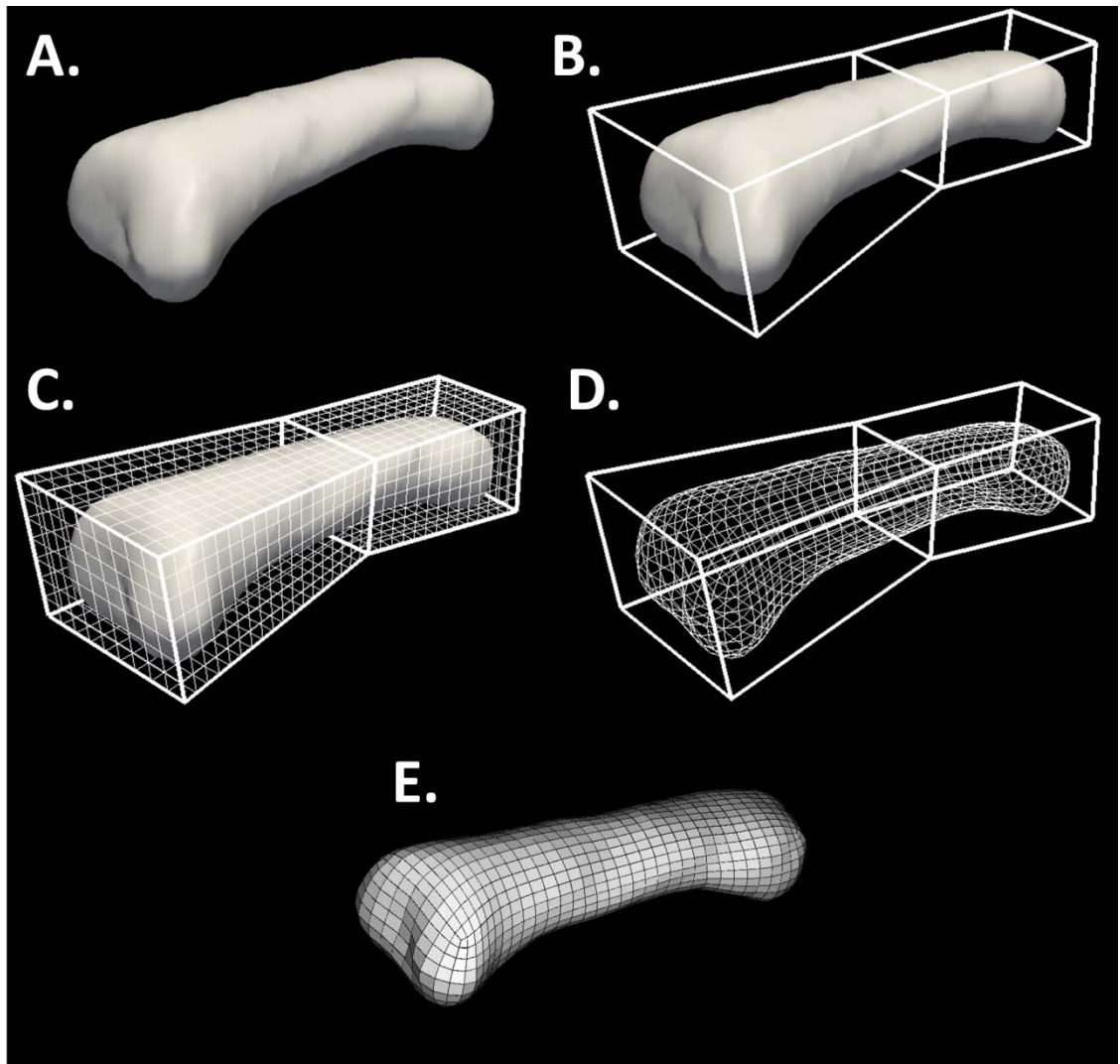


Figure 3.3 The steps used in the multiblock meshing process used in the IA-FEMesh software. A) The multiblock meshing process begins by choosing a surface to mesh (e.g. proximal phalanx of the finger). B) Individual blocks are manually placed around the surface to establish a block structure. C) A hexahedral mesh is assigned to the blocks. D) Closest point projection is used to project the mesh from the blocks onto the surface; internal elements are calculated to form a volumetric mesh. E) The resulting hexahedral mesh can be used for finite element analysis.

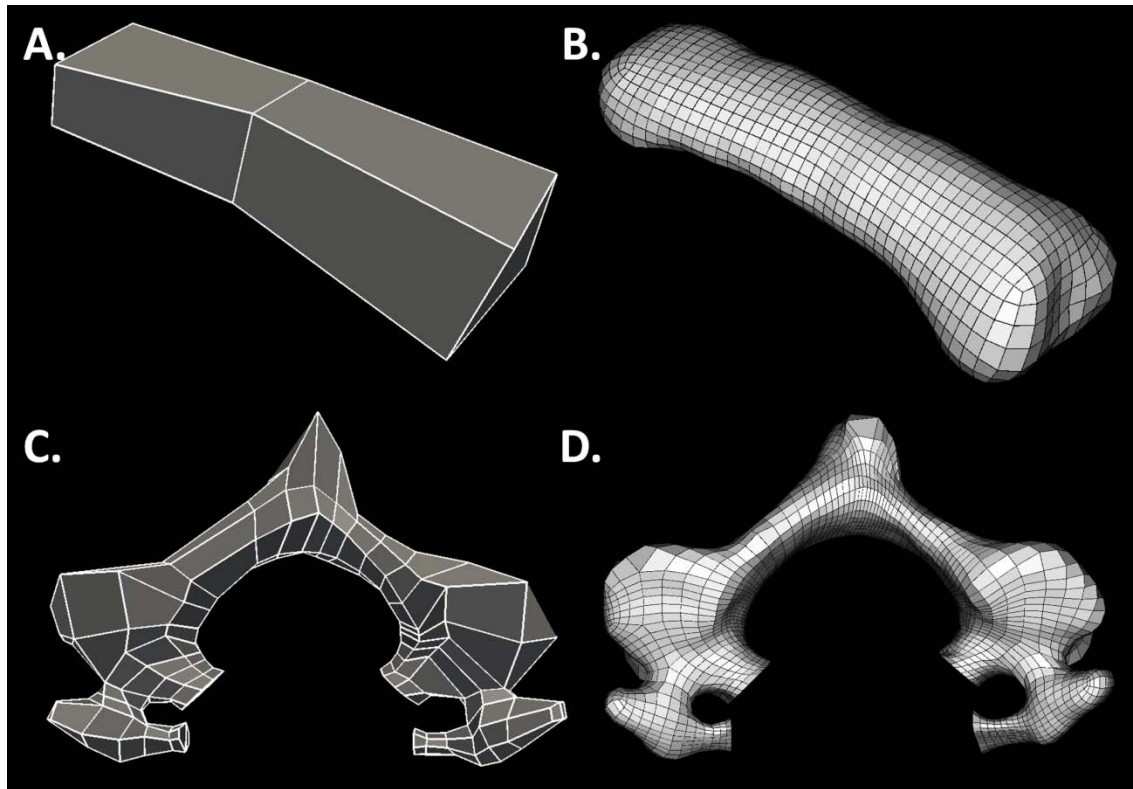


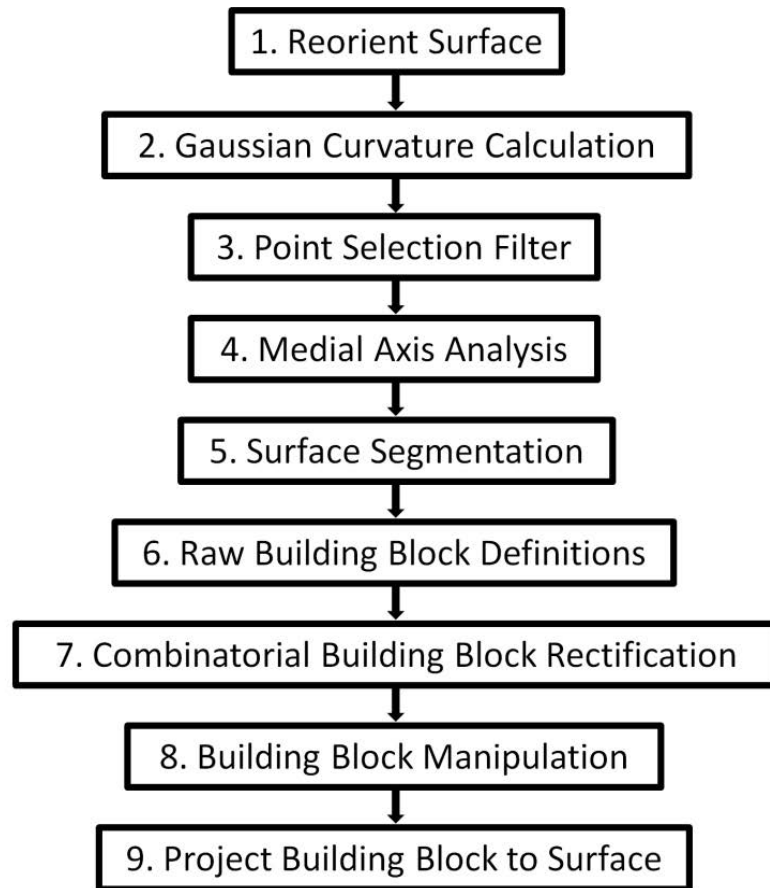
Figure 3.4 Example building block structures of different complexity. A) A manually defined block structure for a proximal phalanx bone of the hand composed of two building blocks. B) The corresponding hexahedral mesh for the proximal phalanx bone generated using IA-FEMesh. C) A manually defined block structure for the posterior elements of the third cervical vertebra composed of 117 building blocks. D) The corresponding hexahedral mesh for the posterior elements of the third cervical vertebra generated using IA-FEMesh.

3.3.3 Methods

3.3.3.1 Automated Building Block Algorithm

The Automated Building Block Algorithm incorporates principles from differential geometry, combinatorics, statistical analysis, and computer science to generate a building block structure for a given surface without prior information. The input to the algorithm is a triangulated representation of the surface of interest (e.g., bone), while the output is a building block structure corresponding to this surface. User-defined parameters have been included to provide flexibility and control over the number and size of the blocks composing the building block structure. The overall goal of this algorithm was to automate the structural building block definitions in the absence of a template or pre-existing building block pattern. Figure 3.5 summarizes the steps of the Automated Building Block Algorithm and provides examples of the results from each step of the process.

A. Automated Building Block Algorithm Steps:



B. Incremental Results:

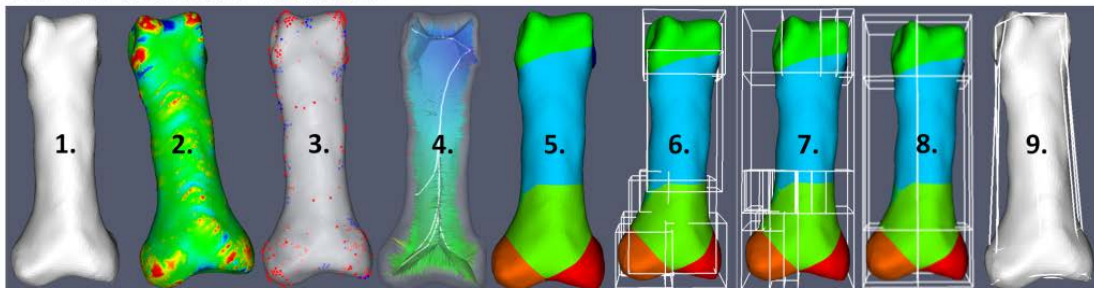


Figure 3.5 The Automated Building Block Algorithm. A) A flow diagram depicting the steps of the Automated Building Block Algorithm. B) Incremental results corresponding to the steps described in (A) demonstrated using a model of the proximal phalanx bone of the index finger.

3.3.3.2 Reorient the Surface

Bony surfaces generated from medical imaging datasets are oriented arbitrarily with respect to the Cartesian coordinate system about which the building blocks are defined. To generate blocks that are of minimum volume, a rigid body transform is estimated that will align the anatomical surface with the Cartesian coordinate system (Figure 3.5, Step 1). This is performed using a simple iterative procedure whereby the bony surface is rotated 180° in 1° increments in each of the three primary axes to determine the minimum volume bounding box for the entire surface. The definition of the building blocks is defined initially with the surface in this minimum volume bounding box orientation, before transforming the finalized block structure back to the original orientation of the bone. Other techniques to adjust the object orientation such as principal component analysis, detection of object symmetry, and feature extraction could be used in place of this brute force approach [85-87].

3.3.3.3 Gaussian Curvature Calculation

To aid building block placement, we have taken advantage of Gaussian curvature calculations to identify significant changes in surface geometry (Figure 3.5, Step 2). Gaussian curvature was calculated for each vertex of the triangulated surface using the Visualization Toolkit (VTK), <http://www.vtk.org/>. Gaussian curvature using VTK is calculated as shown in Eq. 3.1.

$$K(\text{vertex } v) = \frac{3*(2*\pi) - \sum_{\text{facet neighbors of } v}(\text{angle}_f \text{ at } v)}{\sum_{\text{facet neighbors of } v} \text{Area}(\text{facet})} \quad (\text{Eq. 3.1})$$

The calculated curvature at each vertex is accomplished by evaluating all angles from all facets (triangles) that involve a given vertex. The final curvature value is weighted by one third the area of the involved facets. The curvature can be used to classify regions into peaks, valleys, or planar regions corresponding to positive, negative, or zero curvature values, respectively.

3.3.3.4 Point Selection Filter

To identify the points corresponding to regions of complex geometry, statistical analysis is used to filter the Gaussian curvature values (Figure 3.5, Step 3). On occasion, image segmentation techniques can result in extremely large positive or negative curvature values due to noise (Figure 3.6A). In general, bony anatomical regions do not contain these types of features. The first step in the point selection filter is to remove the noisy regions from the analysis, which allows the algorithm to focus on division of the surface based on the complex anatomical geometry. This is accomplished by removing all points greater than or less than three standard deviations from the mean surface curvature value. With these values removed, the points corresponding to anatomical regions of interest were identified by selecting the curvature values greater or less than two standard deviations from the mean. Ultimately, the filtering process yields seed points used to parcellate the surface.

To lend control over the total number of building blocks, several user-defined constraints have been implemented to account for situations where regions of complex geometry are clustered together. These constraints are used to further reduce the number of points corresponding to regions of complex geometry to obtain a reasonable number of building blocks corresponding to anatomic features. The users define three values for two constraints: distance constraint, cluster distance, and cluster size. The constraints can be described as follows (Figure 3.6B):

1. Distance constraint – the distance constraint requires a minimum distance between identified points. If multiple points are too close, then points will be removed from consideration until the minimum distance is achieved.
2. Cluster constraints – regions of complex geometry typically have multiple points with large magnitude Gaussian curvature values clustered together. To ensure that the points represent a large anatomical region as compared to subtle changes

in surface topology, the clustering constraint removes points from consideration unless a user-defined number of points (cluster size) exist within a specified distance (cluster distance) of the point under consideration.

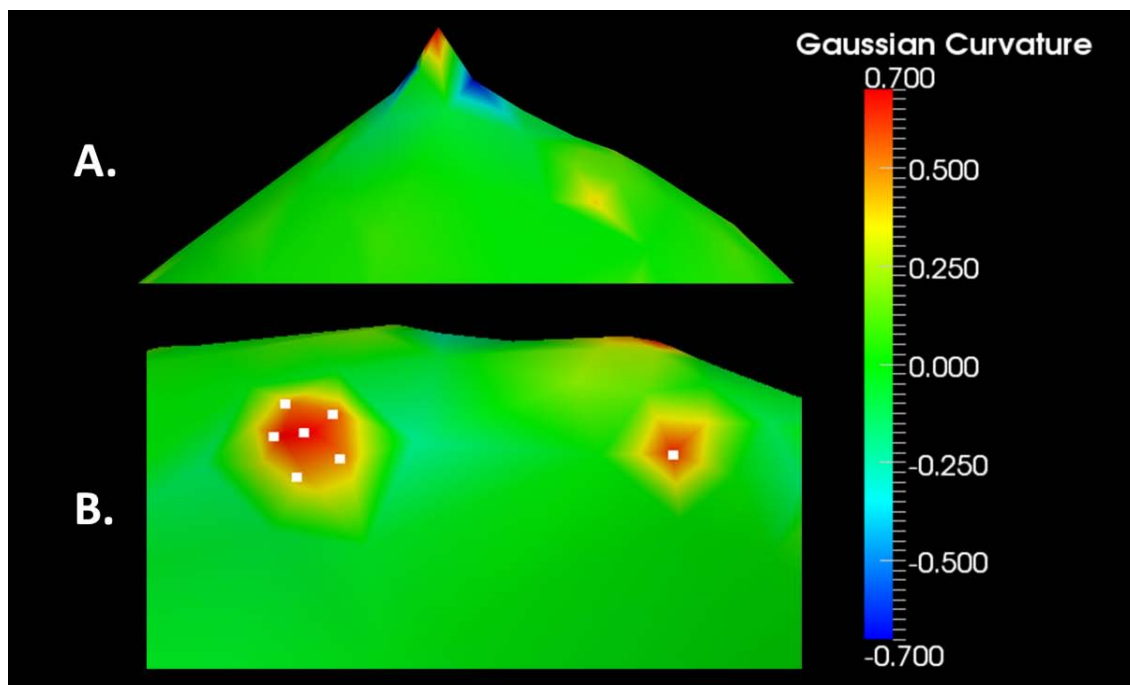


Figure 3.6 Gaussian curvature analysis. A) The first step in the point selection filter involves removing segmentation artifacts that typically have a Gaussian curvature value greater or less than three standard deviations from the mean. B) Two regions identified as being between two and three standard deviations from the mean Gaussian curvature value.

The user-defined parameters allow flexibility in determining the number of regions of complex geometry for a given surface representation. The number of points selected directly corresponds to the number of building blocks that will be defined at the start of the building block generation process. The natural variability in geometry and size of bones requires that appropriate constraint values are used for individual bones. For example, the selected constraints that produce a block structure for the sternum may

not be optimal for generating a block structure for the wrist bones. Some preliminary fine tuning to establish adequate point coverage across the surface is necessary to generate an optimal building block for the structure of interest.

3.3.3.5 Medial Axis Analysis and Surface Subdivision

The Vascular Modeling Toolkit (VMTK) was originally designed for fostering hemodynamic research using medial axis analysis; it has been used to investigate aneurysms and fluid dynamics in the vascular system[43]. Several tools in this toolkit can be applied to models of the musculoskeletal system. VMTK's medial axis analysis tools are used to generate centerlines for the triangulated surfaces based on the point set generated from the previous step. Using VMTK's surface segmentation functionality, the bony surface can be separated into components based upon the individual centerline segments (Figure 3.5, Step 4/5). This allows the surface to be separated into regions corresponding to the points identified in the previous step.

3.3.3.6 Initial Building Block Definitions

After the surface has been subdivided into regions of complex geometry, building blocks are defined (Figure 3.5, Step 6). As a starting point, individual blocks are placed around the extents of each piece of the surface. The number of building blocks defined in this step is the same as the number of points selected by the point selection filter. Unfortunately, this initial building block structure is unsuitable for mesh generation due to resulting overlapping blocks. Consequently, this overlap must be eliminated from the structure.

3.3.3.7 Combinatorial Building Block Rectification

Consider two overlapping blocks. Eliminating overlap between the blocks, while maintaining the total occupied volume, requires that only one of the blocks be modified. Consequently, the overlapping face of one block will be adjusted along the length of the

block to provide correspondence between the two faces in the direction being considered. Empirically, this modification will result in two blocks without overlap; however, the width and depth of the blocks are not necessarily equivalent. Consequently, this modification may result in a loss of volume as compared to the original block configuration. Additional block(s) can be added to compensate for this volume loss. Repeating this procedure throughout the building block structure will result in a set of blocks free of overlap (Figure 3.5, Step 7). Automating this process to handle every potential case of block overlap is vital to a successful algorithm. As a result, a combinatorial look-up table was developed.

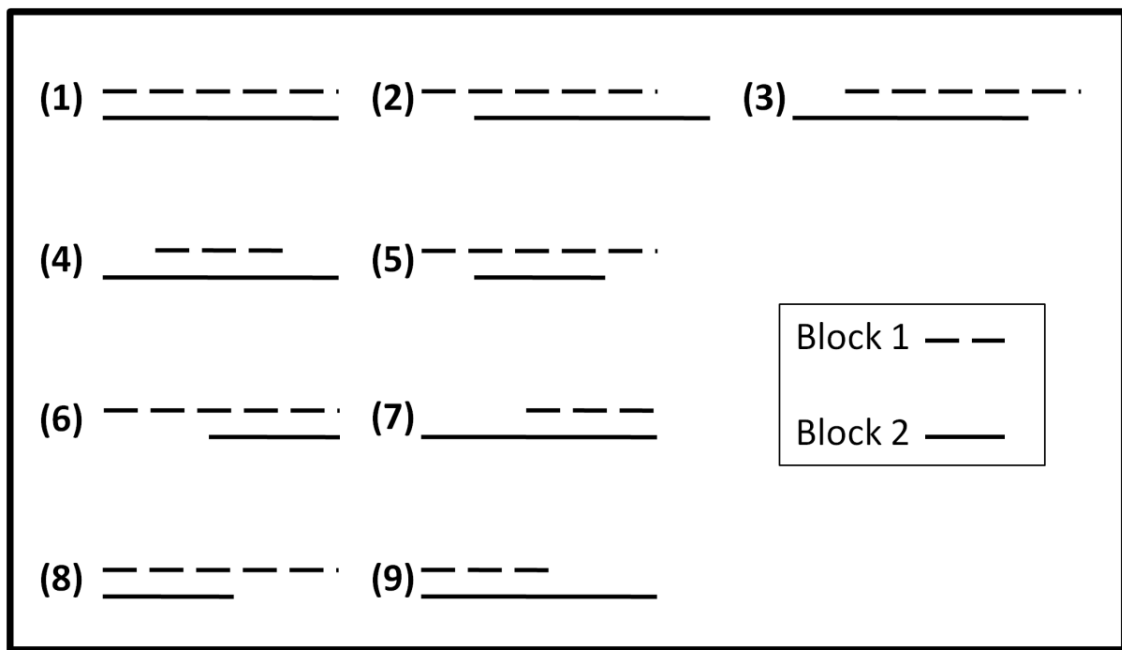


Figure 3.7 A visual depiction of the 9 cases of block overlap demonstrated in one dimension for simplification. The dashed line represents an edge of one block while the solid line represents the edge of another block. The distance between the lines should be ignored, and only the position of the lines considered.

Figure 3.7 describes the 9 cases where two blocks overlap in one-dimension, which extends to 729 ($9 \times 9 \times 9$) unique cases of block overlap in three dimensions. For each case, a method to reconfigure the blocks without volume loss has been defined. A sample case is demonstrated in Figure 3.8. Since only a single direction must be modified and a different direction can be chosen for each pair of blocks, the look-up table accounts for three methods of modification (length, width, depth (or x,y,z)) for each of the 729 cases of block overlap. Further manipulation, as described in the following section, may be required to achieve a desirable building block structure.

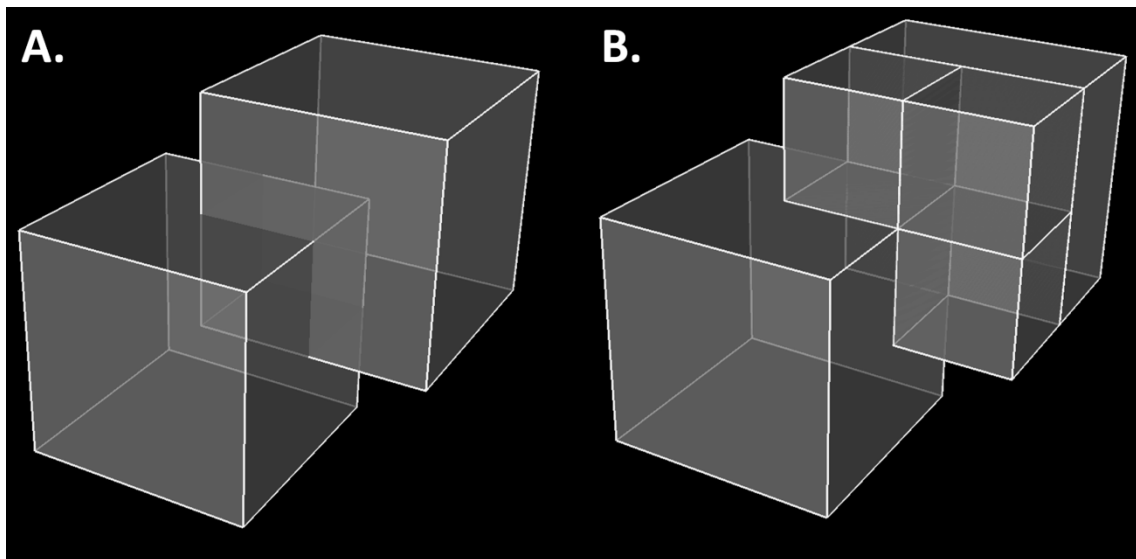


Figure 3.8 A simple case of combinatorial building block rectification. A) Two building blocks overlapping in space. B) The resulting building blocks after rectification of overlap. In this case, one block has maintained its original volume, while the other original block has been modified to remove the region of overlap. Three additional blocks have been added to compensate for volume loss caused by the modification of the second original block.

3.3.3.8. Building Block Manipulation

A final building block structure must meet certain requirements for it to be used for mesh generation. These requirements include 1) a one to one correspondence of faces

between blocks, 2) a counter clockwise orientation of the vertices, and 3) continuity within the block structure such that adjacent blocks share vertices. One to one face correspondence is accomplished by splitting a block into components in the situation that a block shares a single face with multiple blocks. To perform this procedure on the level of the whole block structure, the number of building blocks neighboring each face of each block is checked to ensure that each face has only one neighbor. If more than one neighboring block is identified, the block under consideration is split to match the neighboring blocks. This procedure ceases once one to one face correspondence exists for the entire block structure. A counter clockwise orientation is accomplished by ensuring that the blocks are originally defined using a counter clockwise orientation as the remainder of the algorithm does not modify the vertex order for the blocks. Connectivity between blocks is accomplished by simply reassigning coincident vertices to represent a single vertex in the same location. By performing these three procedures, a theoretically usable block structure is formed; however, practically the block structure may contain very narrow and small blocks that require simplification. To remove these small blocks, simplification procedures were developed to control the size and number of blocks (Figure 3.5, Step 8). This is accomplished using three protocols with user-defined parameters described as follows:

1. Pre-Rectification Merging Factor (PRMF) – this parameter allows for small differences between blocks to be removed prior to the combinatorial building block rectification procedure (Section 3.3.3.7). It was found that removing these small differences drastically reduces the number of narrow blocks in the structure. The value assigned to this parameter corresponds to the definition of what is considered a small difference between blocks. For example, if the PRMF was assigned a value of 5, then differences of 20% or less between blocks would be eliminated (Figure 3.9).

2. Merge blocks – after satisfying the requirements for a usable block structure, these parameters identify blocks that can be merged to simplify the overall block structure. The user has the option to merge blocks along each axis (X, Y, Z) when they have face correspondence in the other two axes. This parameter determines in part the total number of blocks in the resulting block structure. An example is shown in Figure 3.10.
3. Band factor – This factor allows the user to eliminate blocks that are narrow in one of the three axes (Figure 3.11). To remove these band-like patterns from the building block structure, a simple merging operation was developed that merges these small blocks with their neighbors. The user can specify a band factor along each axis that specifies the smallest allowable edge length as a percentage of the overall block size. For example, if the user were to choose 0.2 for the Band factor along the x-axis where the total length was 10mm, then narrow bands will be removed for all blocks that have an x edge length less than 2mm.

The final operation in building block manipulation is the removal of blocks that do not contain any components of the surface.

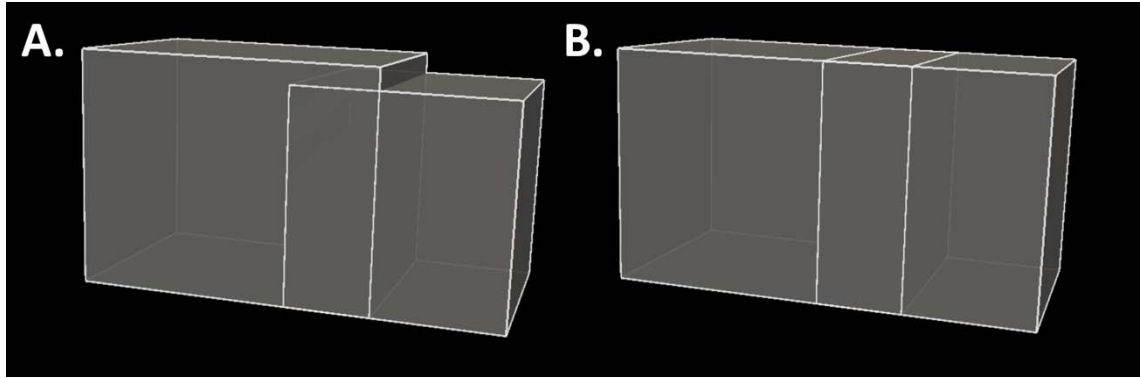


Figure 3.9 The PRMF is used to remove small differences between overlapping blocks. A) Two overlapping blocks that differ by a small amount (in this case $<20\%$ of the overall length of the block edge) along one axis. B) Here, a PRMF value of 5 will remove this small difference and result in two overlapping blocks without a small step off.

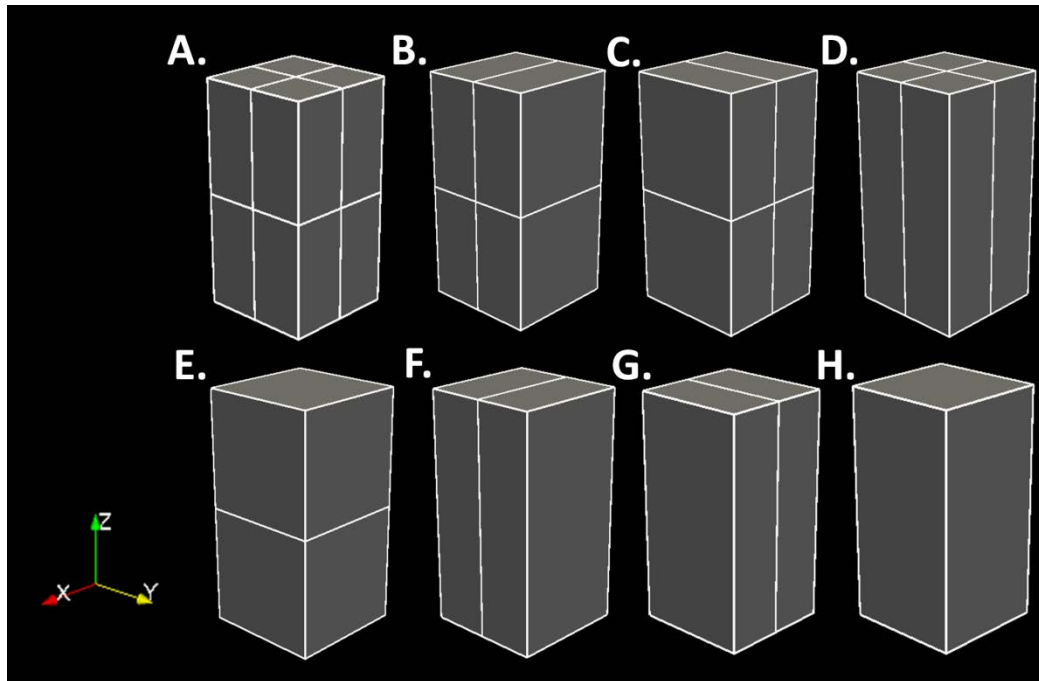


Figure 3.10 The merge blocks parameter can simplify a block structure by merging blocks that share faces with identical coordinates. Here we demonstrate a simple block structure A) composed of eight blocks and the resulting structures after the merge blocks parameter is applied to the B) x-axis, C) y-axis, D) z-axis, E) x- and y-axes, F) x- and z-axes, G) y- and z-axes, and H) the x-, y-, and z-axes.

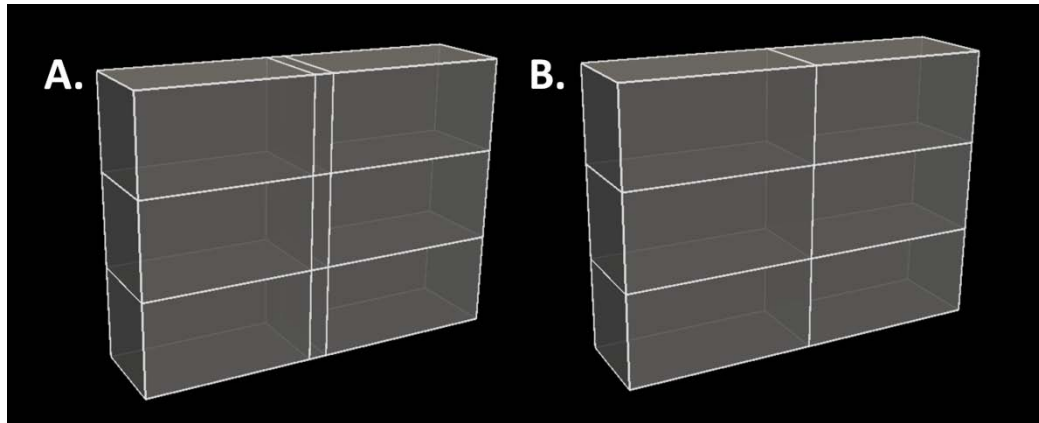


Figure 3.11 The band factor is used to remove narrow bands of blocks within a structure. A) A block structure containing a centrally located narrow band of blocks. B) The resulting block structure after a band factor of 0.2 is applied, which incorporates the narrow blocks into the neighboring blocks.

3.3.3.9 Output Finalized Building Block Structure

After completion of the building block manipulation steps, a closest point projection is used to match the vertices of the building blocks with the closest points on the surface (Figure 3.5, Step 9). Finally, the building block structure is reoriented back to the original orientation of the surface using the inverse of the calculated values used to originally orient the surface. This finalized building block structure is then imported to IA-FEMesh for hexahedral mesh generation.

3.3.3.10 Computational Resources

The C++ programming language was used to develop our algorithm, and the Visualization Toolkit and Vascular Modeling Toolkit were also implemented for their functionalities. The 3D Slicer and BRAINS2 software packages were used for image processing and the IA-FEMesh v1.0 software was used to perform the finite element meshing operations. ABAQUS® finite element solver was used to perform finite element analysis. Programming and testing was performed on an AMD Athlon 64x2 Dual Core

Processor 5200+ (2.6GHz) with 4.00 GB of RAM running a 32-bit version of the Microsoft Vista operating system.

3.3.3.11 Algorithm Testing

To evaluate the Automated Building Block Algorithm, we have chosen 29 bones from the bone model library that represent a variety of shapes and locations from the human skeleton. The algorithm was applied to each of the bones and the run time was recorded. After generating a building block structure for each bone, a hexahedral mesh was developed for each of the bones using the resources available in IA-FEMesh. Laplacian smoothing was applied to improve mesh quality. A minimum element volume mesh quality metric was recorded for each of the hexahedral meshes. Material properties ($E = 15\text{GPa}$, $\nu = 0.3$) were assigned to each of the meshes. A simulated load of 30N was assigned to the distal aspect/articulation of each bone mesh, and the bone mesh's proximal aspect/articulation opposing the load was fully constrained. For example, in the case of the proximal phalanx the distal articulating surface was loaded with 30N and the proximal articulating surface was fully constrained. For the cases where bones have multiple sets of articulating surfaces (e.g. wrist bones), a single set of articulations was chosen for loading and boundary conditions. Each model was saved and the ABAQUS® finite element solver was applied to the model to determine if a solution could be obtained. Appendix Figure A.1 demonstrates sample loading and constraining conditions applied to a hexahedral mesh.

3.3.4 Results

The Automated Building Block Algorithm was tested using the 29 bone models shown in Table 3.1. A subset of 8 bones of varying geometries was selected to show representative user-defined parameters. Tables 3.2 and 3.3 show the parameters used to generate the building blocks and the time required by the algorithm to generate a building block structure for these surfaces. Figure 3.12 and 3.13 illustrate the original surfaces,

the automatically generated building block structures, an overlay of the original bone and the building block structure, and finally the hexahedral meshes generated from the automatically generated building block structures. In all 29 cases, the final mesh representation exhibited a positive minimum element volume (Appendix Figure A.2), and each of the resulting mesh definitions ran in ABAQUS® generating a solution without errors. It should be noted that additional mesh optimization using an in-house code was required to untangle/smooth the meshes defining the talus and the calcaneus. The time required to create the building block structure ranged from 35 to 243 seconds.

Table 3.1 The Automated Building Block Algorithm was applied to 29 bones from various locations in the body and the resulting mesh quality metrics.

Surface	Location	# of Elements	Minimum Volume (mm³)
Proximal Phalanx	2 nd Finger	22176	0.035
Medial Phalanx	2 nd Finger	1848	0.065
Distal Phalanx	2 nd Finger	2244	0.006
Metacarpal	2 nd Finger	4320	0.168
Scaphoid	Wrist	1512	0.133
Lunate	Wrist	1040	0.110
Triquetrum	Wrist	770	0.106
Pisiform	Wrist	320	0.241
Trapezium	Wrist	1350	0.052
Trapezoid	Wrist	672	0.117
Capitate	Wrist	1155	0.175
Hamate	Wrist	936	0.151
Proximal Phalanx	2 nd Toe	840	0.108
Medial Phalanx	2 nd Toe	420	0.494
Distal Phalanx	2 nd Toe	890	0.010
Metatarsal	2 nd Toe	6534	0.098
Calcaneus	Ankle	2352	0.964
Talus	Ankle	3042	0.805
Navicular	Ankle	6720	0.049
Cuboid	Ankle	6750	0.061
1st Cuneiform	Ankle	5966	0.022
2nd Cuneiform	Ankle	13200	0.005
3rd Cuneiform	Ankle	3078	0.094
Patella	Knee	29527	0.016
Rib 12	Chest	1890	0.066
Manubrium	Chest	12340	0.018
Sternum	Chest	20832	0.095
Xyphoid Process	Chest	6300	0.048
Coccyx	Vertebre	1862	0.008

Table 3.2 The parameters used to generate the building blocks for 4 bones.

Parameters	Scaphoid (Wrist)	Trapezium (Wrist)	Rib 12 (Chest)	Sternum (Chest)
Distance Constraint	1	9	8	20
Cluster Number	0	0	3	0
Cluster Distance	1.6	1.6	1.6	1.6
PRMF	1	1	5	5
Merge X	0	1	1	0
Merge Y	0	1	1	0
Merge Z	0	1	1	0
Band X Factor	0.2	0.2	0.2	0.2
Band Y Factor	0.2	0.2	0.2	0.2
Band Z Factor	0.2	0.2	0.2	0.2
Run Time (sec)	35	40	46	243

Table 3.3 The parameters used to generate the building blocks for an additional 4 bones.

Parameters	3 rd Cuneiform (Ankle)	Cuboid (Ankle)	Metatarsal (2 nd Toe)	Patella (Knee)
Distance Constraint	5	0.1	10	2
Cluster Number	0	0	0	0
Cluster Distance	1.6	1.6	1.6	1.6
PRMF	1	2	5	1
Merge X	1	1	1	0
Merge Y	1	1	1	0
Merge Z	1	1	1	0
Band X Factor	0.2	0.2	0.2	0.2
Band Y Factor	0.2	0.2	0.2	0.2
Band Z Factor	0.2	0.2	0.2	0.2
Run Time (sec)	49	47	61	62

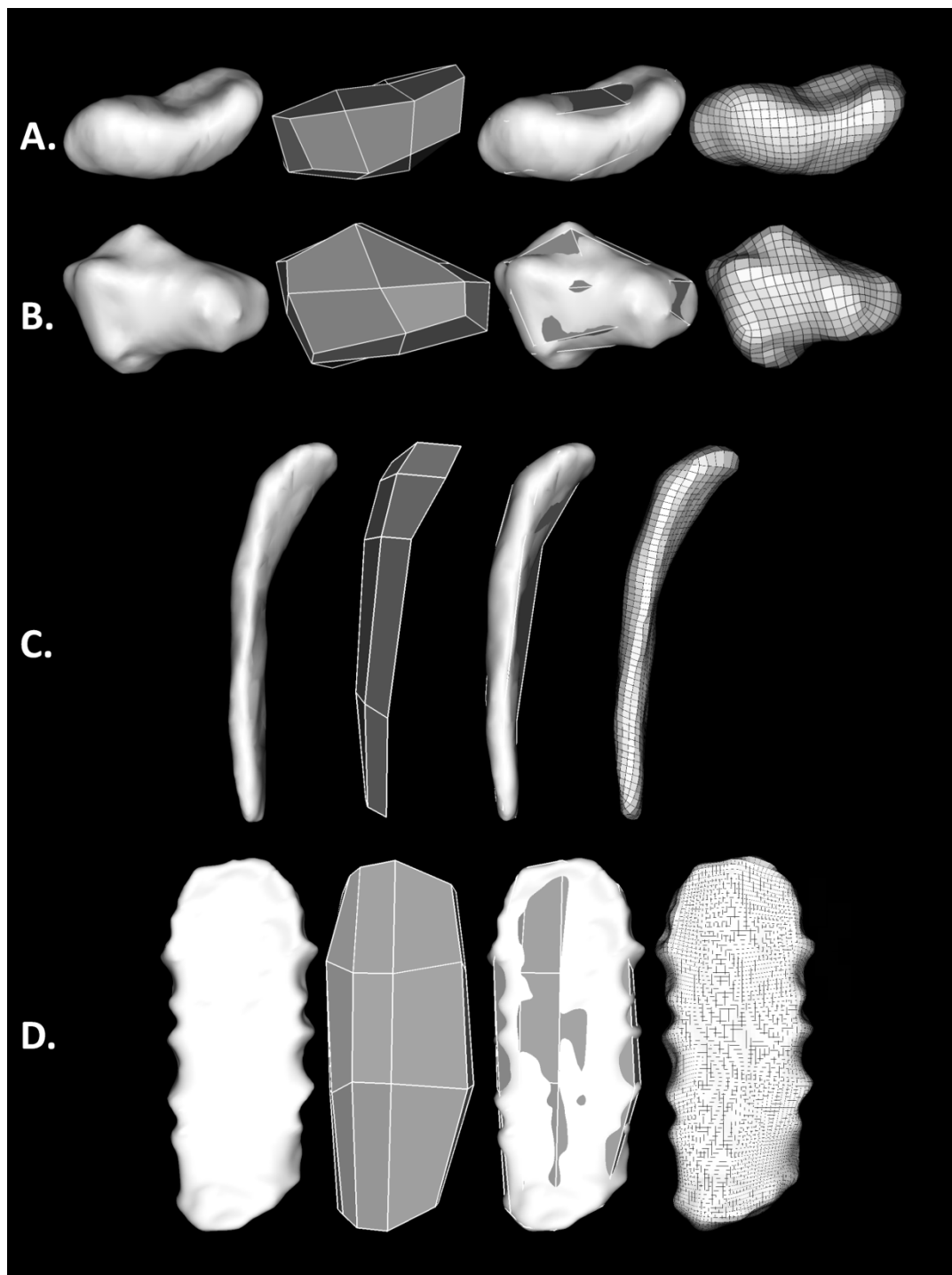


Figure 3.12 From left to right, the objects are the original surface, building block structure generated using the automated algorithm, an overlap view of the building block structure and the surface, and a hexahedral finite element mesh generated using the automatically generated building block structure. The Automated Building Block Algorithm was applied to the A) scaphoid, B) the trapezium, C) the twelfth rib, and D) the sternum.

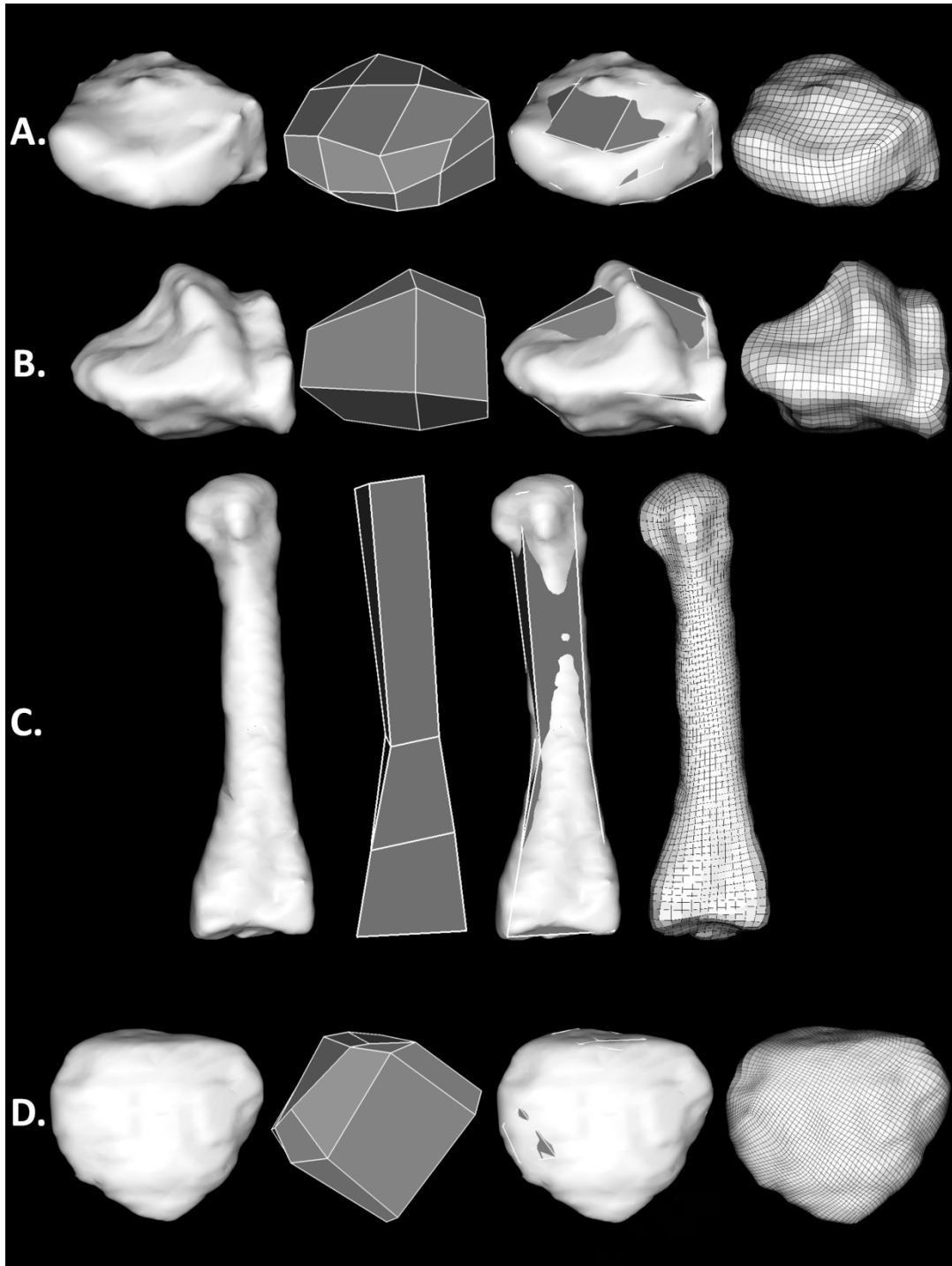


Figure 3.13 From left to right, the objects are the original surface, building block structure generated using the automated algorithm, an overlap view of the building block structure and the surface, and a hexahedral finite element mesh generated using the automatically generated building block structure. The Automated Building Block Algorithm was applied to the A) third cuneiform, B) the cuboid, C) the metatarsal of the second toe, and D) the patella.

3.3.5 Discussion

We have developed an algorithm to automatically define building blocks for hexahedral mesh generation of bony structures using Gaussian curvature analysis. Our investigation has considered 29 bones of varying geometry, and a successful mesh has been generated for all 29 structures. Twenty-seven of the 29 required no additional mesh improvement, while two required mesh optimization using an in-house code. This represents a significant advancement in automating the building block definitions required as input for IA-FEMesh. The demonstrated run times are well within, if not faster than, the amount of time a user would typically need to generate a building block structure.

The two bones (talus and calcaneus) that required additional mesh optimization were investigated. In both cases, the difficulty arose in identifying points corresponding to regions with gradual concavity on the bone surface. Points within these concave regions were not identified by the point selection filter since their Gaussian curvature value did not vary significantly from the mean curvature value. Thus, an individual building block was not created to correspond to this region of the surface. Since the overall geometry of bones is similar between patients with normal anatomy, we would expect that this algorithm would successfully generate a block structure for flat, short, and cuboidal bones from different patients with similar results. If a surface with anatomic variation or pathologic change was to include a region of gradual convexity or concavity, then we could expect a similar difficulty as described above. In the future, we plan to allow manual placement of additional seed points for the VMTK segmentation. This would readily allow the user to overcome this limitation.

The 29 bones considered were by nature flat, short, and/or cuboidal in shape. Our goal is to extend this work to the long bones (e.g. tibia and femur), curved bones (e.g. ribs), and irregular bones (e.g. vertebrae). The Automated Building Block Algorithm currently relies on the assumption that each bone contains a single global coordinate

system that corresponds with the minimum volume bounding box for a given bone surface. This assumption is not necessarily true for all cases, especially if the algorithm aims to replicate the methods by which a user places building blocks. Incorporating a method to determine the optimal orientation for individual segments of a bone surface would allow the Automated Building Block Algorithm to further mimic the process by which a user manually defines blocks.

Another limitation of the Automated Building Block Algorithm is the ability to handle bones containing holes like the ilium and vertebrae. In the future, a hole detection algorithm will be developed to identify surfaces that are not homeomorphic to a sphere. After the hole has been detected, additional code will be developed to modify a given block structure to account for the hole and allow for mesh generation for these structures.

In summary, the Automated Building Block Algorithm was able to generate a building block structure automatically for anatomical regions of interest without manual intervention. The meshes generated from the multiblock structures were valid (contained no zero volume elements) and were appropriate for finite element analysis. The building block structures were generated in between 30 seconds and 4 minutes, which is typically faster than manual generation of the building block structures. In the future, inclusion of the additional features described above will foster the development of a completely automated method of building block structure definition capable of generating a hexahedral mesh for virtually any anatomic structure.

3.4 Building Block Growing Algorithm

3.4.1 Abstract

Hexahedral meshing tools based on the multiblock method currently rely on manual placement of building blocks for mesh generation. Our first effort towards automating this process was described in Section 3.3. Here we present a new and improved method, and we hypothesize that angular analysis of the geometric centerline

of a three-dimensional surface could be used to automatically generate building block structures for multiblock hexahedral mesh generation. Our algorithm uses a set of user-defined points and parameters to automatically generate a multiblock structure based on a surface's geometric centerline. We applied this algorithm to 47 bones of varying geometries and successfully generated a finite element mesh in all cases. This work represents continued advancement in automatically generating multiblock structures for a wide range of geometries.

3.4.2 Introduction

Our first effort towards automating block placement in the multiblock hexahedral meshing process was the Automated Building Block Algorithm (ABBA) as described in Section 3.3[88]. This algorithm was shown to be capable of automatically generating multiblock structures for short, flat, and cuboidal bone geometries. However, its methods were limited by a single coordinate system for block placement, instead of a rotating coordinate system that is most convenient in addressing anatomic structures. In this paper, we present a new algorithm that is not limited by the shortcomings observed in the ABBA. We present the Building Block Growing Algorithm (BBGA) as a semi-automated approach to block placement, and we hypothesize that angular analysis of a surface's geometric centerline will allow for building block placement with a variable coordinate system.

3.4.3 Materials and Methods: The Algorithm

The Building Block Growing Algorithm uses a surface's geometric centerline to generate a building block structure for a surface without prior information. The algorithm follows a tree-like structure whereby a trunk is defined and branches are subsequently added to the trunk. The input to the algorithm is a triangulated representation of the surface of interest (e.g. femur), while the output is a building block structure corresponding to this surface. User-defined parameters provide flexibility and

control over the number and size of blocks composing the building block structure. The overall goal of this algorithm was to automate the structural building block definitions in the absence of a template or pre-existing building block pattern. Figure 3.14 summarizes the steps of the Building Block Growing Algorithm and Figure 3.15 provides incremental results from the dotted pathway through the algorithm described in Figure 3.14.

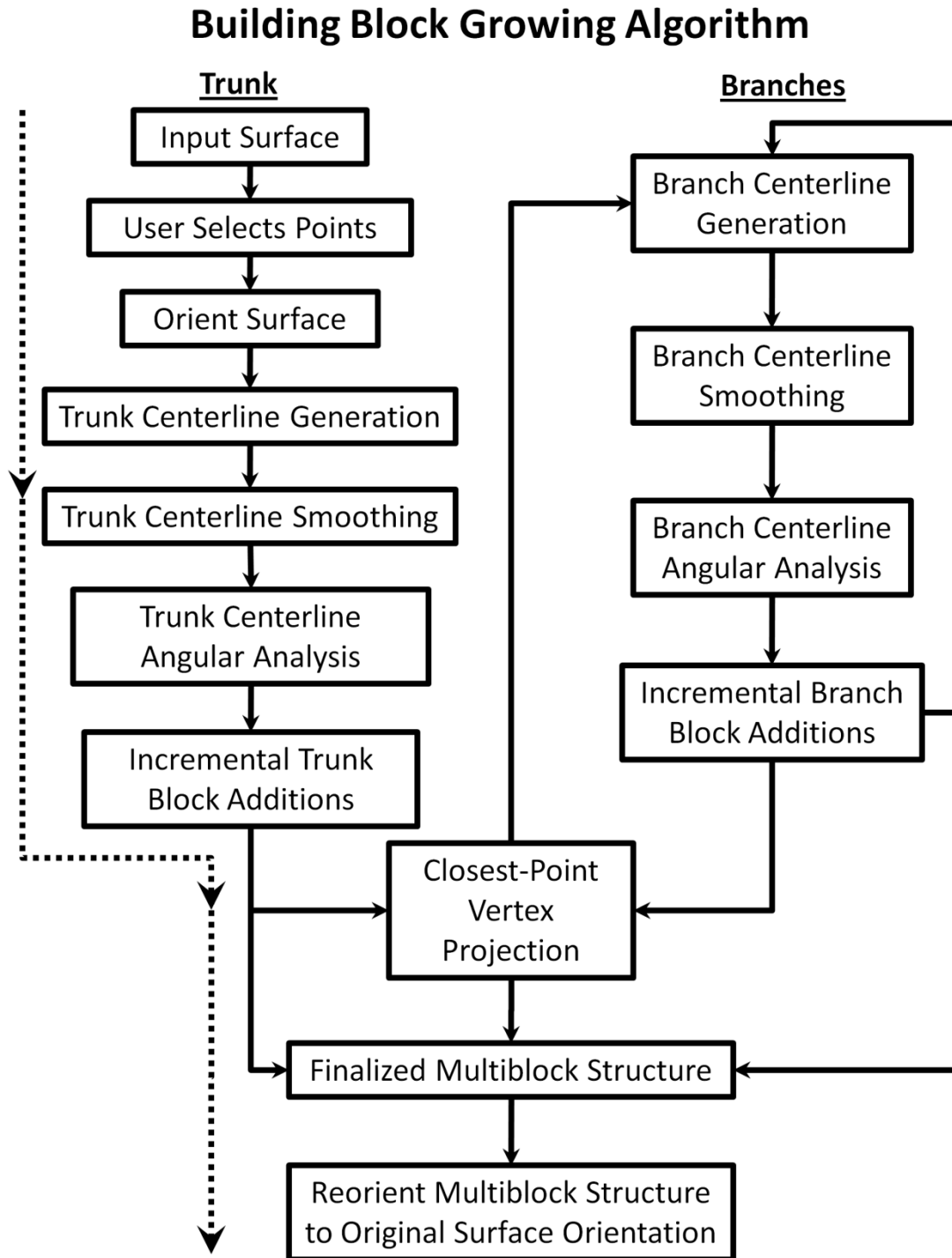


Figure 3.14 A flow diagram describing the steps of the Building Block Growing Algorithm. The dotted set of arrows demonstrates the path used to generate the building block structure in Figure 3.15.

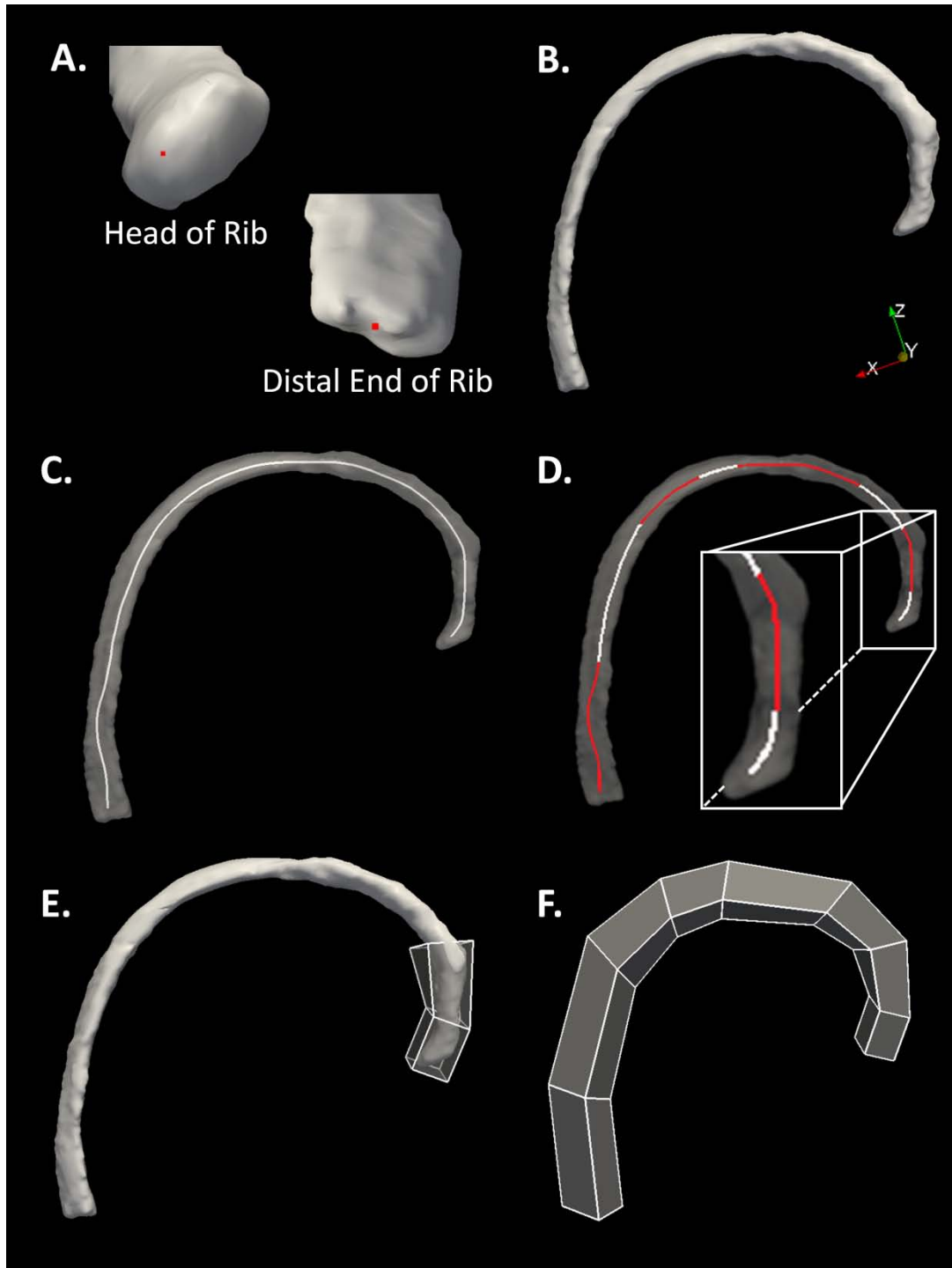


Figure 3.15 Incremental results corresponding to the dotted path described in Figure 3.14 demonstrated using a surface of the third rib. A) Surface point selection by user. B) Reorientation of the selected surface. C) Trunk centerline generation. D) Trunk centerline angular analysis. E) Incremental additions of building blocks along third rib. F) Finalized block structure reoriented back to the original position.

3.4.3.1 Manual Selection of Points

The BBGA relies on user-selected points corresponding to the start and end points of the trunk structure. Additional points corresponding to any branches leaving the trunk can also be defined by the user. Figure 3.15A shows two points selected that correspond to the start (head of rib) and end (distal end of rib) of the trunk structure for the third rib. The selected points are used for construction of the surface's centerline in the medial axis calculation.

3.4.3.2 Reorient the Surface

Three-dimensional surfaces generated from medical imaging datasets are oriented arbitrarily with respect to the Cartesian coordinate system. To establish a known starting position for all surfaces, a rigid body transform is used to align the anatomical surface with the Cartesian coordinate system (Figure 3.15B). This is performed using an optimization procedure to determine the minimum volume bounding box for the entire surface. The reoriented surface simplifies the generation of the multiblock structure by having the bone align with the physical axes.

3.4.3.3 Trunk Centerline Generation

The Vascular Modeling Toolkit (VMTK) is an open-source software tool that uses medial axis analysis for vascular-based research[43]. VMTK's tools are used to generate a centerline for a triangulated surface using a Voronoi Diagram. Using the endpoints for the trunk defined in Section 3.4.3.1, a centerline for the region corresponding to the trunk is generated as depicted in Figure 3.15C.

3.4.3.4 Centerline Smoothing

A smoothing operation is employed to remove local variations in the centerline described in Section 3.4.3.3. A 15 point moving average is used to smooth the centerline.

The smoothed centerline is used to define the variable coordinate system for the building block additions and to automatically determine the lengths of the building blocks.

3.4.3.5 Trunk Centerline Angular Analysis

Angular analysis of the centerline allows for the automatic determination of the required lengths of building blocks for a given surface. Two user-defined parameters are used to automatically determine the number of building blocks needed to represent a centerline: trunk angle and the trunk block length factor. Starting from one end of the centerline, the dot product is used to evaluate the angle between the first and second points and the first and subsequent points on the centerline (Eq. 3.2).

$$\theta_s = \cos^{-1} \left(\frac{\overrightarrow{p_i p_{i+1}} \cdot \overrightarrow{p_i p_n}}{|\overrightarrow{p_i p_{i+1}}| |\overrightarrow{p_i p_n}|} \right) \quad (\text{Eq. 3.2})$$

where θ_s is the current segment angle, p_i is the first point for the current centerline segment, p_{i+1} is the second point for the current centerline segment, and p_n is the n th point for the current centerline segment. The points along the centerline are incrementally evaluated for the endpoint of the block defined by exceeding the trunk angle and minimum length based on the trunk block length factor. The trunk block length factor represents a proportion of the overall length of the trunk's centerline. For example a value of 3, would require that added blocks were at least one-third of the centerline's overall length.

This process continues to define the locations for the block endpoints until the entire length of the centerline has been evaluated (Figure 3.15D). However, in the cases of the first block and the last block, the building block length values are modified to compensate for the fact that the centerline endpoints may not demarcate the distal most points of the surface. For all structures considered, extending the first and last blocks by

three times the average surface radius at these points (defined by the surface's Voronoi diagram) compensated for this length discrepancy.

3.4.3.6. Incremental Trunk Block Additions

After the centerline has been discretized corresponding to the lengths of the building blocks, the surface point clouds surrounding each centerline segment are used to determine the remaining two dimensions for each building block. The first step in this procedure involves isolating the points surrounding each centerline segment. Surface points that are identified to be within three times the local average surface radius are identified as being associated with the centerline segment under consideration.

Once the surface points have been associated with a centerline segment, the rigid body transform described in Section 3.4.3.2 is used to determine the minimum volume bounding box for the surface segment. The bounds of the minimum volume bounding box are used as an estimate for the remaining two dimensions of the building block. However, the local average surface radius can fail to identify surface points in irregular geometries. For this reason, two-user defined factors allow for flexibility in assigning the block dimensions: Trunk Width Factor and Trunk Depth Factor. For example, a Trunk Width Factor of 2 doubles the estimated width for the building block, and the Trunk Depth Factor works similarly for the depth dimension. This is useful to supplement the estimation given by the rigid body transform.

Once the dimensions for a given block have been determined, the next step involves creating the block and orienting it with the surface. The first block is created and aligned such that the long axis of the block corresponds with the endpoints of the first centerline segment[89]. After the first block has been added, additional blocks are “grown” from this base structure to form the trunk. With each block addition, the intermediate block structure is oriented such that the subsequent centerline segment is aligned with the long axis of the block. This procedure continues along the length of the

centerline until the final block for the trunk structure is created. By reorienting the intermediate block structure based on the endpoints of the centerline segments, a variable coordinate system for block addition has been accomplished. This incremental addition process is demonstrated in Figure 3.15E at an intermediate stage and in Figure 3.15F at a final stage.

3.4.3.7 Closest Point Vertex Projection

After the trunk block structure has been completely constructed, an optional closest point projection (Eq. 3.3) is used to match the vertices of the building blocks with the closest points on the surface. If the user has not selected the closest point projection option, the block structure skips to the reorientation procedure described in Section 3.4.3.9. If branches are to be added, a closest point projection is performed on the trunk prior to adding branches to the trunk structure.

$$q'_m = \operatorname{argmin}(\forall p_n: d(q_m, p_n) = \sqrt{(q_m - p_n)^2}) \quad (\text{Eq. 3.3})$$

where q_m is the current building block node and p_n is a surface vertex.

3.4.3.8 Branch Generation

If the user has defined points in Section 3.4.3.1 corresponding to the endpoints of branches, each branch is analyzed independently. A new centerline is generated using the endpoint for the branch and the user-defined starting point for the trunk. The same smoothing operation described in Section 3.4.3.3 is applied. The intersection point between the branch's centerline and the trunk's building block structure allows for the identification of the face where the branch's centerline exits the trunk block structure. This face corresponds to the starting location for adding building blocks around the branch. Next, the branch's centerline points that fall outside the trunk's building block

structure are isolated from the rest of the centerline. The isolated points and the same procedure described in Section 3.4.3.5 and Section 3.4.3.6 are used to define the building block structure for the branch.

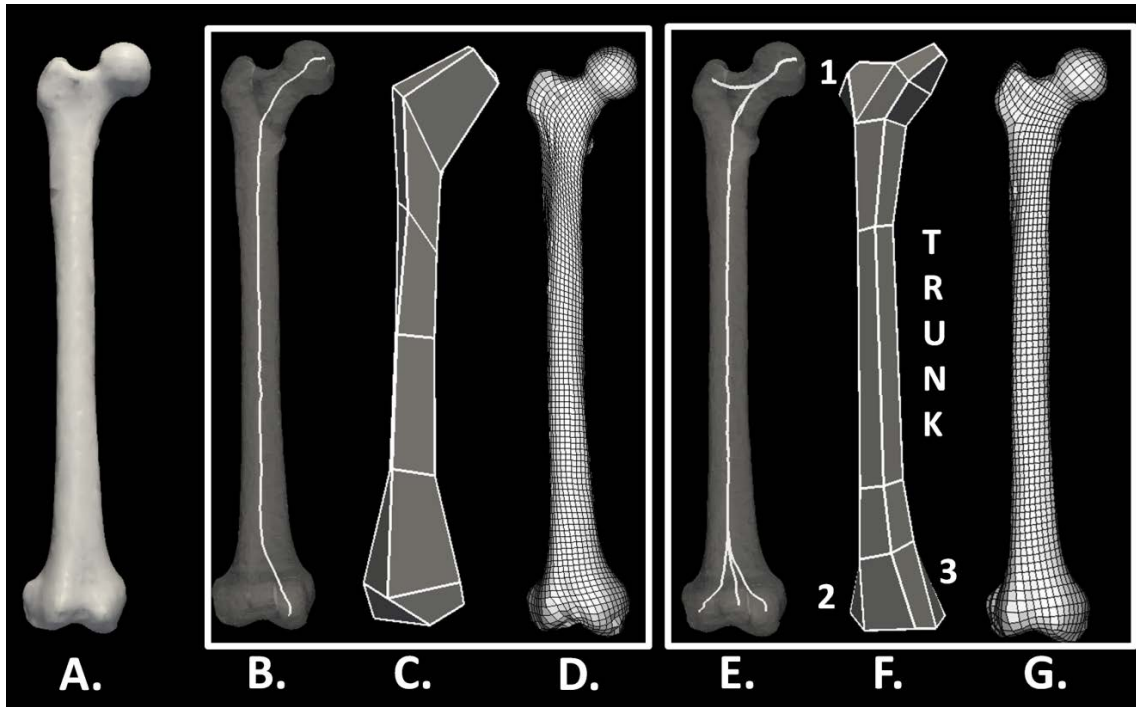


Figure 3.16 A comparison of different outputs from the Building Block Growing Algorithm demonstrating different multiblock structures. A) A surface of the human femur used as an input to the semi-automated algorithm. B) A trunk centerline representation of the femur. C) A multiblock structure of the femur including a trunk structure without branches. D) A hexahedral finite element mesh of the femur generated using the semi-automatically generated building block trunk structure. E) A trunk and 3 branches centerline representation of the femur. F) A multiblock structure of the femur including three branches representing the greater trochanter(1), lateral condyle(2), and medial condyle(3). G) A hexahedral finite element mesh of the femur generated using the semi-automatically generated building block trunk and branch structure.

A set of user-defined parameters have been developed for the branch additions; each of these parameters has a corresponding parameter in the generation of the trunk block structure. The branch parameters include branch angle, branch block length factor,

branch width factor, and branch depth factor. After completion of the all the branches, the user has the option of performing a closest point projection of the building block vertices as was described in Section 3.4.3.7. Figure 3.16 demonstrates two valid block structures for the human femur. Figure 3.16C depicts the multiblock structure generated from a single centerline (trunk only) representation of the femur, while Figure 3.16F depicts the multiblock structure generated from a trunk with three branches.

3.4.3.9 Reorient Block Structure

After completing the trunk and branches, the building block structure is reoriented using the inverse transform estimated in Section 3.4.3.2. This finalized multiblock structure is imported to IA-FEMesh for hexahedral mesh generation.

3.4.4 Evaluation Methods

3.4.4.1 Computational Resources

The C++ programming language, Visualization Toolkit (VTK), and VMTK, were used to develop the Building Block Growing Algorithm. Programming and testing was performed on an Intel Xeon 2.67GHz with 8.00 GB of RAM running a 64-bit version of the Microsoft Vista operating system. The IA-FEMesh software package was used for hexahedral mesh generation from the automatically generated building block structures and assignment of loading and constraining conditions. The ABAQUS[®] finite element solver was used to solve the finite element simulation generation for each hexahedral mesh with an applied load.

3.4.4.2 Algorithm Testing

To evaluate the Building Block Growing Algorithm, 47 bones from the bone surface library were chosen that represented a variety of shapes and locations from the human skeleton (Table 3.4). The algorithm was applied to each of the bones and the run time was recorded. After generating a building block structure for each bone, a

hexahedral mesh was created, smoothed, and optimized for each of the bones using IA-FEMesh. The quality of the resulting meshes was evaluated using several metrics: the minimum element volume, average element volume, and minimum scaled Jacobian. In addition, the resulting meshes were used in a static finite element analysis by applying loading and boundary conditions. Material properties ($E = 15\text{GPa}$, $\nu = 0.3$) were assigned to each of the meshes. A simulated load of 30N was assigned to the distal aspect/articulation of each bone mesh, and the bone mesh's proximal aspect/articulation opposing the load was fully constrained. For example, in the case of the femur the distal articulating surface was loaded with 30N and the proximal articulating surface was fully constrained. For the cases where bones have multiple sets of articulating surfaces (e.g. wrist bones), a single set of articulations was chosen for loading and boundary conditions. Each model was saved and ABAQUS[®] was used to generate a solution for the simulation.

For comparison purposes, the Automated Building Block Algorithm (ABBA) was re-run on the 29 bones reported in our previous manuscript using the same computational resources as the BBGA and the run times were recorded[88]. Finally, manual building block structures were created using IA-FEMesh for a representative sample of bones (ulna, cuboid, sternum, metacarpal, femur, and third rib) by a beginner and an expert user. The time required to generate the building block structures was recorded. As with the BBGA, the block structures that were manually generated and created by the ABBA were tested using the same procedure as described above.

The BBGA was originally designed to generate building block structures for components of the musculoskeletal system. Nevertheless, the technique may benefit countless applications. For example, the human vascular system is tree-like by nature; thereby providing an ideal test of the BBGA. The human abdominal aorta has various smaller branching vessels leaving the aorta along its course at a variety of angles and paths. We applied the BBGA to a human abdominal aorta surface to automatically

generate a building block structure as a proof of concept study for structures outside of the human musculoskeletal system.

Table 3.4 The 47 bones that the Building Block Growing Algorithm was applied where only a trunk multiblock structure was used.

Cuboidal Bones	Short Bones	Long Bones	Flat Bones	Curved Bones
Calcaneus	Proximal Phalanx –Finger	Humerus	Manubrium	Rib 1
Capitate	Medial Phalanx –Finger	Femur	Sternum	Rib 2
Coccyx	Distal Phalanx - Finger	Fibula	Xyphoid Process	Rib 3
Cuboid	2 nd Metacarpal	Radius		Rib 4
1 st Cuneiform	Proximal Phalanx –Toe	Tibia		Rib 5
2 nd Cuneiform	Medial Phalanx –Toe	Ulna		Rib 6
3 rd Cuneiform	Distal Phalanx – Toe			Rib 7
Hamate	2 nd Metatarsal			Rib 8
Lunate				Rib 9
Navicular				Rib 10
Patella				Rib 11
Pisiform				Rib 12
Scaphoid				Clavicle
Talus				
Trapezoid				
Trapezium				
Triquetrum				

3.4.5 Results and Discussion

Tables 3.5-3.7 describe a representative subset of the final meshes that were generated and run times for the BBGA to generate a multiblock structure. A subset of 8 of the structures was selected to demonstrate the parameters used in each case, and are shown in Table 3.8-3.9. Sample outputs from the BBGA for the third rib (Figure 3.15),

femur (Figure 3.16), ulna (Figure 3.17A), cuboid (Figure 3.17B), sternum (Figure 3.17C), and second metacarpal (Figure 3.17D) are provided. This covers several structures that are primarily curved, long, short, flat, or cuboidal in shape. In all 47 cases, the BBGA generated a block structure that produced a final mesh representation with a positive minimum element volume and positive scaled Jacobian. All of the resulting meshes produced a result in ABAQUS® without error. A convergence study was not performed since this is problem dependent and may depend on the loading and boundary conditions. However, the multiblock approach readily supports changing mesh density by specifying the number of divisions or average element edge length for any of the blocks. Figure 3.16 also demonstrates two different block structures for a long bone (the femur) using the functionalities of the BBGA. In both cases, a mesh for the femur was created with positive volume and scaled Jacobian values for all of the elements. The time required to generate the building block structures using the BBGA ranged from 3 seconds to 7 minutes 33 seconds.

Table 3.5 Detailed results from the Building Block Growing Algorithm for a subset of bones that was analyzed.

Metric	Cuboid	Femur	Metacarpal
Location	Ankle	Leg	2 nd Finger
# of Elements	5040	10608	1830
Minimum Element Volume (mm³)	0.101	6.116	0.625
Average Element Volume (mm³)	1.817	30.993	3.369
Minimum Scaled Jacobian	0.035	0.006	0.026
Run-Time (sec)	15	25	17

Table 3.6 Detailed results from the Building Block Growing Algorithm for a subset of bones that was analyzed.

Metric	Rib 3	Sternum	Ulna
Location	Chest	Chest	Forearm
# of Elements	1065	14105	7686
Minimum Element Volume (mm³)	1.902	0.176	0.456
Average Element Volume (mm³)	10.491	1.954	5.441
Minimum Scaled Jacobian	0.0121	0.026	0.025
Run-Time (sec)	53	72	100

Table 3.7 Results from the Building Block Growing Algorithm applied to the femur and aorta.

Metric	Femur	Abdominal Aorta
# of Branches	3	4
# of Elements	3751	5412
Minimum Element Volume (mm³)	6.626	0.127
Average Element Volume (mm³)	87.609	9.777
Minimum Scaled Jacobian	0.007	0.008
Run Time (sec)	62	101

Table 3.8 The parameters used to generate the building blocks for four bones.

Parameters	Cuboid (Ankle)	Femur (w/o Branches)	2 nd Metacarpal (Wrist)	Rib 3 (Chest)
Trunk Angle	1	3	3	15
Trunk Block Length Factor	3	6	3	20
Trunk Width Factor	1	1.2	1	1.3
Trunk Depth Factor	1	1.2	1	1
Vertex Projection	Yes	Yes	Yes	

Table 3.9 The parameters used to generate the building blocks for an additional three bones and one vascular structure.

Parameters	Sternum (Chest)	Ulna (Forearm)	Femur (w/ Branches)	Abdominal Aorta
Trunk Angle	10	5	5	3
Trunk Block Length Factor	10	8	10	10
Trunk Width Factor	1	1.2	0.6	1
Trunk Depth Factor	1.4	1.2	0.6	1
Branch Angle			1	1
Branch Block Length Factor			1	3
Branch Width Factor			1	0.4
Branch Depth Factor			1	0.4
Vertex Projection	Yes	Yes	Yes	Yes

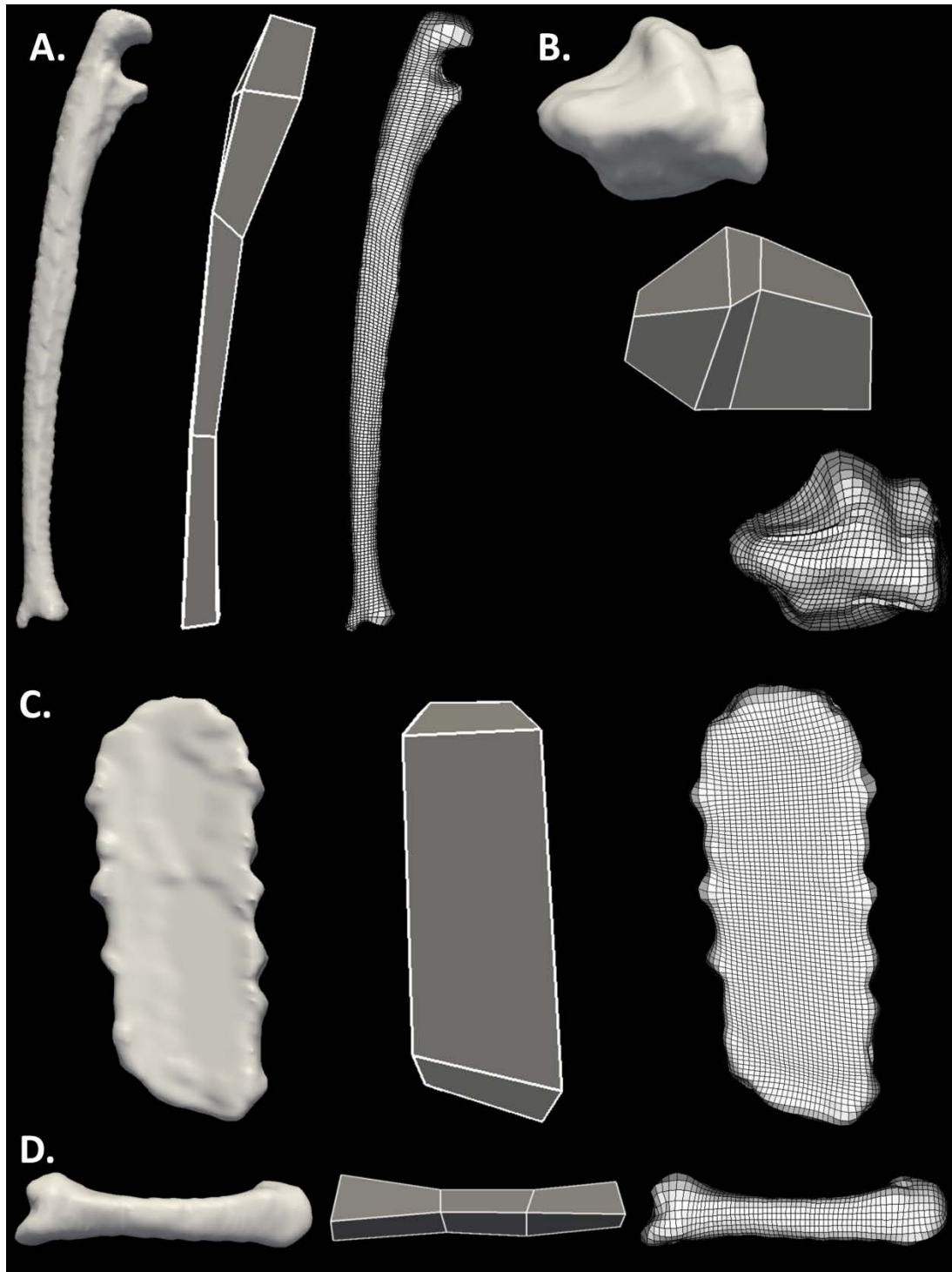


Figure 3.17 From left to right, the objects are the original surface, building block structure generated using the semi-automated algorithm, and a hexahedral finite element mesh generated using the semi-automatically generated building block structure. The Building Block Growing Algorithm was applied to A) the ulna, B) the cuboid, C) the sternum, and D) the second metacarpal.

We have developed an algorithm to automatically generate building block structures for hexahedral multiblock finite element meshing based on angular analysis of a three-dimensional surface's centerline. We have evaluated the algorithm using 47 different bone surfaces derived from the human skeleton. In all cases, a building block structure was generated that produced a mesh with all positive volume and scaled Jacobian elements. The automatically generated block structures did not require any manual manipulation to produce a valid mesh. In a finite element study involving bones, a convergence study would be required to determine the ideal number of elements for each bone surface. The 47 bones represented short, long, flat, curved, and cuboidal bone geometries. This work represents continued advancement towards automating the building block definitions required as input for multiblock meshing packages, such as IA-FEMesh.

A major goal of the BBGA was to automate building block placement while overcoming the limitations of the Automated Building Block Algorithm (ABBA). The ABBA was limited to short, flat, and cuboidal bone geometries due to a fixed coordinate system. By using the centerline as a means to orient building block placement, the BBGA avoids the limitations of a fixed coordinate system inherent to the ABBA. By removing this limitation, the BBGA works on long and curved bones that had previously failed with the ABBA algorithm. It also offers the ability to include branches in a multiblock structure, which was not possible in the ABBA. In this paper, we have shown that the BBGA successfully generated building blocks for 18 additional bones where the ABBA fails[88].

As a means of comparison, six bones were selected as a representative sample of geometries to compare the BBGA, ABBA, and manual definitions. The time needed to generate a valid building block structure for each of the six bones is demonstrated in Figure 3.18. In all six cases, both the ABBA and BBGA are faster than the manual generation times. In addition, the BBGA was between 10 and 138 times faster than the

beginner user and 2 and 54 times faster than the expert. When the BBGA is compared to the ABBA, the BBGA was faster or within 1 second of the run time for the ABBA in 28 of 29 cases. Overall, the automated methods are faster than the manual generation times, and the BBGA offers the fastest solution in the majority of cases.

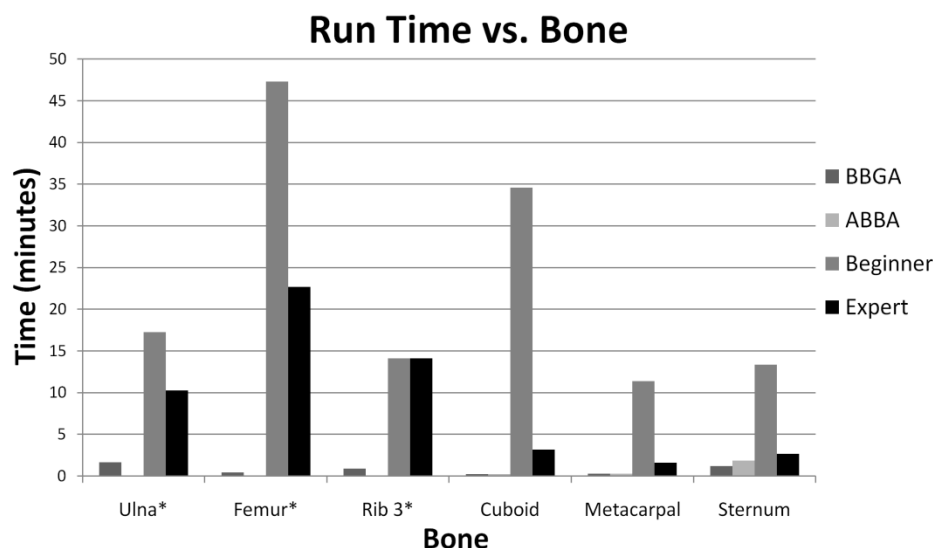


Figure 3.18 A comparison of the run times for six representative cases in the generation of multiblock structures using BBGA, ABBA, manual definitions by a beginning IA-FEMesh user, and manual definitions by an expert IA-FEMesh user. The * indicates a case where the ABBA did not create a building block structure.

As an additional means of comparing the manual and automated block placement methods, the number of building blocks composing the multiblock structure for each of the six representative cases was evaluated. Figure 3.19 shows the number of building blocks in each block structure for each of the multiblock structure generation methods. In most cases, the automated methods generated block structures composed of fewer blocks than manual methods; however, it should be noted that the number of blocks generated by the automated algorithms is dependent on the user-defined parameters.

When comparing the BBGA to the ABBA in the 29 cases where the methods both generated a result, the BBGA required fewer blocks in 22 of 29 cases. Overall, the automated methods produce block structures composed of a smaller number of blocks than the manual methods. Between the two automated methods, the BBGA produces a simpler multiblock structure as compared to the ABBA.

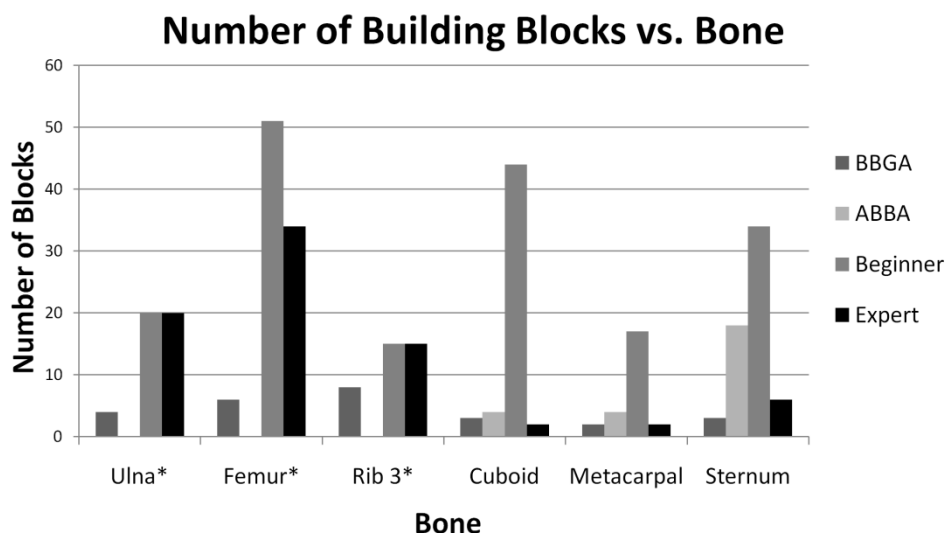


Figure 3.19 A comparison of the number of building blocks for a multiblock structure for six representative cases using BBGA, ABBA, manual definitions by a beginning IA-FEMesh user, and manual definitions by an expert IA-FEMesh user. The * indicates a case where the ABBA did not create a building block structure.

Figure 3.20 demonstrates a comparison between the outputs of the BBGA, ABBA, and manual building block structures in two of the cases. The second metacarpal (Figure 3.20A) is represented by 3 blocks by the BBGA, 4 blocks by the ABBA, 17 blocks by the beginner, and 2 blocks by the expert. The cuboid (Figure 3.20B) is represented by 3 blocks by the BBGA, 4 blocks by the ABBA, 44 blocks by the beginner, and 2 blocks by the expert. This example demonstrates that simple block structures can

be used to develop a valid mesh; overall automated methods more closely resembled the expert manual definitions. Tables 3.10-3.11 provide the mesh quality metrics for the subset of bone meshes generated from the multiblock structures created by each of the building block placement methods. The meshes generated from the building block structures using the BBGA had similar minimum element volumes, average element volumes, and minimum scaled Jacobians when compared to the manual definitions for the six representative cases.

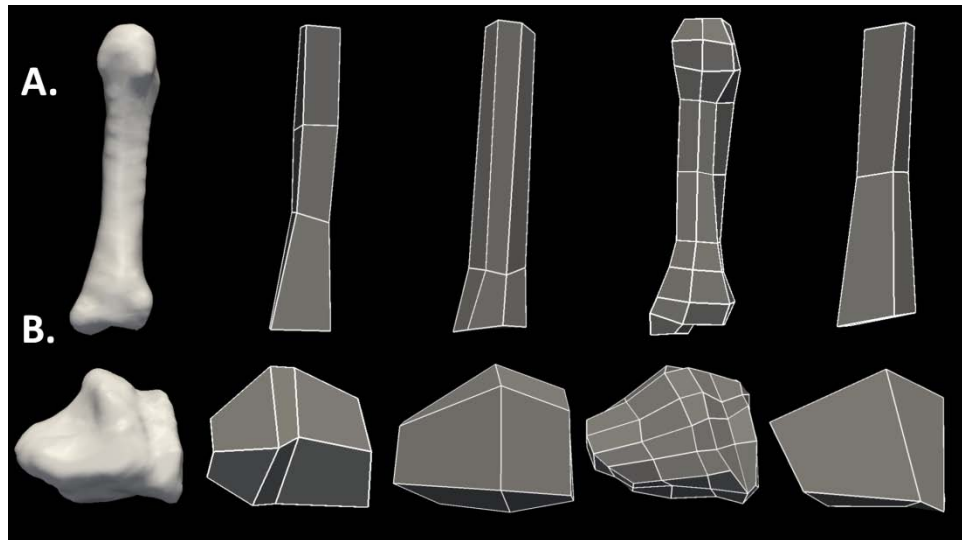


Figure 3.20 From left to right, the objects are the original surface, BBGA building block structure, ABBA building block structure, beginner building block structure, and expert building block structure. The two cases are the A) second metacarpal and B) the cuboid.

Table 3.10 Detailed results from a subset of bones for the BBGA, ABBA, manual definitions by a beginning IA-FEMesh user, and manual definitions by an expert IA-FEMesh.

Block Placement Method	Metric	Ulna	Femur	Rib 3
BBGA	Number of Elements	7686	10608	1065
	Minimum Element Volume (mm ³)	0.456	6.116	1.902
	Average Element Volume (mm ³)	5.441	30.993	10.491
	Minimum Scaled Jacobian	0.025	0.006	0.012
ABBA	Number of Elements	N/A	N/A	N/A
	Minimum Element Volume (mm ³)	N/A	N/A	N/A
	Average Element Volume (mm ³)	N/A	N/A	N/A
	Minimum Scaled Jacobian	N/A	N/A	N/A
Beginner IA-FEMesh User	Number of Elements	7668	5636	1070
	Minimum Element Volume (mm ³)	0.223	7.941	3.074
	Average Element Volume (mm ³)	5.526	59.158	10.369
	Minimum Scaled Jacobian	0.012	0.005	0.031
Expert IA-FEMesh User	Number of Elements	7875	10412	1216
	Minimum Element Volume (mm ³)	0.312	3.426	2.641
	Average Element Volume (mm ³)	5.378	32.166	9.163
	Minimum Scaled Jacobian	0.022	0.003	0.011

Table 3.11 Detailed results from a subset of bones for the BBGA, ABBA, manual definitions by a beginning IA-FEMesh user, and manual definitions by an expert IA-FEMesh.

Block Placement Method	Metric	Cuboid	Metacarpal 2	Sternum
BBGA	Number of Elements	5040	1830	14105
	Minimum Element Volume (mm ³)	0.100	0.625	0.176
	Average Element Volume (mm ³)	1.817	3.369	1.954
	Minimum Scaled Jacobian	0.035	0.026	0.026
ABBA	Number of Elements	6750	4320	20832
	Minimum Element Volume (mm ³)	0.061	0.262	0.184
	Average Element Volume (mm ³)	1.358	1.446	1.328
	Minimum Scaled Jacobian	0.073	0.072	0.045
Beginner IA-FEMesh User	Number of Elements	5130	1904	1360
	Minimum Element Volume (mm ³)	0.163	0.869	0.131
	Average Element Volume (mm ³)	1.792	3.323	2.040
	Minimum Scaled Jacobian	0.033	0.036	0.036
Expert IA-FEMesh User	Number of Elements	5040	1848	14352
	Minimum Element Volume (mm ³)	0.261	0.538	0.245
	Average Element Volume (mm ³)	1.816	3.361	1.930
	Minimum Scaled Jacobian	0.051	0.035	0.047

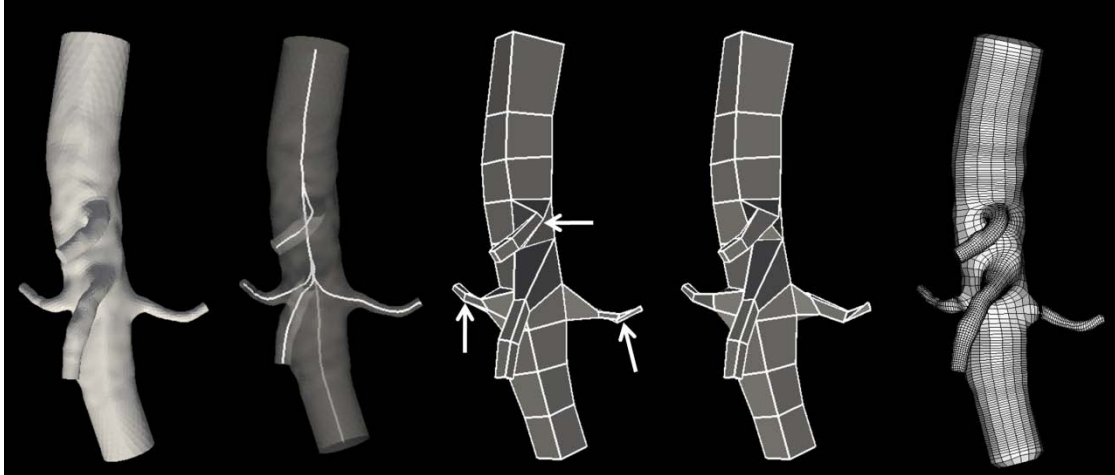


Figure 3.21 The Building Block Growing Algorithm applied to the human abdominal aorta. A) A surface of the human abdominal aorta with four smaller branching vessels. B) Centerlines used to represent the branching vasculature. C) A multiblock structure generated using the BBGA. D) A manually edited multiblock structure that allowed for hexahedral meshing. Regions that were edited are indicated by arrows in (C). E) A hexahedral mesh generated from the multiblock structure in (D).

We applied the BBGA to the human abdominal aorta surface (Figure 3.21A) as a proof of concept study and automatically generated a building block structure shown in Figure 3.21C. Approximately five minutes of manual manipulation of the nodes on three of the branches (indicated by arrows) resulted in a finalized building block structure (Figure 3.21D) that produced a valid mesh (Figure 3.21E) with all elements having positive volume and scaled Jacobian. The BBGA was originally designed to generate building block structures for components of the musculoskeletal system. Here, we also present its potential for application to vascular structures for use in computational fluid dynamics. Due to the sharp angles and narrow passages found in the human vascular system, a minimal amount of manual manipulation was required to generate the mesh shown in Figure 3.21. Additional optimization could help to improve the algorithm for vascular structures to minimize the amount of required manual manipulation.

The BBGA algorithm does have a couple of limitations. First, the algorithm is dependent on the user to select the points used to define the trunk and branch centerlines. However, this allows the user to rapidly provide input regarding the block complexity. It may be possible to automate this process in the future by using this study as an existing database of anatomical structures where the seed points are already defined. Second, the natural variability in geometry and size of bones requires that appropriate user-defined parameters are also chosen. The selected parameters may differ across bones as shown in Tables 3.8-3.9. Some preliminary fine tuning with the values may be required to generate an optimal building block structure for a new geometry. We believe the parameters can be optimized and could eventually be estimated automatically based on the surface being analyzed. Finally, the computational time of the BBGA is approximately linear with respect to the resolution of the surface (i.e. an increase in the number of vertices results in an increased run-time). However, decimation of a surface can drastically reduce the run-time. For example, the tibia took approximately 7.5 minutes to run, while the femur only took 25 seconds. The tibia was composed of 80,288 surface points, while the femur was decimated down to 5,654 surface points (originally 113,016 surface points). When the tibia was decimated down to 4016 points, it only took 14 seconds to run. A high surface resolution is not necessary to generate a multiblock structure to be used for generating the resulting mesh. In our study, the femur was the only bone that was decimated from its original surface resolution. The run time is dependent on the resolution of the surface that the user chooses as an input.

In the future, two improvements will be required for the BBGA. The first is the ability to generate building block structures for irregular bones like the ilium. The second improvement will be developing merging and branching methods to modify a building block structure for the inclusion of holes or drill tunnels in a bone or ring-like structures. With these two improvements, the BBGA will become more widely applicable to anatomic structures and orthopaedic surgical procedures.

3.4.6 Conclusions

Overall, we have developed an algorithm to automatically define building block structures for hexahedral finite element meshing of a variety of bone geometries. The Building Block Growing Algorithm uses angular analysis of a three dimensional surface's geometric centerline and a variable coordinate system to automatically generate a multiblock structure. It relies on several user-defined parameters and user-selected points for its operation. Overall, the BBGA is faster than both the ABBA and manual building block definitions. This algorithm represents continued advancement towards an automated method of building block definition for multiblock hexahedral finite element meshing.

CHAPTER 4

MUSCULOSKELETAL IMAGE ANALYSIS

4.1 Overview

Computed tomography and magnetic resonance technologies have revolutionized medical imaging and our ability to evaluate the human musculoskeletal system. Three-dimensional bone surface models generated using image segmentation techniques provide a means to perform engineering analyses and to optimize individualized orthopedic surgical procedures. A typical process used to generate surface representations of bony anatomy is summarized in Figure 4.1. The process begins with identifying an anatomical region of interest and collecting a three-dimensional image set. Depending on the study, image processing may be necessary to alter the image file size and remove artifacts. Next, the voxels corresponding to the region of interest must be identified from the surrounding background voxels; this process is called image segmentation. Image segmentation is an active area of research with most segmentation methods being optimized for a specific region of the body[17, 62, 63, 65, 66, 90-97]. After segmentation, each segmented image slice can be compiled to form a triangulated surface representation of the region of interest.

Anatomic surface generation has been used for simulation, evaluation, and optimization of surgical procedures. The high contrast of bony structures on CT has made it the modality of choice for evaluating bony structures; however, fully automated segmentation of CT images remains a challenge. In large sample studies and clinical applications, improved methods of anatomic surface generation and high-throughput bone segmentation with minimal user intervention are desirable.

The Insight Toolkit (ITK) is an open-source set of software filters that provides programmers with a means to perform medical image processing operations. With a programming knowledge base, ITK can be used to rapidly process medical image data.

In addition, the Expectation-Maximization (EM) algorithm is an open-source method of image segmentation included in the 3D Slicer toolkit. When combined with atlas to subject image registration, the EM algorithm has been shown to be a viable method of automatic MRI brain segmentation[98-101]. In this chapter, we present a compilation of tools into our own orthopaedic-specific image analysis toolkit: *IA-Image Processing*. We also present two studies demonstrating a novel application of the EM algorithm to the segmentation of musculoskeletal structures.

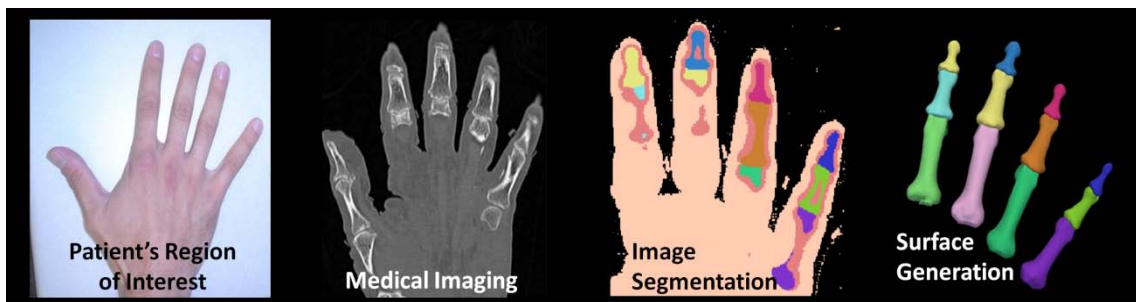


Figure 4.1 The workflow for bone surface generation starts with imaging the region of interest. It proceeds with image processing and segmentation. Finally, a triangulated surface can be generated from the segmented image.

4.2 IA-Image Processing Toolkit

A high-throughput system for orthopaedic image analysis and surface generation is currently not readily available to researchers at The University of Iowa. Medical imaging datasets can be useful for orthopaedic measurement and modeling applications; however, commercial software tools are often unavailable to medical students, residents, and researchers. The National Library of Medicine offers the Insight Toolkit (ITK) and Visualization Toolkit (VTK) as open-source tools for image processing software developers. We have selected several image processing tools that are commonly used among researchers performing orthopaedic research and have created command line

programs for each. Command line programming allows each tool to be easily scriptable; this allows for high-throughput analysis when a large number of image sets require image processing.

In addition, we have used KWWidgets to develop a graphical user interface: *IA-Image Processing* (Figure 4.2). This toolkit was developed to provide a streamlined interface for image processing, segmentation, and surface generation. Figure 4.3 demonstrates the use of multiple tools to generate a surface model of the patella. In our example, an image is loaded, thresholded, mirrored, resampled, and cropped using tools from *IA-Image Processing*. Additionally, a region growing segmentation tool is used to generate a binary mask representation. Surface triangulation, smoothing, and decimation tools are used to create a surface representation that corresponds to the original image. Overall, *IA-Image Processing* is a user-friendly, scriptable, and interactive software package that is catered specifically to the needs of the orthopaedic researcher. A detailed description of the tools available in *IA-Image Processing* is available in Appendix Section B.

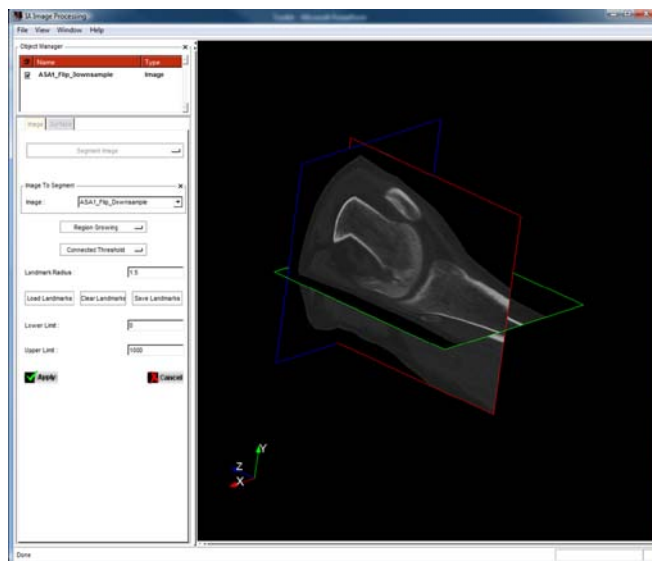


Figure 4.2 A screenshot from the *IA-Image Processing* Graphical User Interface. This application allows access to image processing functionalities in a user-friendly interface.

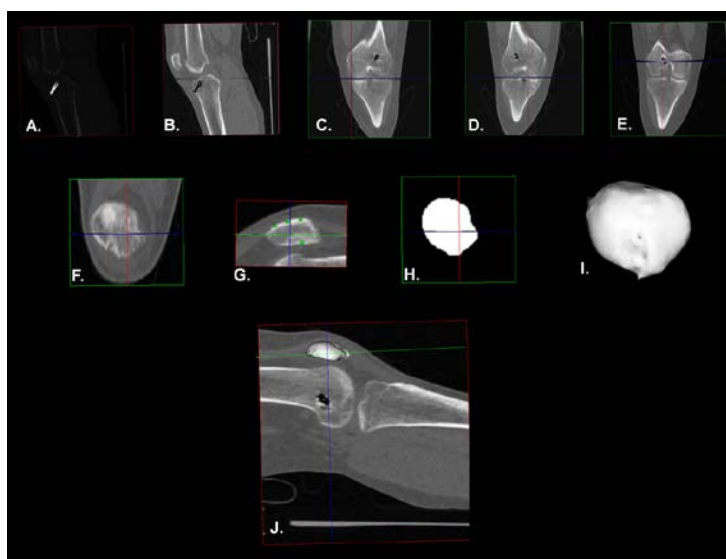


Figure 4.3 The generation of a surface representation of the patella. A) A DICOM image is loaded. B) Hardware beam hardening artifact is thresholded away. C/D) A mirror operation is applied. E) The image is isotropically resampled. F) The image is cropped to isolate the patella. G) Seed points are placed for region growing segmentation. H) The output from the region growing segmentation. I) A surface representation of the patella. J) The surface overlapped with the original image.

4.3 EM Segmentation of the Phalanx Bones of the Hand

4.3.1 Abstract

Medical imaging technologies have allowed for in vivo exploration and evaluation of the human musculoskeletal system. Three-dimensional bone models generated using image segmentation techniques provide a means to optimize individualized orthopaedic surgical procedures using engineering analyses. However, many of the current segmentation techniques are not clinically practical due to the required time and human intervention. As a proof of concept, we demonstrate the use of an expectation maximization (EM) algorithm to segment the hand phalanx bones, and hypothesize that this semi-automated technique will improve on the efficiency while providing similar definitions as compared to a manual rater. Our results show a relative overlap of the proximal, middle, and distal phalanx bones of 0.83, 0.79, and 0.72 for the EM technique when compared to validated manual segmentations. The EM segmentations were also compared to 3D surface scans of the cadaveric specimens, which resulted in distance maps showing an average distance for the proximal, middle, and distal phalanx bones of 0.45, 0.46, and 0.51 mm, respectively. The EM segmentation improved on the segmentation speed of the manual techniques by a factor of eight. Overall, the manual segmentations had greater relative overlap metric values, which suggests that the manual segmentations are a better fit to the actual surface of the bone. As shown by the comparison to the bone surface scans, the EM technique provides a similar representation of the anatomic structure and offers an increase in efficiency that could help to reduce the time needed for defining anatomical structures from CT scans.

4.3.2 Introduction

The application of computed tomography (CT) and magnetic resonance (MR) technologies to medical imaging has allowed for in vivo exploration and evaluation of the human musculoskeletal system. Three-dimensional bone models generated using image

segmentation techniques provide a means to perform engineering analyses and to optimize individualized orthopedic surgical procedures. Traditionally, manual raters have performed the segmentation of bone from medical images. However, these techniques are not clinically practical due to the extensive time and human intervention that is required. This study aims to evaluate a preprocessing and segmentation method to accurately, efficiently, and reliably separate bony regions of interest from CT images. The advantages and insight obtained from engineering analysis of surgical procedures has motivated researchers to automate the process and improve on its efficiency and accuracy. Others in our laboratory are working towards producing automatic hexahedral meshes from the surface definitions appropriate for surface contact analysis using the finite element method. Our ultimate goal is to automate the preprocessing, segmentation, and mesh generation procedures to provide a clinically useful means of surgical analysis and planning.

Many techniques have attempted to segment bone from medical images, many of which have been optimized to certain locations in the body due to some of the inherent difficulties in bone segmenting. One may intuitively expect that bone is very different from the surrounding soft tissues, allowing it to be easily segmented from images. However, bone does not have a homogenous composition[62]. This inhomogeneity results in intensity values that vary greatly throughout a bony structure (e.g. cortical versus trabecular). While cortical bone in younger adults is easy to differentiate from trabecular bone, as the subject ages the density of cortical bone often decreases (e.g. osteoporosis) thereby making the differentiation more difficult. Another complication is the close relationship between bones at the articulating surfaces where the relative positions of these bones is not fixed due to the degrees of freedom allowed by the joint. These close relationships, can make it difficult to differentiate bones of interest especially at the articulating surfaces. The large degree of shape variability at the articulating

surfaces throughout the body also makes it difficult to develop a universal process for bone segmentation.

In attempts at overcoming these difficulties, researchers have tried a variety of modifications to well known techniques including thresholding, region growing techniques, atlas based techniques, artificial intelligence, and various combinations of techniques. Many of these methods have aimed towards the automation of bone segmentation, yet have varying degrees of human intervention. Most of the methods are specific to certain anatomical locations where the techniques have been optimized. Researchers have optimized bone segmentation using various techniques for the acetabulum[90], femoral head[65, 90], cranium[65], pelvis[65, 66], carpal bones[62], mandible[65], vertebrae[91], ribs[92], and various other regions[63, 65, 90, 93-96]. Our laboratory has also developed a segmentation technique using an artificial neural network for the phalanx bones of the hand[97].

Ehrhardt et al. demonstrated an automatic method for segmentation of the hip[66]. This technique used a Thirion atlas based registration, which was followed by a thresholding and nearest neighbor interpolation. The authors report a 98.5% accuracy of their technique when compared to manual segmentations, but mention that several areas were in need of improvement. In particular, an algorithm was needed to increase the precision of the segmentation of the acetabulum and femoral head joint region. Sebastian et al. surveyed various methods of segmentation in an effort to generate models of the carpal bones from CT images[62]. An optimum method for the carpal bones was found to be a combination of active contour models, seed growing, and competition between neighboring regions that was coined the “skeletonally coupled deformable model” (SCDM). A clinical evaluation of the segmentations was performed; however, a quantitative comparison was not presented. Staal et al. demonstrated a method for automated rib segmentation that utilized four preprocessing steps followed by region growing[92]. The preprocessing steps were designed to isolate regions of interest from surrounding tissues

and included 1D ridge voxel detection, generation of line elements from ridge voxels, classification of primitives to remove background information, and finally grouping of generated primitives. Overall, these preprocessing steps were aimed at generating grouped primitives to identify the centerlines of the ribs. This information was then used for a region growing segmentation. The authors report 97.5% accuracy, 96.8% sensitivity, and 97.8% specificity and a total processing time of around 6.5 minutes.

In this study, we demonstrate the use of a semi-automated segmentation technique for segmenting the phalanx bones of the hand that face similar challenges to those seen by Ehrhardt et al.[66], Sebastian et al.[62], and Staal et al.[92]. The Expectation Maximization (EM) algorithm coupled with atlas to image registration has been used for brain segmentation using MR images[98-100, 102]. This approach has been shown to identify and account for image inhomogeneities, incorporate anatomical priors, and produce reliable segmentations of the brain. Using the EM algorithm, we have applied this technique to the phalanx bones of the hand excluding the thumb in this proof of concept study. The thumb was excluded since manual segmentations of the thumb were not available. The phalanx bones of the hand were chosen as the bony region of interest due to the fact that a single scan of one hand supplies twelve separate bones that vary in size and geometry. This allows for a large amount of data from a single scan and an evaluation of a segmentation technique's ability to handle variable bone geometry. Also, the three phalanx bones of each finger are oriented within close proximity, which challenges a segmentation technique's ability to differentiate not only bone from surrounding tissues, but also bone from neighboring bone. For these reasons, the phalanx bones of the hand were an ideal choice for our study. In the future we hope to extend our techniques to other structures of the skeletal system.

4.3.3 Methods

4.3.3.1 Collection of CT Data

Fifteen fresh cadaveric upper extremities were amputated above the elbow and screened to rule out any pre-existing pathology, including evidence of prior trauma. The donor set consisted of thirteen female and two male specimens with a mean age of 73.7 years. Each specimen was mounted on a customized Plexiglas frame in the neutral anatomic position. The neutral position was defined by aligning the back of the hand with the back of the forearm and the third metacarpal with the long axis of the forearm. Using a Siemens Sensation 64 slice CT scanner, three-dimensional voxel datasets of the hand were acquired for each specimen (matrix = 512x512, FOV = 172mm, KVP = 120, Current = 94mA, Exposure = 105mAs) with a 0.34mm in-plane resolution and a 0.4mm slice thickness. Slices spanning the entire limb were obtained for each dataset.

4.3.3.2 Manual Tracing

Following image acquisition, the data was processed using the BRAINS2 software[46]. The images were spatially normalized and resampled to 0.2 mm isotropic voxels aligning the vertical plane of the frame along the superior/inferior axis in the coronal view. This vertically aligned the third metacarpal. The images were cropped to contain only the phalanges for ease of data management. Two trained technicians manually traced 15 index fingers and three complete hands using the BRAINS2 software with an emphasis on creating the most accurate segmentations possible. The regions of interest (ROIs) defining the distal, middle, and proximal bones were manually traced by each technician. The average time required to manually segment the three bones of the index finger was 58.47 minutes, ranging from 39 to 83 minutes. In order to ensure minimal inter-rater variability a study was conducted to compare the performance of the two tracers by determining the relative overlap. The relative overlap computed between

the two raters was 0.89 for all the bones. The individual bones, the proximal, middle, and distal phalanges, had relative overlaps of 0.91, 0.90, and 0.87, respectively[103].

4.3.3.3 Registration of Images and Mirroring

To streamline our registration and segmentation techniques, the images of the left hands were transformed into right hands by a mirror function along the x-axis of the hand. This produced fifteen right hand images for our study. One of the specimens was chosen as the atlas since this specimen had manual traces for all the phalanx bones from each of the four digits, and a visual inspection of all the data showed this specimen to be of average size. The atlas image was registered to each of the subjects using a three stage registration technique which included landmark identification. A total of thirty-two landmarks (eight per finger) were identified using the BRAINS2 software. Six of the twelve landmarks were placed at the endpoints of the phalanx bones corresponding to the anterior, middle, and posterior aspect of the metacarpophalangeal (MCP) joint and the superior tip of the distal phalanx. The remaining two landmarks were placed in the middle of the proximal interphalangeal (PIP) and distal interphalangeal (DIP) joints. Landmark placement was visually verified to be within one voxel using three viewing planes provided by the BRAINS2 software. Several examples of landmark selection are available in Figure 4.4. Based on preliminary work, landmark identification was found to be necessary in order to account for the large anatomic variability that existed across subjects. The number of landmarks was optimized using an iterative process. Fewer than eight landmarks per finger were found to decrease the registration accuracy. More than eight landmarks per finger did not significantly improve the registration and only extended the time for the thin plate spline registration. Following landmark identification, a thin plate spline registration based on the manually defined landmarks[104] was used to initialize a higher order Thirion Demon's algorithm[105] that was used to warp the atlas specimen into correspondence with each of the other specimens. The resulting transform

was saved as a deformation field. The resulting deformation field was then applied to the anatomical priors as described in the following section.

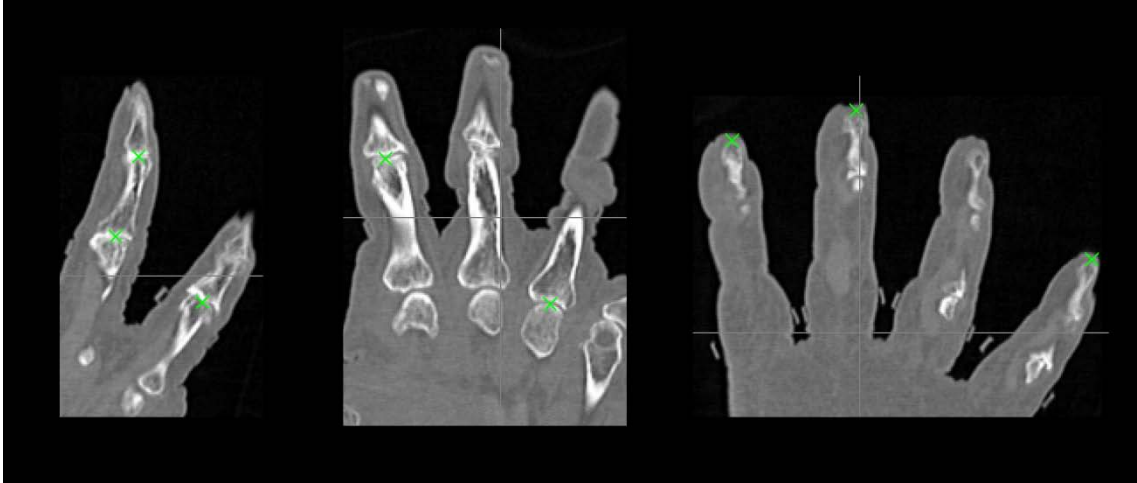


Figure 4.4 Sample landmark identification at various locations on CT images of the hand.

4.3.3.4 EM Bone Segmentation and Post-Processing Techniques

The Expectation Maximization (EM) algorithm is part of the 3D Slicer toolkit and is provided by the National Alliance for Medical Imaging Computing (NA-MIC), one of the National Centers for Biological Computing sponsored by the National Institutes of Health. The algorithm is a two-stage iterative algorithm that uses probability maps and signal intensity information to generate anatomical labels. This process requires a subject image and a probability map for each bone that is to be segmented from the subject image. The probability maps for each phalanx bone were obtained from manual traces from the atlas CT image. The manual traces defining the border of the structure were first converted to a binary representation and then filtered using a Gaussian filter with a variance of 2.0mm. The resulting image was then scaled from 0 to 255 and converted to an 8-bit representation. This was done separately for each of the ROIs resulting in 12

probability maps defining the proximal, middle, and distal phalanx bones for the index, middle, ring, and little fingers. The deformation field mapping the atlas image to each subject, as described previously, was applied to the probability maps warping them from the atlas space to each of the individual subjects.

The EM algorithm was then applied to the subject datasets using optimized parameters for bone segmentation. The EM algorithm was organized using a hierarchical method which first defined signal intensity means and variance for the background, soft tissue, and regions of probable phalanx bone. The regions of probable phalanx bone were further divided into 12 separate regions that corresponded to the phalanx bones of the four fingers. Each region of probable bone was then assigned a respective probability map. The twelve regions of probable bone were further differentiated into regions of bone and regions of soft tissue. This procedure proved effective at finding cortical bone, but produced hollow regions within the trabecular bone. The resulting regions of interest from the EM algorithm were then post-processed to keep the largest connected region thereby eliminating islands that had been misclassified. The hollow regions were then filled to generate an anatomical label for each phalanx bone. Finally, a triangle surface was generated from the binary segmentation and smoothed using Laplacian smoothing.

4.3.3.5 3D Surface Scans

As described previously by DeVries[103] the cadaveric specimens were utilized for validation with a 3D laser surface scanner. Specimen preparation and laser scanning are described briefly here, for more details see DeVries et al. In preparation for the physical scanning procedure, the bones were carefully dissected from each hand/wrist. Care was taken not to alter the bony surface during dissection due to nicking or scratching by instruments. The majority of the surrounding soft tissue was removed during dissection. What tissue remained post-dissection was removed following the defleshing process prescribed by Donahue et al.[106]. The bones were placed in a 5.25%

sodium hypochlorite (bleach) solution for approximately four to six hours to remove the remaining tissue. The bones were examined hourly to avoid decalcification and to remove any extraneous loose tissue. Once denuded, the bones were degreased in a soapy water solution followed by a period of air-drying. Due to the bone's natural coloring and texture, a white primer was applied to the surface before scanning. This produced better scan results since the scanner has difficulty with "fuzzy", dull objects. Three-dimensional surface scans of each physical specimen were ascertained using a Roland LPX-250 3D laser scanner (0.2 inch resolution). The surfaces were cleaned of non-manifold, redundant, and crossing faces. These abnormal faces may cause severe errors in geometric calculations and were removed. Finally, the individual shell was smoothed within a tolerance of 0.01mm. A tight smoothing tolerance was chosen so the actual surface characteristics were kept intact[104].

4.3.3.6 Evaluation of the EM Algorithm

Three metrics were used to compare the resulting regional definitions from the EM algorithm. First, a relative overlap metric (Eq. 3.1) and similarity index metric (Eq. 3.2) were used to compare the binary segmentations generated from the EM algorithm to those created by the manual rater[107].

$$\textit{Relative Overlap} = \frac{\textit{Volume}(\textit{EM Segmentation} \cap \textit{Manual Segmentation})}{\textit{Volume}(\textit{EM Segmentation} \cup \textit{Manual Segmentation})} \quad (\text{Eq. 3.1})$$

$$\textit{Similarity Index} = \frac{\textit{Volume}(\textit{EM Segmentation} \cap \textit{Manual Segmentation})}{\frac{(\textit{Volume}(\textit{EM Segmentation}) \cup \textit{Volume}(\textit{Manual Segmentation}))}{2}} \quad (\text{Eq. 3.2})$$

The third method was used to test the validity of the EM segmentation algorithm. We compared models generated from the EM segmentations to bone surface scans performed on five index fingers from specimens including the proximal, middle, and

distal phalanx bones (15 bones total). The acquisition orientation of the laser and CT scanners differed; consequently, the bony surface definitions required alignment. Once a common orientation was established, an iterative closest point (ICP) rigid registration[108] was used to register the two surfaces. Thereafter, the distance between the two surfaces was computed. The resulting distance map is based on a Euclidean distance metric, or the shortest distance from a source point to the target surface along the surface normal. The surfaces generated from the EM algorithm were considered the source, while the physical laser scans were considered the target surfaces. Custom written software was used to create the Euclidean distance maps as a means of comparison between the surface scans and the EM segmentation models.

In addition to the reliability and validity measures obtained above, a simple time trial was applied to the EM segmentation technique. A stopwatch was synchronized with both the start and the end of the segmentation process including the definition of the anatomical landmarks used in the registration process. Prior work had provided time trial values for the manual segmentations[97].

4.3.4 Results

A complete phalanx bone model from the EM based segmentation from a single subject is shown in Figure 4.5. The average relative overlap and average similarity index results for each of the phalanx bones can be seen in Table 4.1. Overall, the average relative overlap values for all of the fingers were 0.83, 0.79, and 0.72 for the proximal, middle, and distal bones, respectively. The relative overlap for the index finger where 13 subjects' data was available for comparison showed similar relative overlap measures of 0.87, 0.80, and 0.70 for the proximal, middle, and distal bones. Overall, the average similarity index values for all of the fingers were 0.91, 0.88, and 0.83 for the proximal, middle, and distal bones, respectively. This is as one would expect given the difference in how the metrics are computed. The similarity index for the index finger where 13

subjects' data was available for comparison showed similarity index measures of 0.93, 0.89, and 0.82 for the proximal, middle, and distal bones. A relative overlap or similarity index of 1.0 would be an exact match between the images being compared and a value of 0 would indicate no overlap of the regions of interest.

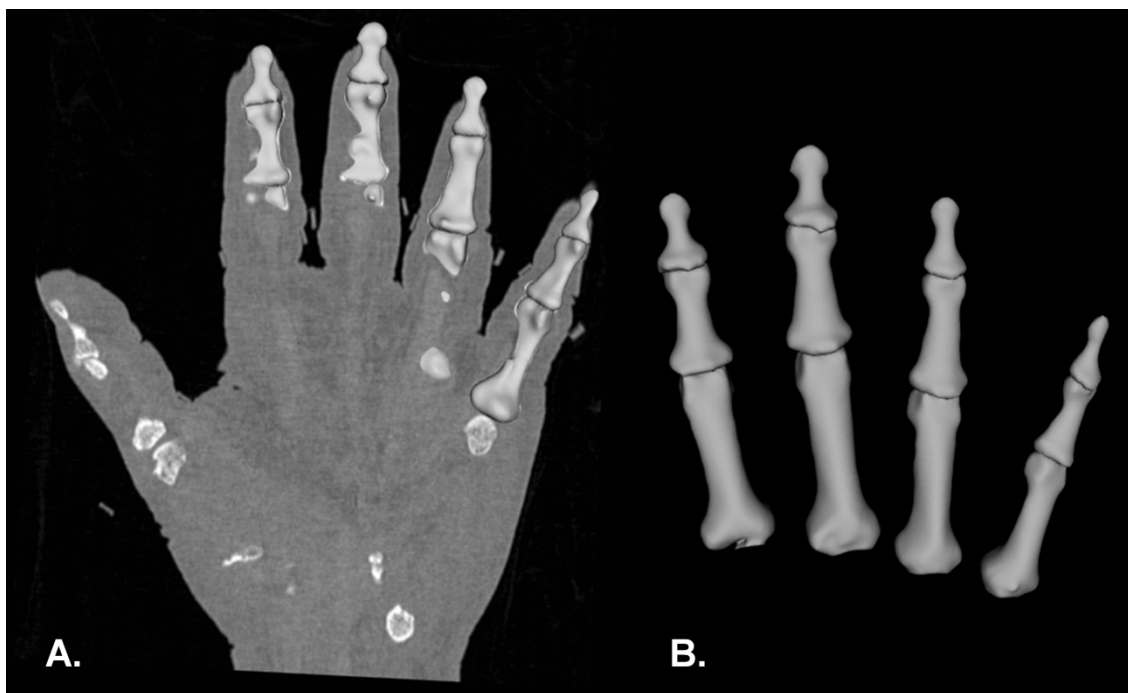


Figure 4.5 The Expectation Maximization algorithm used to segment the phalanx bones from a CT image of the hand. A) Surface models of the anterior aspects of the twelve phalanx bones. B) The posterior aspects of the bone models pictured alone.

Table 4.1 Average relative overlap metric and average similarity index values with standard deviations for the phalanx bones of the hand.

Finger	Phalanx Bone	Average Relative Overlap	Average Similarity Index
Index (13 subjects)	Proximal	0.87 (0.045)	0.93 (0.027)
	Medial	0.80 (0.044)	0.89 (0.027)
	Distal	0.70 (0.124)	0.82 (0.090)
Middle (2 subjects)	Proximal	0.79 (0.012)	0.89 (0.008)
	Medial	0.74 (0.061)	0.90 (0.040)
	Distal	0.71 (0.031)	0.91 (0.021)
Ring (2 Subjects)	Proximal	0.76 (0.025)	0.88 (0.016)
	Medial	0.82 (0.049)	0.88 (0.016)
	Distal	0.80 (0.058)	0.88 (0.036)
Little (2 subjects)	Proximal	0.70 (0.055)	0.86 (0.038)
	Medial	0.73 (0.013)	0.87 (0.009)
	Distal	0.72 (0.005)	0.88 (0.003)
All Data (14 subjects)	Proximal	0.83	0.91
	Medial	0.79	0.88
	Distal	0.72	0.83

The Euclidean distance maps produced an average distance for the proximal, middle, and distal phalanx bones of 0.45, 0.56, and 0.51mm, respectively. It is evident that Specimen-1 is an outlier in this data set. The segmentation for this specimen appears to have not included the proximal portion of the distal phalanx resulting in large distance measures for this subject. The average Euclidean distances are summarized in Table 4.2 and demonstrated in Figure 4.6. In most cases, the average distance between the bone surface scan and the EM segmentation model are near the resolution of the laser scanner (0.34mm) and are therefore close in shape to the physical laser scanned surface of the bone.

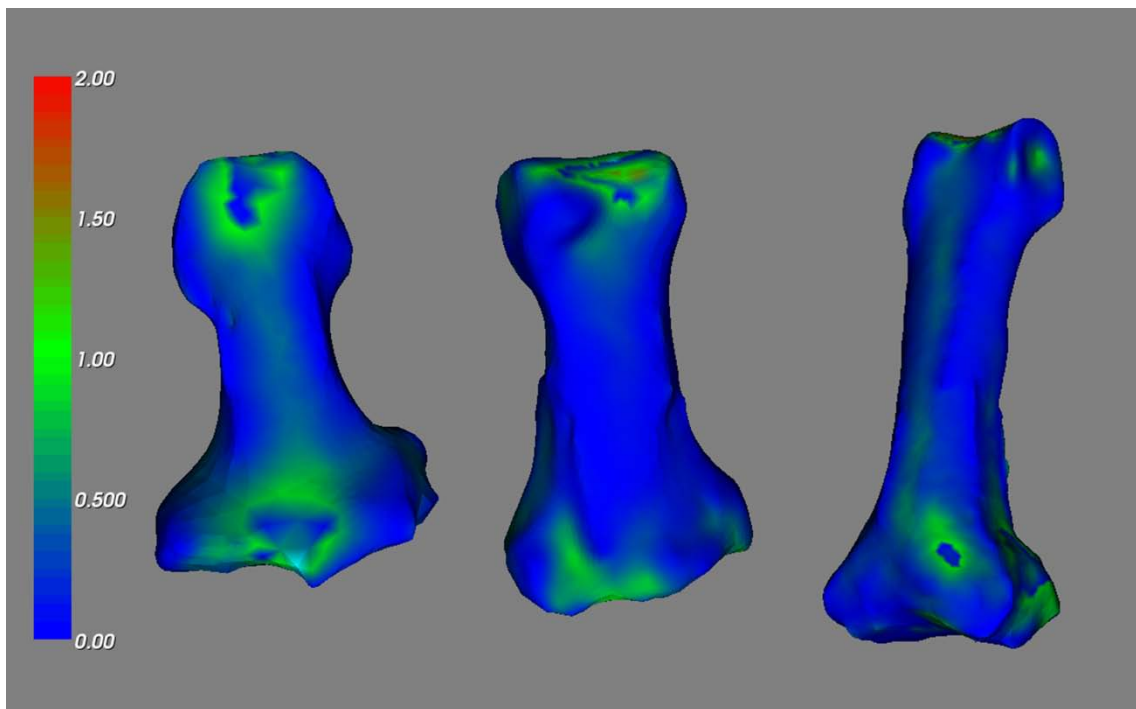


Figure 4.6 Euclidean distance map comparison between the physical surface scans and the Expectation Maximization algorithm based segmentation of a CT hand image. The three phalanx bones of the index finger (distal, medial, and proximal) are pictured from left to right. Distances are presented in mm.

Table 4.2 Average Euclidean distance and standard deviation between the Expectation Maximization segmented surfaces and the physical surface scans.

Finger ID	Proximal Phalanx (mm)	Medial Phalanx (mm)	Distal Phalanx (mm)	Finger Average (mm)
Specimen 1	0.55 (0.49)	0.59 (0.39)	0.89 (0.60)	0.67
Specimen 2	0.43 (0.33)	0.41 (0.29)	0.37 (0.20)	0.40
Specimen 3	0.39 (0.25)	0.44 (0.29)	0.44 (0.28)	0.41
Specimen 4	0.41 (0.24)	0.47 (0.28)	0.46 (0.27)	0.45
Specimen 5	0.45 (0.27)	0.38 (0.20)	0.40 (0.22)	0.41
Bone Average	0.45	0.46	0.51	

The total time required to segment the four fingers (twelve phalanx bones) of the hand was 30 min. This total time is distributed as follows: 8 min for landmark identification, 3 min for image registration, and 19 min for EM segmentation and post-processing. Recall that the average time to segment a single finger manually was 58.47 min, which would equate to an average of 233.88 min for the manual segmentation of all four fingers. The EM segmentation is nearly 8 times faster than manual tracing and only requires 5% of the human time required for segmenting the 12 regions of interest.

4.3.5 Discussion

The comparison of the EM technique to the manual segmentation methods has revealed advantages and disadvantages to both methods. In our previous work, the manual segmentation methods were validated as an accurate representation of the surface of the bone. The EM segmentations were not an exact match to the validated manual segmentations and thus are not as accurate a representation as the manual methods. Nevertheless, the average distances from the bone scans show that the EM method is performing well for the proximal and middle phalanx bones as their average distances are approximately the order of a pixel in the raw CT data away from the laser scanned

surface. In addition, the relative overlap and similarity index values between the EM segmentation and the manual rater were high for these regions as well.

However, the average distance for distal phalanx was slightly larger. The average location of the inferior aspect of the distal phalanx overlaps with the average location of the superior aspect of the middle phalanx. This naturally leads to an overlap in the probability maps that were used. The probability map overlap is problematic to the sequential segmentation technique utilized by the EM Segment module. This issue results in portions of the distal phalanx erroneously being identified as the middle phalanx. This error has manifested itself as a larger average distance of the distal phalanx shown by the Euclidean distance mapping. Another difficulty in the EM bone segmentation can be attributed to the advanced age of the subjects and the level of cortical bone deterioration. In the absence of the “cortical shell”, it is very difficult for the EM segmentation to differentiate trabecular bone from surrounding tissues due to their similar intensity values on CT images.

The previous works presented in the context of segmentation of bony regions of interest suffer from similar issues as the EM segmentation algorithm. Sebastian et al. showed that their segmentation technique was sensitive to partial volume artifacts[62]. In particular, regions with small distances between bones sometimes resulted in joined bone models. Staal et al. suffered from leaky region growing in small joint spaces where portions of the vertebrae were identified as ribs[92]. In addition, primitives were sometimes misclassified resulting in missing or added ribs. The author suggests the inclusion of shape features and a feedback program to cross check the primitive classification would help to eliminate these errors. The work presented by Ehrhardt et al. is based in part on thresholding[66]. This step is dependent on the difference in intensity between bone and surrounding tissues. This may not be problematic for regions of bone with thick cortical layers, but it does not address the issue of normal anatomical regions with thin cortical layers that exist in older adults or as a result of osteoporosis. This study

utilized cadaveric specimens that had an average age of 73.7 years. Many of these subjects exhibited very little cortical shell in the phalanx bones. The reduced cortical thickness results in intensity values that may not significantly differ from surrounding tissues and trabecular bone. The similarity between these intensity values makes it difficult for the EM segmentation process to segment bone. Images from a younger population may offer a better representation of the EM segmentation ability.

Errors in the EM segmentation algorithm can be introduced in several ways. First, the manual segmentation defined on the atlas image is used as probability that the region is at any given location in the atlas space. This will tend to bias the results towards what the guidelines used to define the region on the atlas subject. To minimize this bias, the manual segmentations were smoothed with a Gaussian filter. This has the effect of weighting the interior voxels more than the edge voxels where the error introduced by the manual rater is the greatest. The algorithm is also susceptible to errors in the definition of the landmarks for registration. Since these landmarks are only used to initialize the Thirion Demons deformable registration algorithm, the errors introduced by the manual rater will be minimized since the registration algorithm will tend toward a global optimum. As long as the landmarks are not significantly different from the actual location, the errors in the landmark location should be minimal. The EM segmentation step depends on the registered subject image and image intensity values to accurately segment bone. The registration step was already discussed, but the image intensity values are also important.

Previous research has shown the average time for manually segmenting the three phalanx bones of the index finger to be 58.47 min[97]. The EM segmentation improved on the efficiency of the manual techniques by a factor of 8. This improvement in segmentation time brings us one step closer to a clinically practical segmentation technique. As a semi-automated technique, the EM segmentation offers an improvement in efficiency with a minimal loss to segmentation accuracy.

We have previously evaluated an artificial neural network (ANN) based segmentation using the same research subjects. As reported by Gassman et al., the ANN was compared to the manual segmentations and was shown to have a relative overlap metric of 0.87, 0.82, and 0.76 for the proximal, middle, and distal phalanx bones of the index finger, respectively[97]. These relative overlap values are very close to those of the EM based segmentation; however, it should be noted that the ANN based segmentation does result in slightly higher relative overlap values for the distal and middle phalanx bones. When compared to the 3D laser scans, the ANN segmentations were shown to have an average distance (mm) of 0.35, 0.29, and 0.40 for the proximal, middle, and distal phalanx bones, respectively[97]. When compared to the EM based segmentation, the ANN average distance values are closer to the scanned surface for all three phalanx bones of the index finger. The ANN was also shown to be 10 times faster than the manual segmentations[97], which is 1.3 times faster than the EM based segmentation. The advantage of the EM segmentation method is that the whole hand (excluding the thumb) was being segmented while the ANN was only evaluated on the phalanx bones of the index finger in this previous work.

To make the EM segmentation process even more clinically relevant, it would be necessary to minimize user interaction in the process. Currently, our registration technique requires a user to place eight landmarks for each finger. This is a significant amount of user interaction which could lend itself to user error. Improving this registration technique will help to minimize user interaction. Secondly, the EM Segment module could be altered to better segment bony regions of interest. Instead of sequentially segmenting individual probability maps, a problem described earlier, the algorithm could be amended instead to recognize regions of probability map overlap. In the regions of overlap, a second step could be added to determine the most probable identification between the two overlapping probability maps. This simple modification could help to avoid misidentification of structures where boundaries are ambiguous.

Another approach would be to add shape constraints using a principle components analysis thereby allowing the bone shape to be optimized in these overlapping probability regions. This has previously been proposed by Pohl et al. for segmentation of subcortical brain structures[102]. These improvements would help to improve the accuracy of the EM segmentation technique and bring it one step closer to clinical relevancy.

The EM segmentation technique has been shown to offer a reliable and accurate means of bone segmentation in this proof of concept study. The slight loss of accuracy when compared to the manual tracing techniques is not disappointing when the segmentation times between the two techniques are compared. Even without modifying the EM Segment module, minimal human intervention could be used to improve accuracy by manually fixing problematic areas of segmentation with minimal loss of overall efficiency. Overall, this work represents a step towards a clinically relevant, fully automated bone segmentation process that attempts to match the accuracy of human manual raters while improving the segmentation speed.

4.4 EM Segmentation of the Femur and Tibia

4.4.1 Abstract

Fully automated segmentation of computed tomography (CT) images remains a challenge for musculoskeletal researchers. The surfaces generated from image segmentations are valuable for surgical evaluation and planning. Previously, we demonstrated the Expectation Maximization (EM) algorithm as a semi-automated method of bone segmentation from CT images. In this work, we improve upon the methodology of probability map generation and demonstrate extended applicability of EM-based segmentation to the distal femur and proximal tibia using 72 CT image sets. We also compare the resulting EM segmentations to manual tracings using overlap metrics and time. In the case of the distal femur, the resulting quality metrics had mean values of 0.91 and 0.95 for the Jaccard and Dice metrics respectively. For the proximal tibia, the

Jaccard and Dice metrics were 0.90 and 0.95, respectively. The EM segmentation method was 8 times faster than the average manual segmentation and required less than 4% of the human rater time. Overall, the EM algorithm offers reliable image segmentations with an increased efficiency in comparison to manual segmentation techniques.

4.4.2 Introduction

Magnetic resonance (MR) and computed tomography (CT) imaging allow for accurate measurements of musculoskeletal structures for simulation, evaluation, and optimization of surgical procedures. The high contrast of bone on CT has made it the modality of choice for evaluating bony structures; however, similarity of intensity values to surrounding tissues, age-related variability in cortical bone thickness, proximity of articulating surfaces, image quality, heterogeneity in positioning, and bone's inhomogeneous signal makes segmentation of orthopaedic structures a challenging task. Manual tracing is time intensive and has limited large-scale three-dimensional analysis of orthopaedic images. To address this challenge, several methods of bone segmentation have been developed including global and adaptive local thresholds, snakes, region growing, contours, atlas-based techniques, artificial neural networks, and various combinations of these techniques. Most of the techniques have strived for a completely automated method of bone segmentation, but have varying degrees of user interaction. Many segmentation techniques have been optimized to specific regions of the musculoskeletal system including the femur[65, 90, 109, 110], tibia[65, 110, 111], skull[65, 110], vertebrae[91, 112], carpal bones[62], phalanges[15, 97, 103], as well as various other regions[63, 65, 66, 90, 92-96]. Others have developed methods of automated segmentation for the cartilage-bone interface of the knee[113].

As part of a study involving the evaluation of tunnel placement during an anterior cruciate ligament (ACL) reconstruction, the segmentation and surface generation of 72

CT image sets of the bones of the human knee was required. Therein, improved methods of high-throughput bone segmentation with minimal user intervention became desirable. The CT images of the knee not only posed the traditional challenges of bone segmentation, but also additional challenges due to beam hardening artifacts resulting from metal and varying degrees of flexion and extension of the knees during imaging.

The Expectation-Maximization (EM) algorithm combined with atlas to subject image registration has been shown to be a viable method of automated MRI brain segmentation[98-101, 114]. It is a statistically-based iterative algorithm that couples pixel intensity and probability information to automatically assign label maps to desired regions of interest. The EM algorithm is available in the 3D Slicer software. 3D Slicer was developed by the National Alliance of Medical Image Computing (NA-MIC), one of the National Centers for Biological Computing sponsored by the National Institutes of Health.

In Section 4.3, we demonstrated a semi-automated method of phalanx bone segmentation using the EM algorithm[15]. It involved the selection of 8 anatomical landmarks per finger to initialize a Thirion Demon's registration between an atlas and a subject image. The deformation field from the registration was then used to warp the probability maps from the atlas onto the subject's individual phalanx bones. This method was shown to improve upon the efficiency of manual tracing with minimal effect on overall segmentation accuracy. When compared to 3D surface scans of the bones, the EM segmentation was on average within a voxel of the laser-scanned bone surface. In terms of human interaction, placement of the anatomic landmarks was a limitation, but was essential to achieve an accurate registration.

In this work, we demonstrate a pre-processing method for nearly automated alignment of the atlas with the subject. The resulting deformation field then provides a mapping of the probability map into the subject image, which is used as an initial probability estimate for the EM segmentation. The preprocessing eliminates the need for

placement of specific anatomic landmarks for initialization of the Thirion Demon's registration even in the presence of beam hardening artifacts and varying degrees of knee flexion. We also demonstrate extended applicability of the EM algorithm for segmentation of bony structures from CT images to additional regions of the musculoskeletal system; specifically, the distal femur and proximal tibia. We hypothesize that pre-processing a CT dataset to selectively remove soft tissues will allow deformable registration to accurately map cortical bone from an atlas onto a subject image and allow for EM segmentation of the distal femur and proximal tibia without the need for specifically selected anatomic landmarks. In this paper, we describe our method of pre-processing and segmentation and compare our segmentation results to manual traces.

4.4.3 Materials and Methods

4.4.3.1 Collection of CT Data

Seventy-two fresh-frozen human cadaveric knees were collected (37 left and 35 right); each specimen included the full joint and a portion of the proximal tibia and distal femur. Prior to scanning, tunnels were drilled in the tibia and the femur of each specimen as performed during an ACL reconstruction on each specimen. A Siemens Sensation 64 slice CT scanner was used to collect three-dimensional voxel datasets of the knee for each specimen (matrix = 1005x512, FOV = 261mm x 133mm, KVP = 120, Current = 128mA, Exposure = 160mAs) with a 0.26mm in-plane resolution and a 0.75mm slice thickness. Slices spanning the entire specimen were obtained for each dataset with the knee oriented between full extension and 45° of flexion.

4.4.3.2 Computational Resources

The Insight Toolkit (ITK) and C++ programming language were used to perform the image processing operations on an Intel Xeon 2.67GHz with 8.00GB of RAM

running a 64-bit version of the Microsoft Vista operating system. The 3D Slicer software package was used to perform the fiducial selection, EM Segmentation, and surface generation. Manual tracing and Thirion Demon's registration were performed using BRAINS2[46].

4.4.3.3 Image Pre-Processing

The CT datasets were resampled to 1.0mm isotropic voxels. To simplify our registration and segmentation procedures, all left knees were mirrored to yield a total of 72 right knees. These pre-processed images were used in the remainder of the study.

4.4.3.4 Manual Tracing and Timing

In a previous study, it was demonstrated that manual tracing of CT images is an accurate method of representing the surface geometry of bony structures[103]. Consequently, we recruited two trained manual raters to perform axial slice by slice tracings for this study. One rater manually traced the distal femur and proximal tibia from all 72 CT image sets. Segmentations of the overall bone were the focus of this study; the bone tunnels created during the ACL reconstruction tunnel drilling procedure were not considered by either the manual raters or the EM segmentation procedure. To evaluate inter-rater reliability, a second rater manually traced the distal femur and proximal tibia from a subset of 10 specimens. The union overlap metric (Jaccard coefficient) was used to compare the performance of the two raters[115].

$$\text{Union Overlap(Jaccard Coefficient)} = \frac{\sum_r |\text{ManualRater } 1_r \cap \text{ManualRater } 2_r|}{\sum_r |\text{ManualRater } 1_r \cup \text{ManualRater } 2_r|} \quad (\text{Eq. 3.3})$$

4.4.3.5 Patient-Specific Probability Map Generation

The EM algorithm requires a subject image and probability information for each anatomical region of interest to generate a label maps defining the regions of interest[99, 100, 102]. For this study, an unfiltered subject image and patient-specific probability maps for the distal femur and proximal tibia were required. Generation of the patient-specific probability maps was accomplished with the development of a novel image pre-processing procedure. The output from this image pre-processing procedure was used as the input to a Thirion Demon's deformable registration that mapped the atlas to the subject of interest[105].

Figure 4.7A demonstrates the Thirion Demon's registration process performed on an image set without using anatomical landmarks for initialization. As shown, the perimeter of the registered atlas image matches the perimeter of the subject image; however, the bony regions in the warped atlas image do not resemble the subject image. Museyko et al. demonstrated that rigid registration of binary masks of bony structures was superior to rigid registration of gray-scale masks of the same structures[109]. Removal of soft tissues from the CT image by binary thresholding prior to deformable Thirion Demon's registration resulted in an improved registration as demonstrated in Figure 4.7B.

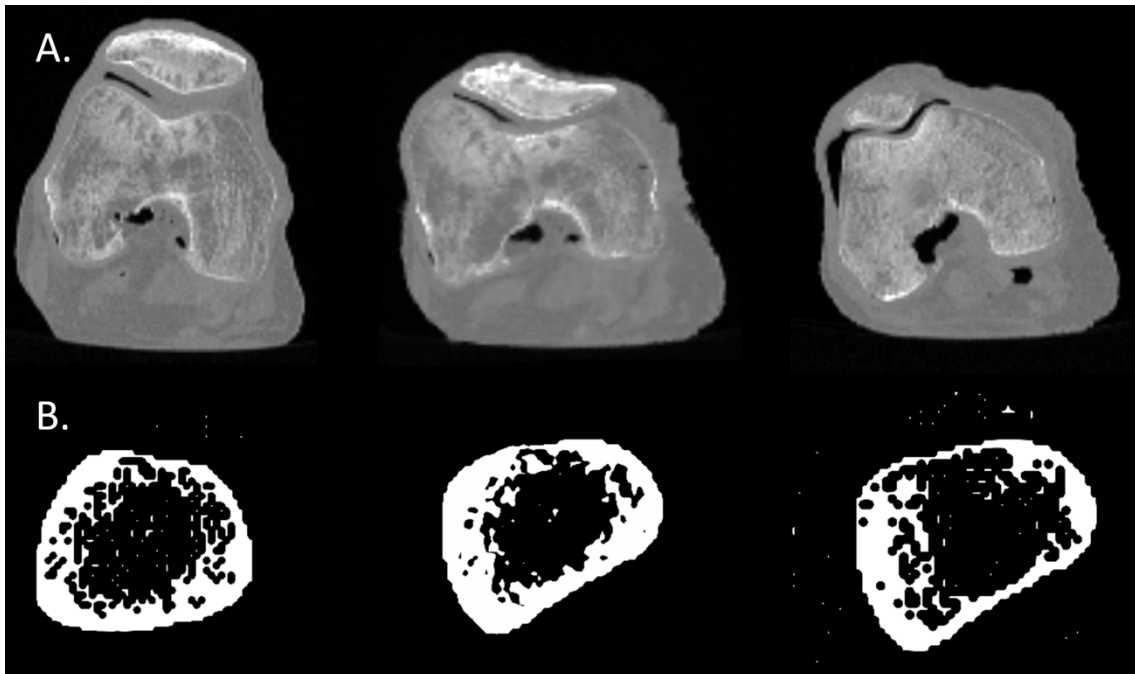


Figure 4.7 Thirion Demon's registration demonstrated on two images. A) The Thirion Demon's registration applied to a CT image of the knee with soft tissues present. The axial images represent the atlas (left), the registered atlas (center), and the subject (right). B) The Thirion Demon's registration applied to a binary CT image of the knee with soft tissues thresholded away. The axial images represent the atlas (left), the registered atlas (center), and the subject (right).

The mapping of the atlas probability information onto the subject CT images includes four steps: 1) binary thresholding the CT images to isolate regions of cortical bone, 2) smoothing and post-processing the binary segmentation to fill gaps in cortical bone, 3) Thirion Demon's registration of the atlas to a subject image, and 4) applying the resulting deformation field to map the atlas probability information into the subject coordinate system. A more detailed description of each step follows:

- 1) Isolation of Cortical Bone – An image-specific threshold value was determined by sampling the intensity from regions of cortical bone. The user selected approximately 20-30 voxels corresponding to regions of cortical bone from a single sagittal CT slice. The mean and standard deviation of the selected voxels was calculated. A binary

- threshold value defined as the mean minus one standard deviation was used to isolate the cortical bone from the soft tissues in the CT images. The resulting image is shown in Figure 4.8A-B. It should be noted that gaps are present in the epiphyseal and metaphyseal regions of the cortical bone that prevents simple thresholding alone from being a method of segmentation. Figure 4.9 displays the calculated image-specific threshold values for the 72 knee CT datasets.
- 2) Cortical Bone Gap Filling – A Gaussian filter ($\sigma=1.5\text{mm}$ and a kernel width of 5mm) was applied to the binary image. The resulting floating point image was then rescaled to contain intensity values ranging from 0 to 255 (Figure 4.8C). The smoothed image from the previous step was thresholded to remove voxels with an intensity value less than 10 (Figure 4.8D). Note that the gaps in the cortical bone present in Figure 4.8B are now filled. This result represents an estimation of the shape of the cortical bone; however, the Gaussian filter has dilated the estimation and has merged the voxels representing the tibia, femur, and patella in the final binary image. Finally, the largest connected region in the binary image was identified and all smaller misclassified regions are removed (Figure 4.8E).
 - 3) Atlas to Subject Thirion Demon's Image Registration – A single subject from the CT dataset was chosen as the atlas image after manual tracing had defined the distal femur and proximal tibia. The manual definitions were smoothed with a Gaussian filter ($\sigma = 3.0\text{mm}$ and a kernel width of 10mm) and used as probability images. Thirion Demon's algorithm was then used to warp the pre-processed binary atlas image onto each of the pre-processed binary subject images using four levels of refinement with 1000, 500, 250, 125, and 60 iterations respectively at each level of refinement.
 - 4) Patient-Specific Probability Map Finalization – The resulting deformation field from the atlas to subject registration was then used to map the atlas-based probability

images onto the subject CT scans (Figure 4.8F). The resulting patient-specific probability maps were then rescaled to 8 bits for input to the EM algorithm.

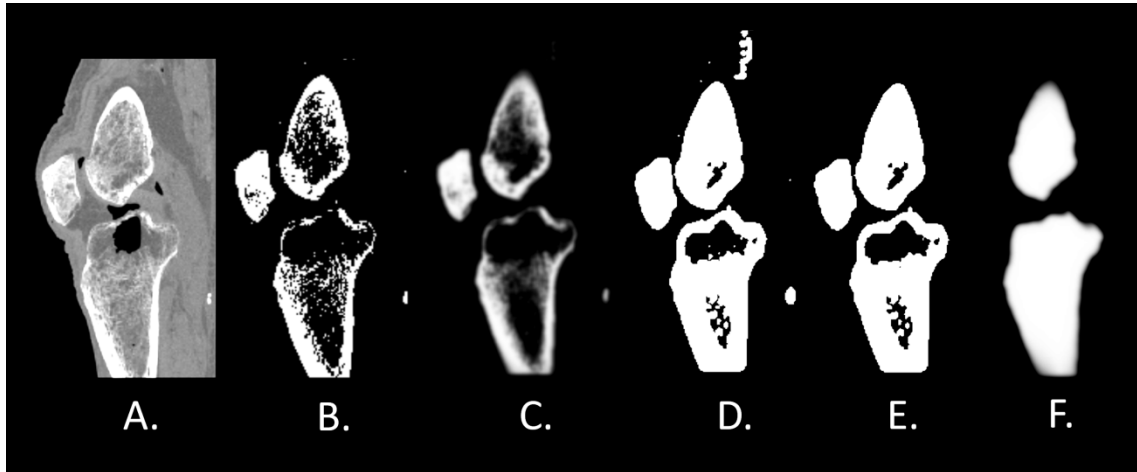


Figure 4.8 The patient-specific probability map generation process. A) A sagittal CT slice of a human knee. B) A thresholded sagittal CT slice of the knee demonstrated in Figure 4.8A. C) The Gaussian ($\sigma=1.5$ and kernel width = 5) smoothed sagittal slice applied to Figure 4.8B. D) The resulting image after thresholding Figure 4.8C. E) The resulting image after removing islands using a connectivity filter from Figure 4.8D. F) The finalized patient-specific probability map after atlas to subject registration to map the probability images onto the subject CT scan.

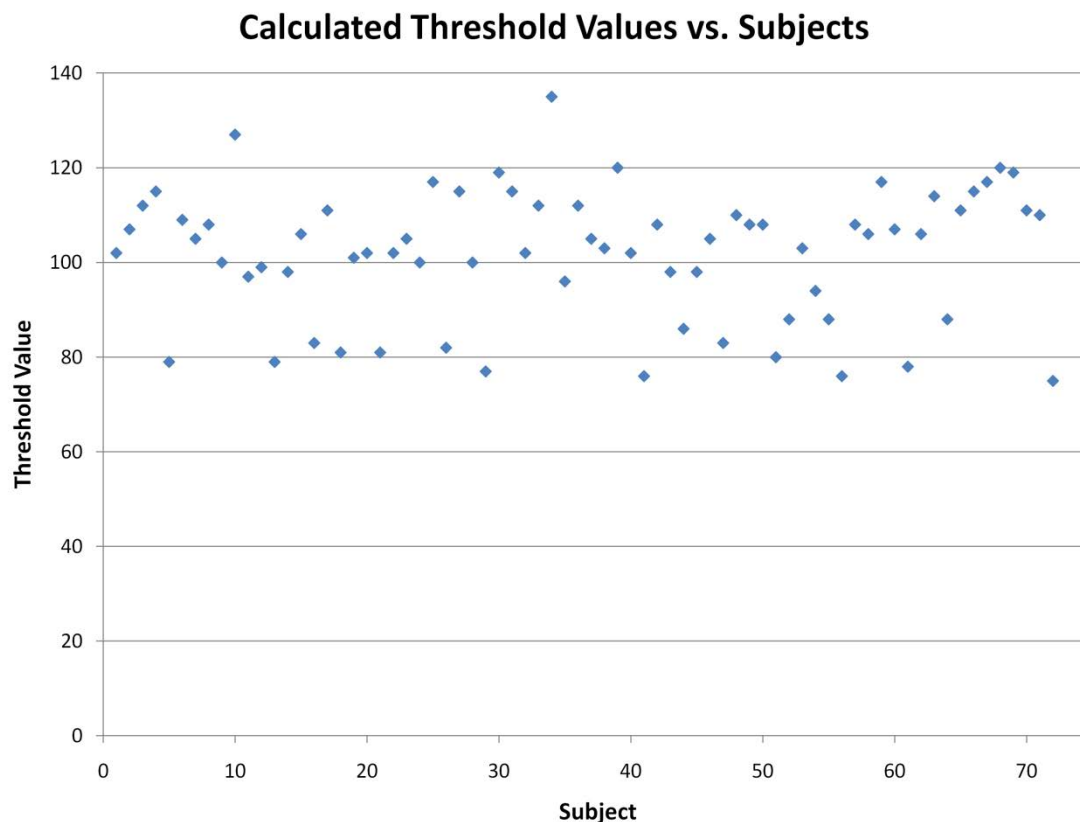


Figure 4.9 The calculated threshold value used by the patient-specific probability map generation procedure on 72 CT datasets of the knee.

4.4.3.6 EM Bone Segmentation

For bone segmentation, the EM algorithm is organized into a tree-like structure that first differentiates bone from background (soft tissue, vasculature, air, etc.). Bone is divided into regions corresponding to the tibia and regions corresponding to the femur. The regions corresponding to the femur and tibia were each further divided into two categories of cortical bone (i.e. high intensity cortical bone and low intensity cortical bone) and trabecular bone. The average voxel intensity values for each of these regions are described in Table 4.3. The unfiltered CT images and the probability maps were used as the inputs to the EM algorithm.

Table 4.3 Parameters used for segmenting the distal femur and proximal tibia using the EM segmentation algorithm.

Region	Intensity Log Mean	Intensity Log Covariance
Background	3.60	0.05
Femur – High Intensity Cortical Bone	4.25	0.01
Femur – Low Intensity Cortical Bone	3.88	0.03
Femur – Trabecular Bone	3.64	0.01
Tibia – High Intensity Cortical Bone	4.14	0.01
Tibia – Low Intensity Cortical Bone	3.89	0.03
Tibia – Trabecular Bone	3.64	0.01

4.4.3.7 Label Map Post-Processing

The resulting label maps from the EM segmentation were post-processed to remove misclassified island voxels while maintaining the two largest connected regions (i.e. tibia and femur). The label maps were then filled to remove holes. To ensure a fair comparison between the manual and EM segmentations, the label maps were cropped in the superior/inferior direction to compare the same extent of the bone between methods. This was done because the entire length of the femur and tibia were not acquired and the articulating surface of the bones was of interest for this study. A triangulated surface representation was created for both the femur and tibia using 3D Slicer.

4.4.3.8 EM Segmentation Evaluation

Six metrics (Eqs. 4.4-4.8) were used to evaluate the quality of each segmentation: union overlap (Jaccard coefficient), total overlap (sensitivity), mean overlap (Dice coefficient), volume similarity, false negative, and false positive (1-specificity)[115, 116]. These six overlap metrics have been a traditional method of comparing two segmentation techniques. The union and mean overlap metrics are measures of

agreement between segmentations; these metrics are typically complemented by false negative and false positive measures to characterize the proportion of mislabeled voxels. Volume similarity is a metric that compares the volumes between image segmentations. For additional information regarding these overlap metrics, we refer the reader to Klein et al[115, 116]. Perfect matching segmentations would be represented by a value of 1 for the union overlap, total overlap, and mean overlap and a value of 0 for false negative, false positive, and volume similarity. Each of the 72 segmentations generated using the EM algorithm was compared to its corresponding manual segmentation using the six described metrics. In addition, the time required for a representative case of EM segmentation was recorded from start to finish.

$$\text{Total Overlap} = \frac{\sum_r |\text{ManualSegmentation}_r \cap \text{EMSegmentation}_r|}{\sum_r |\text{EMSegmentation}_r|} \quad (\text{Eq. 4.4})$$

$$\text{Mean Overlap} = 2 * \frac{\sum_r |\text{ManualSegmentation}_r \cap \text{EMSegmentation}_r|}{\sum_r (|\text{ManualSegmentation}_r| + |\text{EMSegmentation}_r|)} \quad (\text{Eq. 4.5})$$

$$\text{Volume Similarity} = 2 * \frac{\sum_r (|\text{ManualSegmentation}_r| - |\text{EMSegmentation}_r|)}{\sum_r (|\text{ManualSegmentation}_r| + |\text{EMSegmentation}_r|)} \quad (\text{Eq. 4.6})$$

$$\text{False Negative} = \frac{\sum_r (|\text{ManualSegmentation}_r| / |\text{EMSegmentation}_r|)}{\sum_r |\text{ManualSegmentation}_r|} \quad (\text{Eq. 4.7})$$

$$\text{False Positive} = \frac{\sum_r (|\text{EMSegmentation}_r| / |\text{ManualSegmentation}_r|)}{\sum_r |\text{EMSegmentation}_r|} \quad (\text{Eq. 4.8})$$

4.4.4 Results

Example segmentations of the distal femur and proximal tibia generated using the EM algorithm are shown in Figure 4.10. A breakdown of the segmentation metrics are summarized in Tables 4.4 and 4.5 for the distal tibia and proximal femur, respectively. Overall, the 72 cases of the distal femur had mean values of 0.91 and 0.95 for the Jaccard and Dice metrics, respectively. The proximal tibia had one outlier that was removed from the results because it failed to properly segment the tibia. The proximal tibia had mean values of 0.90 and 0.95 (Jaccard and Dice, respectively). Figure 4.11 provides a scatter plot describing the Dice Coefficient for all 72 subjects.

The human manual raters were compared on ten cases. The Jaccard coefficient was 0.98 with a standard deviation of 0.01 for both the femur and the tibia. A value of 1 would indicate identical manual traces. Table 4.6 summarizes the ten cases and their corresponding metrics between the manual raters.

The total time required to segment the distal femur and proximal tibia using the EM algorithm was 24 minutes 12 seconds. The time distribution can be broken down as described in Table 4.7. Note that 1 minute was dedicated to manual selection of points and 6.5 minutes dedicated to manual setup of the segmentation module in 3D Slicer. The setup time for the EM segmentation could be eliminated in future applications by scripting the segmentation process. The average time required to manually trace the two bones was 3.2 hours. The EM segmentation process is nearly 8 times faster than manual tracing and only requires 4% (7.5 minutes) of the human time needed for segmenting the distal femur and proximal tibia.

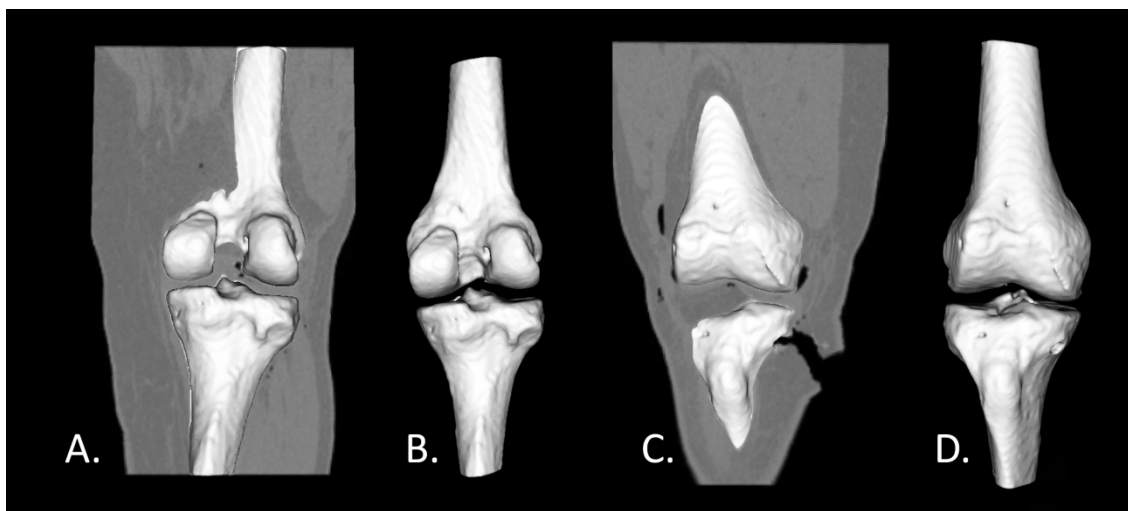


Figure 4.10 The Expectation Maximization algorithm applied to CT images of the human knee. A) Surface models of the posterior aspect of the distal femur and proximal tibia. B) The anterior aspect of the bone models pictured alone.

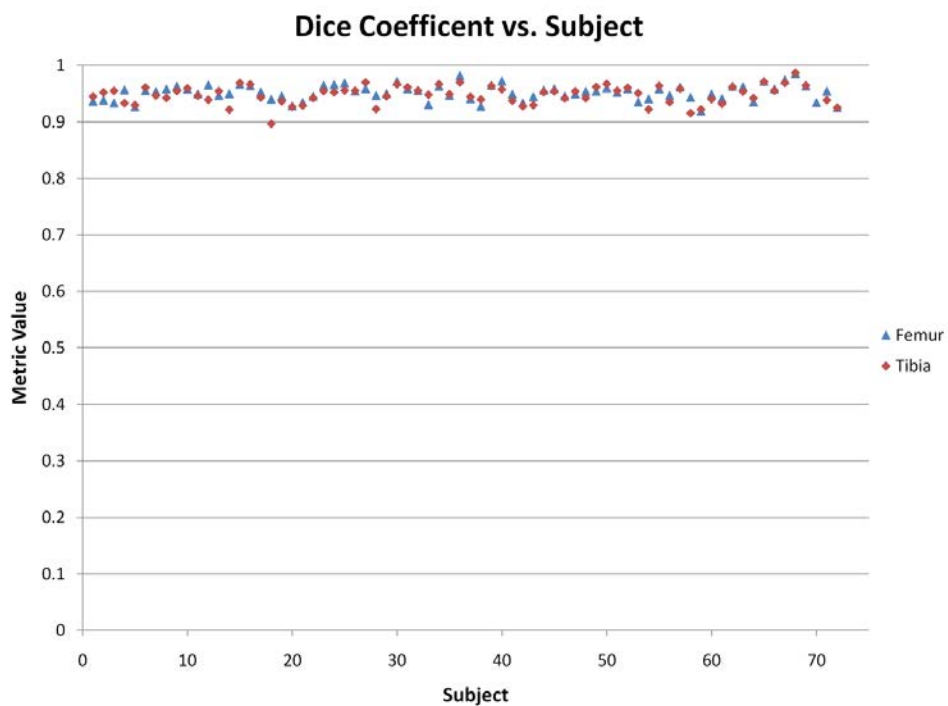


Figure 4.11 The Dice coefficient comparing the EM segmentation to a manual segmentation for 72 CT datasets of the knee.

Table 4.4 Segmentation evaluation metrics comparing the EM segmentations to the manual segmentations for the 72 femurs.

Evaluation Method	Minimum Value	Maximum Value	Mean Value	Standard Deviation
Total Overlap	0.87	0.98	0.93	0.025
Union Overlap	0.85	0.97	0.91	0.025
Mean Overlap	0.92	0.99	0.95	0.014
Volume Similarity	-0.12	0.033	-0.048	0.033
False Negative	0.018	0.13	0.070	0.025
False Positive	0.0038	0.081	0.025	0.016

Table 4.5 Segmentation evaluation metrics comparing the EM segmentations to the manual segmentations for the 72 tibias.

Evaluation Method	Minimum Value	Maximum Value	Mean Value	Standard Deviation
Total Overlap	0.85	0.98	0.92	0.028
Union Overlap	0.81	0.97	0.90	0.029
Mean Overlap	0.90	0.99	0.95	0.016
Volume Similarity	-0.16	0.026	-0.066	0.037
False Negative	0.022	0.15	0.082	0.028
False Positive	0.0019	0.08	0.020	0.16

Table 4.6 Union overlap (Jaccard coefficient) segmentation evaluation metrics comparing the EM segmentations to each of the manual raters.

		Union Overlap (Jaccard Coefficient)	
Specimen	Bone	EM vs. Manual Rater 1	EM vs. Manual Rater 2
1	Femur	0.89	0.91
1	Tibia	0.90	0.91
2	Femur	0.90	0.92
2	Tibia	0.92	0.94
3	Femur	0.92	0.94
3	Tibia	0.93	0.94
4	Femur	0.93	0.93
4	Tibia	0.90	0.91
5	Femur	0.91	0.90
5	Tibia	0.88	0.89
6	Femur	0.93	0.92
6	Tibia	0.93	0.93
7	Femur	0.97	0.96
7	Tibia	0.94	0.94
8	Femur	0.93	0.92
8	Tibia	0.91	0.91
9	Femur	0.94	0.92
9	Tibia	0.93	0.93
10	Femur	0.96	0.95
10	Tibia	0.93	0.92

Table 4.7 Breakdown of times required for the semi-automated segmentation process.

Procedure	Sample Time Requirement
Point Selection (manual)	1 minute
Image Resampling and Mirroring	24 seconds
Registration Preprocessing	9 seconds
Thirion Demons Registration	15 minutes 8 seconds
Register probability maps to subject image	11 seconds
Gaussian smooth registered probability maps	13 seconds
Setup EM Segmentation in 3D Slicer (manual)	6 minutes 30 seconds
Processing Time for EM Segmentation	34 seconds
Segmentation Post-Processing	3 seconds
Total Time	24 minutes 12 seconds

4.4.5 Discussion

We have developed an improved pre-processing method for patient-specific probability map generation for EM bone segmentation and have applied it to 72 cases of the distal femur and proximal tibia. This advancement removes the necessity for specifically placed anatomical landmarks to initialize the deformable registration process, thereby eliminating the most user-demanding portion of the previously published method. Our improved method has been shown to be effective at assigning probability maps regardless of the degree of flexion and extension of the knee in our study. Also, the knee joint is adequately spaced such that overlapping label maps for the bones was not a limitation as was the case for the phalanx bones in our previous study.

The segmentation metrics demonstrate that EM segmentation is an accurate method of bone segmentation when compared to the manual segmentations. Although the comparison between the two human raters had slightly higher overlap statistics when compared to the EM segmentation, the EM segmentation was still a close match to the

manually defined regions of interest. In addition, the EM segmentation was compared across all 72 scans while the human raters were evaluated in only ten cases because of the time required for the manual segmentations. Nevertheless, the metrics revealed overlap values better than those observed in the EM segmentation evaluation of the phalanx bones[15]. One EM segmentation of the tibia, out of the 144 regions segmented, was an outlier in our dataset; this resulted from a suboptimal registration for that specific image. In this case, manual editing of the EM label map could be utilized to provide an accurate segmentation.

The EM segmentation process took a total of 24 minutes 12 seconds with only 7.5 minutes of manual time. The registration step of our method is the most time consuming portion of the process; however, it does not require user intervention. In addition to 1 minute required for intensity sampling, the other manual step was the setup of the segmentation in 3D Slicer, which was reported to take 6.5 minutes. Further optimization using 3D Slicer's scripting capabilities would require only 1 minute of user time to generate the final labeling. Recall that on average, an accurate manual tracing of the distal femur and proximal tibia took 3.2 hours. The EM segmentation method was nearly 8 times faster than the manual method and only required 4% of the human time. This is a significant step towards removing human interaction from the bone segmentation procedure.

The proposed method is not without limitation. Manual sampling was required to define the threshold value required to extract the bony region from soft tissue. In the future, it may be possible to automatically define this threshold value. In addition, the post-processing operation used to fill trabecular bone also filled the drill tunnels produced during the ACL reconstruction. With accurate segmentations of the overall femur and tibia, manually defining the drill tunnels is currently a minimal time commitment that also ensures high accuracy in the ACL tunnel definitions. Automatic identification of ACL tunnels in future studies will allow for their incorporation into bone segmentations.

In the future, we also hope to show extended applicability of the EM algorithm to other regions of the human musculoskeletal system.

4.4.6 Conclusion

In this study, we have continued to show the EM algorithm to be a reliable method of bone segmentation from CT images. Our proposed improvement to patient-specific probability map generation reduces the amount of user interaction necessary to identify regions of bone from a CT image. We have also shown that the EM bone segmentation method extends beyond the phalanx bones to the distal femur and proximal tibia. These improved methods allow for a nearly automated method of bone segmentation that fosters high-throughput surface generation and avoids the cumbersome nature of manual tracing in large-scale studies. Overall, this work represents continued advancement towards a clinically applicable, automated method of bone segmentation that maintains the accuracy of manual tracing but improves upon its efficiency.

CHAPTER 5

THE ANTERIOR CRUCIATE LIGAMENT

5.1 Anatomy

The human knee is composed of three bones (femur, tibia, and patella), four major ligaments (anterior cruciate, posterior cruciate, lateral collateral, and medial collateral), articular cartilage, menisci (lateral and medial), and a variety of muscular attachments[117]. The ligaments function to stabilize the knee during motion and load bearing. The location of the ACL with respect to the anatomy of the human knee can be visualized in Figure 5.1. The first description of the anterior cruciate ligament (ACL) was found on an Egyptian papyrus scroll dating back to 3000 BC[118]. Later, Claudius Galen of Pergamon named the ligaments of the knee, “ligament genu cruciate” circa 199 BC. The ACL acts as the primary restraint to anterior tibial translation and internal tibial rotation. The ultra-structure of the ACL can be described in terms of its femoral insertion, tibial insertion, and midsubstance[118]. The ligament is composed of dense connective tissue that is enveloped within two layers of synovium[118]. The fibers of the ligament have a distinct crimped structure that straightens as the ligament is lengthened[119]. It is typically 30-40mm in length and 11mm wide with an average cross-sectional area of 44mm^2 [120, 121]. On average, the ACL is smaller in females than in males[119]. The structure and mechanical properties of the native ACL have been shown to decrease with advancing age.

The femoral insertion of the ACL is oval in shape and is located at the nonarticular medial aspect of the lateral femoral condyle[118, 121], just posterior to the lateral intercondylar ridge or Resident’s ridge[122]. The center of the attachment site has been estimated at 24.8% of the distance from the intersection of Blumensaat’s line and the contour of the lateral femoral condyle on lateral x-rays. Traditionally, a clock system (Figure 5.2) has been used to describe the location of the ACL insertion whereby a clock

is placed in the intercondylar notch as if an observer were looking down the long axis of the femur[121]. For the left femur, the fibers attach at the one o'clock position and for the right femur, the fibers attach at the 11 o'clock position[123]. The femoral insertion of the ACL is supplied by the middle genicular artery. Histologically, the ACL insertion has been described as a chondral apophyseal enthesis composed of four layers: ligament fibers, fibrocartilagenous cells within collagen bundles, mineralized cartilage, and a fibrocartilage insertion into the subchondral bone plate[118].

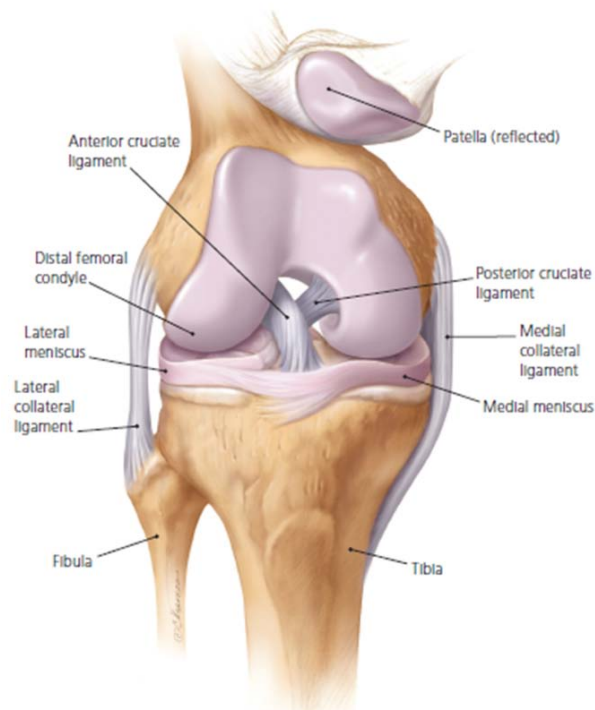


Figure 5.1 The anatomy of the human knee including bones, menisci, ligaments, and cartilage.

(Source: Cimino F, et al. [117])

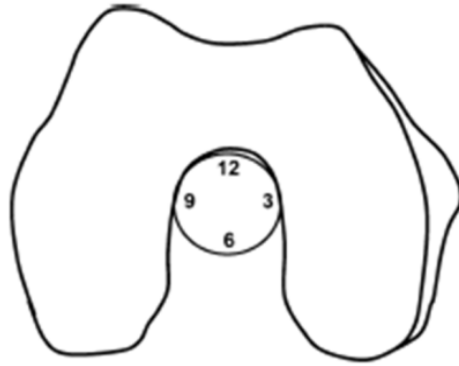


Figure 5.2 The clock method for defining the ACL insertion on the lateral femoral condyle.

(Source: Giron F, et al.[121]).

The midsubstance of the ACL has a mean length of 32mm but can range from 22-41mm[118]. The central region of the ACL is oval shaped and has the smallest cross section of the ligament. It is primarily composed of Type I collagen fibrils that are surrounded by connective tissue containing Type III collagen. The fibers of the ligament run obliquely through the midsubstance from the femoral insertion to the tibial insertion. The tibial insertion of the ACL is the broadest portion of the ligament and has an oval shape that is wider in the anteroposterior direction[121]. It is located in the nonarticular region known as the anterior intercondylar fossa between the medial and lateral tibial spines[121, 122]. The anteromedial portion of the ligament is merged with the medial meniscus and the posterolateral portion of the ligament is merged with the lateral meniscus[118, 123]. The tibial insertion is supplied by branches of the lateral and medial inferior genicular artery. This insertion is also considered to be a chondral apophyseal entheses and has a histological structure similar to the femoral insertion. The ACL is innervated by the posterior articular branches of the tibial nerve[122]. Ruffini corpuscles,

Golgi tendon organ-like receptors, Pacinian corpuscles, and nociceptors are present within the ligament to allow for identification of changes in acceleration, motion, position, and angle of rotation of the joint.

Modern descriptions of the ACL break it into multiple components corresponding to functional fiber bundles whose tension varies based on knee motion[118, 119]. The three bundle system includes an anteromedial, intermediate, and posterolateral bundle; however, a two bundle system is more widely accepted. The two bundle system is divided into anteromedial (AM) and posterolateral (PL) bundles. The bundle names correspond to the location of the bundle insertion on the tibia. The AM bundle originates in the most proximal part of the femoral origin of the ACL, while the PL bundle originates in the distal part of the femoral origin close to the anterior inferior articular cartilage margin. When the knee is in extension, the PL bundle is taut and the AM bundle is lax. When moving from extension to flexion, the AM bundle becomes taut and the PL bundle becomes lax. Studies have shown that the AM bundle is mostly responsible for constraining anterior tibial translation with respect to the femur at high flexion angles, while the PL bundle is mostly responsible for constraining internal tibial rotation and anterior tibial translation at low flexion angles (less than 20°)[118].

5.2 Injury

5.2.1 Epidemiology

The ACL is the most frequently completely torn ligament of the knee. It is a rare injury in the general population, but is common among athletes, especially female athletes. It is estimated that one in every 3,500 people will tear their ACL during their lifetime[119]. Each year it is estimated that up to 175,000 ACL reconstructions are performed in the United States with a cost of up to \$3 billion[119, 124-127]. It has been estimated that surgical reconstruction and postoperative care cost \$11,500 per patient[128]. ACL reconstruction is the sixth most common orthopaedic surgical

procedure currently performed[129]. More male athlete ACL reconstructions are performed each year, but female athletes have a 2.4-9.7 times greater chance of ACL injury than male athletes participating in similar activities[119, 130, 131]. Small intercondylar notch, greater posterior tibial slope, and a contralateral ACL injury are factors that have shown increased risk to ACL injury[131].

5.2.2 Mechanism

Injury of the ACL has been described as multiplanar and is classified as a contact or noncontact injury[132, 133]. Noncontact mechanisms account for 70% of injuries and involve a change in direction or landing motion coupled with a sudden deceleration[117]. Examples of activities causing noncontact injuries include team handball, soccer, basketball, alpine skiing, and tennis[134]. Noncontact injuries are most common where the leg is near full extension at foot strike. At full extension, the ACL is strained by contraction of the quadriceps, which can cause substantial anterior tibial translation, axial compressive force, and ACL injury[119, 130]. Contraction of the hamstrings act as a passive protective mechanism for the ACL[135]. Typically, patients describe a popping sound and immediate pain that is followed by swelling of the knee. Contact mechanisms occur with a valgus collapse of the knee caused by a planted foot and applied torque that causes the ligament to tear. After injury, the ACL does not heal[136, 137]. The chronic ACL deficient knee has four times the amount of anterior tibial translation as compared to the ACL intact knee[136].

5.2.3 Associated Injuries

Isolated injury of the ACL occurs only in 10% of cases[119, 126]. Additional ligamentous injuries can range from mild strains to complete tears of multiple ligaments including the medial collateral ligament. Meniscal and articular cartilage are also commonly damaged, which can lead to early onset osteoarthritis later in life (10-20 years post-injury) in 10-90% of patients[117, 134]. An ACL injury without meniscal damage

has been shown to have a 0-13% rate of developing osteoarthritis 10 years after the injury[134]. Bone contusions are associated with 80% of ACL lesions with the most common location being the lateral compartment of the knee where the lateral tibial plateau contacts the lateral femoral condyle[138]. Additionally, hemarthrosis commonly occurs immediately after an ACL injury, which results in a modified gait, asymmetric appearance, pain, reduced range of motion, and loss of full extension. MRI is the imaging modality of choice to evaluate for ACL disruption and associated soft tissue injury.

5.2.4 Functional Testing

Clinical testing of the ACL integrity is typically performed using several tests that measure the amount of anterior displacement of the tibia with respect to the femur and also joint stability. Anterior displacement of the tibia can be estimated in the physical exam using the Lachman test and the anterior drawer test[128, 139]. The anterior drawer test is demonstrated in Figure 5.3 and the Lachman test is demonstrated in Figure 5.4. Both of these exams involve placing the patient supine on the exam table. With the anterior drawer test, the hip is flexed to 45° and the knee is flexed to 90°. The examiner sits on the patient's foot, grasps the lower leg just below the knee joint, and pulls the tibia forward. More than 5mm of motion in comparison to the normal limb is positive for ACL injury. The Lachman test is often the preferred clinical test since it is both specific and sensitive for ACL rupture. It involves flexing the knee to 20-30°, grasping and stabilizing the distal femur with one hand, grasping the proximal tibia with the other hand, and pulling forward on the tibia. More than 5mm of motion in comparison to the normal limb is positive for ACL injury. ACL injuries can be graded as Grade 1 for 0-5mm, Grade 2 for 6-10mm, and Grade 3 for > 10 mm of anterior laxity. The amount of anterior tibial displacement can also be objectively quantified using a KT1000/2000 device[129, 140, 141].

Joint stability is evaluated using the pivot-shift test (Figure 5.5), which can simulate the sensation of “giving way” felt by patients[139, 140, 142]. This test allows for testing of the ACL’s ability to restrain rotation by applying an internal and valgus torque to the tibia during the full range of flexion and extension of the knee[136]. In the test, the patient is placed supine on the exam table. The examiner places the hip in 45° of flexion while maintaining extension of the knee by grasping the heel with one hand. The other hand grasps the knee with the thumb placed below the fibular head. With both hands, the examiner applies strong internal rotation forces and the knee is allowed to flex to about 20°. The examiner then pushes medially with the proximal hand and pulls the distal hand to induce valgus stress on the knee. If joint instability is present, then the tibia starts subluxated and reduces between 20-40° of flexion. A positive pivot-shift test is highly suggestive of ACL rupture.



Figure 5.3 The anterior drawer test.

(Source: Thompson J.C. [139])



Figure 5.4 The Lachman test.

(Source: Thompson J.C. [139])



Figure 5.5 The pivot-shift test.

(Source: Thompson J.C. [139])

5.3 Reconstruction

5.3.1 Indications

Controversy exists as to whether all ACL deficient knees require reconstruction since no evidence exists to show that surgical reconstruction prevents osteoarthritis later in life[119]. Indications for surgery include patients that perform heavy work or participate in sports and those that have repeated episodes of giving way in spite of rehab. Complete and partial ACL disruptions can be treated with surgical reconstruction with proper patient selection[137]. Typically, this patient population desires to return to full activity levels that would not be possible without ACL reconstruction. Indications for conservative treatment include those with little exposure to high risk activities (heavy work and sports), those over 40 years of age, those who will adapt to ACL insufficiency, those with advanced osteoarthritis, and those unwilling to comply with post-surgical rehabilitation. The natural history of an ACL deficient knee is largely unknown; however, studies have shown that functional instability of the knee can lead to meniscal injuries and intra-articular damage over time[135].

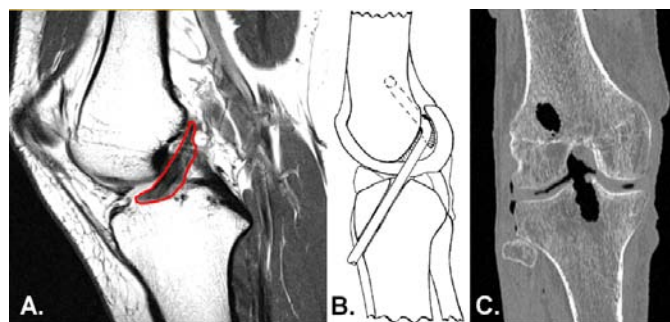


Figure 5.6 Diagrams of the ACL and ACL reconstruction. A) A proton density weighted MRI image highlighting an intact ACL. B) An ACL reconstructed knee demonstrating the tibial and femoral tunnels and initial graft placement. C) A CT image demonstrating portions of the tibial and femoral tunnels.

5.3.2 Techniques

The first primary repair of the ACL was performed in 1895[143]. In 1915, the first ACL reconstruction was performed. Shortly thereafter, it was recognized that reconstruction had a better success rate than primary repair. The guiding principle in modern surgical ACL reconstruction is to replace the torn ACL with a graft. Ideally, the graft is placed in the exact location of the native ACL. Placing the ACL in the native location is technically challenging; the current method requires drilling two tunnels: one through the femur and one through the tibia (Figure 5.6). Over time, the graft grows into the healing bone to act as a replacement for the ACL. Many factors are involved with a successful reconstruction, but misplacement of the bone tunnels has been described as the most common cause for a failed reconstruction[129, 144, 145]. Multiple methods have been described in the literature including both single and double bundle arthroscopic techniques. According to a 2009 survey, 80% of orthopaedic surgeons perform less than 10 ACL reconstructions per year[143].

5.3.2.1 Single Bundle Reconstruction

Single bundle ACL reconstruction has been the mainstay of ACL repair. It can be divided into two approaches: the single incision and two incision approaches. The two incision approach is the more traditional method of ACL reconstruction (Figure 5.7). It is considered to be less demanding than a single incision technique and also easier to achieve accurate placement of the drill tunnels since they are performed independently[119, 146, 147]. The tibial tunnel is performed through an anteromedial incision and the femoral tunnel is performed through an incision over the lateral femoral metaphysis[121].

The transtibial method and the anteromedial portal method are both considered single incision techniques[121, 148]. In the transtibial method (Figure 5.8), the tibial tunnel is created through an anteromedial incision and the femoral tunnel is created

through the tibial tunnel with the leg correctly positioned[149]. In 2009, 70% of orthopaedic surgeons reported using the transtibial technique[143]. The anteromedial portal method (Figure 5.9) places the femoral tunnel using the anteromedial arthroscopy portal and the tibial tunnel is placed through an anteromedial incision[150].

Proponents of the two incision technique argue that the single incision technique has a greater possibility of common peroneal nerve injury, damage to the posterior articular cartilage, screw divergence, tunnel/graft length mismatch, and posterior wall breakthrough[119, 151]. Proponents of the single incision techniques argue that their technique has fewer incisions, better cosmetics, shorter hospital stay, less operative time, and less post-operative pain. Studies have shown similar outcomes for both single and double incision procedures[121, 146]. Each technique has advantages and disadvantages; the surgeon's preference guides the treatment of choice. Surgical guides have been developed to aid the surgeon in correctly placing the tunnels; however, anatomic variation between patients and variation in surgical technique has resulted in variable placement of the ACL tunnels[152].

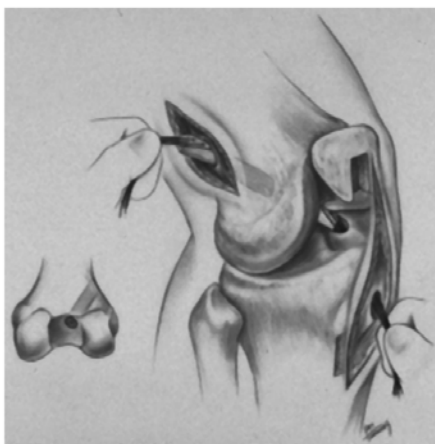


Figure 5.7 The two-incision single bundle ACL reconstruction technique.

(Source: Flik, K.R. et al. [153])



Figure 5.8 The transtibial single bundle ACL reconstruction technique.

(Source: Yerys, P. [149])

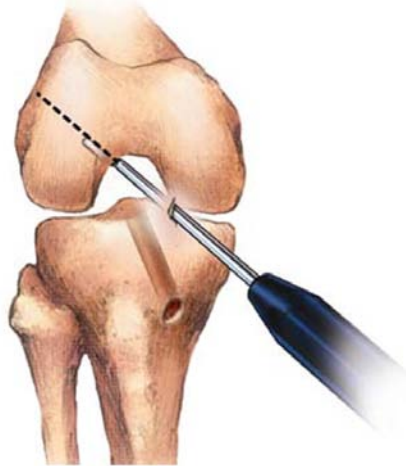


Figure 5.9 The medial portal single bundle ACL reconstruction technique.

(Source: Michaelson, J. [154])

5.3.2.2 Anatomic Double Bundle Reconstruction

Anatomic double bundle reconstruction offers the theoretical advantage of better reconstructing the functional double bundle structure of the native ACL[118, 119, 155, 156]. In this procedure, two grafts are placed to simulate the AM and PL bundles of the native ACL as seen in Figure 5.10. The arthroscopic anteromedial portal is used to visualize both the AM and PL bundles of the ACL during the reconstruction[155]. Proponents of double bundle reconstruction techniques have demonstrated in some cases that single bundle reconstruction techniques have not returned full rotational stability to the knee[118]. The double bundle reconstruction has been demonstrated to more closely return the motion of the knee to its natural state and better outcome scores in some cases[156]. However, the double bundle reconstruction adds an increased degree of complexity to the surgery in multiple ways[129, 157]. For example, the two tunnels are located relatively close together, which leaves a narrow bridge of bone (2mm) that can be easily fractured[158].

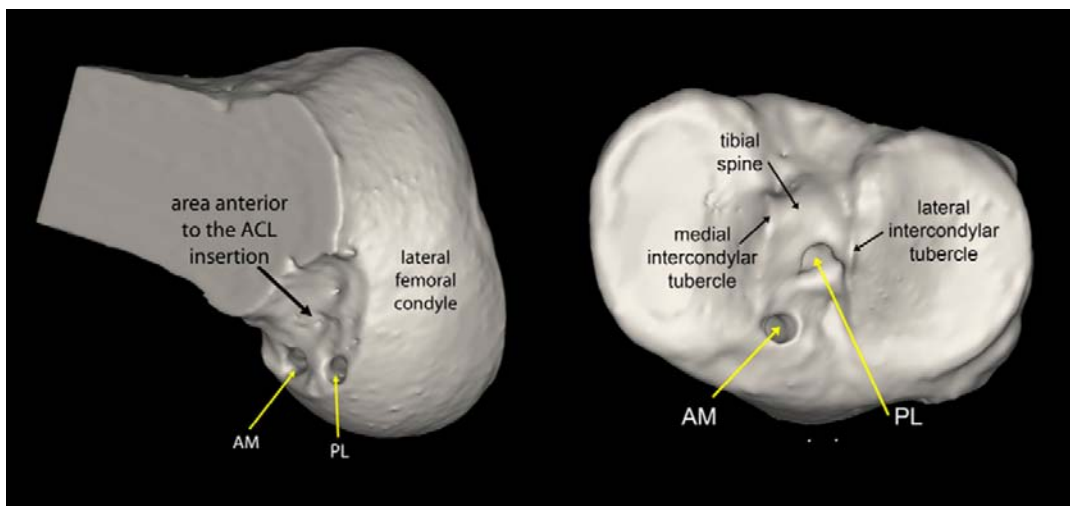


Figure 5.10 Drill tunnels resulting from a double bundle ACL reconstruction.

(Source: Forsythe, B. et al. [159])

Biomechanical studies have shown that carefully placed single bundle grafts in the center of the femoral and tibial ACL insertions have comparable stability to anatomic double bundle procedures[160, 161]. Both procedures resulted in grafts that were capable of resisting anterior tibial translation and rotational torques[160]. Clinical studies have not been performed to show better patient outcomes of double bundle over single bundle reconstructions[129]. Single bundle reconstructions offer the advantages of less reported tunnel widening, fewer complications, easier revisions, lower allograft costs, shorter surgical times, and greater technical ease[129].

C. Computer-Assisted Surgery

Computer-assisted surgery offers another means to accurately place tunnels[162, 163]. These surgical systems use medical imaging and real-time visual feedback to aid the surgeon during a procedure. In ACL reconstructions, computer-assisted surgical techniques can help guide ACL tunnel placement to ensure reliable and accurate placement of ACL tunnels. Studies have shown computer-assisted ACL replacements are more reliable and less variable than manually placed tunnels[124, 125].

5.3.3 Grafts

5.3.3.1 Types

The ideal graft for an ACL reconstruction should allow for stable fixation, rapid incorporation, minimal morbidity, and mimic the biomechanical properties of the native ACL[120, 129]. Autografts and allografts are the two most commonly used grafts. Multiple graft donor locations have been evaluated including the quadriceps tendon, patellar tendon, Achilles tendon, hamstring tendon, anterior/posterior tibialis tendon, or a piece of the fascia lata. Autografts offer the advantages of a higher stability rate, lower graft failure rate, lower infection rate, lower cost, and faster overall recovery times. Allografts offer the advantages of less post-operative pain, no donor site morbidity,

improved cosmesis, and faster immediate post-operative recovery. If a cadaveric allograft is used, sterilization procedures are used to minimize the chances of disease transmission, which is not an issue with autografts. These procedures have been shown to negatively affect the strength of the graft in some instances[129]. Overall, allografts have been shown to have a failure rate three times greater than autografts[126, 129]. Flexible technique in autograft harvest, fixation, and tensioning can avoid complications during the surgical procedure[164]. Synthetic grafts have also been proposed including carbon-fiber scaffolds and polyethylene stents that allow for tissue ingrowth; however, the results to date from synthetic grafts have not been satisfactory[119].

5.3.3.2 Incorporation

The goal of ACL reconstruction is to restore the native transition from soft tissue to fibrocartilage to calcified fibrocartilage to bone, which is accomplished through incorporation of a graft into bone[165]. Incorporation of a graft into the knee is a three stage process for allografts and autografts[120, 166, 167]. In the first stage, the graft undergoes an inflammatory response and degeneration. Fibroblasts in the graft undergo apoptosis and the remaining tissues act as a scaffold for incorporation of host cell migration and matrix production. The second stage, ligamentization, begins around 20 days after the procedure and continues for 3-6 months following the surgery. In this stage, additional cells migrate towards the graft and the graft is vascularized.

The third stage is a remodeling stage whereby the collagen structure of the graft is organized to more closely resemble a ligament. The material properties of the graft improve over time in the healing process. Autografts have a faster healing rate than allografts. During the process of graft incorporation, the fixation of the graft to the surrounding bone is the weakest link in the reconstruction system. With full incorporation of a graft into the surrounding bone, the ACL graft can restrain the motion of the knee. Full ligamentization has been reported to take up to three years[166]. Bone

morphogenic protein-2 (BMP-2) has been investigated as a means to expedite the rate of graft incorporation[168].

5.3.3.3 Fixation

The process of holding a graft in place prior to incorporation is called fixation. Interference screws, cortical techniques, and cross pins are three methods of fixation that have been used[129]. Interference screws generate a friction holding force between the graft and bone tunnel wall. Cortical fixation techniques typically involve threading a graft through a loop that is held tightly against the cortical bone. Cross pins are passed transversely through a graft and anchored in bone. No consensus as to the best technique has been established.

5.3.4 Rehabilitation

There is no consensus as to the most appropriate rehabilitation technique following ACL reconstruction; however, some guidelines have been established[165]. Early joint motion has been shown to reduce pain and prevent the formation of motion restricting scar tissue in the joint. Immediate weight bearing as tolerated after ACL reconstruction has been shown to decrease the likelihood of anterior knee pain in the future. Closed chain exercises have been associated with decreased anterior knee pain and faster return to activity. Rehabilitation braces have been shown to effectively reduce swelling, hemarthrosis, and wound drainage early in the course of rehabilitation, but have not been shown to have long term functional benefits[169]. A combination of rehabilitative exercise and neuromuscular stimulation has been shown to better improve restoration of muscle strength than exercise alone. Cold therapy and functional braces have not been shown to affect outcomes. Home physical therapy regimens typically are designed for patients using these guidelines. Once full range of motion of the knee is achieved, treadmill activity can begin[144].

5.3.5 Outcomes

Both the single and double bundle reconstruction techniques have been shown to be capable of reproducing the function of the native ACL; however, failed ACL reconstruction is not uncommon even amongst experienced surgeons[129]. After reconstruction, patients have had good success at activities involving straight line motions like jogging and cycling; however, movements involving cutting, turning, or pivoting are problematic[142]. These types of motions indicate that the rotational stability of the knee may not be sufficiently addressed in current procedures[155]. This has been the motivation for anatomic double bundle procedures and also the motivation for evaluating single bundle methods to optimize their results. Up to 40% of ACL reconstructions require revision, which is typically determined based on the patient's history and clinical exam[125]. As aforementioned, tunnel misplacement has been determined to be the primary cause of reconstruction failure. Studies evaluating the placement of tunnels in single bundle procedures have determined that up to 50% of tunnels may be misplaced [165]. Incorrect tunnel position has been shown to result in abnormal graft tension, graft impingement, reduced range of motion, and recurrent instability[144, 145].

Multiple scoring systems have been used in the evaluation of patient outcomes after ACL reconstructions including Lysholm, Tegner, IKDC, KOOS, and PPLP[170]. Here, we briefly describe two of these scoring systems: KOOS and PPLP. The Knee Injury and Osteoarthritis Outcome Score (KOOS) has been used to follow patients after ACL reconstruction to correlate changes in symptoms and level of function with long term development of osteoarthritis[171, 172]. The scale evaluates 42 items in 5 categories: pain (9 items), other symptoms (7 items), activities of daily living (17 items), function in sport and recreation (5 items), and knee-related quality of life (4 items). The system is rated from 0% (extreme problems) to 100% (no problems). These outcome scores have been found useful in following patients in both the short term and long term.

The PPLP scoring system is another scoring system that aims to evaluate athletes after ACL reconstruction[173]. This system involves subjective, clinical, and functional data contained in two parts: the PPLP1 and PPLP2. The PPLP1 occurs at post-operative follow-up and investigates pain, apprehension, patient sensation, and clinical examination factors; it has a maximum of 100 possible points. The PPLP2 occurs at long-term follow-up and investigates running, cardiovascular training, and isokinetic evaluation; it also has a maximum of 100 possible points. Higher scores are associated with fewer complications and faster return to play.

5.3.6 Reconstruction Complications

Complications after reconstruction of the ACL have been reported in the literature and have been described as early or late failures[174-176]. MRI has been described as the imaging modality of choice for evaluating symptomatic complications. An early failure occurs within 6 months of the procedure and is attributed to poor surgical technique, failure of graft incorporation, or errors in rehabilitation. Misplacement of the tibial tunnels has been associated with graft impingement against the intercondylar roof. MR imaging shows spurring of the anterior margin of the intercondylar roof and posterior bowing of the graft. Failure of graft incorporation can lead to synovial fluid collections in the ACL tunnels and tunnel widening, which can be easily visualized as fluid-filled tunnels on MR imaging studies. The causes of drill tunnel widening are believed to be multifactorial including motion of the graft with respect to the tunnel[177]. Hardware complications have also been recorded in the literature. Beyond loosening and displacement, some hardware has been shown to cause inflammation of surrounding tissues and can lead to conditions like iliotibial band friction syndrome.

The risk of infection is always present in surgical interventions; septic arthritis has been recorded in 0.1-0.9% of ACL reconstructions[174, 176]. MR imaging can be used to validate the diagnosis of infection by demonstrating evidence of synovitis, bone

erosion, periarticular edema, marrow edema, and soft-tissue abscess. Arthrofibrosis, the presence of scar tissue in at least one compartment of the knee joint, is a complication that can lead to decreased range of motion and is reported in 1-10% of ACL reconstructions[174]. This complication often has a stereotypical “cyclops” appearance where a nodular fibrous lesion is located in the anterior intercondylar notch and has a mixed enhancing appearance on T1, T2, and proton density MR images[175].

Late failures occur after one year and are generally attributed to an additional traumatic insult to the graft[174]. Common examples of late failure include partial and complete graft tears. A partial graft tear enhances on T2 imaging showing areas of increased intensity covering a portion of the graft; however, this can be confused with the ligamentization process which can show a similar pattern up to 4 years after the original reconstruction. A complete graft tear shows fluid-filled defect and absence of intact graft fibers. It can also be characterized by a horizontal graft orientation and resorption of graft fibers, and is accompanied by a large joint effusion and lateral bone bruises.

5.4 Evaluation of Tunnel Placement

5.4.1 Overview

To improve patient outcomes, much effort has been put towards determining the best method of placing ACL tunnels. Various studies have aimed at evaluating procedural modifications for the various reconstruction techniques to achieve more anatomical graft placements and more natural knee kinematics[142, 146, 178-181]. Very slight variations in tunnel placement can have dramatic effects on the success of the reconstruction[118, 121, 182]. For example, anterior misplacement of the femoral tunnel can result in knee instability and reduced flexion ability[118, 165], and anterior misplacement of the tibial tunnel can result in graft impingement that is associated with decreased extension ability and graft abrasion[118, 146, 165]. Burkart et al. and Howell et al. have reported variability between surgeons in tunnel placement[183, 184].

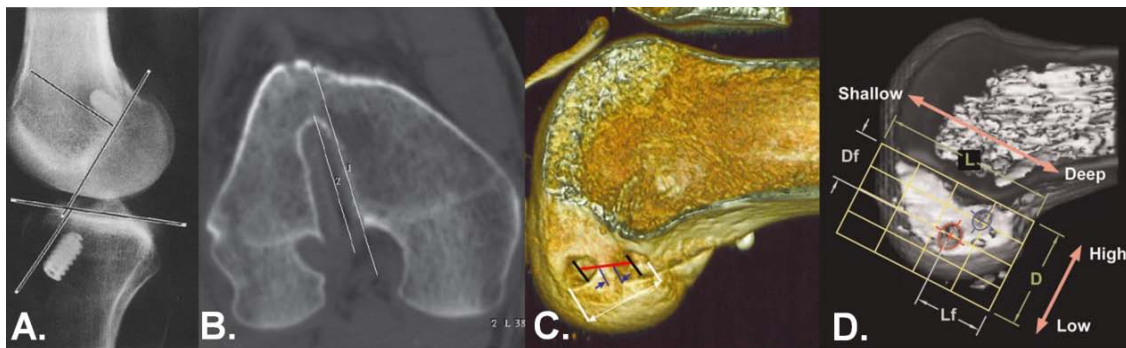


Figure 5.11 Different methods of evaluating ACL reconstructions. A) An example of a lateral radiograph based tunnel measurement system using Blumensaat's line and the medial tibial plateau. B) An example of a CT based tunnel measurement system using a single CT slice. C) A CT reconstructed femur based measurement system using straight-line measurements. D) A CT reconstructed femur based tunnel measurement system using a grid oriented with plain lateral radiographic landmarks.

(Source: A) Aglietti P, et al.[140] B) Chan YS, et al.[185] C)Basdekis G, et al.[186] D)Miller MD, et al.[179])

Multiple measurement methods have been described for evaluating ACL tunnel placement (Figure 5.11). Post-operative evaluation of tunnel placement has traditionally been performed using plain radiographs. Two-dimensional measurements using radiologic landmarks have been the standard in describing tunnels. These measurements are typically either represented as distances from radiologic landmarks (e.g. Blumensaat's line, femoral condyles, medial tibial plateau) or percentages of overall bone dimensions[123, 140, 152, 165]. Unfortunately, tunnel placement is inherently three-dimensional. Studies have shown that measurements from two-dimensional radiographs can be insufficient to accurately describe tunnel placement due to poor visibility and inaccurate radiographic technique[187]. Two-dimensional measurements from CT slices have been investigated as an alternative method to describe tunnel placement[185, 187]. Others have reconstructed surfaces of the tibia and femur using CT datasets and have described tunnel locations based on measures similar to those used to evaluate plain radiographs[180, 186, 188]. Typically, these studies compare two procedures performed

on a limited number of specimens by a limited number of surgeons. Here, we briefly describe several methods of ACL tunnel characterization.

5.4.2 The Tibial ACL Tunnel Aperture

Describing the location on the tibial plateau has traditionally been more consistent between research groups due to the relatively more simple 3D geometry of the tibial plateau in comparison to the femoral condyles. The European Society for Sports Traumatology and Knee Arthroscopy published recommendations[51] for describing the tibial ACL attachment with respect to a perfect lateral radiograph of the knee (Figure 5.12A) and anterior-posterior (AP) radiograph of the knee (Figure 5.12B). For the anterior-posterior measurement (from the lateral radiograph), a line is constructed across the medial tibial plateau that is tangent to the anterior and posterior most aspects of the tibial plateau. The anterior-most aspect is considered 0% and the posterior most aspect is considered 100%. The medial-lateral measurements (from the AP radiograph) are based at the joint line and extend from the medial edge of the tibial plateau to the lateral edge of the tibial plateau. The medial most edge is considered 0% and the lateral most edge is considered 100%. The position of the anatomic insertion is given in percentages based on the previous described measurements.

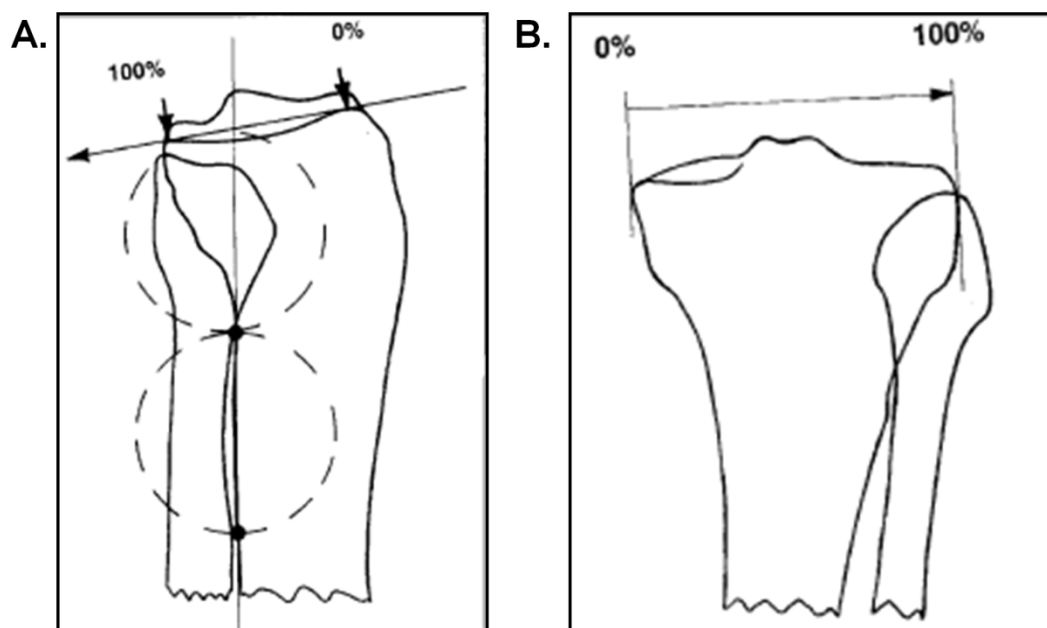


Figure 5.12 Suggested measurements for the tibia. The suggested measurement criteria from the ESSKA for the tibia demonstrated using a A) lateral radiographic view and B) anterior-posterior radiographic view.

(Source: Amis A, et al.[51]) [123]

Axial views of the tibial plateau from CT imaging allowed for simultaneous medial-lateral and anterior-posterior measurements from a single CT slice[183]. Figure 5.13 demonstrates these measurements. It should be noted that the tibial plateau is oriented with the posterior-most aspects of the medial and lateral components of the tibial plateau linearly aligned. Like the ESSKA radiographic measurements, the measurements originate (0%) at the anterior aspect and medial aspect of the tibial plateau. They can be described as A/B and C/D for the anterior-posterior and medial-lateral measurements, respectively.

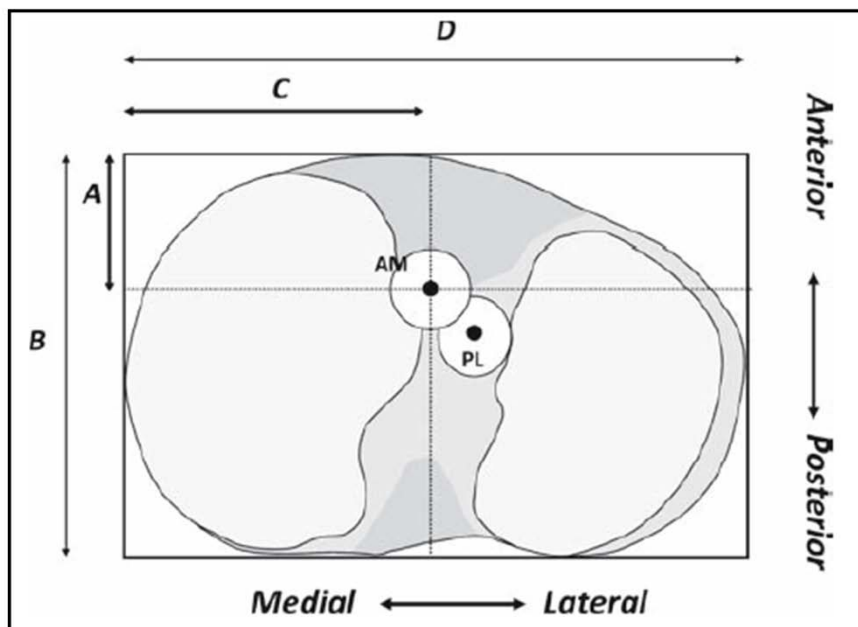


Figure 5.13 A tibial measurement system established from the “bird’s eye view” of the tibial plateau using similar measurements as those recommended from the ESSKA.

(Source: Tsukada H, et al. [183]) [189]

Recently, measurements from surface reconstructions have been proposed as an alternative to single CT slice measurements. Compensating for rotation in CT images can be challenging, while surface reconstructions can be easily oriented for measurements. Forsythe, et al has suggested that the tibial ACL attachment be described using a similar anterior-posterior and medial-lateral measurement system[171]; however, the tibia surface is oriented based on the mechanical axis of the tibia and the tibial malleoli. This measurement system and orientation is demonstrated in Figure 5.14 with two measurements a/c and A/C giving the medial-lateral and anterior-posterior measurements, respectively.

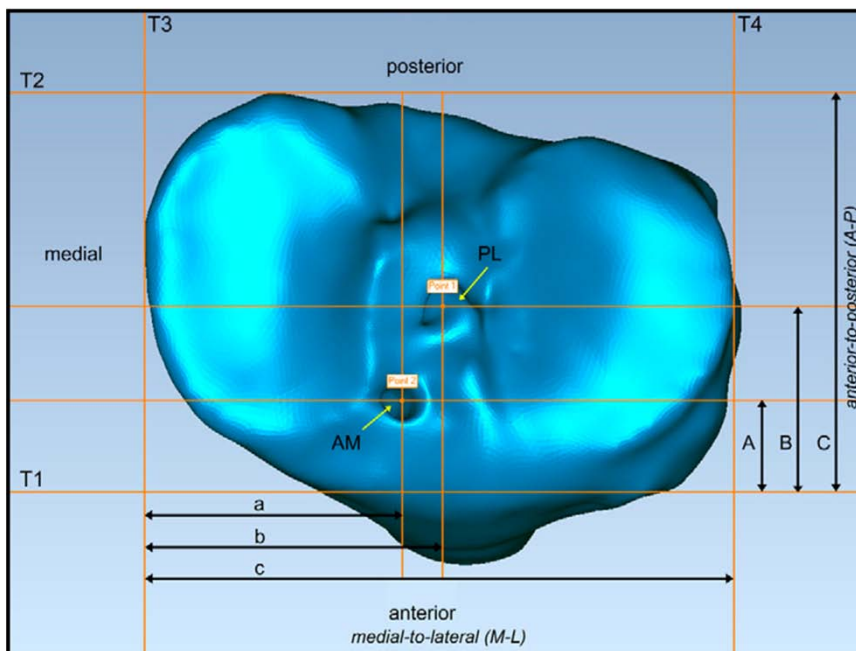


Figure 5.14 Forsythe's method of describing the tibial attachment of the ACL using surface reconstructions.

(Source: Forsythe B, et al. [171])[159]

5.4.3 The Femoral ACL Tunnel Aperture

Multiple methods of describing the femoral ACL attachment have been proposed. Most depict a sagittal cross-section of a femur that views the medial aspect of the lateral condyle. Watanabe's method[189] is demonstrated in Figure 5.15. Point O describes the "over-the-top position" and Point A describes the anterior notch outlet point. Point I describes the interface between bone and cartilage along the lateral femoral condyle. Percentage measurements based on these points establish the location of the ACL attachment site with respect to superior-inferior (c/d) and shallow-deep (a/b) descriptors.

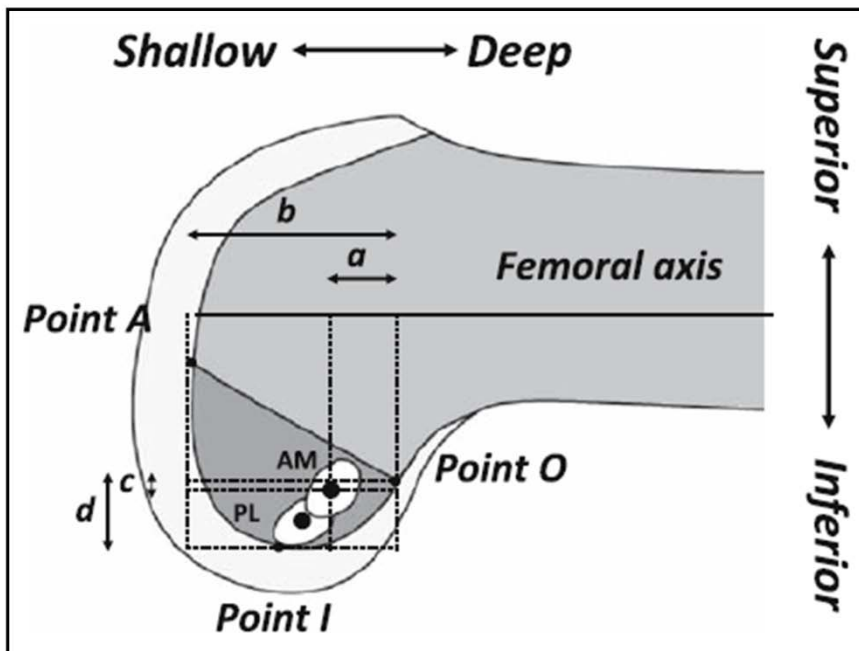


Figure 5.15 Watanabe's method of describing the femoral attachment of the ACL.

(Source: Tsukada H, et al. [183])

The quadrant method has been widely described as a means to locate the femoral ACL attachment as described in Figure 5.16[189]. In this method, the total diameter of the lateral femoral condyle along Blumensaat's line (t) and the total intercondylar height (h) are used to establish the position of the ACL attachment site. A grid is typically positioned along Blumensaat's line to help estimate the locations of the ACL attachment site. Percentage measurements or grid positions are used to describe the location perpendicular (b/h) and parallel (a/t) to Blumensaat's line.

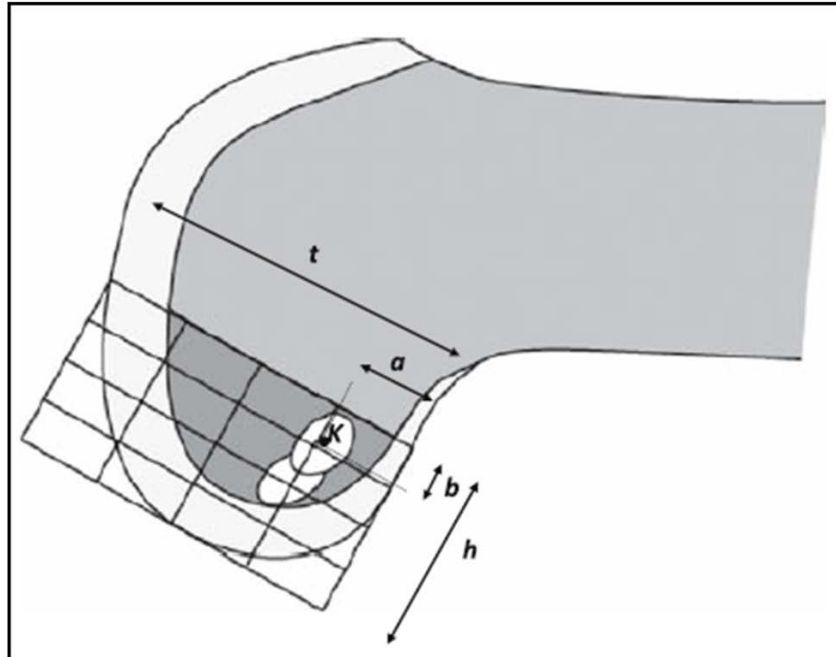


Figure 5.16 The quadrant method of describing the femoral attachment of the ACL.

(Source: Tsukada H, et al. [183])

Takahashi's method for describing the femoral ACL attachment site is described in Figure 5.17[189]. The ACL location is described as a proportion of the distance between the ACL attachment center and the bone to articular surface interface (FA) and the distance between the intercondylar notch outlet and the deep margin of the lateral condyle (F-AP). The percentage was calculated as $FA/F-AP$.

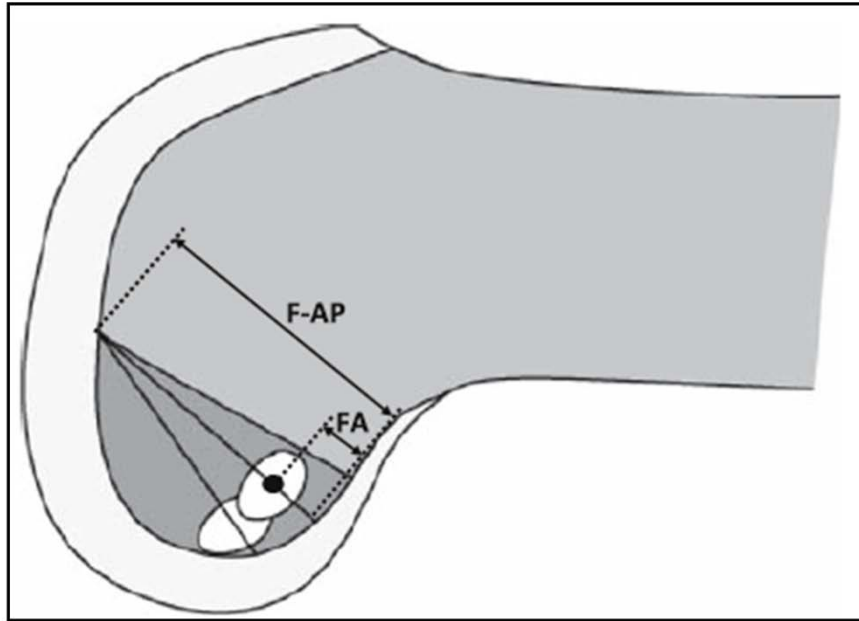


Figure 5.17 Takahashi's method of describing the femoral attachment of the ACL.

(Source: Tsukada H, et al. [183])

Mochizuki's method for describing the femoral ACL attachment is described in Figure 5.18[189]. This method measured the distance of the femoral ACL attachment from the border between the articular surface and bone interface (A1). These measurements are performed parallel with Blumensaat's line and are expressed as percentages with respect to the deep interface between bone and articular surface (A2). The measurement is expressed as A1/A2.

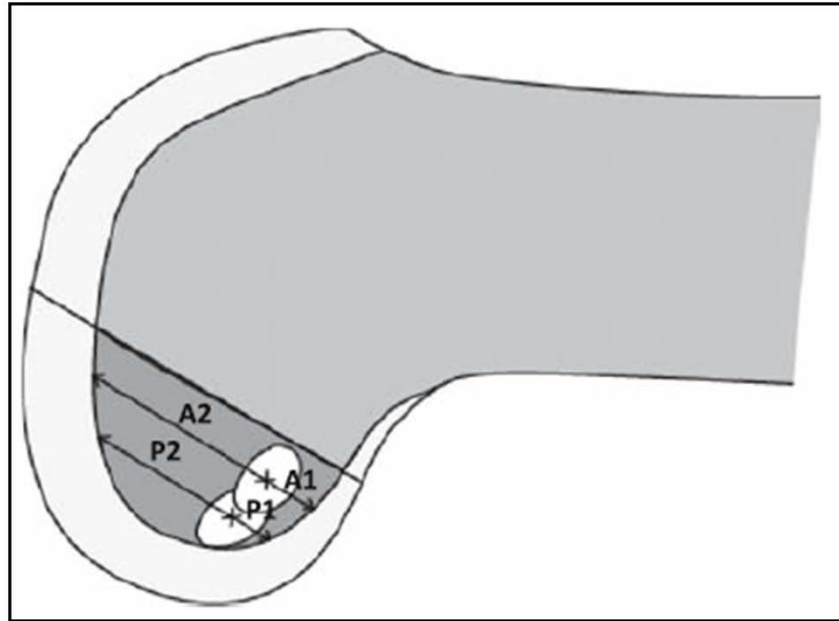


Figure 5.18 Mochizuki's method of describing the femoral attachment of the ACL.

(Source: Tsukada H, et al. [183])

Forsythe, et al. has also proposed a method of describing the femoral tunnel attachment site on surface reconstructions of the femur as shown in Figure 5.19[159]. This system orients the femur surface based on the femoral mechanical axis. Two measurements are used to describe relationships anterior to posterior and proximal to distal with respect to the medial wall of the lateral condyle. The proximal to distal measurement (c) uses a line through the posterior border of the medial wall of the lateral condyle and a line running through the most anterior point on the intercondylar notch. The anterior to posterior measurement (C) uses a line through the proximal border of the notch and a line through the distal most point on the notch roof. Measurements are made from the proximal and posterior aspects of the medial wall to give a/c and A/C, which are the proximal to distal and posterior to anterior measurements, respectively.

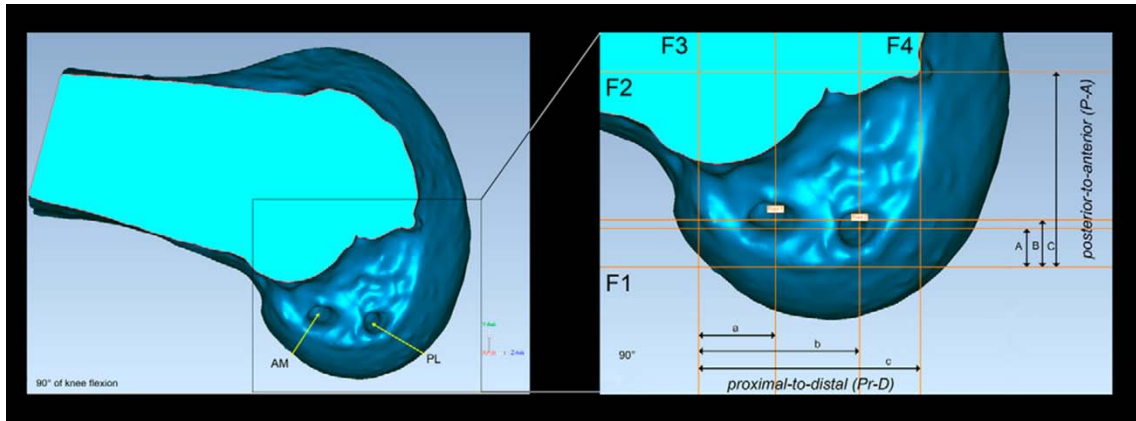


Figure 5.19 Forsythe's method of describing the femoral attachment of the ACL on surface reconstructions.

(Source: Forsythe B, et al. [171])

5.5 Finite Element Studies

The anatomy and kinematics of the knee are complex, which is evidenced by the fact that minor changes to the normal anatomy can result in disrupted knee motions and stress distributions. ACL reconstructions have been investigated using the finite element method to describe the stress distributions before and after an ACL reconstruction. Experimentally validated models of the intact knee have been presented by Papaioannou et al. and Peña et al.[190, 191]. Both were patient-specific models that were composed of hexahedral meshes and were derived from CT and MR image sets. Bone, ligaments, cartilage, and menisci were meshed and evaluated in the models under various loading conditions. Limbert et al. and Zhang et al. have developed patient-specific finite element models of the ACL to evaluate the ligament under various states of flexion and extension of the knee[192, 193]. Zhang et al. was able to incorporate an hourglass shape, spiral bundle orientation, and transverse isotropy into their patient-specific model of the ACL[193]. Yao et al. has investigated the effects of ACL injury on surrounding

structures using a patient-specific finite element model of the medial compartment of the knee[194]. Other groups have developed patient-specific models for specific scenarios involving the knee including patellofemoral interactions[195], joint mechanics in total knee replacements[196], and joint biomechanics in rehabilitative exercises after ACL reconstruction[197].

In regards to ACL reconstructions, Peña et al. investigated the effects of various tunnel angles using a previously validated finite element model of the knee[198]. In this study, coronal tunnel angle was varied and the knee model was evaluated in various degrees of flexion and extension. The effects of variable tunnel position on graft tension, meniscal stress, stress on surrounding ligaments, and chances of impingement were evaluated. This study found that a femoral angle had the largest impact on graft tension and impingement, while the tibial tunnel mainly affects laxity and meniscal stress. Peña et al. continued their investigation by also investigating the effect of graft stiffness on surrounding tissues under different degrees of flexion and extension[199]. Grafts that are too tight have been shown to result in decreased motion at the joint, delayed vascularization, graft failure, and increased cartilage contact pressure that can lead to early onset osteoarthritis. Grafts that are too loose result in persistent instability. Shirazi et al. has investigated the effects of ACL reconstruction on the ACL graft, meniscus, and cartilage using a finite element model that included depth dependent properties of cartilage and also fiber networks in cartilage and menisci[200]. They found that ACL reconstruction affects the contact forces on the meniscus and cartilage, which could contribute to early onset osteoarthritis.

CHAPTER 6

THREE-DIMENSIONAL EVALUATION OF GRAFT PLACEMENT IN ANTERIOR CRUCIATE LIGAMENT RECONSTRUCTION

6.1 Overview

The anterior cruciate ligament (ACL) is an important knee ligament that often requires reconstruction when injured. Optimally, ACL reconstruction exactly replaces the native ligament to replicate normal knee biomechanics. However, up to 40% of ACL reconstructions require revision, with the primary cause of reconstruction failure being graft tunnel misplacement[125]. Graft misplacement can result in abnormal knee biomechanics and subsequently early onset osteoarthritis. The ability to characterize tunnel placement is needed to identify factors that may improve patient outcomes. The European Society of Sports Traumatology Knee Surgery and Arthroscopy (ESSKA) has published radiographic guidelines for describing ACL tunnels and past studies have used them to perform 2D measurements using radiographs and CT slices[123]. Three-dimensional surface reconstructions have recently been investigated as a means to characterize graft tunnel placement[159]; however, a standardized evaluation of a large number of 3D surface reconstructions has not been performed.

In collaboration with the Multicenter Orthopaedic Outcomes Network (MOON), we have obtained 150 CT datasets of postoperative, ACL reconstructed knees. This dataset includes ACL reconstructions performed using three single bundle surgical techniques, two levels of surgeon experience, and numerous operating surgeons. Given the high revision rate and reports from previous 2D studies, it is apparent that anatomically similar reconstructions are not consistently achieved. We hypothesize that a 3D evaluation of ACL drill tunnel placement will identify statistically significant differences in graft placement related to surgical technique, level surgeon of experience,

and operating surgeon. It is our hope that novel 3D analysis will ultimately lead to improved graft placement and better patient outcomes in ACL reconstructions.

Many of the tools necessary to perform this type of 3D analysis are not commercially or freely available. In order to analyze graft placement in 3D, we have developed tools to allow for 3D measurement, and visualization of the CT datasets. We have applied these tools to the MOON dataset and analyzed the results. It is our hope that this software will ultimately become a mainstay of 3D ACL reconstruction research at institutions worldwide. Furthermore, these software tools can easily be extended to other surgical procedures including PCL reconstructions and tendon repairs.

This chapter begins with a discussion of our novel, surgeon oriented 3D measurement system that was developed for analysis of ACL graft placement and also a discussion of an initial effort towards automating virtual drill bit alignment for this measurement system. Next, two novel methods of visualization for large datasets from ACL reconstruction studies are presented. A discussion of the MOON dataset and its analysis follows. Finally, we compare the MOON dataset results to an estimated ACL footprint and also investigate the known revision cases from the MOON dataset at The University of Iowa.

6.2 Surgeon Oriented 3D Measurement System

6.2.1 Abstract

Injury of the anterior cruciate ligament of the human knee is common, and can result in knee instability and early onset osteoarthritis. Repair of this ligament is currently performed using one of several established techniques; incorrect graft tunnel placement during surgical ACL reconstruction is the primary cause of poor patient outcomes. Traditionally, two-dimensional methods have been used to describe the locations and angles of graft tunnels with respect to surrounding radiographic landmarks (e.g. Blumensaat's line). We present novel techniques for defining graft tunnel

placement and orientation from three-dimensional surface representations of the ACL reconstructed knee. The angular and spatial measurements described herein have demonstrated intraclass correlation coefficients ranging from 0.95-0.99. The proposed three-dimensional measurements were used to evaluate multiple ACL reconstruction techniques including medial portal, transtibial, and two-incision procedures. These measurements may be readily extended to other procedures involving bone tunnels such as PCL reconstruction. In the future, we plan to apply our methods to evaluate the variability in ACL tunnel placement and to identify factors that improve patient outcomes.

6.2.2 Introduction

Disruption of the anterior cruciate ligament (ACL) is a common injury of the human knee, especially in athletes. It has been estimated that nearly 175,000 ACL reconstructions are performed each year with an estimated cost of up to \$3 billion[119, 124, 125, 201]. Up to 40% of ACL reconstructions require revision, with graft tunnel misplacement being the primary cause of reconstruction failure[125]. Studies evaluating the placement of graft tunnels have shown that up to 50% of tunnels may be misplaced[165]. Surgical ACL reconstructions typically fall into one of two categories: single bundle and double bundle procedures. Single bundle techniques (e.g. medial portal, transtibial, two-incision approaches) involve the placement of a single drill tunnel and graft to replace the torn ACL, while double bundle techniques use two independent drill tunnels and grafts to replace the functional anteromedial and posterolateral bundles of the native ACL.

Due to the large number of ACL tunnels that are misplaced, the characterization of ACL tunnels has been considered important with much effort being concentrated on two-dimensional measurements from standard radiographic views. The European Society of Sports Traumatology Knee Surgery and Arthroscopy (ESSKA) Workshop on

Reconstruction of the Anterior and Posterior Cruciate Ligaments has provided guidelines for describing tunnel locations on the distal femur and proximal tibia[123]. Two-dimensional tunnel evaluation studies using plain films have been performed using these guidelines and variations of them[121, 140, 145, 181, 184]. With the advent of CT technologies, several studies have extrapolated the two-dimensional measurements to CT slices[148, 185, 187]. Surface generation from CT images has also been investigated as a method of tunnel placement evaluation[147, 159, 179, 180, 202]. Three-dimensional surface-based techniques are desirable due to their ability to visualize not only the bone but also the tunnels through the bone. However, a standardized three-dimensional measurement system does not currently exist that allows for direct translation of measurements from the laboratory to the operating theater. Herein, we describe a reliable and flexible three-dimensional measurement system capable of characterizing ACL tunnel position and orientation.

6.2.3 Materials and Methods

6.2.3.1 Three-Dimensional Measurement System

We have developed a three-dimensional measurement system for characterizing femoral and tibial drill tunnels from ACL reconstructions. Our ability to characterize the drill tunnels relies on simulating the positioning of the drill bit originally used to create the tunnels within the bone. Based on positioning virtual drill bits, we are able to describe the drill tunnels both angularly and spatially with respect to previously described anatomic landmarks and radiographic views. An overview of this process is outlined in Figure 6.1. The following sections describe the methods used to develop a standardized three-dimensional coordinate system, align the bone surfaces to this coordinate system, generate and align virtual drill bits, match virtual drill bits to drill tunnel apertures, and automatically spatially and angularly measure the virtual drill bits.

To ensure accurate and reproducible measurements, a standardized coordinate system is required for both the femur and the tibia. We have created separate coordinate systems for the femur and tibia based on anatomical landmarks. For the femur, the coordinate system is illustrated in Figure 6.2A. The X-axis is defined by a line through the femoral condyles, such that the posterior-most aspects of the medial and lateral condyles are aligned. The Z-axis is defined by the femoral diaphysis after compensating for the approximately 7° of anatomic valgus. The Y-axis is then defined by the cross-product of the X- and Z- axes. For the tibia, the coordinate system is illustrated in Figure 6.2B. The Y-Axis is defined by the tibial plateau, and the Z-axis is defined by a line through the posterior-most aspects of the medial and lateral components of the tibial plateau. The X-axis is then defined by the cross-product of the Y- and Z-axes.

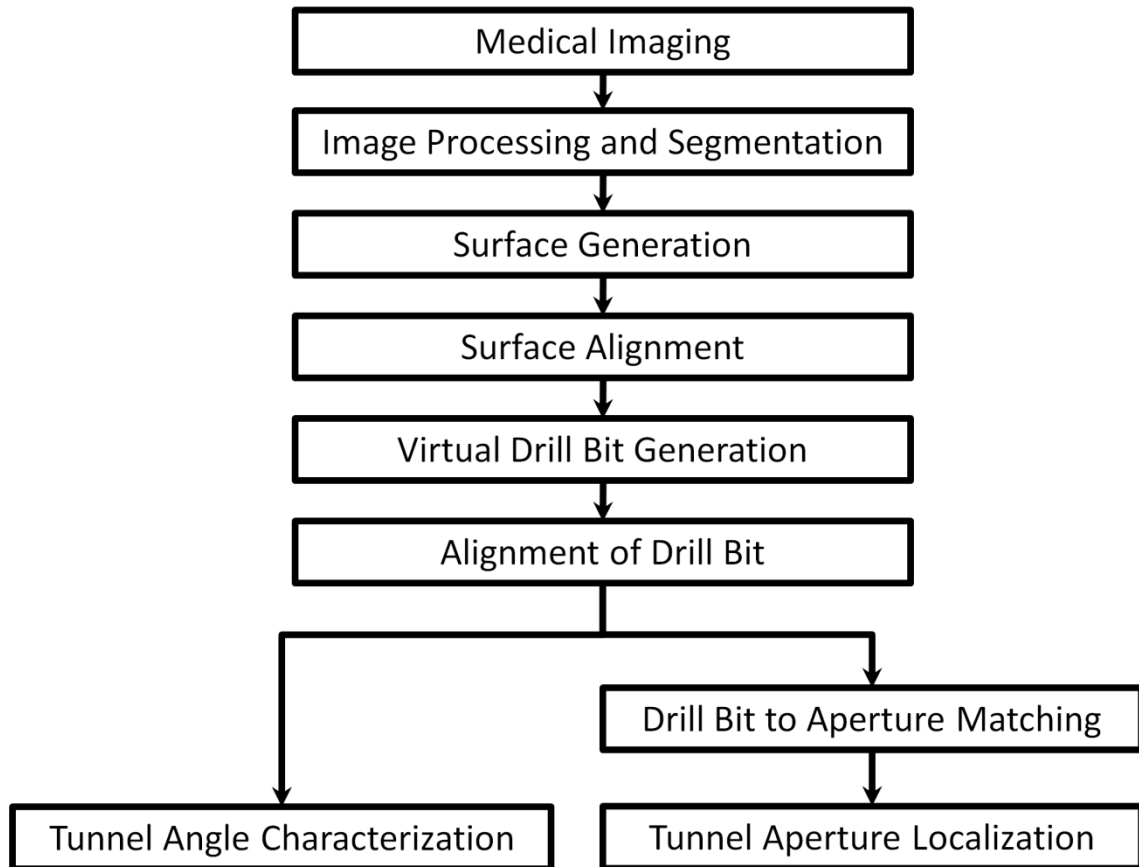


Figure 6.1 A flow diagram describing the process to determine positional and angular information for the femoral and tibial tunnels using a virtual drill bit.

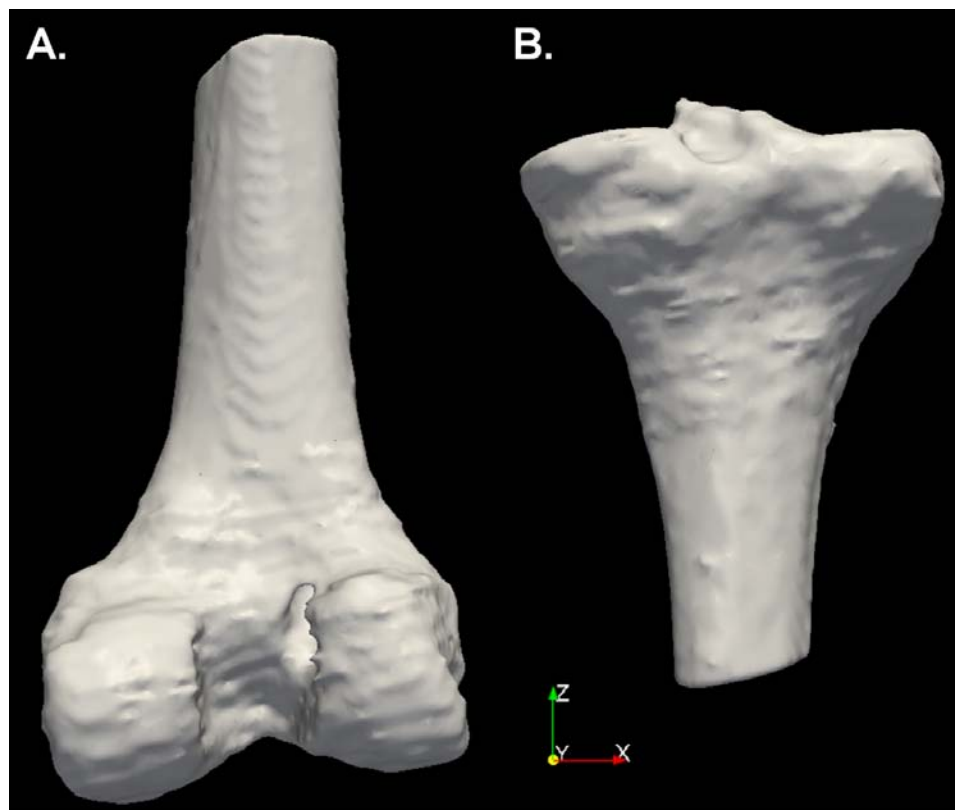


Figure 6.2 Standardized bone orientations. A) Femur. B) Tibia.

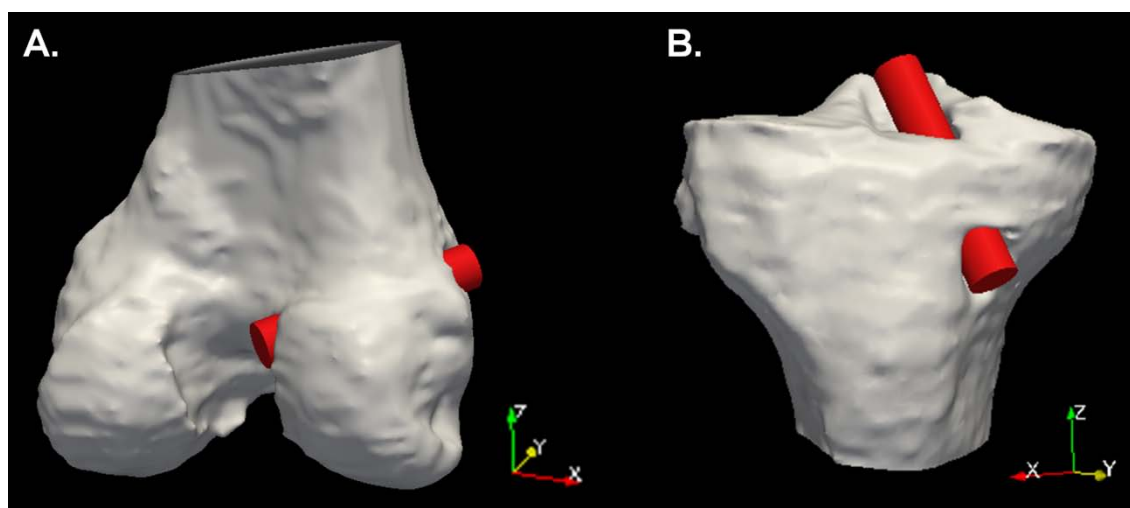


Figure 6.3 A cylinder with a diameter of 10mm was used to simulate the drill bit used to create the ACL tunnels. The cylinders were manually aligned in the tunnels of the A) femur and B) tibia.

6.2.3.2 Estimating ACL Tunnel Position

As an estimate of the drill bit used for the surgical procedure, a cylinder was generated with a diameter equivalent to that of the drill bit. For this study, all procedures were performed using a 10mm diameter drill bit; thus, a virtual drill bit with a diameter of 10mm was created. The cylinder was assigned a length to adequately traverse the entire length of the drill tunnel; a 50mm long drill bit was satisfactory for all of the specimens used in this study. To compute the position of the tunnel within the bone, the cylinder was placed within the tunnel (Figure 6.3) using custom tools[203]. Modifying the opacity of the bone surfaces allowed for proper positioning of the virtual drill bits within the tunnels.

Once the virtual drill bits were aligned with the tunnels, three angles were calculated: α (Eq. 6.1), β (Eq. 6.2), and γ (Eq. 6.3); the angles represent the deviation of the tunnel from the X-, Y-, and Z- axes, respectively (Figures 6.4 and 6.5).

$$\alpha = \cos^{-1} \left(\frac{\overline{p_1 p_2} \cdot \overline{p_1 p_x}}{|\overline{p_1 p_2}| |\overline{p_1 p_x}|} \right) \quad (\text{Eq. 6.1})$$

$$\beta = \cos^{-1} \left(\frac{\overline{p_1 p_2} \cdot \overline{p_1 p_y}}{|\overline{p_1 p_2}| |\overline{p_1 p_y}|} \right) \quad (\text{Eq. 6.2})$$

$$\gamma = \cos^{-1} \left(\frac{\overline{p_1 p_2} \cdot \overline{p_1 p_z}}{|\overline{p_1 p_2}| |\overline{p_1 p_z}|} \right) \quad (\text{Eq. 6.3})$$

where p_1 is the centroid of the end cap of the virtual drill bit closest to the knee joint, p_2 is the centroid of the end cap at the opposite end of the drill bit, p_x represents $p_1 + 1$ unit in the X-direction, p_y represents $p_1 + 1$ unit in the Y-direction, and p_z represents $p_1 + 1$ unit in the Z-direction. A brief description of the process used to perform these calculations is available in Figure 6.6.

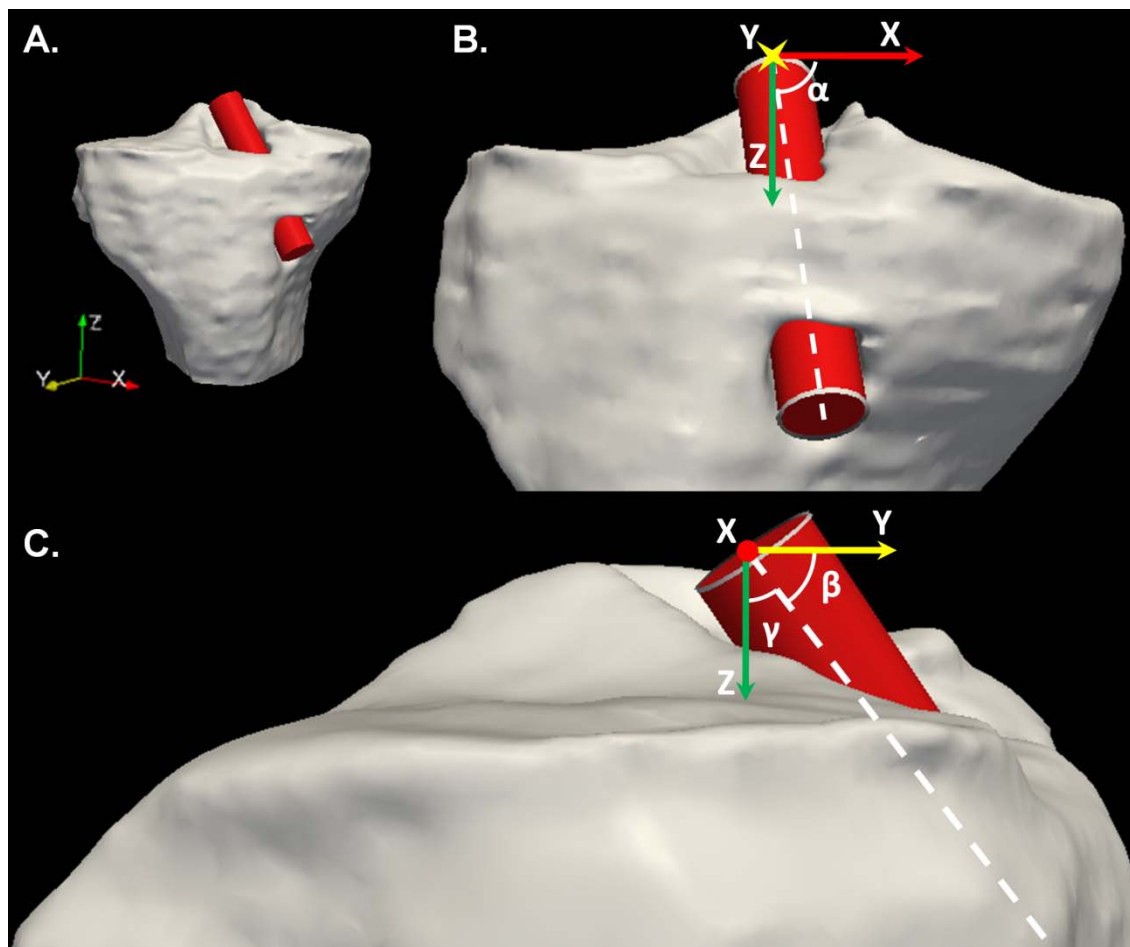


Figure 6.4 Tibial tunnel angles (α , β , γ) were measured based on the tunnel centerline's deviation from the A) surgically oriented coordinate system as demonstrated B) looking down the y-axis and C) looking down the x-axis.

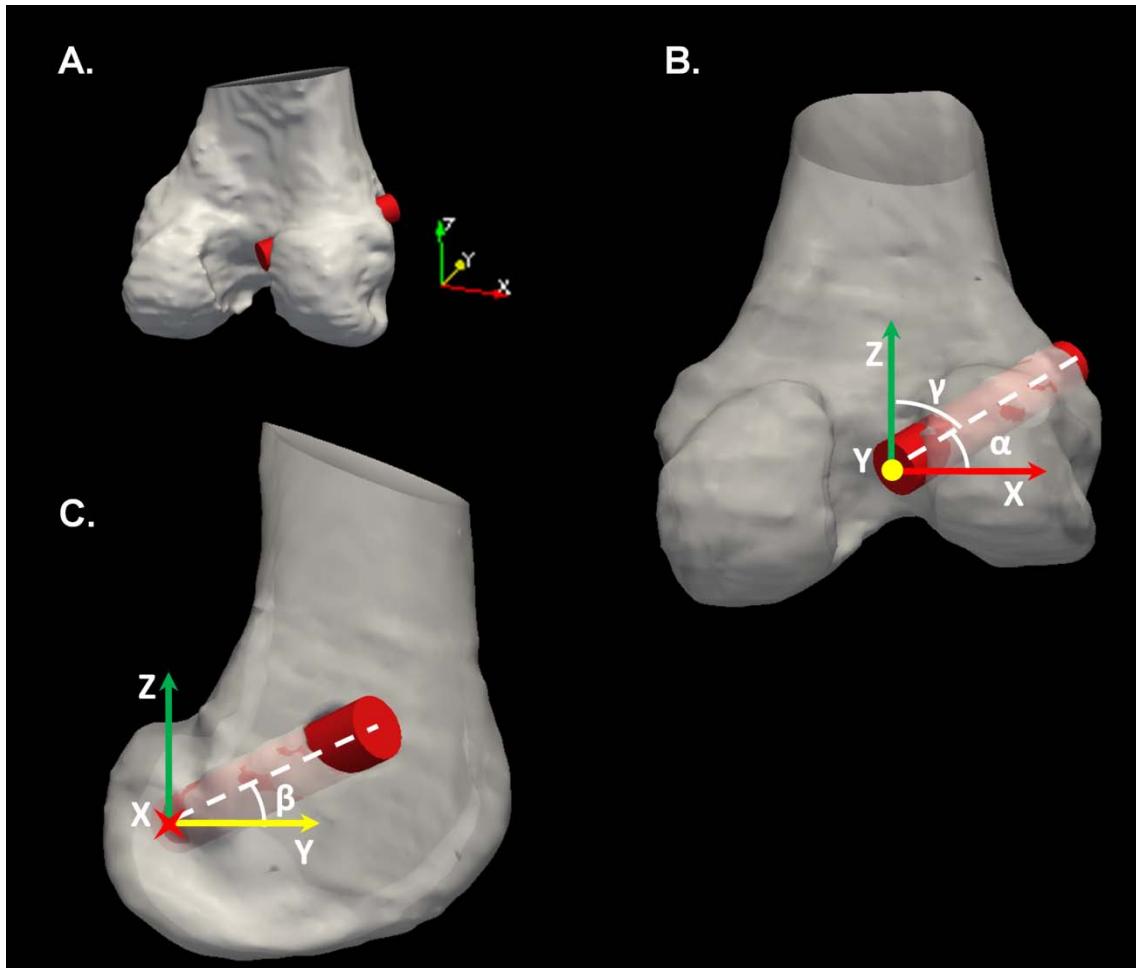


Figure 6.5 Femoral tunnel angles (α , β , γ) were measured based on the tunnel centerline's deviation from the A) surgically oriented coordinate system as demonstrated B) looking down the y-axis and C) looking down the x-axis.

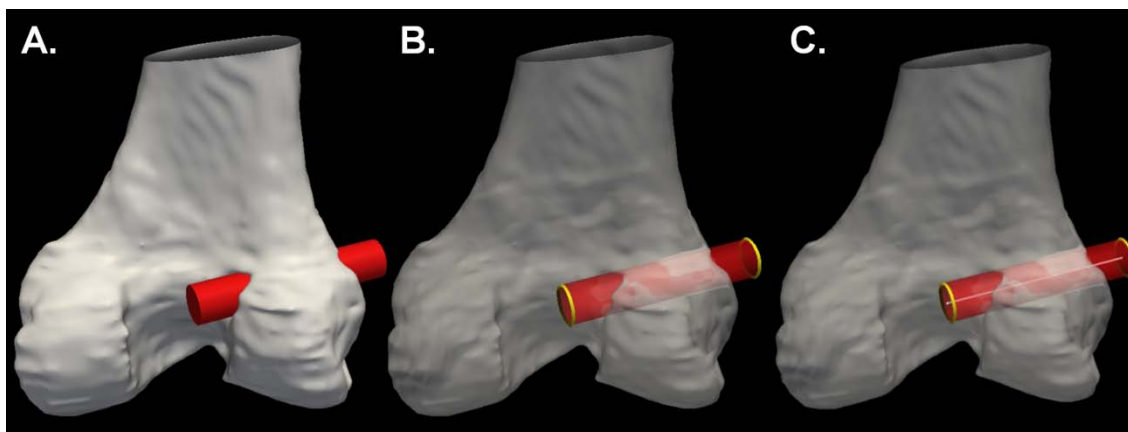


Figure 6.6 The drill bit centerline identification process. A) A virtual drill bit aligned in a femoral tunnel. B) The end caps of the drill bit are isolated. C) The end cap centroids are calculated and define the centerline of the drill bit.

Spatial localization of the ACL drill tunnel apertures allows for correlation of surgical tunnel positioning with respect to the anatomic ACL footprint. To estimate the tunnel apertures from the virtual drill bits, the cylindrical surface was cropped at the tunnel aperture using custom software[203]. After the virtual drill bits were cropped to match the tunnel apertures (Figure 6.7), custom code automatically calculates two spatial measurements for each bone were calculated: m/M and a/A for the tibia and n/N and c/C for the femur. For the tibia, the position of the aperture centroid is measured as a proportion of the distance from the anterior aspect of the tibial plateau (a) with respect to the total tibial depth (A) as shown in Figure 6.8A, and also as a proportion of the distance from the medial aspect of the tibial plateau (m) with respect to the total width of the tibial plateau (M) as shown in Figure 6.8B. For the femur, the position of the aperture centroid is measured as a proportion of the distance from the distal-most aspect of the lateral condyle (c) with respect to the total diameter of the lateral condyle (C) as shown in Figure 6.9A and also as the proportion of the distance from the posterior-most aspect of the lateral condyle (n) with respect to the apex of the intercondylar notch (N) as demonstrated in Figure 6.9B.

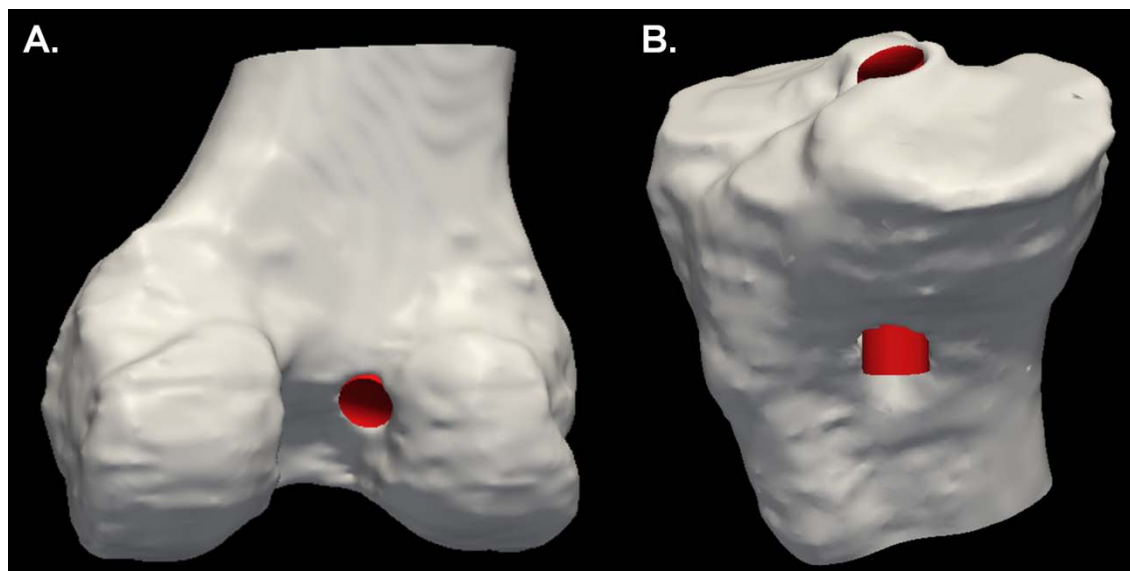


Figure 6.7 The virtual drill bits were cropped to match the tunnel aperture. A) Femur. B) Tibia.

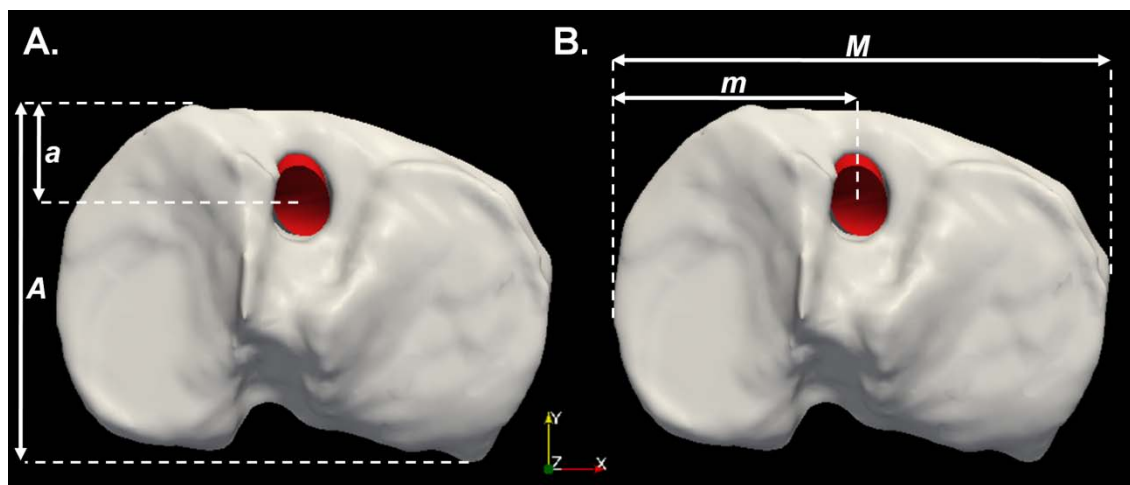


Figure 6.8 Measurements of the tibial plateau. A) A measurement (a/A) of the tunnel aperture centroid based on the anterior-posterior distance of the tibial plateau. B) A measurement (m/M) of the tunnel aperture centroid based on the medial-lateral distance of the tibial plateau.

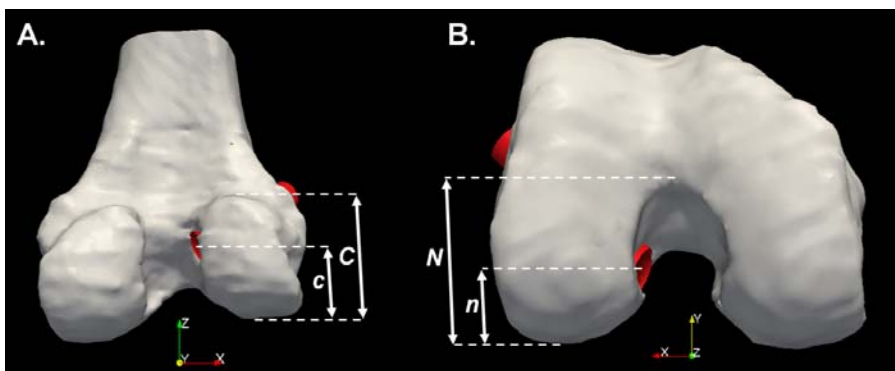


Figure 6.9 Measurements of the lateral femoral condyle. A) A measurement (c/C) of the tunnel aperture centroid based on the diameter of the lateral femoral condyle. B) A measurement (n/N) of the tunnel aperture centroid based on the height of the intercondylar notch.

6.2.3.3 Evaluation Using Digital Phantoms

To validate the angular and spatial measurements, two digital phantoms were created. The angular measurements were validated using 9 virtual drill bits in different orientations as shown in Figure 6.10A. The spatial measurements were validated using 3 virtual drill bits encased in a cube as shown in Figure 6.10B. The resulting angular and spatial measurements were compared to the known values used to generate the digital phantoms.

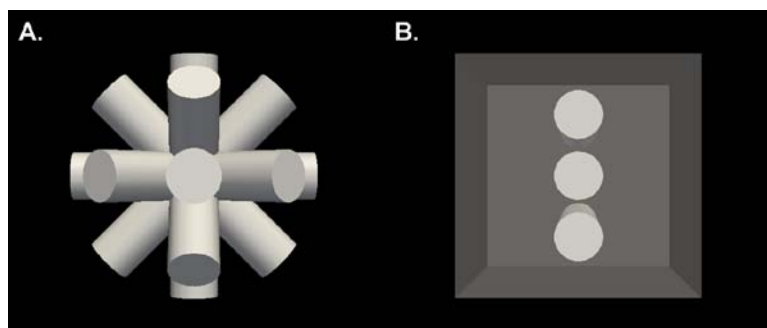


Figure 6.10 Evaluation using digital phantoms. A) Nine virtual drill bits used to test the angular measurements. B) Three virtual drill bits used to test the aperture localization measurements.

6.2.3.4 Evaluation Using Cadaveric Specimens

Ten cadaveric knee joints were collected (4 left and 6 right); each specimen included the full knee joint and a portion of the proximal tibia and distal femur. Prior to scanning, a single bundle ACL reconstruction was performed by a fellowship trained orthopaedic surgeon on each specimen using either the medial portal, transtibial, or two incision techniques. The 10 specimens included four medial portal operations, four transtibial operations, and two two-incision operations from six fellowship trained orthopaedic surgeons. A Siemens Sensation 64 slice CT scanner was used to collect three-dimensional voxel datasets of the knee for each specimen (matrix = 1005x512, FOV = 261mm x 133mm, KVP = 120, Current = 128mA, Exposure = 160mAs) with a 0.26mm in-plane resolution and a 0.75mm slice thickness. Slices spanning the entire specimen were obtained for each dataset.

The CT datasets were resampled to 1.0mm isotropic voxels, and all left knees were mirrored along the x-axis to produce 10 right knees for analysis. The BRAINS2 software was used to manually segment the distal femur and proximal tibia[46]. 3D Slicer was used to generate and smooth surface representations from the manual tracings of the 10 femur surfaces and 10 tibia surfaces.

An average sized femoral and tibial surface were aligned such that the surface coordinate systems corresponded to the physical coordinate system described above. The resulting orientations were verified to match the desired standardized orientation by an experienced orthopaedic surgeon. An Iterative Closest Point surface registration (Figure 6.11) using 100 iterations and 5000 landmarks was used to rigidly align the remaining specimen surfaces to the standardized orientation[108, 204].

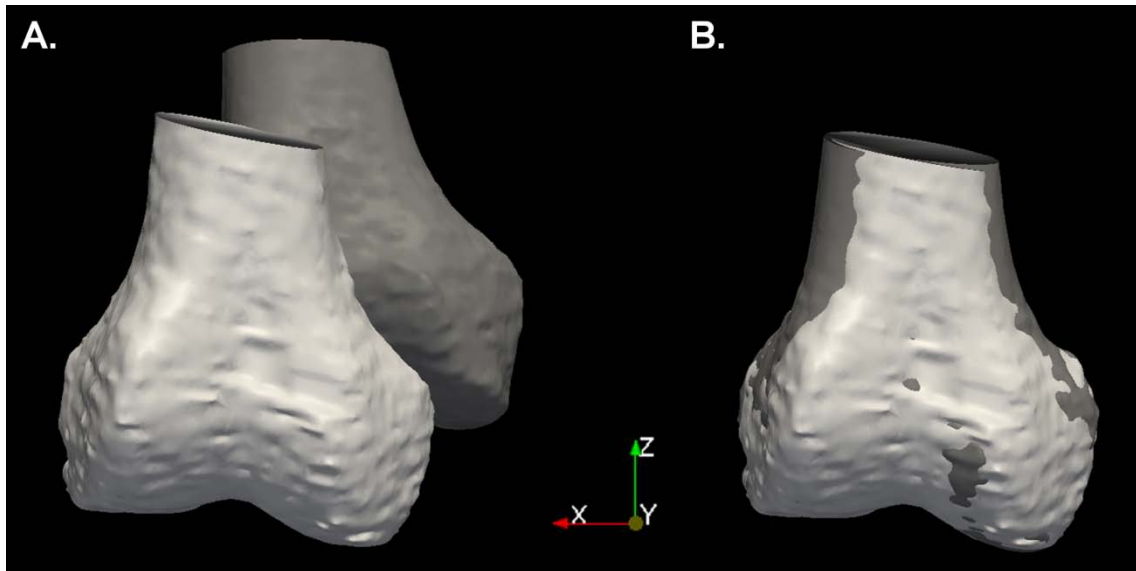


Figure 6.11 Mapping of subjects onto an oriented surface. A) Original bone orientations prior to iterative closest point (ICP) registration. B) Aligned surfaces after ICP registration.

Four users, two biomedical engineers and two orthopaedic residents, used the proposed measurement techniques to evaluate the femoral and tibial ACL tunnels on each of the 10 specimens. Each user was independently trained and performed placement and aperture matching of virtual drill bits into the tibia and femur for the 10 cadaveric datasets on a single occasion. The resulting virtual drill bits were processed using the 3D measurement techniques described above. The reliability of the raters was evaluated by computing the intraclass correlation coefficients for the described spatial and angular measures using SAS[®]. As a test of the robustness of our measurement system, an additional two femur surfaces from a pre-existing dataset with grossly misplaced tunnels (i.e. tunnels that missed the lateral femoral condyle) were also evaluated by a single user.

6.2.4 Results

We have developed a novel three-dimensional measurement system to characterize ACL tunnel placement. The digital phantom evaluation verified the measurement methods by computing angular and spatial values that matched the known values in all cases. The evaluation of the cadaveric specimens for a single user is summarized in Tables 6.1 and 6.2 for the femur and tibia, respectively. The ten specimens showed average values of $\alpha = 60^\circ$, $\beta = 50^\circ$, $\gamma = 56^\circ$, $n/N = 0.54$, and $c/C = 0.68$ for the femur and $\alpha = 77^\circ$, $\beta = 59^\circ$, $\gamma = 34^\circ$, $a/A = 0.49$, and $m/M = 0.46$ for the tibia. The intraclass correlation coefficient was calculated for the four users and found to range from 0.95 to 0.99 for the femoral and tibial measurements (Table 6.3). Two grossly misplaced femoral tunnels were successfully evaluated and can be seen in Figure 6.12.

Table 6.1 Femoral tunnel and aperture location measurements from 10 CT datasets.

Specimen	α ($^\circ$)	β ($^\circ$)	γ ($^\circ$)	n/N	c/C
1	65	53	46	0.53	0.68
2	58	44	62	0.44	0.70
3	62	28	84	0.42	0.63
4	62	49	52	0.61	0.58
5	74	49	44	0.58	0.70
6	30	64	74	0.53	0.79
7	55	55	53	0.49	0.67
8	69	46	50	0.66	0.84
9	74	56	37	0.59	0.55
10	55	52	55	0.55	0.71
Average	60	50	56	0.54	0.68
Standard Deviation	13	9	14	0.09	0.07

Table 6.2 Tibial tunnel and aperture location measurements from 10 CT datasets.

Specimen	α (°)	β (°)	γ (°)	a/A	m/M
1	75	62	31	0.51	0.49
2	80	61	30	0.51	0.41
3	90	41	48	0.46	0.45
4	75	53	39	0.41	0.46
5	76	63	30	0.58	0.44
6	76	65	28	0.44	0.46
7	78	62	30	0.46	0.46
8	75	64	30	0.55	0.45
9	80	56	35	0.47	0.48
10	68	62	35	0.54	0.47
Average	77	59	34	0.49	0.46
Standard Deviation	6	7	6	0.05	0.02

Table 6.3 Intraclass correlation coefficients for 4 trained users for each measurement.

Measurement	Femur	Tibia
α	0.99	0.98
β	0.99	0.99
γ	0.99	0.98
n/N	0.98	
c/C	0.98	
a/A		0.95
m/M		0.96

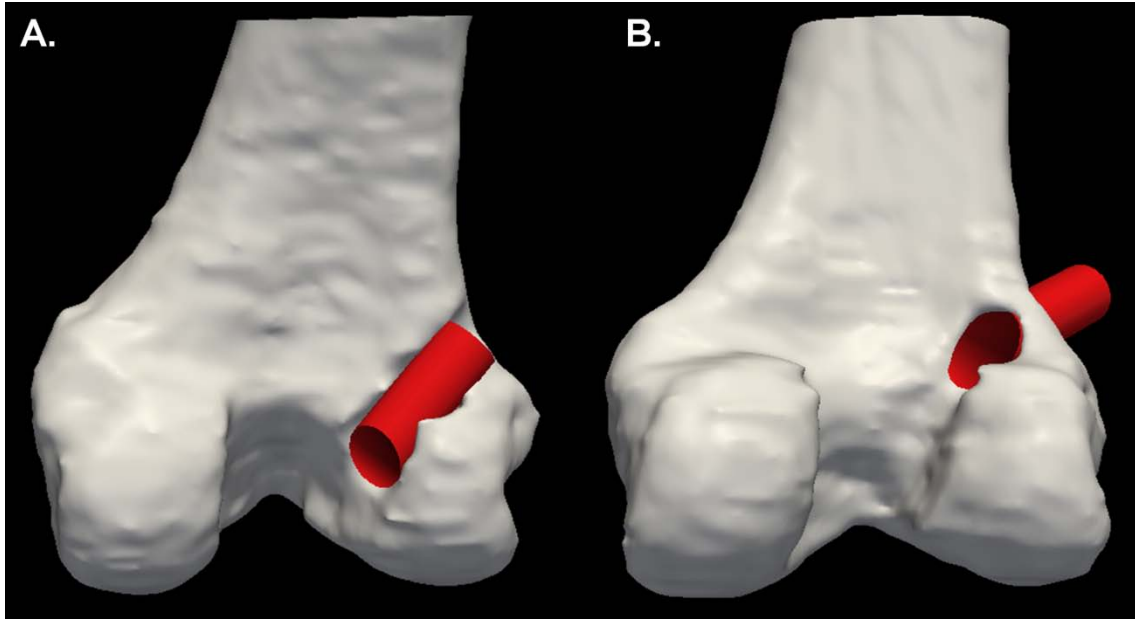


Figure 6.12 Two examples of grossly misplaced tunnels. A) A case where the femoral drill tunnel penetrated the cortex. B) A case where the femoral drill tunnel missed the lateral condyle.

6.2.5 Discussion

We have presented a surgically oriented tunnel localization system for ACL reconstructions based on estimating the positioning of surgically generated tunnels for the tibia and femur using surface models. Our methods are intentionally designed to be of practical use in the operating theater and provide measurements based on the ESSKA recommendations[123] as well as the new measurements that we have proposed. By establishing a surgically oriented coordinate system, the aperture spatial measurements and the tunnel angular measurements provide a novel three-dimensional method to describe this inherently three-dimensional procedure. In addition, our methods allow for measurement of grossly misplaced tunnels that could be difficult to describe using two-dimensional methods.

Our methods are widely applicable. We have demonstrated their application on single bundle ACL reconstructions including the transtibial, medial portal, and two incision techniques. Simply incorporating a second drill bit would also allow this to be a method of evaluation for double bundle ACL reconstructions. In addition, this method could be used to evaluate PCL reconstruction and other procedures involving bone tunnels for graft placement. Our methods are reliable with intraclass correlation coefficients ranging from 0.95 to 0.99 between four users with both surgical and nonsurgical backgrounds. These high values can be attributed to a small degree of variability between raters in placing the virtual drill bits and a high degree of variability in the tunnel angles themselves.

Blumensaat's line has traditionally been a radiographic landmark important in describing the placement of ACL tunnels in two dimensions. Recently, Forsythe et al.[159] and Kopf et al.[202] have demonstrated the use of three-dimensional surfaces to characterize tunnel locations using quadrants and spatial dimensions based on Blumensaat's line; however, this landmark is difficult to reliably define across all anatomical variants on three-dimensional surfaces. In addition, it is difficult to apply measurements from Blumensaat's line in the operating room. For these reasons, we have chosen to base one of our measurements on the diameter of the lateral femoral condyle, an alternative to Blumensaat's line[123].

Currently, image segmentation may be seen as a limitation of this work; however, we recently developed semi-automated methods that require less than 60 seconds of manual intervention to perform the segmentation[205]. While this study used surfaces generated from CT images, MRI could also be used for surface generation as it is more

commonly obtained for an ACL revision. Surfaces generated from MRI scans would also act as an input to our measurement process.

Our surgically oriented coordinate system does deviate from orientations that have been proposed in the past. With respect to the femur, Grood et al.[206] proposed orienting the Z-axis corresponding to the femoral mechanical axis (partially defined with the femoral head). With respect to the tibia, Grood et al.[206] proposed aligning the Z-axis with the tibial mechanical axis (partially defined with the tibial malleoli). Forsythe et al.[159] and Kopf et al.[202] based their coordinate system on the recommendations from the International Society of Biomechanics and Grood et al[206]. During ACL reconstructions, the femoral head is typically draped and is difficult to reference intraoperatively. In our measurement system, we have aligned the diaphysis of the femur with the Z-axis; this allows measurements to be taken with respect to a portion of the femur directly visible during the procedure. Our X- and Y- axes are defined similarly to that described by Grood et al[206]. For the tibia, instead of orienting with respect to the tibial malleoli, we have oriented the tibia with regards to surface features of the tibial plateau. Overall, our orientations were defined by aligning the femur and tibia with landmarks visible during the operative procedure.

In the future, we hope to apply our methods to evaluate ACL reconstructions and provide a three-dimensional characterization to improve patient outcomes. We also hope to apply our techniques beyond ACL reconstructions to other surgical procedures. Future improvements to our methods will include fully automated segmentation of the tibia and femur, and automated placement of the virtual drill bits into the drill tunnels to foster an

automated measurement system. To promote applicability, we plan to compile our tools into a user-friendly graphical user interface.

In summary, we have presented a surgically oriented three-dimensional method of evaluating tunnel placement/orientation for ACL reconstructions. Our methods are applicable to both the femur and tibia and were based on the measurement recommendations made by the ESSKA[123]. We have demonstrated our methods to be reliable and applicable to multiple techniques of ACL reconstruction. In the future, we will apply these methods to study the effects of multiple factors on the variability of tunnel placement to improve patient outcomes.

6.3 Automatic Virtual Drill Bit Alignment

6.3.1 Abstract

Reconstruction of the anterior cruciate ligament (ACL) is a common orthopaedic procedure that has a surprisingly high rate of revision. Drill tunnel misplacement has been identified as the primary cause of reconstruction failure; the ability to localize drill tunnels in 3D has been a challenge to researchers. In Section 6.2, we described a method of 3D ACL drill tunnel localization that required manual alignment of virtual drill bits. The ability to automatically align drill bits with the tunnel surfaces is desirable to expedite the process and ensure measurement reproducibility. We have developed a method of drill bit alignment that aligns a virtual drill bit with a patient-specific tunnel surface based on the calculation of the tunnel surface's major axis and Laplacian smoothing. We have applied our method to 10 drill tunnel surfaces from the femur and tibia and compared the results to 4 manual alignments and also an iterative closest point (ICP) registration. On average, our alignment method was within 1-1.5° from the average manual alignment, which falls within the range of the standard deviation for the

manual alignments. In the future, we hope to apply these methods to expedite the process of virtual drill bit alignment to evaluate the variability in ACL reconstruction tunnels and improve patient outcomes.

6.3.2 Introduction

The anterior cruciate ligament (ACL) is a commonly injured knee ligament that often requires reconstruction. Up to 40% of ACL reconstructions require revision, with the primary cause of reconstruction failure being tunnel misplacement[125]. The ability to characterize tunnel placement is needed to identify factors that may improve patient outcomes. In Section 6.2, we described a consistent 3D surgeon oriented method of post-operative ACL drill tunnel characterization and in Section 4.4 we described a method of high-throughput surface generation of the femur and tibia. These methods were based on simulating the tunnel creation process with the placement of virtual drill bits within patient-specific surfaces of the post-operative femur and tibia. The methods required the subject femur and tibia surfaces to be oriented with a surgically relevant coordinate system to standardize the measurement procedure. Next, virtual drill bits were manually aligned with the femoral and tibial surfaces, an automated measurement process allowed for an angular description of the virtual drill bits defined by three angles: α , β , and γ . These angles correspond to the virtual drill bit's deviation from the x-, y-, and z- axes of the surgically oriented coordinate system. Additionally, spatial measurements were utilized to characterize the drill tunnel's aperture with respect to surgically relevant surface features: femoral shaft, lateral femoral condyle, and tibial plateau.

The automatic alignment of surface models has been an active research area in developing automated surgical simulation systems. Principal components analysis (PCA) and variations of PCA have been used as a standard of automated 3D model orientation to align a surface with the surface's mathematical major axis[87, 207, 208]. Others have developed efficient systems based on oriented bounding boxes (OBBs) that are also based

on calculating the major axis of given surface and enclosing the surface based on its extents[209, 210]. The ability to align a subject surface based on the alignment of a second, similar surface has also been a research area. Iterative Closest Point (ICP) registration has been mainstay of subject to atlas alignment; it is an iterative algorithm that minimizes the distance between the two point sets[108, 204]. It can be applied as a rigid body transformation (e.g. translation and rotation), which does not affect the original geometry of the subject surface.

The alignment of virtual drill bits in the 3D post-operative ACL drill tunnel characterization system required the user to perform a series of rigid body translations and rotations. Automating this process would help to reduce the amount of time for drill bit alignment, to remove variability between users alignments, and to produce a more fully automated method of ACL tunnel characterization. We hypothesize that a 3D surface representation of the drill tunnels can be used to automatically orient virtual drill bits and obviate the need for manual drill bit alignment.

6.3.3 Materials and Methods

6.3.3.1 Drill Tunnel Surface Generation

The 10 surface representations described in Section 6.2.3.4 were also used in this study. In addition to the surfaces described in Section 6.2.3.4, surface representations were generated and Laplacian smoothed for the femoral drill tunnel and tibial drill tunnel. Figure 6.13 demonstrates the femoral drill tunnel surfaces (Figure 6.13A) and the tibial drill tunnel surfaces (Figure 6.13B). As depicted in Figure 6.13, hardware removal in several cases resulted in non-uniform tunnels.

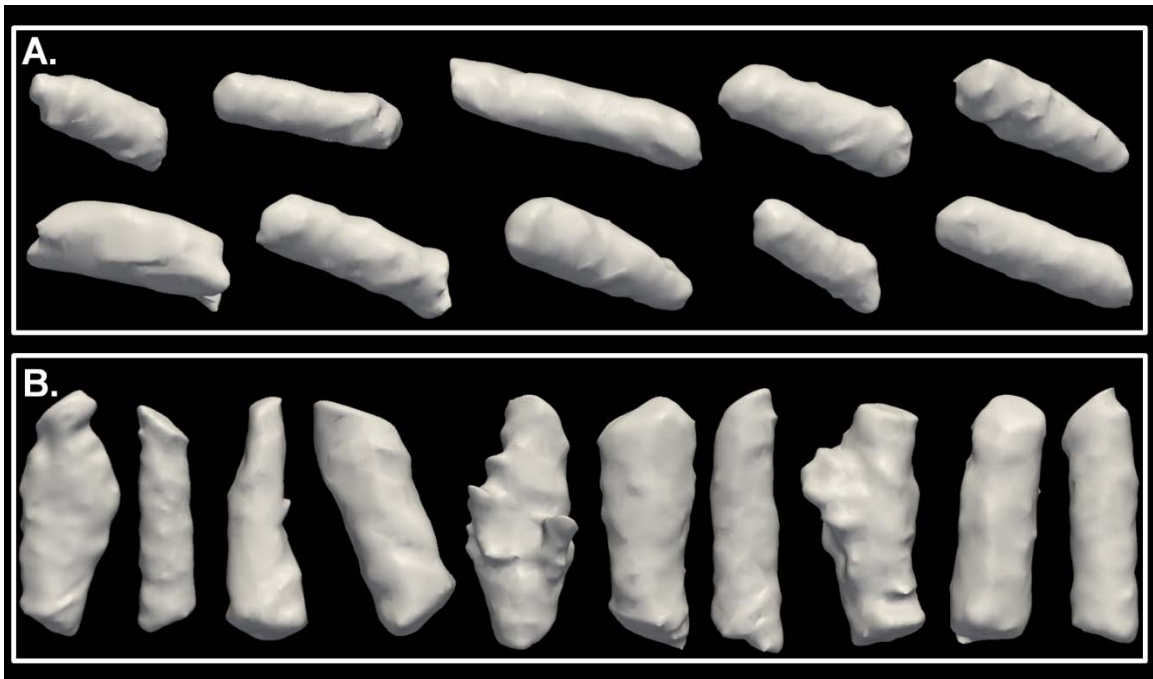


Figure 6.13 Ten surface representations of drill tunnels. A) Femur. B) Tibia.

6.3.3.2 AutoBit Alignment

We have developed a method of automated drill bit alignment, AutoBit, based on Laplacian smoothing and calculation of the major axis of the tunnel surface using OBBs. After creation of the tunnel surfaces, the tunnel surface is Laplacian smoothed to remove local disruptions of the tunnel surface caused by the drilling procedure. We have optimized the amount of smoothing using a convergence study; 100 iterations of smoothing are applied to the femoral tunnel surfaces and 200 iterations of smoothing are applied to the tibial tunnel surfaces. An oriented bounding box is calculated for the tunnel surface and the longest axis is identified[210]. The centroid of the 3D tunnel surface is used to position a virtual drill bit (diameter = 10mm, length = 50mm) along the longest axis of the tunnel's OBB[89]. This procedure is demonstrated in Figure 6.14.

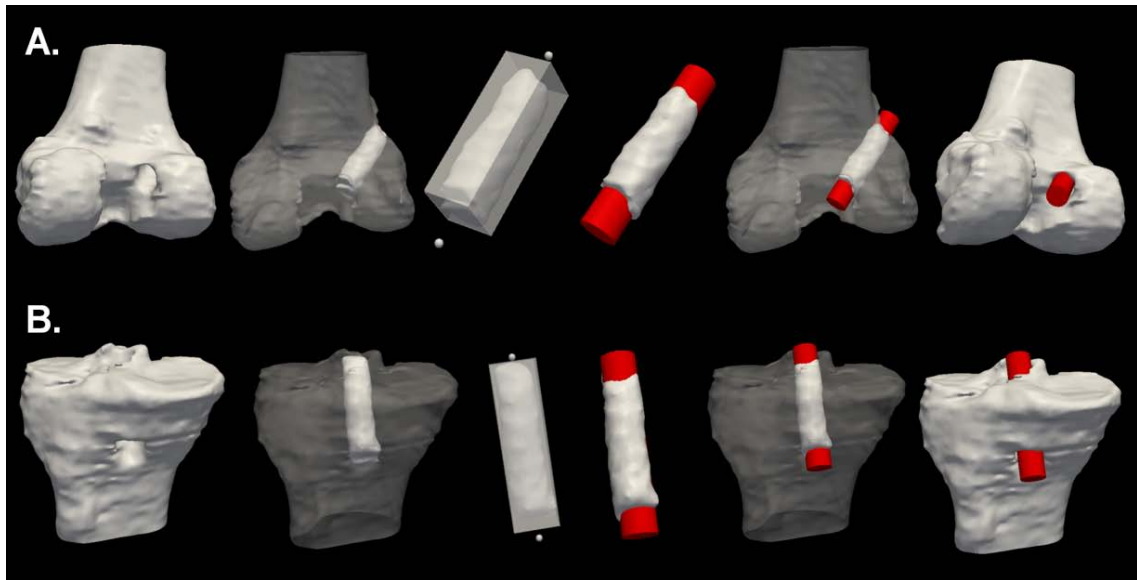


Figure 6.14 The automated drill bit alignment process. This process is demonstrated using a A) femoral tunnel and a B) tibial tunnel. From left to right, the objects are the bone surface, the bone surface highlighting the drill tunnel, the oriented bounding box and major axis (represented by two spheres) for the bone tunnel, the AutoBit aligned drill bit with the tunnel surface, the AutoBit aligned drill bit within the bone surface, and another view of the AutoBit aligned drill bit within the bone surface.

6.3.3.3 Manual Alignment

The manual alignments described in Section 6.2.3.4 were also used in this study.

6.3.3.4 ICP Alignment

As a means of comparison, an iterative closest point (ICP) alignment was also utilized to align a virtual drill bit with the patient-specific tunnel surface[108, 204]. A virtual drill bit with a diameter of 10mm and a length of 50mm was aligned to each of the ten subject drill tunnel surfaces. The ICP alignment involved 100 iterations and 5000 landmarks.

6.3.3.5 Computational Resources

The Visualization Toolkit (VTK) and C++ programming language were used to develop the automated alignment process on an Intel Xeon 2.67 GHz with 8.00 GB of RAM running a 64-bit version of Microsoft Vista operating system. The 3D Slicer software package was used for surface generation. Manual tracings were performed using BRAINS2[46].

6.3.4 Results

Standard descriptive statistics from the four manual alignments for the 10 subjects is demonstrated in Table 6.4. Table 6.5 presents the absolute difference between the average manual alignment and the two automated alignment methods for the femoral and Table 6.6 presents the results for the tibial tunnels. The average absolute difference for the AutoBit alignment for angles α , β , and γ were 0.8° , 1.1° , and 1.3° for the femur and 1.3° , 0.9° , and 1.4° for the tibia. The average absolute difference for the ICP alignment for angles α , β , and γ were 4.5° , 3.6° , and 3.3° for the femur and 1.7° , 2.4° , and 2.2° for the tibia. Figure 6.15 demonstrates a comparison between the AutoBit alignment and the average manual alignment for the femur (Figure 6.15A) and the tibia (Figure 6.15B).

Table 6.4 The average angular measures (α , β , γ) from 4 manual drill bit placements of each of the ten subjects.

Specimen	Femur			Tibia		
	α (°)	β (°)	γ (°)	α (°)	β (°)	γ (°)
1	67.3	52.3	45.3	76.8	58.5	33.5
2	60.0	44.0	60.0	79.3	61.8	29.3
3	62.3	27.3	84.0	89.0	41.5	47.5
4	60.3	50.8	52.3	74.3	53.5	39.3
5	72.5	49.0	44.8	75.8	64.0	29.0
6	31.3	62.0	74.8	77.3	64.8	27.5
7	56.5	54.8	51.3	77.0	60.5	31.8
8	69.5	46.3	49.3	76.3	61.0	32.0
9	72.0	57.0	37.0	80.5	55.8	34.5
10	54.3	52.5	55.5	70.8	62.8	33.0
Overall Average	60.6	49.6	55.4	77.7	58.4	33.7
Average Standard Deviation	1.2	1.1	1.0	1.1	1.4	1.3

Table 6.5 The absolute difference between the average manually aligned drill bits and the automated alignment methods for the femur where ' X_M ' represents the manual alignment, ' X_A ' represents the AutoBit alignment, and ' X_I ' represents the ICP alignment.

Specimen	AutoBit Alignment			ICP Alignment		
	$ \alpha_M - \alpha_A $ (°)	$ \beta_M - \beta_A $ (°)	$ \gamma_M - \gamma_A $ (°)	$ \alpha_M - \alpha_I $ (°)	$ \beta_M - \beta_I $ (°)	$ \gamma_M - \gamma_I $ (°)
1	0.3	0.3	0.8	5.8	0.8	4.3
2	1.0	2.0	1.0	5.0	5.0	0.0
3	1.8	1.3	1.0	4.8	4.3	2.0
4	0.3	0.3	0.8	3.8	5.8	2.8
5	0.5	3.0	2.8	2.5	3.0	3.8
6	0.8	1.0	0.8	5.3	2.0	6.3
7	0.5	0.8	0.8	6.5	5.8	0.3
8	1.5	1.8	2.3	6.5	0.3	3.3
9	0.0	0.0	1.0	0.0	8.0	7.0
10	1.8	0.5	1.5	4.8	1.5	3.5
Overall Average	0.8	1.1	1.3	4.5	3.6	3.3
Average Standard Deviation	0.6	0.9	0.7	2.0	2.5	2.3

Table 6.6 The absolute difference between the average manually aligned drill bits and the automated alignment methods for the tibia where ' X '_M represents the manual alignment, ' X '_A represents the AutoBit alignment, and ' X '_I represents the ICP alignment.

Specimen	AutoBit Alignment			ICP Alignment		
	$ \alpha_M - \alpha_A $ (°)	$ \beta_M - \beta_A $ (°)	$ \gamma_M - \gamma_A $ (°)	$ \alpha_M - \alpha_I $ (°)	$ \beta_M - \beta_I $ (°)	$ \gamma_M - \gamma_I $ (°)
1	2.3	0.5	1.5	5.3	1.5	0.5
2	0.8	1.3	2.3	1.8	1.3	2.3
3	0.0	2.5	2.5	0.0	4.5	4.5
4	1.3	0.5	0.8	3.8	5.5	3.8
5	0.3	0.0	0.0	1.3	1.0	1.0
6	2.3	0.3	1.5	2.3	2.3	1.5
7	0.0	0.5	0.8	0.0	1.5	1.8
8	5.3	1.0	2.0	0.8	1.0	0.0
9	0.5	1.8	2.5	0.5	4.8	5.5
10	0.3	0.3	0.0	1.3	0.3	1.0
Overall Average	1.3	0.9	1.4	1.7	2.4	2.2
Average Standard Deviation	1.6	0.8	1.0	1.7	1.9	1.8

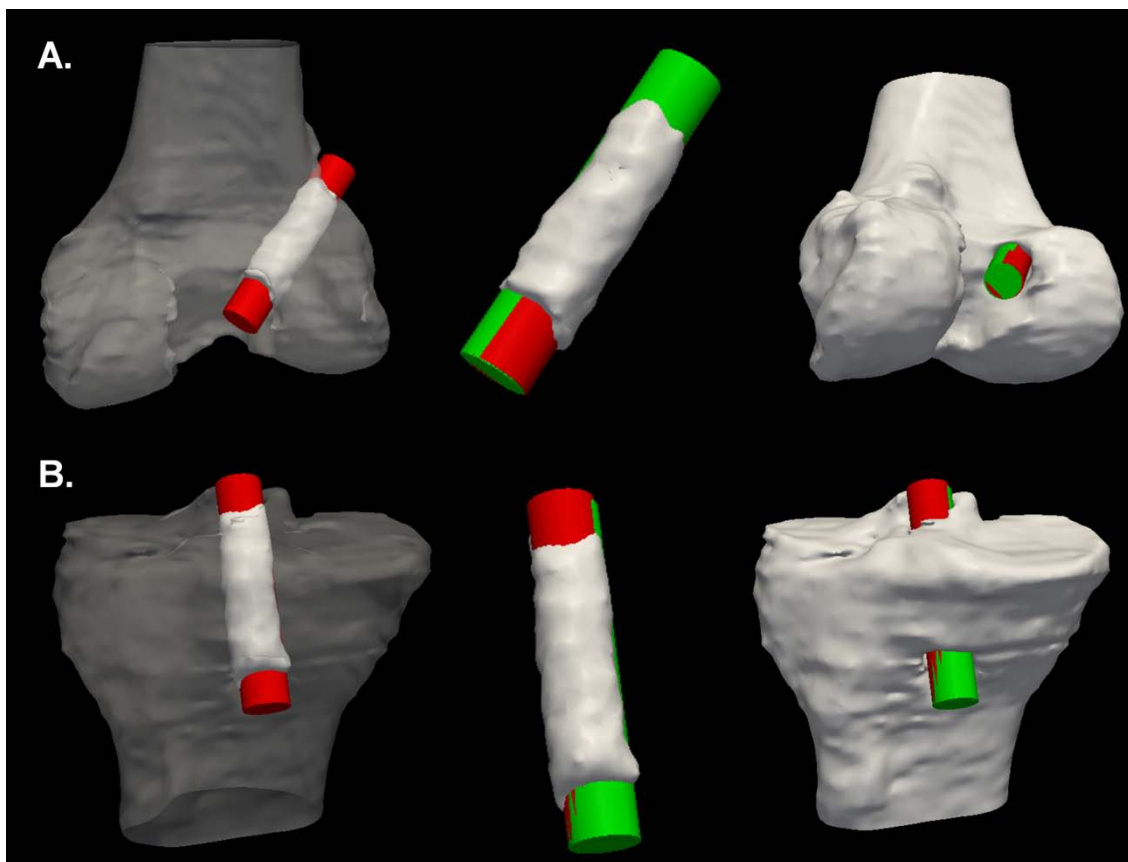


Figure 6.15 A comparison between the AutoBit alignment (red) and the average manually aligned drill bit (green). This is demonstrated for a A) femoral tunnel and a B) tibial tunnel. From left to right, the objects are the AutoBit aligned drill bit within the bone surface, a view of both the AutoBit aligned drill bit and manually aligned drill bit and the bone tunnel surface, and finally the automatically aligned drill bit and the manually aligned drill bit visualized within the bone surface.

6.3.5 Discussion

We have developed a method for automated drill bit alignment that obviates the need for manual alignments for evaluation of ACL reconstruction variability. On average, the AutoBit aligned drill bits are within $1-1.5^\circ$ from the average manual alignment demonstrating the efficacy of our method. The AutoBit method aligned drill bits more accurately than the ICP method when compared to the average manual alignments. The ICP aligned drill bits were within $1.7-4.5^\circ$ from the average manual

alignments. These alignments also had a larger standard deviation than drill bits which were aligned using the AutoBit method.

It should be noted that multiple femoral and tibial specimens contained varying degrees of non-uniformity due to hardware removal in Figure 6.13, which would not be expected in most patient datasets. The amount of Laplacian smoothing we have applied in the AutoBit method has compensated for this non-uniformity and has ultimately yielded alignments very close to the manual alignments.

A single outlier was apparent in the tibial tunnel from Specimen 8 for the AutoBit method. This specimen had a large degree of unilateral noise resulting from removal of hardware in the study. The unilateral nature of the noise offset the definition of the major axis that was defined by the OBB and resulted in a suboptimal alignment. If similar tunnels were generated in other studies, the drill bit orientation could be modified by the user to perfect the alignment. However, the noisy nature of our tunnels was due to the removal of the hardware, which is typically not performed in ACL reconstructions. In vivo datasets would be expected to be more uniform than those where the hardware was removed.

6.3.6 Conclusions

Overall, we have developed an automated method of virtual drill bit alignment for 3D localization of patient-specific arthroscopic drill tunnels. Our method has been evaluated using 20 drill tunnel surfaces of varying levels of surface uniformity and has achieved an average alignment very close to the average manual alignments. In the future, we hope to apply these methods to expedite the process of virtual drill bit alignment necessary to evaluate the variability in ACL reconstruction tunnels and improve patient outcomes.

6.4 Visualization Techniques

6.4.1 Overview

The methods described in Sections 6.2 & 3 primarily describe techniques for nearly automated computation of measurements for quantitative analysis; however, the methods are lacking in terms of large-scale visualization of the data from a qualitative standpoint. Here, we describe two methods of visualization of large-scale data: discrete ACL aperture centroid mapping and ACL tunnel aperture overlap mapping.

6.4.2 Discrete ACL Aperture Centroid Mapping

Discrete ACL Aperture Centroid Mapping allows visualization of the tunnel centroids as individual spheres mapped onto the bone surface. Figure 6.16 demonstrates the process used for mapping the subject tunnel aperture centroids onto the surface of the native femur; the same method was also used for the native tibia. As an initial step, the native femur (Figure 6.16A) from the Human Bone Surface Library described in Section 3.2 was aligned with the atlas surfaces (Figure 6.16B) using ICP registration as described in Section 6.2. This procedure results in a native femur surface aligned to the orientation of the atlas orientation (Figure 6.16C). As described in Section 6.2 & 3, a virtual drill bit was aligned with the postoperative drill tunnel for each given patient and the centroid of the drill tunnel aperture was calculated. A sphere with a radius of 1mm was used to represent the tunnel aperture centroid for each subject (Figure 6.16D).

Due to anatomic variability between subjects, the native femur surface was not an exact match to each of the subject surface. Thus, a closest-point projection (Figure 6.16E) was used to map the center of the spherical representations of the subject-specific tunnel aperture centroids onto the surface of the native femur (Figure 6.16F). With this final step, a discrete representation of a single ACL reconstruction was visualized on a non-operative bone surface for qualitative evaluation. In the case of a large-scale study, this process can be performed for all subjects in the study and multiple spheres can be

visualized simultaneously. If multiple variables were recorded for a given study, the spheres can be grouped according to a given variable and color-coded to allow for qualitative visualization of a large number of datasets on a single bone surface.

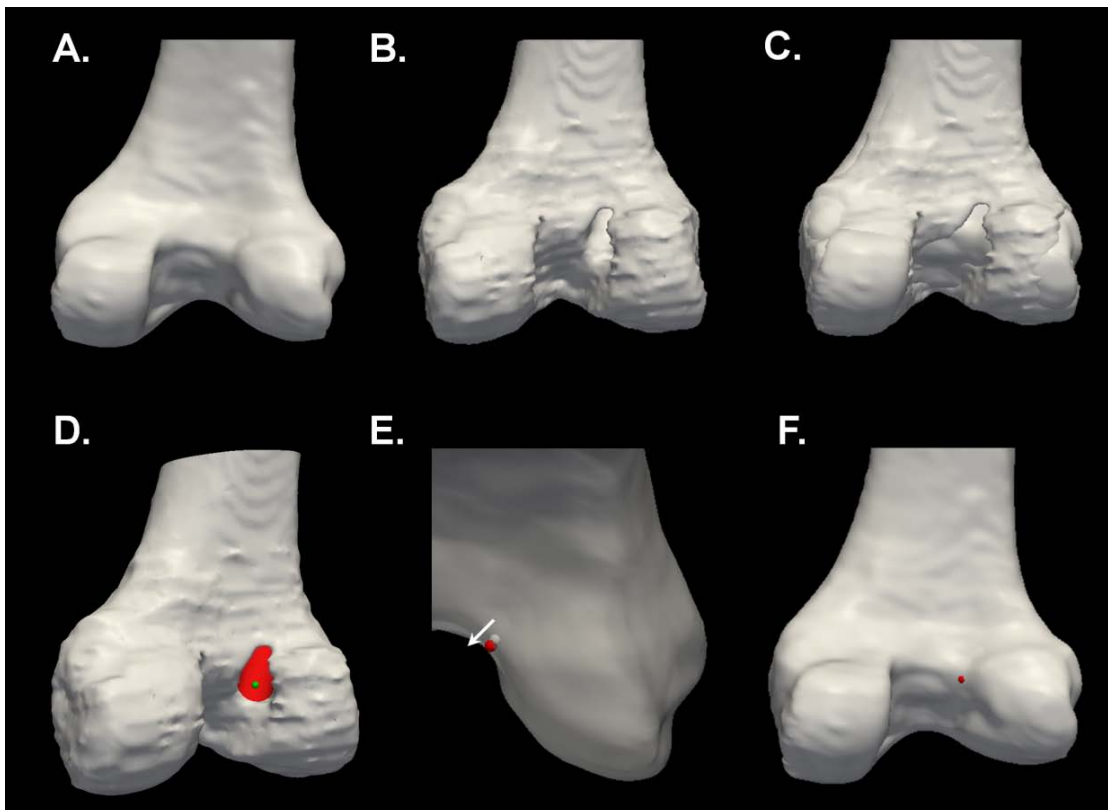


Figure 6.16 The process used for Discrete ACL Aperture Centroid Mapping. A) A native bone surface is selected: the femur. B) The atlas surface is selected. C) The native bone surface is aligned to the atlas. D) A sphere is generated to represent the tunnel aperture centroid that was previously calculated. E) A closest-point projection is used to map the sphere onto the native bone surface. F) The sphere can be visualized on the native bone surface.

6.4.3 ACL Tunnel Aperture Overlap Mapping

Discrete ACL Aperture Centroid Mapping allows for a discrete visualization of the centroid of large datasets; however, it lacks in describing the full tunnel aperture area. As an alternative approach to visualization, ACL Tunnel Aperture Overlap Mapping was

developed. Its methods are visualized in Figure 6.17 using a native femur as an example. These methods act as an extension to the methods described in Section 6.4.2. Instead of generating a sphere with a radius of 1mm (Figure 6.17A), a sphere with a diameter matching the drill bit used in a subject-specific ACL reconstruction (e.g. 10mm) was generated and mapped to the native bone surface (Figure 6.17B). Due to the large size of the sphere, visualization of multiple spheres on a native bone surface can be difficult (Figure 6.17C).

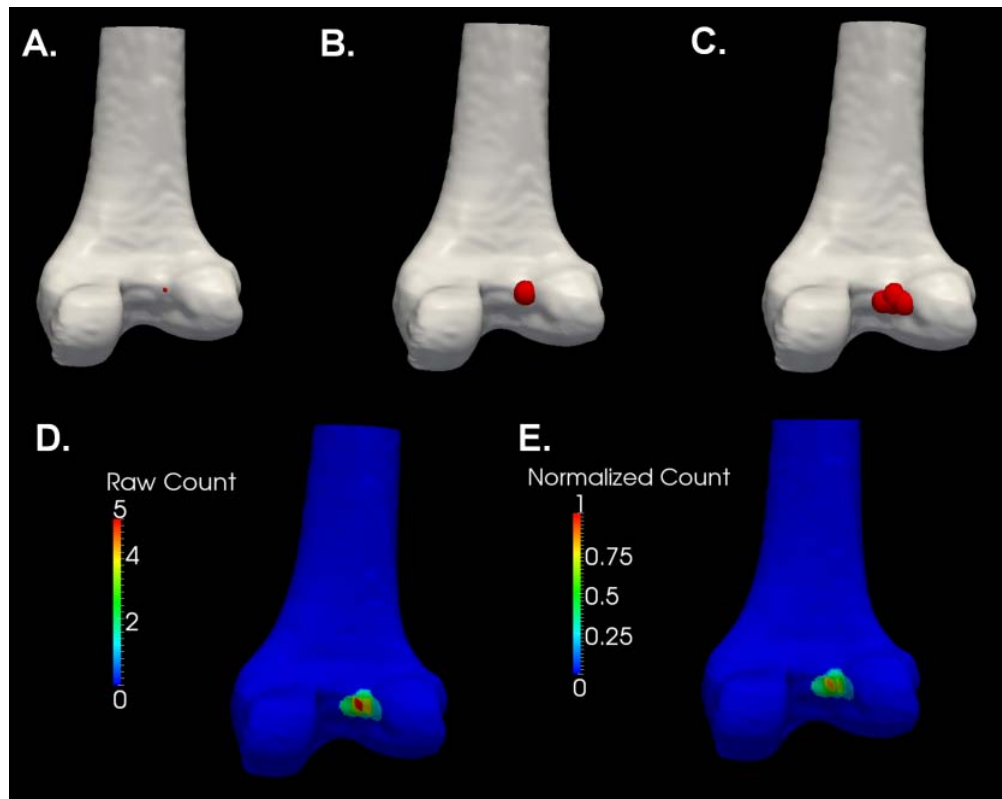


Figure 6.17 The process used for ACL Tunnel Aperture Overlap Mapping. A) A small sphere from the Discrete ACL Aperture Centroid Mapping visualization method. B) The sphere bound to the native surface is enlarged on a subject specific basis to match the size of the drill bit used for the ACL reconstruction. C) Multiple large spheres represented simultaneously are difficult to visualize. D) The number of times a bone surface point is encapsulated in a sphere can be used to color code the surface. E) The color scale is normalized by dividing the point “count” data by the total number of spheres considered to give a 0 to 1 scale.

Since the center of the sphere was bound to the surface, points on the surface of the native bone surface are encapsulated within the sphere. Using an iterative procedure, the number of times a surface point was encapsulated by spheres was recorded for each surface point; this point “count” data can be represented using different colors on the surface (Figure 6.17D). Regions of the bone surface that are more frequently contained within a drill tunnel aperture are represented by red, while regions less frequently contained are represented by blue. Due to variability in the number of subjects in different studies, a normalization of the color scale was necessary. The point “count” data was simply divided by the total number of spheres and the scale was reassigned to values ranging from 0 (blue) to 1 (red). The final normalized color scheme (Figure 6.17E) can be used to compare different variables in an experiment based on different groupings of spherical representations of the tunnel aperture (i.e. surgical technique and level of surgical experience).

6.4.4 Conclusions

Both methods offer a unique qualitative means of visualizing large-scale studies of ACL reconstruction. The Discrete ACL Aperture Centroid Mapping allows for visualization of a multiple variables by color coding data on a single surface. The ACL Tunnel Aperture Overlap Mapping allows for a more continuous representation of the entire ACL tunnel aperture. A limitation of both techniques is the degree of anatomic variation within the human knee. Since we are mapping all subject data onto a single native bone surface, some anatomic detail may be lost from the individual subjects when looking at the data on a large-scale. However, the quantitative measurements described in Section 6.2 preserve individual anatomic features relevant to the procedure. Overall, these two novel visualization techniques allow for easy qualitative visualization of our data on a large-scale.

6.5 Multicenter Orthopaedic Outcomes Network Datasets

The Multicenter Orthopaedic Outcomes Network (MOON) is collaboration of seven institutions (Ohio State University, Vanderbilt University, The University of Iowa, Cleveland Clinic Foundation, Washington University St. Louis, Hospital for Special Surgery, and the University of Colorado) that aims to evaluate patient outcomes from orthopaedic surgical procedures such as ACL reconstructions. We are involved with two studies investigating the variability in tunnel placement in ACL reconstructions: a cadaver study and a patient study. The tools developed herein were used to evaluate these datasets.

The cadaver study involved 72 cadaveric knee joints (37 left and 35 right); each specimen included the full knee joint and a portion of the proximal tibia and distal femur sawed off along the diaphysis of the bone. Twelve orthopaedic surgeons were recruited including six experienced surgeons (>10 years in practice) and six surgeons that were new in practice (<10 years in practice). Three, single-bundle ACL reconstruction techniques were utilized in the study: medial portal, transtibial, and two-incision. Four surgeons (two experienced, and two new in practice) performed a single technique on 24 of the knee specimens (6 specimens per surgeon). The variables involved in the cadaveric study are summarized in Table 6.7.

When all ACL reconstructions were performed, the specimens were frozen and later thawed for imaging. A Siemens Sensation 64 slice CT scanner was used to collect three-dimensional voxel datasets of the knee for each specimen (matrix = 1005x512, FOV = 261mm x 133mm, KVP = 120, Current = 128mA, Exposure = 160mAs) with a 0.26mm in-plane resolution and a 0.75mm slice thickness. Slices spanning the entire specimen were obtained for each dataset with the specimen oriented in anatomical position. Three-dimensional surface representations for each of the 72 cadaveric datasets were generated using the techniques discussed in Chapter 4. Figure 6.18 demonstrates the surface representations for the cadaver dataset.

Table 6.7 A summary of the variables from the cadaver study organized by surgeon.

Surgeon	Technique	Experience Level	Number of Subjects
1	Medial Portal	Young	6
2	Medial Portal	Young	5
3	Transtibial	Young	5
4	Transtibial	Young	6
5	Two Incision	Young	5
6	Two Incision	Young	5
7	Medial Portal	Experienced	5
8	Medial Portal	Experienced	6
9	Transtibial	Experienced	6
10	Transtibial	Experienced	6
11	Two Incision	Experienced	6
12	Two Incision	Experienced	6

Table 6.8 A summary of the variables from the patient study organized by surgeon.

Surgeon	Technique	Experience Level	Number of Subjects
1	Medial Portal	Young	7
2	Medial Portal	Young	10
3	Medial Portal	Young	10
4	Medial Portal	Experienced	10
5	Medial Portal	Experienced	10
6	Medial Portal	Experienced	11
7	Transtibial	Experienced	10
8	Two Incision	Experienced	10

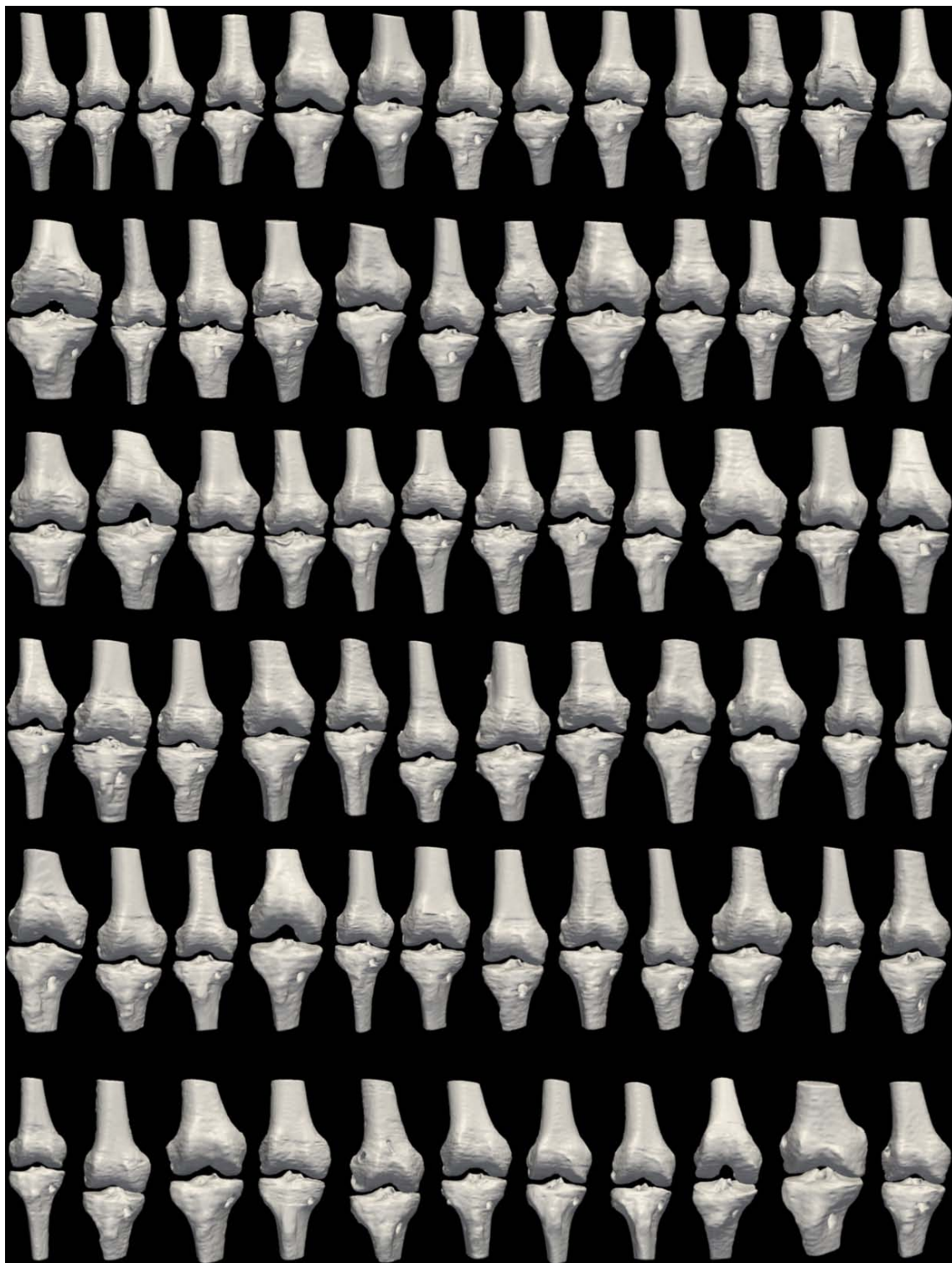


Figure 6.18 The 72 cadaveric knee surface representations generated from CT datasets.

The patient study involved 78 patient knee datasets (44 left and 34 right) from four institutions: The University of Iowa, Washington University, Cleveland Clinic, and the University of Colorado. Eight orthopaedic surgeons were recruited including five experienced surgeons and three surgeons that were new in practice. Three, single-bundle ACL reconstruction techniques were utilized in the study: medial portal, transtibial, and two-incision. Six surgeons (three experienced, and three new in practice) performed medial portal ACL reconstructions; a single surgeon performed a transtibial and a two-incision ACL reconstruction.

After the surgical procedure, each of the patients was scanned using the institution's CT scanner and the institution's clinical scanning protocol. Six of the ten surgeons contributed 10 patient CT datasets; one surgeon provided 11 CT datasets and another 7 CT datasets. The variables involved in this patient study are summarized in Table 6.8. Three-dimensional surface representations for each of the 78 patient datasets were generated using the techniques discussed in Chapter 4. Figure 6.19 demonstrates the surface representations for the patient dataset.

As previously described in Chapter 4, a resampling procedure to generate 1.0mm isotropic voxels was applied to both the cadaveric and patient datasets. The resampled data for the 150 knee CT datasets involved the evaluation of 33,908 axial slices of data which is equivalent to approximately 124,000 axial slices of the raw data. The automated techniques were used as a first pass at the data, and manual editing was used as a means to generate the most perfect segmentations possible. With surface representations generated for the 150 CT datasets, the measurement techniques developed in Chapter 6.2 – 6.4 were applied and a statistical analysis of the results are presented in the following sections.

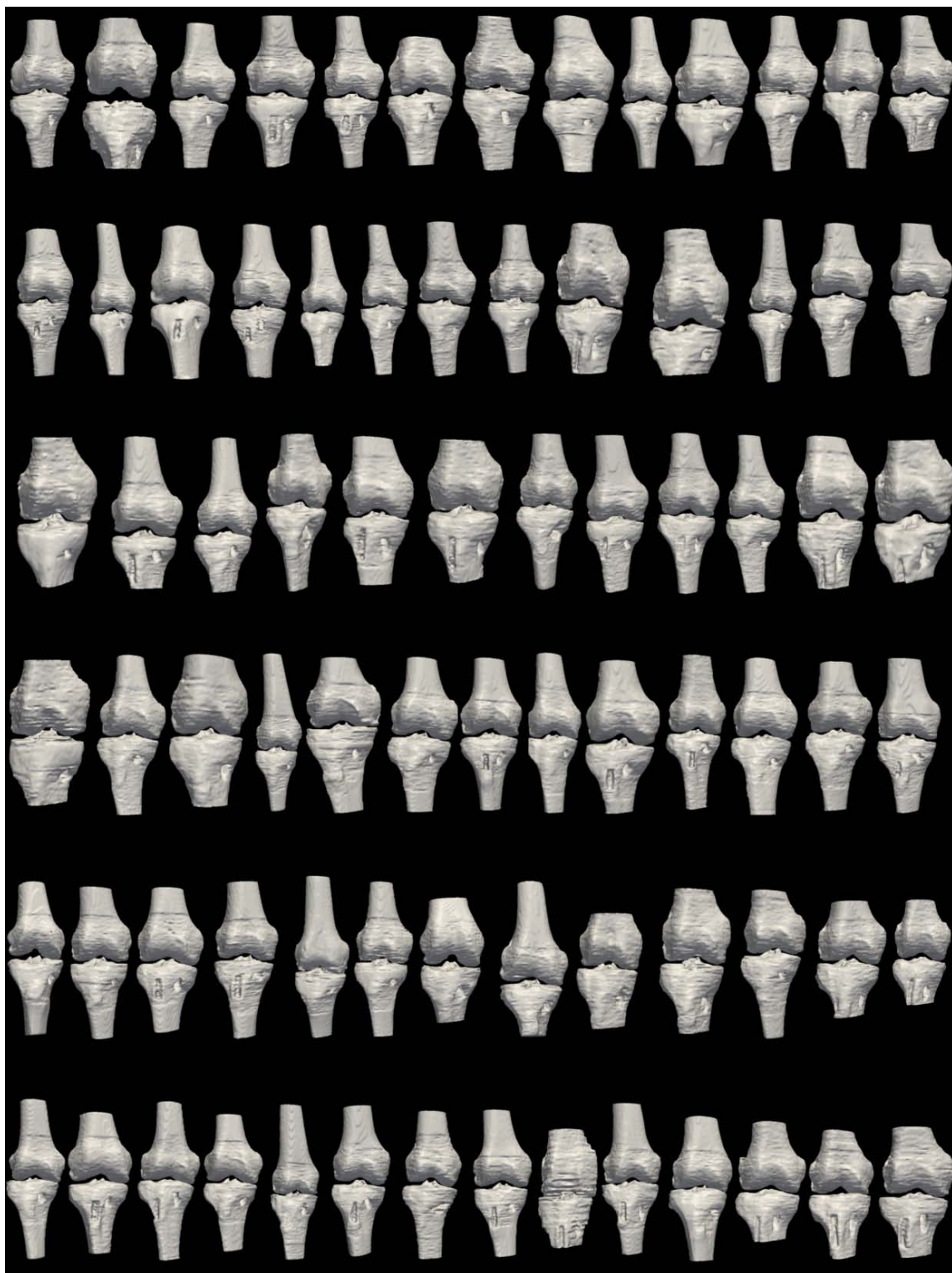


Figure 6.19 The 78 patient knee surface representations generated from CT datasets.

6.6 Analysis of the MOON Datasets

6.6.1 Moon Dataset Goals

The Multicenter Orthopaedic Outcomes Network (MOON) designed the cadaver and patient studies with specific aims to investigate ACL graft placement variability. The cadaver dataset was designed to investigate surgical technique and level of surgeon experience with respect to graft placement. The patient dataset was designed to address whether there was a difference between surgeons in ACL tunnel placement. By grouping different variables from the studies and using our variety of analysis methods, we hope to identify patterns that could act as gateway to future investigations.

6.6.2 Analysis Methods

6.6.2.1 Standard Descriptive Statistics

Standard descriptive statistics were calculated using Microsoft Excel[®] for each of the five measurements (three angular and two spatial measurements) made on each ACL tunnel. Each of the study's variables was also considered in these calculations; tables describing these calculations are provided to complement our discussion in the text. Appendix Tables C.1, C.2, C.9, C.10 provide the overall standard descriptive statistics for both MOON datasets. Appendix Tables C.1.3 and C.1.4 provide a summary of the standard descriptive statistics of the cadaver dataset with respect to surgical technique. Appendix Tables C.5, C.6, C.7, C.8 provide a summary of the standard descriptive statistics of the cadaver dataset with respect to level of surgeon experience. Appendix Tables C.11 and C.12 provide a summary of the standard descriptive statistics of the patient dataset with respect to operating surgeon. To help simultaneously quantitatively visualize the dataset, scatter plots were created in Microsoft Excel[®] for each measurement for the cadaver and patient datasets. Appendix Figures C.1, C.2, C.3, C.4,

C.17, C.18, C.19, C.20 provide overall scatter plot representations for both MOON datasets.

Box and whisker plots were created using Minitab[®] to help visualize subsets of the larger datasets organized by a specific variable for the study. Within the box and whisker plots, the line in the box represents the median of the dataset. The box itself represents the second and third quartiles of the data, while the whiskers represent the distribution of the data within two standard deviations from the median. In addition, outliers from the dataset are represented by asterisks. Box and whisker plots for comparisons that were statistically significant are provided in the text; box and whisker plots for comparisons that were not statistically significant are provided in Appendix Section C.

6.6.2.2 Moon Dataset Visualization

To accompany the standard descriptive statistics and graphical representations, the methods described in Section 6.4.2 & 6.4.3 were used to visualize the MOON dataset. Appendix Figures C.21 and C.25 provide overall discrete sphere representations for both MOON datasets. Appendix Figures C.26 and C.31 provide overall tunnel aperture overlap maps for both MOON datasets.

6.6.2.3 Statistical Methods

To address each of the specific study goals, statistical analysis was performed using SAS[®] on each of the five measurements (three angular and two spatial measurements). Data normality was tested using the Shapiro-Wilk test for normality. For the study investigating surgical technique, a general linear model (GLM) with a post-hoc Tukey test was used. To investigate the two levels of surgical experience (experienced and new to practice) when the data was normal, a t-test was performed using the folded F method to test for equality of variance. If the data was not normal for surgical experience and surgical technique and also in the case of investigating the difference between

surgeons, a Wilcoxon Rank Sum test followed by a Kruskal Wallis test was applied. The results from our statistical analysis are presented in the following sections.

6.6.3 Surgical Technique Results

The cadaver dataset was designed to investigate whether a difference existed between tunnel placements based on surgical technique. Three surgical techniques were investigated: medial portal (MP), transtibial (TT), and two incision (TI). Standard descriptive statistics for both the cadaver and patient datasets were evaluated for comparison purposes. Figures 6.20 and 6.21 provide discrete sphere representations for the surgical techniques in the MOON cadaver dataset. Appendix Figures C.27 provide tunnel aperture overlap maps for the surgical techniques in the MOON cadaver dataset. Statistical testing was performed only on the cadaver dataset due to sample size. The Shapiro-Wilk test for normality demonstrated that the datasets were normally distributed with the exception of angle γ for the cadaver dataset. The null hypothesis was that no difference existed between surgical techniques in ACL reconstruction tunnel placement for the five measurements for each bone that was tested.

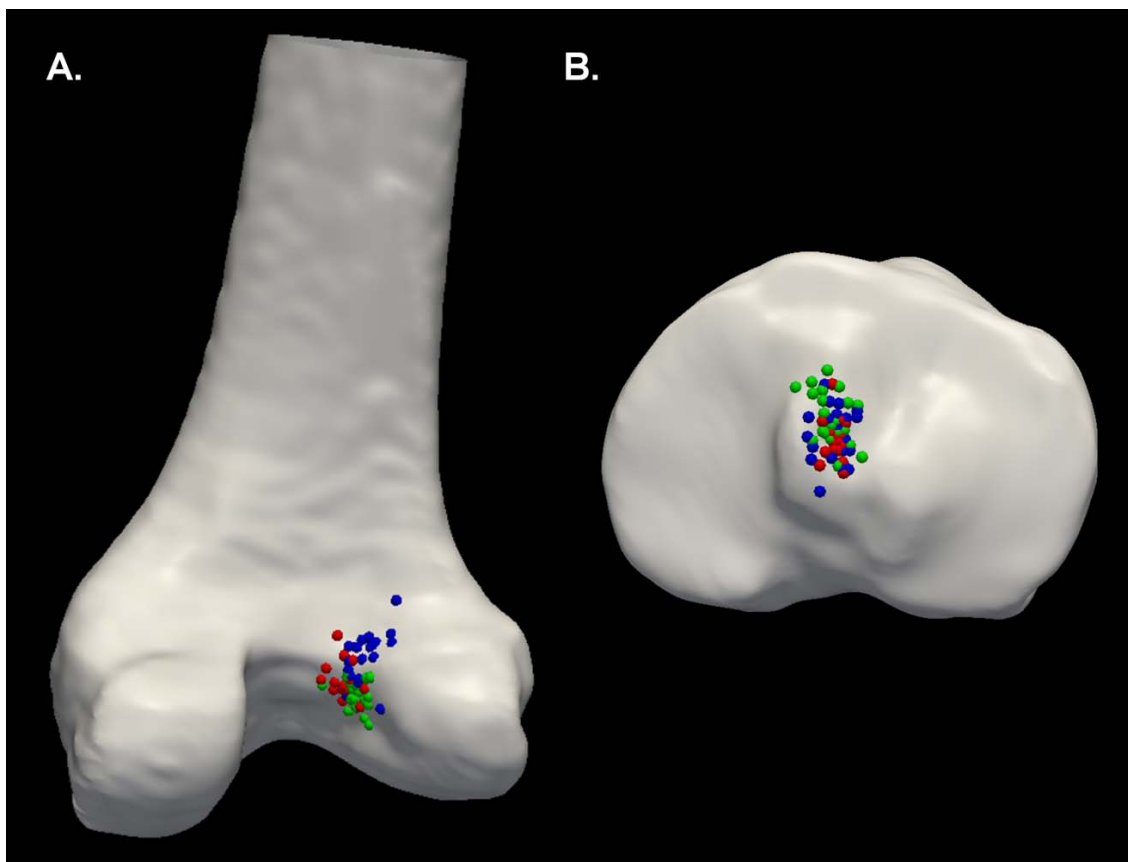


Figure 6.20 A color coded discrete sphere representation of the A) femur and B) tibia for the cadaver dataset organized by surgical technique: medial portal (green), transtibial (red), and two incision (blue).



Figure 6.21 Discrete sphere representations of the femur (3 views) and the tibia for the cadaver dataset organized by the technique used for the ACL reconstruction.

6.6.3.1 Femoral ACL Tunnel

6.6.3.1.1 Angle α

The cadaver dataset showed a difference of $\sim 20^\circ$ between the averages of the three methods. The order of increasing angle α for the three techniques was TI, MP, and TT. This suggests that on average the TI technique places femoral tunnels more horizontally with respect to the surgically oriented coordinate system, while the TT technique placed the tunnels more vertically. The MP technique average falls between the TT and TI techniques. The patient dataset angle α averages agreed with these results.

Statistical testing showed a significant difference (p-value < 0.0001) between the three surgical techniques with respect to femoral angle α . Post-hoc Tukey testing showed the difference to exist between TT and MP as well as between TT and TI. Figure 6.22 demonstrates the box and whisker plot for this comparison.

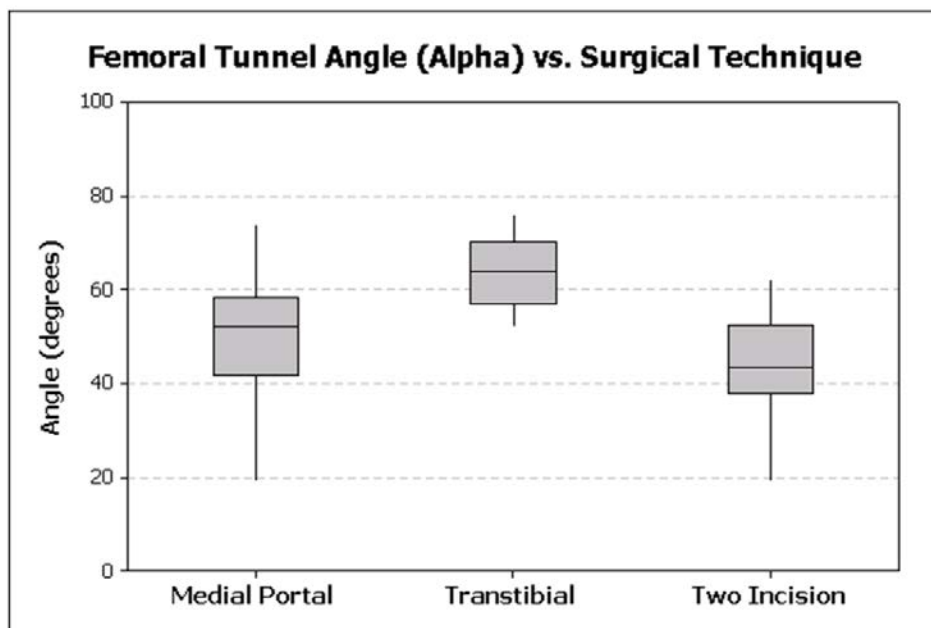


Figure 6.22 A box and whisker representation of the cadaver dataset's femoral tunnel angle α organized by ACL reconstruction technique.

6.6.3.1.2 Angle β

The cadaver dataset showed a difference of $\sim 10^\circ$ between the averages of the three methods. The order of increasing angle β for the three techniques was TI, TT, and MP. This suggests that on average the TI technique places femoral tunnels more horizontally with respect to the surgically oriented coordinate system, while the MP and TT techniques similarly placed the tunnels more vertically. The patient dataset angle β averages agreed with these results.

Statistical testing showed a significant difference (p-value < 0.003) between the three surgical techniques with respect to femoral angle β . Post-hoc Tukey testing showed the difference to exist between MP and TI as well as between TT and TI. Figure 6.23 demonstrates the box and whisker plot for this comparison.

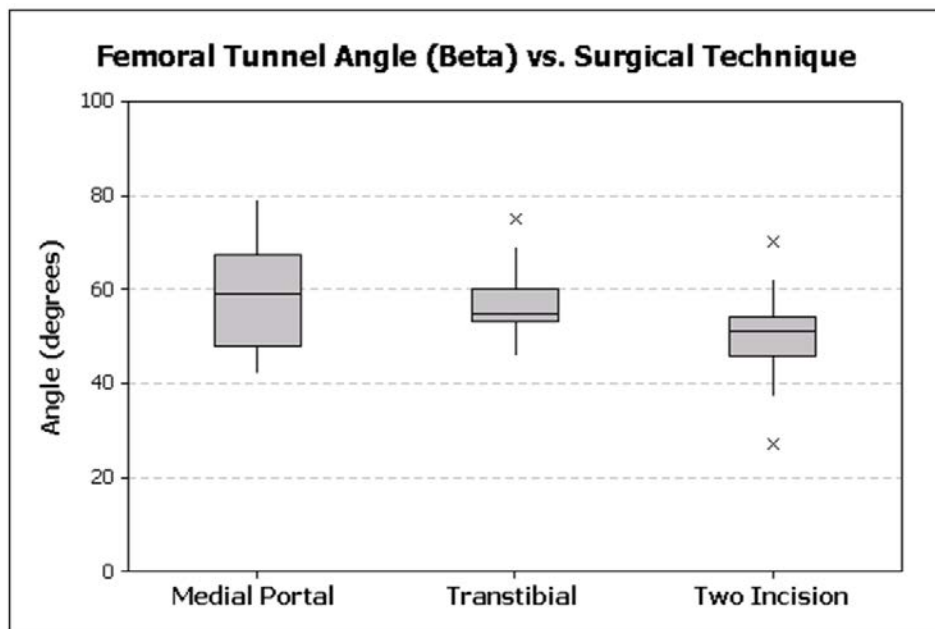


Figure 6.23 A box and whisker representation of the cadaver dataset's femoral tunnel angle β organized by ACL reconstruction technique.

6.6.3.1.3 Angle γ

The cadaver dataset showed a difference of $\sim 30^\circ$ between the averages of the three methods. The order of increasing angle γ for the three techniques was TT, MP, and TI. This suggests that on average the TT technique places femoral tunnels more vertically with respect to the surgically oriented coordinate system, while the TI technique placed the tunnels more horizontally. The MP technique average falls between the TT and TI technique on average. The patient dataset angle γ averages showed the TI averages to be more horizontally placed, while the MP and TT averages were similarly more vertically placed.

Nonparametric statistical testing showed a significant difference (p-value < 0.0001) between the three surgical techniques with respect to femoral angle γ . Figure 6.24 demonstrates the box and whisker plot for this comparison.

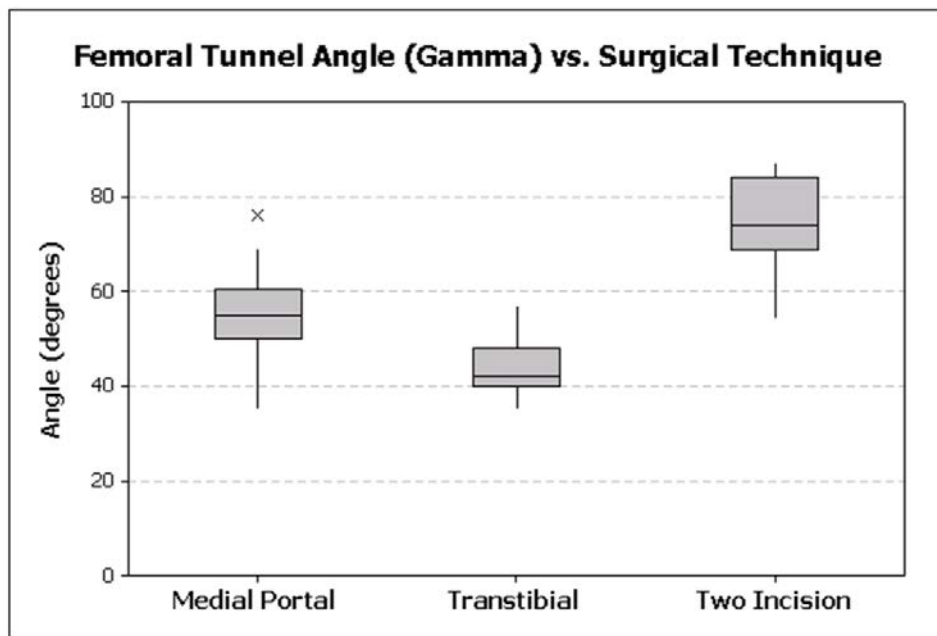


Figure 6.24 A box and whisker representation of the cadaver dataset's femoral tunnel angle γ organized by ACL reconstruction technique.

6.6.3.1.4 Proportional Position Measure c/C

The cadaver dataset showed a difference of ~14% between the averages of the three methods. The order of increasing proportional position measure c/C for the three techniques was MP, TT, and TI. This suggests that on average the MP technique places the tunnel aperture more anterior on the lateral femoral condyle with respect to the “Notch View” of the femur, while the TI technique places the tunnel aperture more posterior on the lateral femoral condyle. The TT technique average falls between the MP and TI techniques. The patient dataset proportional position measure c/C averages agreed with these results.

Statistical testing showed a significant difference (p -value < 0.0001) between the three surgical techniques with respect to femoral proportional position measure c/C . Post-hoc Tukey testing showed the difference to exist between MP and TI as well as between TT and TI. Figure 6.25 demonstrates the box and whisker plot for this comparison.

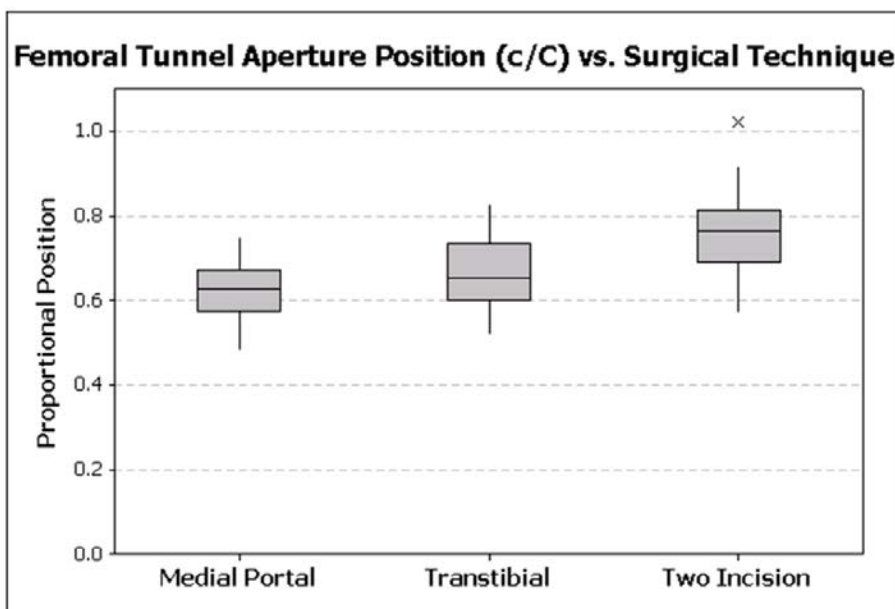


Figure 6.25 A box and whisker representation of the cadaver dataset’s femoral tunnel aperture position measure c/C organized by ACL reconstruction technique.

6.6.3.1.5 Proportional Position Measure n/N

The cadaver dataset showed a difference of ~4% between the averages of the three methods. The order of increasing proportional position measure n/N for the three techniques was MP, TI, and TT. This suggests that on average the MP technique places the tunnel aperture lower in the intercondylar notch of the femur, while the TT technique places the tunnel aperture higher in the intercondylar notch of the femur. The TI technique average falls between the MP and TT techniques. The patient dataset showed the TI technique's average to be less than the MP and TT techniques for the n/N positional measure. A statistically significant difference was not found between the three techniques for femoral proportional position measure n/N . Appendix Figure C.5 demonstrates the box and whisker plot for this comparison.

6.6.3.2 Tibial ACL Tunnel

6.6.3.2.1 Angle α

The cadaver dataset showed a difference of ~10° between the averages of the three methods. The order of increasing angle α for the three techniques was TI, TT, and MP. This suggests that on average the TI technique surgeons place tibial tunnels more horizontally with respect to the surgically oriented coordinate system, while the MP technique surgeons placed the tunnels more vertically. The TT technique average falls between the TT and TI techniques, but closer to the MP technique surgeon's average. The patient dataset angle α averages were within ~10° and were ordered from smallest to largest as follows: MP, TT, and TI.

Statistical testing showed a significant difference (p -value < 0.0001) between the three surgical techniques with respect to tibial angle α . Post-hoc Tukey testing showed the difference to exist between MP and TI as well as between TT and TI. Figure 6.26 demonstrates the box and whisker plot for this comparison.

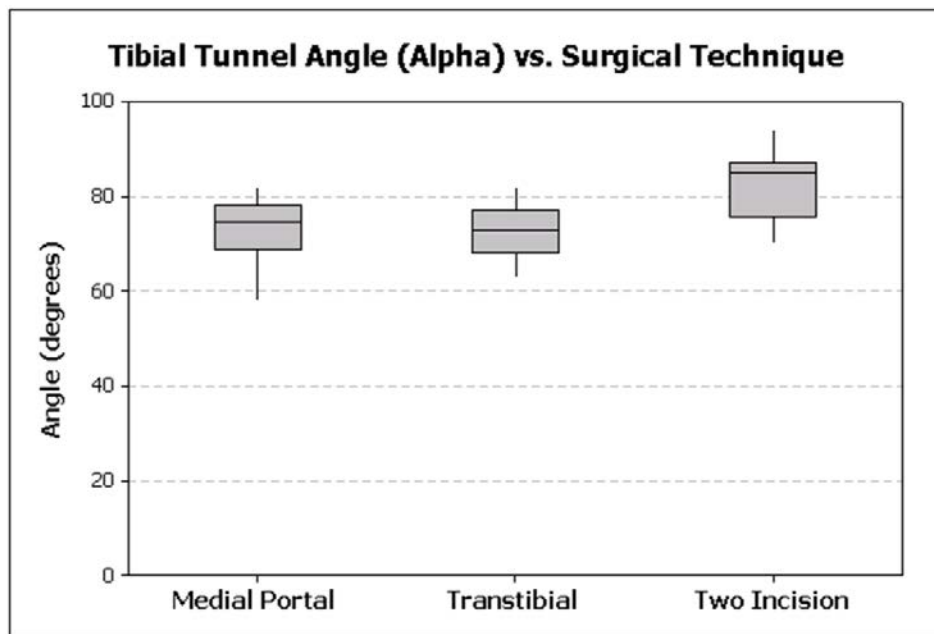


Figure 6.26 A box and whisker representation of the cadaver dataset's tibial tunnel angle α organized by ACL reconstruction technique.

6.6.3.2.2 Angle β

The cadaver dataset showed a difference of $\sim 3^\circ$ between the averages of the three methods. The order of increasing angle β for the three techniques was TI, TT, and MP. This suggests that on average the TI technique surgeons place tibial tunnels more horizontally with respect to the surgically oriented coordinate system, while the MP technique surgeons placed the tunnels more vertically. The TT technique surgeon's average falls between the MP and TI techniques, but closer to the TT technique surgeon's average. The patient dataset angle β averages were within $\sim 10^\circ$ and were ordered from smallest to largest as follows: TT, TI, and MP. A statistically significant difference was not found between the three techniques for tibial angle β . Appendix Figure C.6 demonstrates the box and whisker plot for this comparison.

6.6.3.2.3 Angle γ

The cadaver dataset showed a difference of $\sim 5^\circ$ between the averages of the three methods. The order of increasing angle γ for the three techniques was TI, TT, and MP. This suggests that on average the TI technique surgeons place tibial tunnels more vertically with respect to the surgically oriented coordinate system, while the MP technique surgeons placed the tunnels more horizontally. The TT technique average falls between the MP and TI techniques. The patient dataset angle γ averages agreed with these results. A statistically significant difference was not found between the three techniques for tibial angle γ . Appendix Figure C.7 demonstrates the box and whisker plot for this comparison.

6.6.3.2.4 Proportional Position Measure a/A

The cadaver dataset showed a difference of $\sim 14\%$ between the averages of the three methods. The order of increasing proportional position measure a/A for the three techniques was MP, TI, and TT. This suggests that on average the MP technique surgeons place the tunnel aperture more anterior on the tibial plateau, while the TT technique surgeons place the tunnel aperture more posterior on the tibial plateau. The TI technique surgeon's average falls between the MP and TI techniques. The patient dataset proportional position measure a/A averages agreed with these results.

Statistical testing showed a significant difference (p-value < 0.004) between the three surgical techniques with respect to tibial proportional position measure a/A. Post-hoc Tukey testing showed the difference to exist between the MP and TT. Figure 6.27 demonstrates the box and whisker plot for this comparison.

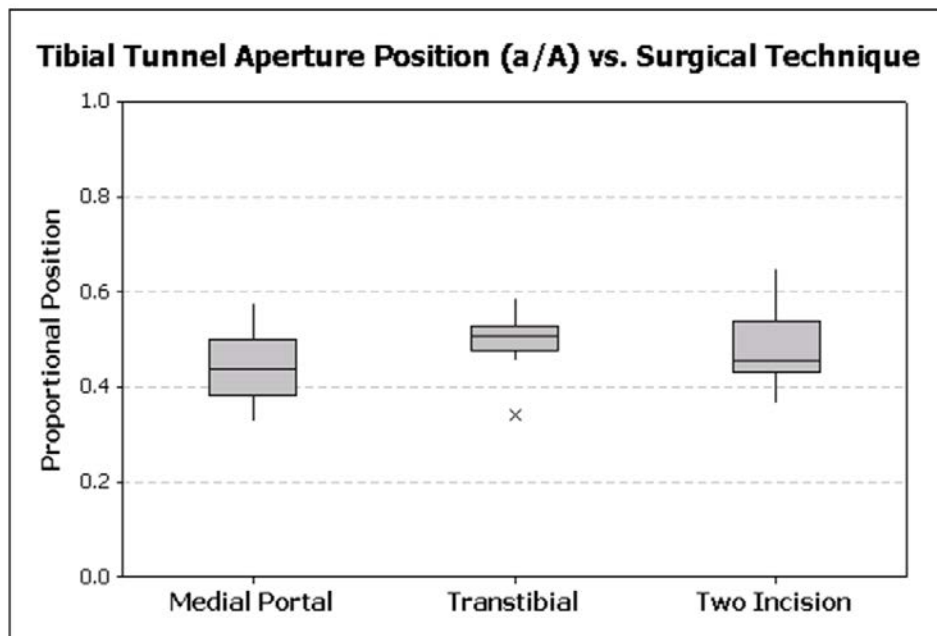


Figure 6.27 A box and whisker representation of the cadaver dataset's tibial tunnel aperture position measure a/A organized by ACL reconstruction technique.

6.6.3.2.5 Proportional Position Measure m/M

The cadaver dataset showed a difference of ~1% between the averages of the three methods. Surgeons from each of the three techniques had nearly the same placement, which suggests that on average all three techniques are placing the tunnel aperture in nearly the same position along the medial-lateral axis. The patient dataset proportional position measure m/M averages agreed with these results. A statistically significant difference was not found between the three techniques for proportional position measure m/M . Appendix Figure C.8 demonstrates the box and whisker plot for this comparison.

6.6.4 Level of Surgical Experience Results

The cadaver dataset was also designed to investigate whether a difference existed between tunnel placements based on the level of experience of the operating surgeon.

Two levels of experience were established: experienced and new to practice. Both groupings contained fellowship trained knee surgeons that regularly performed ACL reconstructions in their surgical practice. Figures 6.28, 6.29, and 6.30 provide discrete sphere representations for each technique and the level of surgeon experience in the MOON cadaver dataset. Additional views of the femur using sphere representations are provided in Appendix C.22, C.23, and C.24. Appendix Figures C.28, C.29, and C.30 provide tunnel aperture overlap maps for each technique and the level of surgeon experience in the MOON cadaver dataset.

Standard descriptive statistics for both the cadaver and patient datasets were evaluated for comparison purposes. In addition, a breakdown based on experience with respect to technique using standard descriptive statistics was also performed. Statistical testing was performed only on the cadaver dataset using the two levels of experience due to sample size. The folded F method demonstrated that with respect to experience level the variances were equal with the exception of femoral tunnel angles α and β . T-testing of each of the ACL tunnel measurements was performed using the appropriate method based on whether or not the variance was determined to be equal. The null hypothesis was that no difference existed between surgeon experience levels in ACL reconstruction tunnel placement for the five measurements that were tested for each bone.

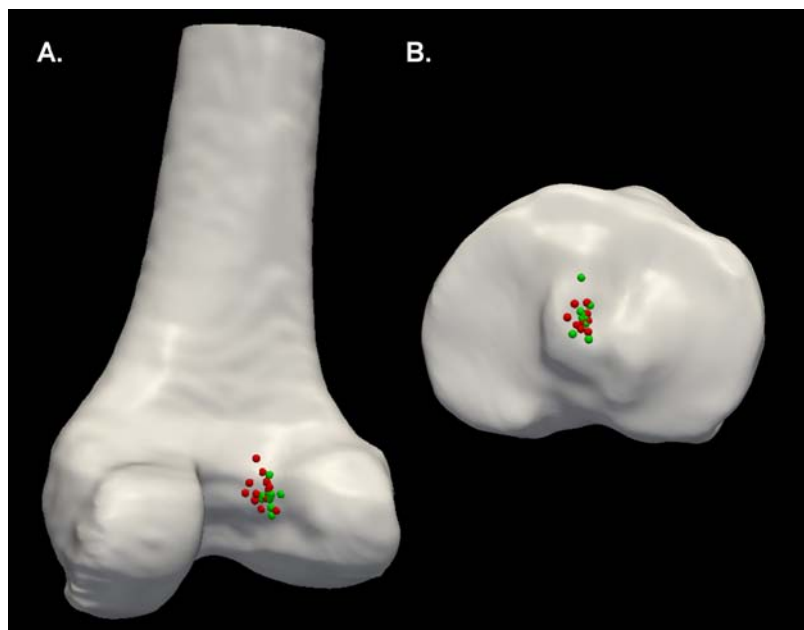


Figure 6.28 A color coded discrete sphere representation of the A) femur and B) tibia for the transtibial surgical technique from cadaver dataset organized by level of surgical experience: experienced (red) and new to practice (green).

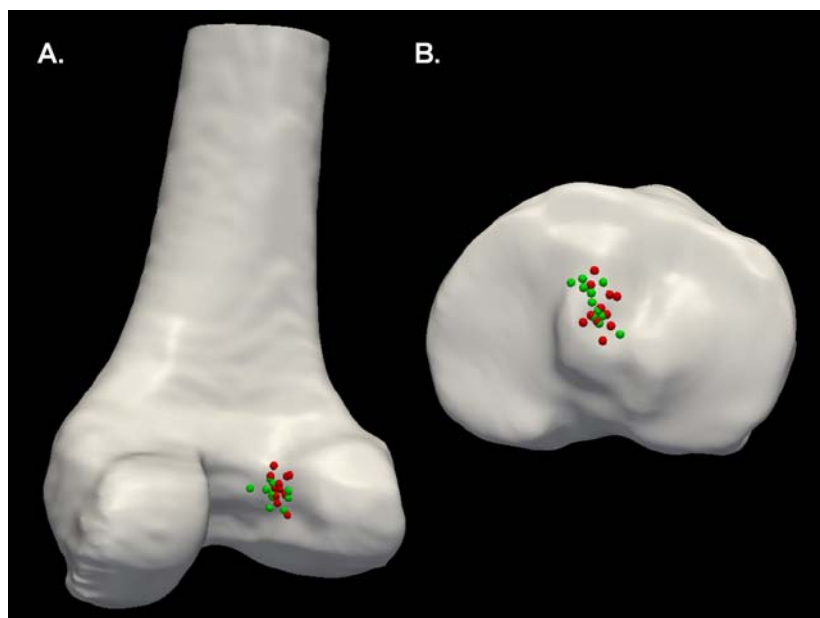


Figure 6.29 A color coded discrete sphere representation of the A) femur and B) tibia for the medial portal surgical technique from cadaver dataset organized by level of surgical experience: experienced (red) and new to practice (green).

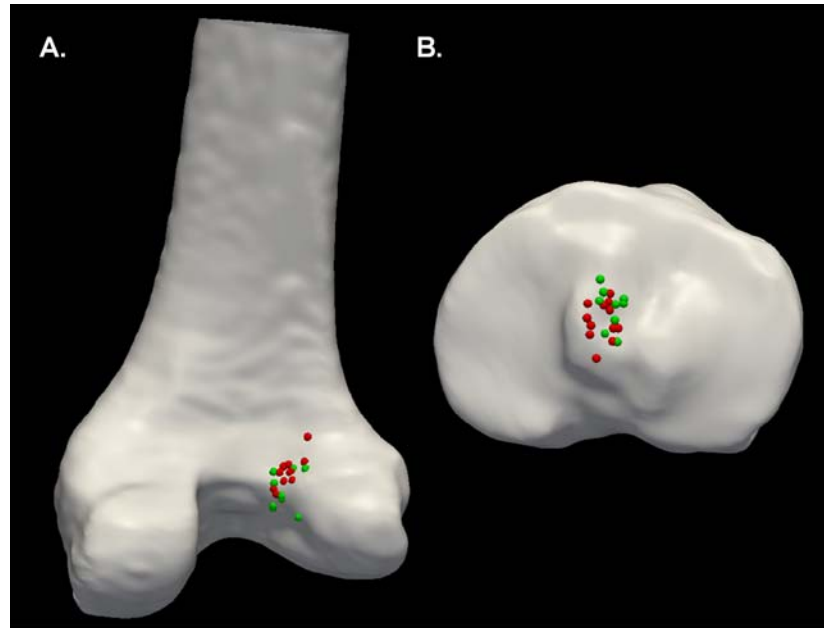


Figure 6.30 A color coded discrete sphere representation of the A) femur and B) tibia for the two incision surgical technique from cadaver dataset organized by level of surgical experience: experienced (red) and new to practice (green).

6.6.4.1 Femoral ACL Tunnel

6.6.4.1.1 Angle α

The cadaver dataset showed a difference of $\sim 2^\circ$ between the averages of the two experience levels. On average, the experienced surgeons placed the femoral tunnels more horizontally with respect to the surgically oriented coordinate system, while the new surgeons placed the tunnels more vertically. A statistically significant difference was not found between the two levels of surgical experience for angle α .

When grouped by surgical technique in the cadaver dataset, the femoral tunnels placed by an experienced surgeon using the MP technique were on average $\sim 13^\circ$ more horizontal than those placed by new surgeons. With the TT technique, the femoral tunnels placed by an experienced surgeon were on average $\sim 7^\circ$ more vertical than those placed by a new surgeon. With the TI technique, the femoral tunnels placed by an

experienced surgeon were on average placed in nearly the same position as the new surgeons. In the patient dataset which contained a larger number of samples, the femoral tunnels placed by an experienced surgeon using the MP technique were on average placed in nearly the same position as those placed by new surgeons. Appendix Figure C.9 demonstrates the box and whisker plot for this comparison.

6.6.4.1.2 Angle β

The cadaver dataset showed a difference of $\sim 1^\circ$ between the averages of the two experience levels. On average, the experienced surgeons placed the femoral tunnels more horizontally with respect to the surgically oriented coordinate system, while the new surgeons placed the tunnels more vertically. A statistically significant difference was not found between the two levels of surgical experience for angle β .

When grouped by surgical technique in the cadaver dataset, the femoral tunnels placed by an experienced surgeon using the MP technique were on average $\sim 10^\circ$ more vertical than those placed by new surgeons. With the TT technique, the femoral tunnels placed by an experienced surgeon were on average $\sim 5^\circ$ more horizontal than those placed by new surgeons. With the TI technique, the femoral tunnels placed by an experienced surgeon were on average $\sim 1^\circ$ more horizontal than those placed by new surgeons. In the patient dataset, the femoral tunnels placed by an experienced surgeon using the MP technique were on average $\sim 2^\circ$ more vertical than those placed by new surgeons. Appendix Figure C.10 demonstrates the box and whisker plot for this comparison.

6.6.4.1.3 Angle γ

The cadaver dataset showed a difference of $\sim 3^\circ$ between the averages of the two experience levels. On average, the experienced surgeons placed the femoral tunnels more horizontally with respect to the surgically oriented coordinate system, while the new surgeons placed the tunnels more vertically. A statistically significant difference was not found between the two levels of surgical experience for angle γ .

When grouped by surgical technique in the cadaver dataset, the femoral tunnels placed by an experienced surgeon using the MP technique were on average $\sim 5^\circ$ more horizontal than those placed by new surgeons. With the TT technique, the femoral tunnels placed by an experienced surgeon were on average $\sim 1^\circ$ more vertical than those placed by new surgeons. With the TI technique, the femoral tunnels placed by an experienced surgeon were on average $\sim 3^\circ$ more horizontal than those placed by new surgeons. In the patient dataset, the femoral tunnels placed by an experienced surgeon using the MP technique were on average $\sim 2^\circ$ more vertical than those placed by new surgeons. Appendix Figure C.11 demonstrates the box and whisker plot for this comparison.

6.6.4.1.4 Proportional Position Measure c/C

The cadaver dataset showed a difference of 6% between the averages of the two experience levels. On average, the experienced surgeons placed the femoral tunnel aperture more posterior on the lateral femoral condyle with respect to the “Notch View” of the femur, while the new surgeons placed the femoral tunnel aperture more anterior on the lateral femoral condyle. Statistical testing showed a significant difference (p -value < 0.016) between the two levels of surgical experience with respect to femoral proportional position measure c/C .

When grouped by surgical technique in the cadaver dataset, the femoral tunnel apertures placed by an experienced surgeon using the MP technique were on average $\sim 4\%$ more posterior on the lateral femoral condyle than those placed by new surgeons. With the TT technique, the femoral tunnels placed by an experienced surgeon were on average $\sim 1\%$ more posterior on the lateral femoral condyle than those placed by new surgeons. With the TI technique, the femoral tunnels placed by an experienced surgeon were on average $\sim 3\%$ more posterior on the lateral femoral condyle than those placed by new surgeons. In the patient dataset, the femoral tunnels placed by an experienced

surgeon using the MP technique were on average ~5% more posterior on the lateral femoral condyle than those placed by new surgeons. Figure 6.31 demonstrates the box and whisker plot for this comparison.

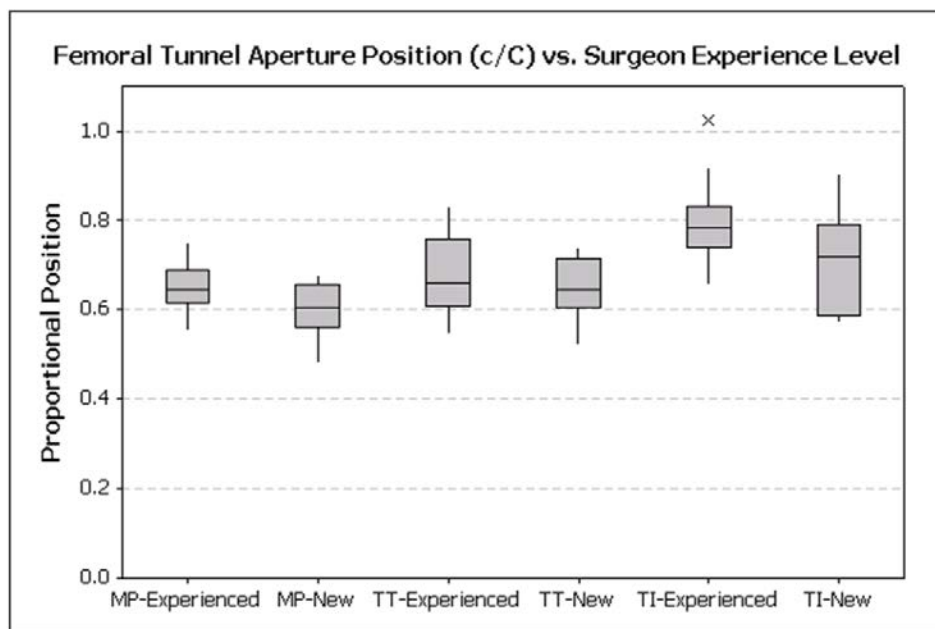


Figure 6.31 A box and whisker representation of the cadaver dataset's femoral tunnel aperture position measure c/C organized by level of surgeon experience and ACL reconstruction surgical technique (MP = medial portal, TT = transtibial, TI = two incision).

6.6.4.1.5 Proportional Position Measure n/N

The cadaver dataset showed a difference of 2% between the averages of the two experience levels. On average, the experienced surgeons placed the femoral tunnel aperture higher in the intercondylar notch of the femur, while the new surgeons placed the femoral tunnel lower in the intercondylar notch of the femur. A statistically significant difference was not found between the two levels of surgical experience for femoral proportional position measure n/N .

When grouped by surgical technique in the cadaver dataset, the femoral tunnel apertures placed by an experienced surgeon using the MP technique were on average ~6% lower in the intercondylar notch of the femur than those placed by new surgeons. With the TT technique, the femoral tunnels placed by an experienced surgeon were on average ~9% higher in the intercondylar notch of the femur than those placed by new surgeons. With the TI technique, the femoral tunnels placed by an experienced surgeon were on average ~8% higher in the intercondylar notch of the femur than those placed by new surgeons. In the patient dataset, the femoral tunnels placed by an experienced surgeon using the MP technique were on average ~5% lower in the intercondylar notch than those placed by new surgeons. Appendix Figure C.12 demonstrates the box and whisker plot for this comparison.

6.6.4.2 Tibial ACL Tunnel

6.6.4.2.1 Angle α

The cadaver dataset showed a difference of ~5° between the averages of the two experience levels. On average, the experienced surgeons placed the tibial tunnels more vertically with respect to the surgically oriented coordinate system, while the new surgeons placed the tunnels more horizontally. Statistical testing showed a significant difference (p-value < 0.005) between the two levels of surgical experience with respect to tibial angle α .

When grouped by surgeon performing a given surgical technique in the cadaver dataset, the tibial tunnels placed by an experienced surgeon using the MP technique were on average ~1° more vertical than those placed by new surgeons. With the TT technique, the tibial tunnels placed by an experienced surgeon were on average ~4° more vertical than those placed by a new surgeon. With the TI technique, the tibial tunnels placed by an experienced surgeon were on average ~9° more vertical than those placed by new surgeons. In the patient dataset, the tibial tunnels placed by an experienced surgeon using

the MP technique were on average $\sim 2^\circ$ more horizontal than those placed by new surgeons. Figure 6.32 demonstrates the box and whisker plot for this comparison.

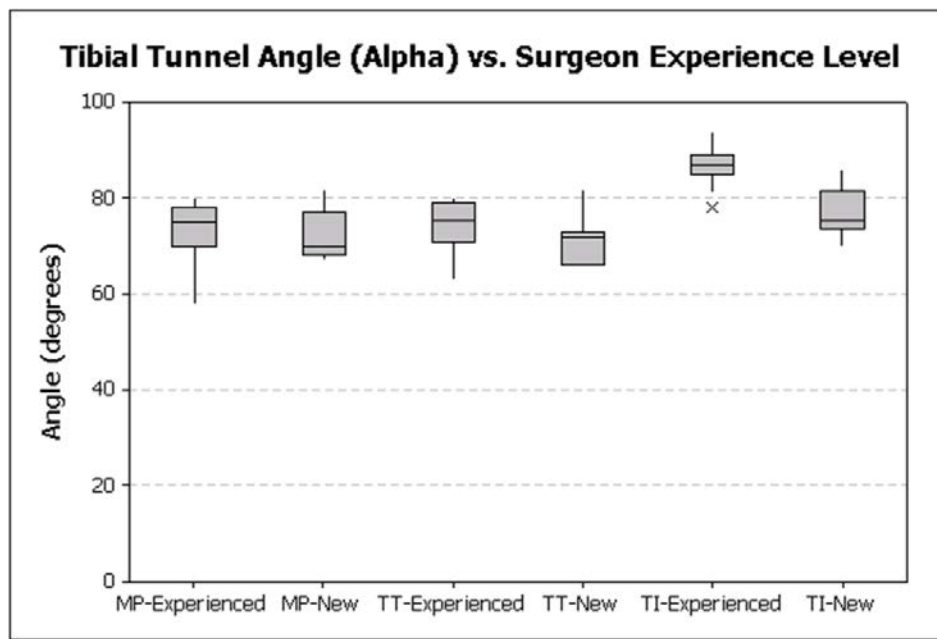


Figure 6.32 A box and whisker representation of the cadaver dataset's tibial tunnel angle α organized by level of surgeon experience and ACL reconstruction surgical technique (MP = medial portal, TT = transtibial, TI = two incision).

6.6.4.2.2 Angle β

The cadaver dataset showed a difference of $<1^\circ$ between the averages of the two experience levels. On average, the two levels of experience were nearly the same with respect to angle β . A statistically significant difference was not found between the two levels of surgical experience for angle β .

When grouped by surgical technique in the cadaver dataset, the tibial tunnels placed by an experienced surgeon using the MP technique were on average $\sim 3^\circ$ more vertical than those placed by new surgeons. With the TT technique, the tibial tunnels placed by an experienced surgeon were on average $\sim 7^\circ$ more vertical than those placed

by a new surgeon. With the TI technique, the tibial tunnels placed by an experienced surgeon were on average $\sim 9^\circ$ more horizontal than those placed by new surgeons. In the patient dataset, the tibial tunnels placed by an experienced surgeon using the MP technique were on average $\sim 3^\circ$ more vertical than those placed by new surgeons. Appendix Figure C.13 demonstrates the box and whisker plot for this comparison.

6.6.4.2.3 Angle γ

The cadaver dataset showed a difference of $\sim 2^\circ$ between the averages of the two experience levels. On average, the experienced surgeons placed the tibial tunnels more vertically with respect to the surgically oriented coordinate system, while the new surgeons placed the tunnels more horizontally. A statistically significant difference was not found between the two levels of surgical experience for angle γ .

When grouped by surgical technique in the cadaver dataset, the tibial tunnels placed by an experienced surgeon using the MP technique were on average $\sim 3^\circ$ more vertical than those placed by new surgeons. With the TT technique, the tibial tunnels placed by an experienced surgeon were on average $\sim 9^\circ$ more vertical than those placed by a new surgeon. With the TI technique, the tibial tunnels placed by an experienced surgeon were on average $\sim 6^\circ$ more horizontal than those placed by new surgeons. In the patient dataset, the tibial tunnels placed by an experienced surgeon using the MP technique were on average $\sim 1^\circ$ more vertical than those placed by new surgeons. Appendix Figure C.14 demonstrates the box and whisker plot for this comparison.

6.6.4.2.4 Proportional Position Measure a/A

The cadaver dataset showed a difference of $\sim 3\%$ between the averages of the two experience levels. On average, the experienced surgeons placed the tibial tunnel aperture more posterior on the tibial plateau, while the new surgeons placed the tibial tunnel aperture more anterior on the tibial plateau. A statistically significant difference was not

found between the two levels of surgical experience for tibial proportional position measure a/A.

When grouped by surgical technique in the cadaver dataset, the tibial tunnel apertures placed by an experienced surgeon using the MP technique were on average ~2% more posterior on the tibial plateau than those placed by new surgeons. With the TT technique, the tibial tunnel apertures placed by an experienced surgeon were in nearly the same anterior-posterior position as those placed by a new surgeon. With the TI technique, the tibial tunnels placed by an experienced surgeon were on average ~3% more anterior on the tibial plateau than those placed by new surgeons. In the patient dataset, the tibial tunnels placed by an experienced surgeon using the MP technique were on average ~2% more posterior on the tibial plateau than those placed by new surgeons. Appendix Figure C.15 demonstrates the box and whisker plot for this comparison.

6.6.4.2.5 Proportional Position Measure m/M

The cadaver dataset showed a difference of ~1% between the averages of the two experience levels. On average, the experienced surgeons placed the tibial tunnel aperture more medial on the tibial plateau, while the new surgeons placed the tibial tunnel aperture more lateral on the tibial plateau. A statistically significant difference was not found between the two levels of surgical experience for tibial proportional position measure m/M.

When grouped by surgical technique in the cadaver dataset, the tibial tunnel apertures placed by an experienced surgeon using the MP technique were on average placed in nearly the same medial-lateral position as those by new surgeons. With the TT technique, the tibial tunnel apertures placed by an experienced surgeon were on average placed in nearly the same medial-lateral position as those by new surgeons. With the TI technique, the tibial tunnels placed by an experienced surgeon were on average placed in nearly the same medial-lateral position as those by new surgeons. In the patient dataset,

the tibial tunnels placed by an experienced surgeon using the MP technique were on average placed in nearly the same medial-lateral position as those by new surgeons. Appendix Figure C.16 demonstrates the box and whisker plot for this comparison.

6.6.5 Surgeon Variability Results

The patient dataset was designed to investigate whether a difference existed between tunnel placements based on the surgeon performing the procedure. Ten surgeons from four institutions were involved in the patient study. Figures 6.33 and 6.34 provide discrete sphere representations for the operating surgeon's in the MOON patient dataset. Appendix Figures C.32 and C.33 provide tunnel aperture overlap maps for the operating surgeon's in the MOON patient dataset. Standard descriptive statistics for both the cadaver and patient datasets were evaluated for comparison purposes. Statistical testing was performed only on the patient dataset due to sample size. To determine statistical significance, the Wilcoxon Rank Sum test was applied followed by a Kruskal Wallis test. The null hypothesis was that no difference exists between surgeons in ACL reconstruction tunnel placement for the five measurements for each bone that were tested.



Figure 6.33 Discrete sphere representations of the femur (3 views) and the tibia for the patient dataset organized by surgeon. Four surgeons are depicted.



Figure 6.34 Discrete sphere representations of the femur (3 views) and the tibia for the patient dataset organized by surgeon. Four more surgeons are depicted.

6.6.5.1 Femoral ACL Tunnel

6.6.5.1.1 Angle α

The patient dataset showed standard deviations ranging from 2.0° to 19.9° between the ten different surgeons with respect to angle α . Standard deviations from the cadaver dataset showed similar values. A statistically significant difference (p-value = 0.001) was found with respect to surgeon for angle α . Figure 6.35 demonstrates the box and whisker plot for this comparison.

6.6.5.1.2 Angle β

The patient dataset showed standard deviations ranging from 2.5° to 13.2° between the ten different surgeons with respect to angle β . Standard deviations from the cadaver dataset showed similar values. A statistically significant difference (p-value < 0.0001) was found with respect to surgeon for angle β . Figure 6.36 demonstrates the box and whisker plot for this comparison.

6.6.5.1.3 Angle γ

The patient dataset showed standard deviations ranging from 6.0° to 18.1° between the ten different surgeons with respect to angle γ . Standard deviations from the cadaver dataset showed similar values. A statistically significant difference (p-value = 0.002) was found with respect to surgeon for angle γ . Figure 6.37 demonstrates the box and whisker plot for this comparison.

6.6.5.1.4 Proportional Position Measure c/C

The patient dataset showed standard deviations ranging from 3% to 10% between the ten different surgeons with respect to proportional position measure c/C . Standard deviations from the cadaver dataset showed similar values. A statistically significant difference (p-value < 0.0001) was found with respect to surgeon for proportional position measure c/C . Figure 6.38 demonstrates the box and whisker plot for this comparison.

6.6.5.1.5 Proportional Position Measure n/N

The patient dataset showed standard deviations ranging from 4% to 8% between the ten different surgeons with respect to proportional position measure n/N. Standard deviations from the cadaver dataset showed similar values. A statistically significant difference (p-value = 0.0002) was found with respect to surgeon for proportional position measure n/N. Figure 6.39 demonstrates the box and whisker plot for this comparison.

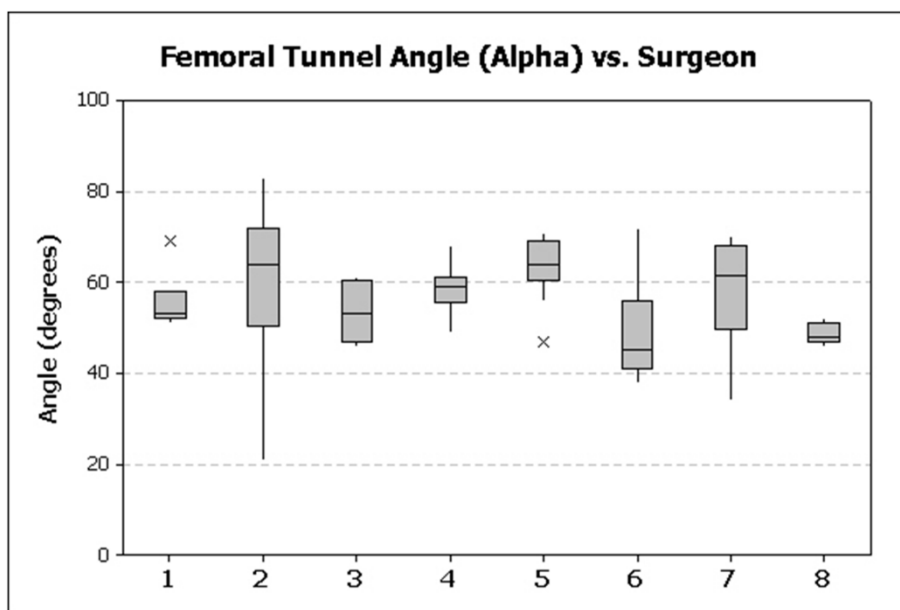


Figure 6.35 A box and whisker representation of the patient dataset's femoral tunnel angle α organized by surgeon. Eight surgeons are depicted.

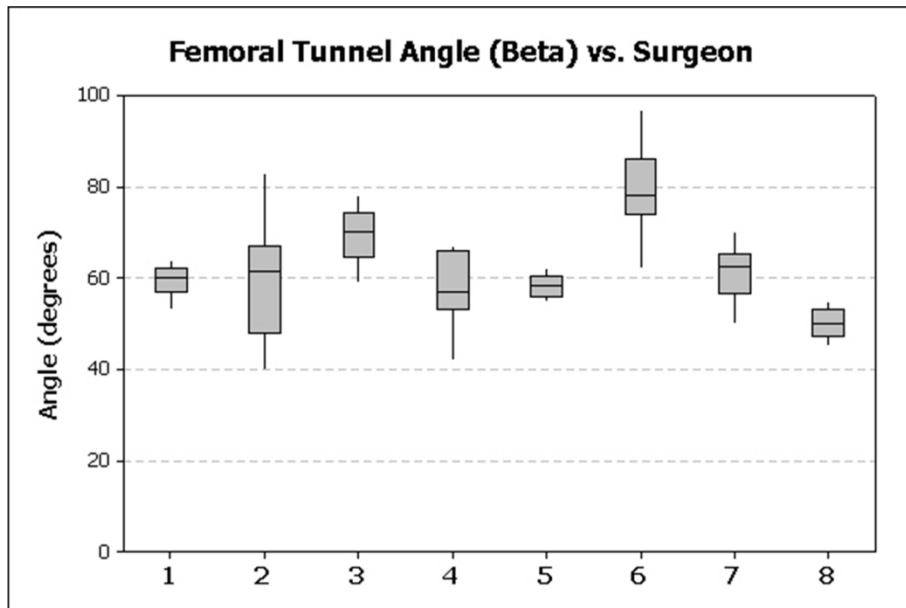


Figure 6.36 A box and whisker representation of the patient dataset's femoral tunnel angle β organized by surgeon. Eight surgeons are depicted.

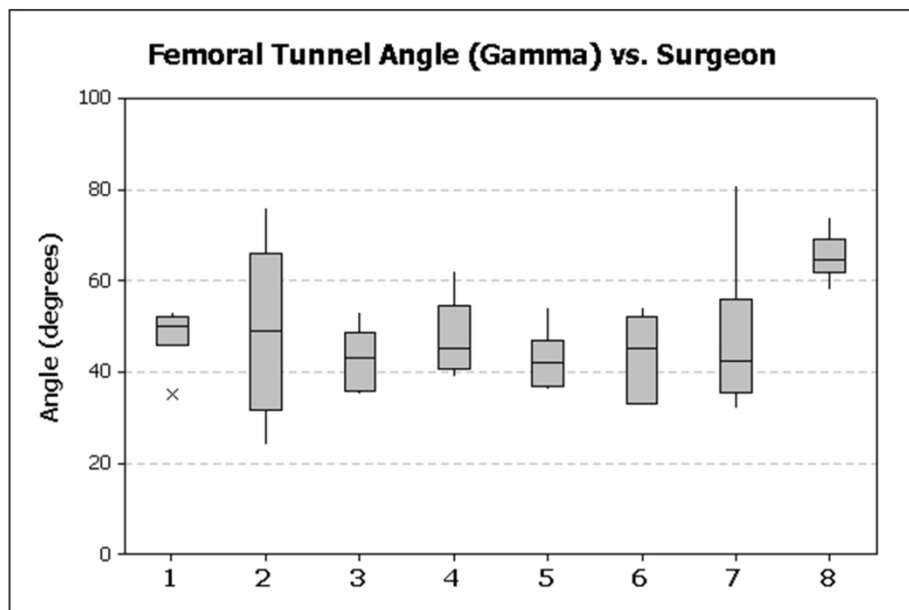


Figure 6.37 A box and whisker representation of the patient dataset's femoral tunnel angle γ organized by surgeon. Eight surgeons are depicted.

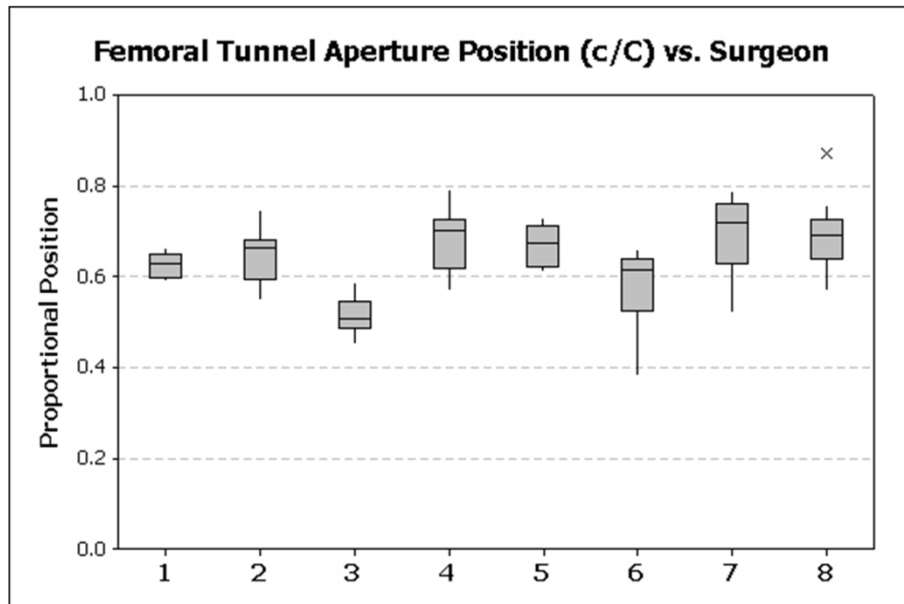


Figure 6.38 A box and whisker representation of the patient dataset's femoral tunnel aperture position measure c/C organized by surgeon. Eight surgeons are depicted.

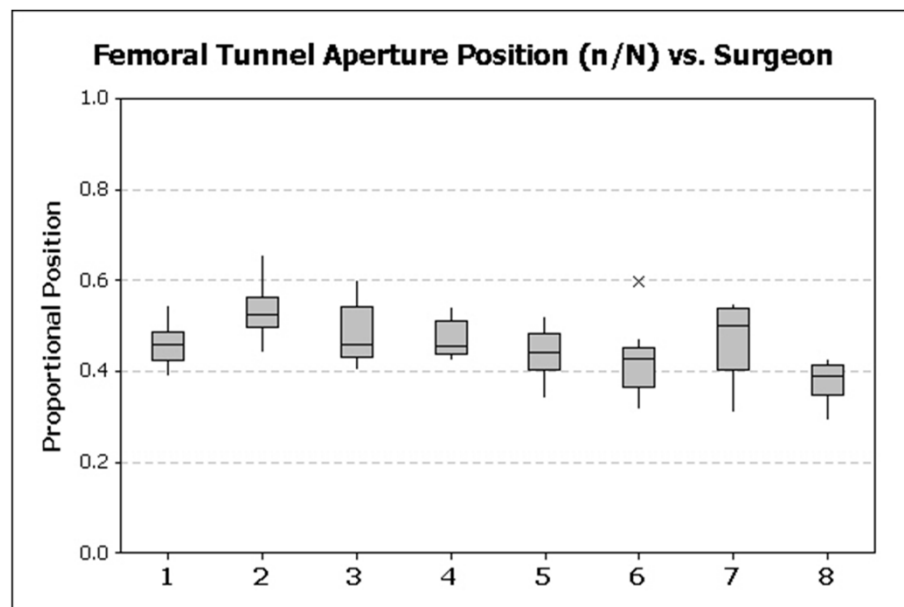


Figure 6.39 A box and whisker representation of the patient dataset's femoral tunnel aperture position measure n/N organized by surgeon. Eight surgeons are depicted.

6.6.5.2 Tibial ACL Tunnel

6.6.5.2.1 Angle α

The patient dataset showed standard deviations ranging from 2.4° to 6.1° between the ten different surgeons with respect to angle α . Standard deviations from the cadaver dataset showed similar values. A statistically significant difference (p-value < 0.0001) was found with respect to surgeon for angle α . Figure 6.40 demonstrates the box and whisker plot for this comparison.

6.6.5.2.2 Angle β

The patient dataset showed standard deviations ranging from 4.6° to 6.7° between the ten different surgeons with respect to angle β . Standard deviations from the cadaver dataset ranged from 1.1° to 13.7° . A statistically significant difference (p-value < 0.0001) was found with respect to surgeon for angle β . Figure 6.41 demonstrates the box and whisker plot for this comparison.

6.6.5.2.3 Angle γ

The patient dataset showed standard deviations ranging from 4.5° to 6.1° between the ten different surgeons with respect to angle γ . Standard deviations from the cadaver dataset showed similar values. A statistically significant difference (p-value < 0.0001) was found with respect to surgeon for angle γ . Figure 6.42 demonstrates the box and whisker plot for this comparison.

6.6.5.2.4 Proportional Position Measure a/A

The patient dataset showed standard deviations ranging from 3% to 8% between the ten different surgeons with respect to proportional position measure a/A. Standard deviations from the cadaver dataset showed similar values. A statistically significant difference (p-value < 0.0001) was found with respect to surgeon for proportional position measure a/A. Figure 6.43 demonstrates the box and whisker plot for this comparison.

6.6.5.2.5 Proportional Position Measure m/M

The patient dataset showed standard deviations ranging from 1% to 3% between the ten different surgeons with respect to proportional position measure a/A . Standard deviations from the cadaver dataset showed similar values. A statistically significant difference (p -value < 0.006) was found with respect to surgeon for proportional position measure a/A . Figure 6.44 demonstrates the box and whisker plot for this comparison.

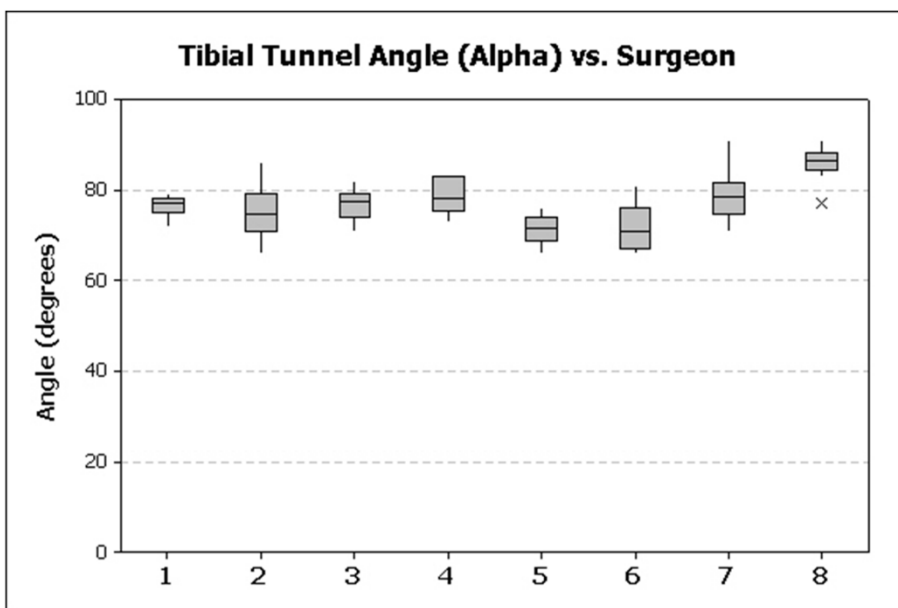


Figure 6.40 A box and whisker representation of the patient dataset's tibial tunnel angle α organized by surgeon. Eight surgeons are depicted.

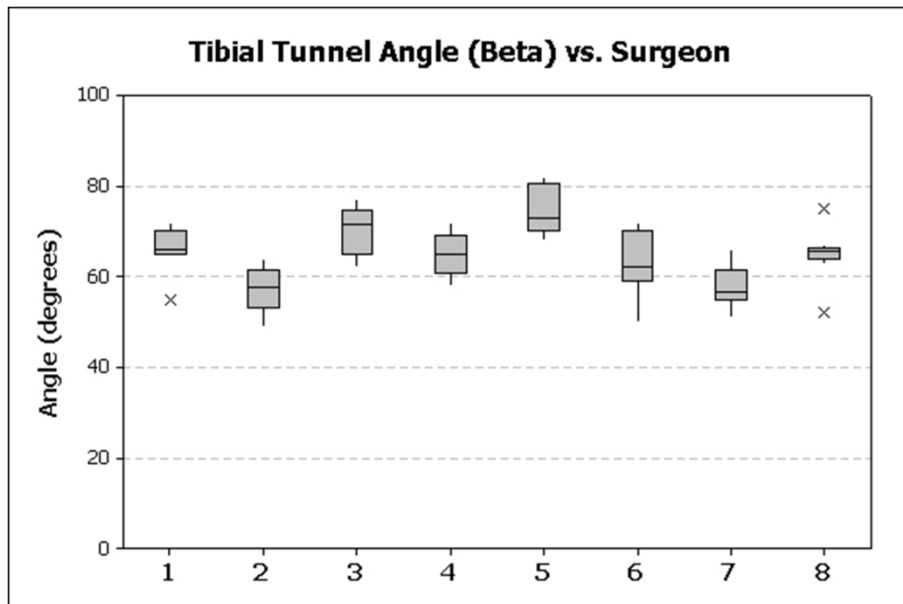


Figure 6.41 A box and whisker representation of the patient dataset's tibial tunnel angle β organized by surgeon. Eight surgeons are depicted.

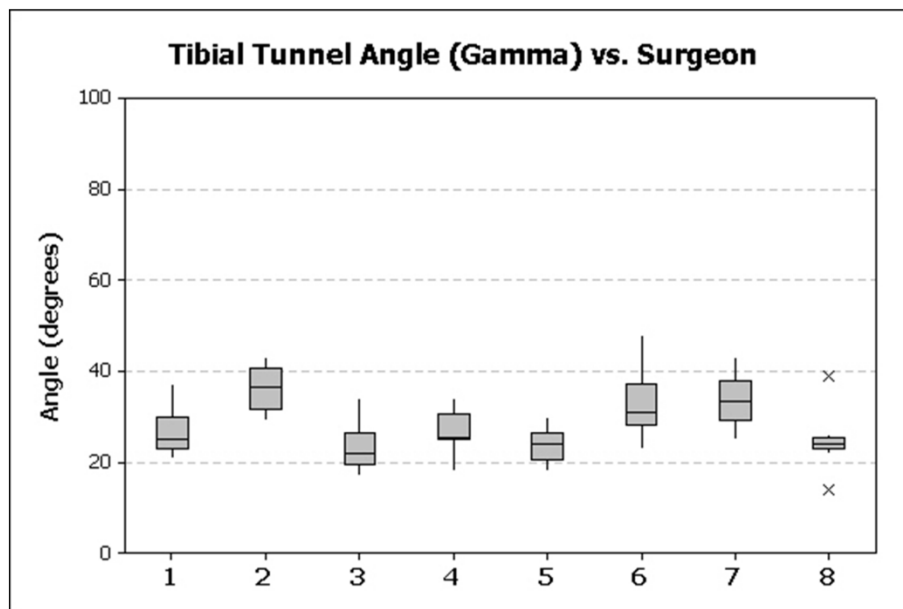


Figure 6.42 A box and whisker representation of the patient dataset's tibial tunnel angle γ organized by surgeon. Eight surgeons are depicted.

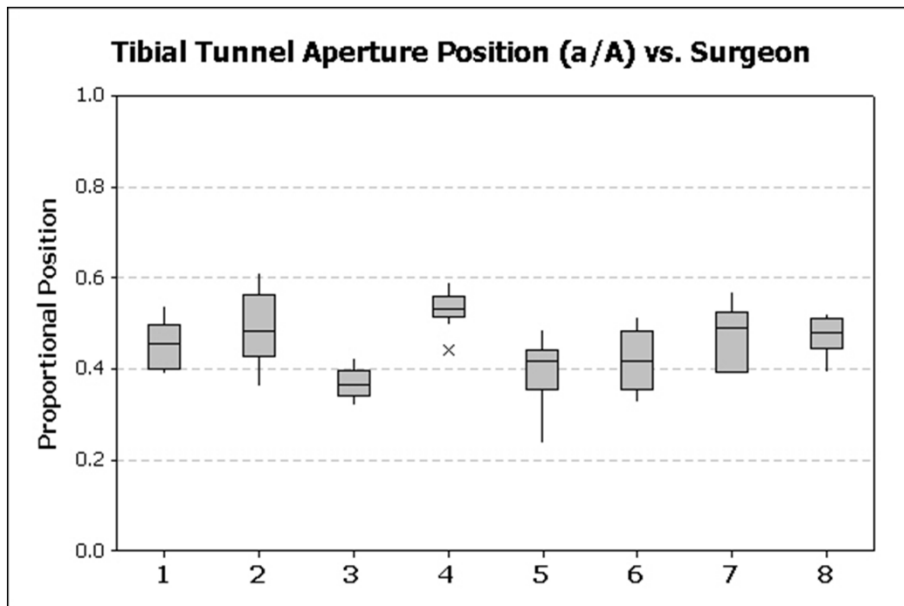


Figure 6.43 A box and whisker representation of the patient dataset's tibial tunnel aperture position measure a/A organized by surgeon. Eight surgeons are depicted.

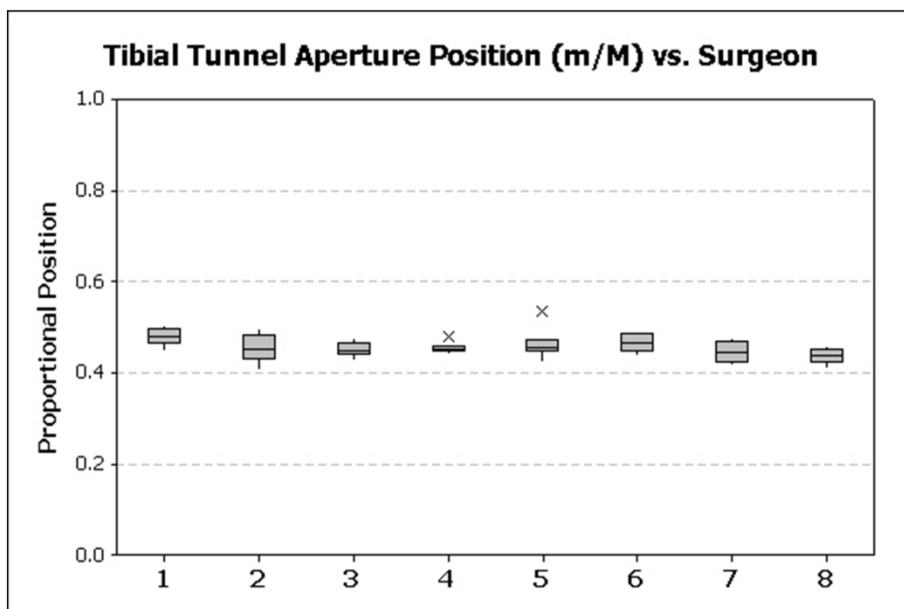


Figure 6.44 A box and whisker representation of the patient dataset's tibial tunnel aperture position measure m/M organized by surgeon. Eight surgeons are depicted.

6.6.6 Discussion and Conclusions

With regards to surgical technique, the femoral tunnel angles demonstrated significant variability and statistically significant differences between the three techniques for all three tunnel angles. Overall, the two incision technique placed the femoral tunnels most horizontally and the transtibial technique most vertically with regards to the three angular measurements. The spatial measurements for the femoral tunnel aperture showed significant difference with respect to c/C but not n/N. Overall, the medial portal technique placed the tunnel aperture most anterior with regards to the “Notch View” and the two incision technique placed the tunnel aperture most posterior with regards to the “Notch View.”

The tibial tunnel angles were less variable than the femoral tunnel angles. It should be noted that the three techniques are named for the femoral tunnel drilling procedure; the tibial tunnels are generated using similar methods in all three cases. Only angle α demonstrated a statistically significant difference with the two incision technique surgeons producing the most horizontal tunnels and the medial portal technique surgeons producing the most vertical tunnels. The spatial measurements for the tibial tunnel aperture showed statistically significant difference with respect to a/A but not m/M. Overall, the medial portal technique surgeons placed the tunnel aperture most anterior on the tibial plateau and the transtibial technique surgeons placed the tunnel aperture most posterior on the tibial plateau.

Overall with respect to surgical technique, more femoral tunnel angles were statistically different than tibial tunnel angles. With regards to spatial measurements, both the tibia and femur had one spatial measurement that was different between the two techniques. Both of the statistically significant spatial measures deal with a surgeon’s perspective of depth on the tibial plateau and lateral femoral condyle. Future studies investigating arthroscopic improvements to depth perception along the tibial plateau and

lateral femoral condyle could decrease the variability we have observed in tunnel aperture positioning and improve the surgical outcomes of our patients.

With regards to level of surgeon experience, no statistically significant difference was apparent between the femoral tunnel angles. The spatial measurements only demonstrated a significant difference for the c/C measurement with the experienced surgeons placing the tunnel apertures more posteriorly than the new surgeons. With respect to the tibia, the tunnel angle α was statistically significant with experience surgeons placing the tunnels more vertically. This study demonstrates that the tibial aperture is consistently placed, even with a statistically significant difference in angle α . It also demonstrates that the femoral aperture is not consistently placed in the same position by surgeons of different experience levels.

With regards to surgeon, statistically significant differences were seen for all angular and spatial measures for both the femur and tibia. The femur showed the largest standard deviation with respect to angle α and spatial measure c/C . The tibia showed the largest standard deviation with respect to angle α and spatial measure a/A . This study demonstrates that surgeons are placing the ACL tunnel and aperture in different positions.

The results from the patient and cadaver study have demonstrated that significant differences exist between the placement of ACL drill tunnels based on surgical technique, experience level, and surgeon. Ideally, each technique aims to replace the ACL by placing the drill tunnel within the anatomic footprint of the ACL. Placement of an ACL graft at the midpoint of the AM and PL bundles has been shown to similarly restore restraints to anterior translation and internal tibial rotation when single bundle and double methods are compared[160, 161]. With the current thought that as long as the graft is placed in this position, the method by which the graft attains this position is left to the surgeon's discretion[211]. Since this study did not identify the patient-specific location of the anatomic footprint, we cannot make direct measurements from that location; it is

difficult to make conclusions regarding the resulting knee biomechanics without this measure.

However, we can compare some of our results to trends seen in the literature. In our study, we have observed the transtibial technique to result in more vertical tunnel placement on the femur than the medial portal and two incision techniques which corresponds to that reported in the literature[148, 211]. We also observed that the transtibial technique results in a more anterior femoral tunnel aperture than the two incision technique as has been reported[147]. We also found the transtibial technique to place the femoral tunnel highest in the intercondylar notch of all three techniques as has been reported[143]. In addition, we have confirmed that the transtibial technique results in a posterior placement of the tibial tunnel with respect to the footprint[143].

Without knowledge of the relationship of the tunnels with respect to the anatomic footprint, it is difficult to assess whether a particular method, level of experience, or surgeon has an impact on the biomechanics of the knee joint. However, we can look at trends in the literature with regards to tunnel placement and reconstructed knee biomechanics. With regards to tunnel angle, tunnels that are placed too obliquely have been shown to lead to increased contact pressure in the aperture, which can lead to tunnel enlargement[121, 198]. Tunnel enlargement can impede graft healing, increase joint laxity, and lead to the necessity of a revision surgery.

With respect to the tibia, tunnel apertures that are placed anterior to the femoral intercondylar roof on the tibial plateau can lead to graft impingement with the intercondylar notch[121, 184]. Placement of the tibial tunnels medial to the tibial eminence can cause loss of flexion, while placement lateral to the tibial eminence can cause anterior joint laxity. More vertical tibial tunnels have been shown to inadequately stabilize the knee to pivot-shift testing[143]. Finite element studies have demonstrated that the tibial tunnel angle has the greatest effect on joint laxity, which in turn has an

effect on meniscal stresses and strains that can lead to early onset osteoarthritis[198]. More horizontally placed tibial tunnels demonstrated decreased joint laxity.

With respect to the femur, it has been reported that placing the tunnel aperture in the posterior 60% of the lateral femoral condyle results in satisfactory knee biomechanics[121]. Positioning the tunnel aperture more posterior with respect to Blumensaat's line has been reported to decrease tibial translation[211]. Some have reported that femoral tunnel angles have a minimal effect on rotational stability[142, 178], while others have shown that more horizontally oriented femoral tunnels better mimic normal knee biomechanics[148]. Finite element studies have demonstrated that the femoral tunnel angle has the greatest effect on graft tension and graft impingement with more horizontal femoral tunnel placement resulting in decreased graft tension[198].

In conclusion, statistically significant differences have been identified in all three studies with relation to surgical technique, level of surgical experience, and surgeon. Our results are comparable to previous studies when comparisons were possible. Overall, the placement of ACL grafts with respect to drill tunnels is not consistent between techniques, level of experience, or surgeon. Future comparisons to the anatomic footprint will provide additional insight as to how these differences compare to the footprint of the native ligament. Finite element simulations and biomechanical cadaveric testing offer a means to test and validate the effects of tunnel positioning on the biomechanics of the knee joint.

6.7 The Estimated Anatomic Footprint

6.7.1 Introduction

The MOON study was designed to look at variability in ACL tunnel placement; however, it would also be interesting to evaluate tunnel placement with respect to the anatomic ACL footprint. Ideally, we would have information related to each specimen's anatomic ACL position, which would have required either physical measurement during

the procedure or a preoperative MRI that could be correlated to the postoperative tunnel placement. Alternatively, a postoperative MRI of the contralateral knee could be mirrored and registered to the reconstructed knee to establish the placement of the drill tunnel with respect to the subject's anatomic footprint. Unfortunately, MRI datasets and intraoperative measurements were not available for either the cadaver or patient datasets. We do not have the ability to measure exact distances for each subject; we do, however, have the ability to estimate the position of the footprint from the location of the footprint described in previous studies. These measurements must be viewed as an estimate; future studies specifically addressing this goal would allow for valid statistical analysis of the placement of the drill tunnels with respect to the anatomic footprint.

A number of studies have investigated the anatomic placement of the ACL footprint; however, as aforementioned a number of different techniques have been used to describe this location with respect to the surrounding bony anatomy. In addition, there is not a consensus agreement as to the location of the anatomic ACL footprint when the literature is reviewed. Anatomic variability in the shape of the human knee may be one factor in this disagreement between studies. A comparison between values determined by a number of different studies have demonstrated the center of the femoral AM bundle is located between 18.5% - 25.9% from the proximal edge of the subchondral bone with respect to the total condylar width along Blumensaat's line and between 17.8% - 33.2% from Blumensaat's line with respect to the perpendicular distance from Blumensaat's line to the extent of the medial wall of the lateral condyle[159, 189, 212, 213]. The center of the femoral PL bundle has been reported to be between 27.0% - 35.1% from the proximal edge of the subchondral bone with respect to the total condylar width along Blumensaat's line and between 42.1% - 55.3% from Blumensaat's line with respect to the perpendicular distance from Blumensaat's line to the extent of the medial wall of the lateral condyle[159, 189, 212, 213]. The center of the tibial AM bundle has been reported to be between 25.0% - 37.6% from the anterior edge of the tibial plateau with

respect to the total depth of the tibial plateau and between 34.6% - 52% from the medial edge of the tibial plateau with respect to the total width of the tibial plateau[159, 189, 212-215]. The center of the tibial PL bundle has been reported to be between 38.4% - 50.1% from the anterior edge of the tibial plateau with respect to the total depth of the tibial plateau and between 50.0% - 52.4% from the medial edge of the tibial plateau with respect to the total width of the tibial plateau[159, 189, 212-215].

Others have simply described the overall position of the center of the ACL bundle without regards to the two bundle centers. The femoral ACL footprint has been described as occupying the superior 66% of the lateral aspects of the intercondylar notch and the posterior 32% of the notch[136, 215]. The center of the tibial ACL footprint has been described as being 51% from the medial edge with respect to the total width of the tibial plateau and 40% from the anterior edge with respect to the total depth of the tibial plateau[136, 215].

In addition to describing the spatial relationships of the AM and PL bundles with respect to the bony anatomy, other studies have investigated the area of the footprints of the bundles on the bone surface[213, 216-220]. Variable shapes, positions with respect to the other bundle, and footprint sizes have been reported. Correlating positional information of the bundle centers with footprint sizes from different studies often results in inconsistent and overlapping measurements. Our brief review of the literature demonstrates that there isn't a consensus as to the location and size of the ACL footprint. As a means to compare our tunnel positions with an estimated ACL bundle location, we have selected the Lorenz, et al. study[212] to use for establishing an estimated ACL bundle footprint. This study was chosen as it demonstrated average values with respect to the other reviewed papers.

6.7.2 Materials and Methods

The measurements describing the locations of the centers of the AM and PL bundles of the ACL were obtained from Lorenz et al.[212]. Spherical representations of the AM and PL bundle centroids were placed on a surface representation of the native femur and tibia (Figure 6.45). The methods described in Figure 6.16 were used to project the centroid for each subject drill tunnel centroid from the patient and cadaveric dataset onto the native femur and tibia.

Three Euclidean distances were calculated for each subject based on the projected spheres: the distance of each tunnel centroid to the AM bundle centroid, the distance of each tunnel centroid to the PL bundle centroid, and the distance of each tunnel centroid to the midpoint between the AM and PL bundle centroids. These calculations were performed for both the patient and cadaver datasets. Standard descriptive statistics were calculated for the patient and cadaver datasets and were grouped based on surgical technique. Qualitatively, the footprint described by Lorenz, et al. was overlapped with similar views of the native femur and tibia from our study[212]. This was used as an estimate of the native footprint since dimensional information was not provided in the paper. In addition, ACL Tunnel Aperture Overlap Maps with the AM and PL bundle centroids were also created.

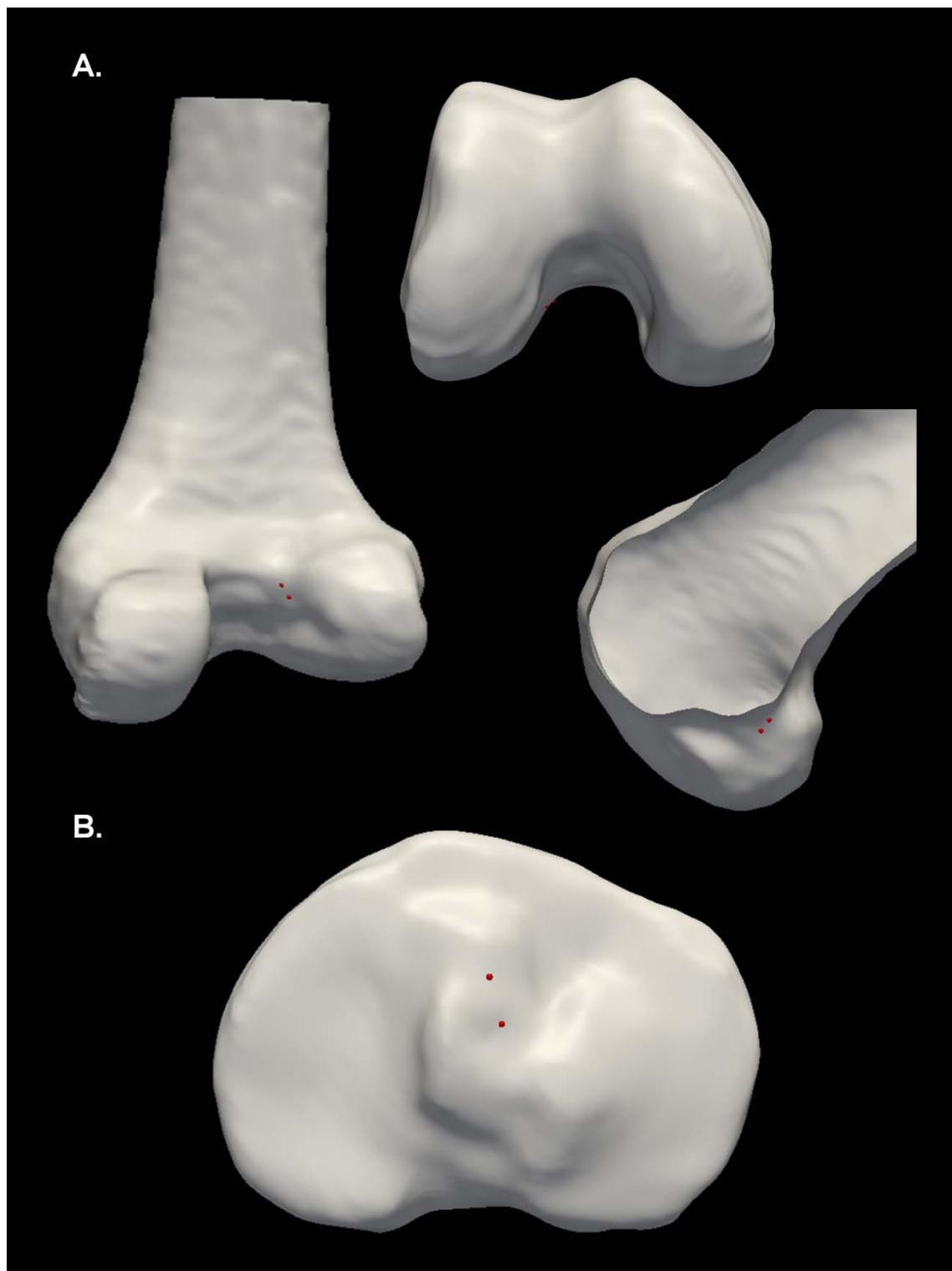


Figure 6.45 The estimated positions of the ACL bundle centers (AM and PL) positioned on the A) femur and the B) tibia using published measurements.

6.7.3 Results

The estimated ACL footprint overlaid on the projected spheres are demonstrated in Figure 6.46 and Figure 6.47 for the femur and tibia, respectively. The ACL Tunnel Aperture Overlap Maps for the patient and cadaver study are available in Figure 6.48 and Figure 6.49. Finally, the Euclidean distances are presented in Tables 6.9 – 6.14.

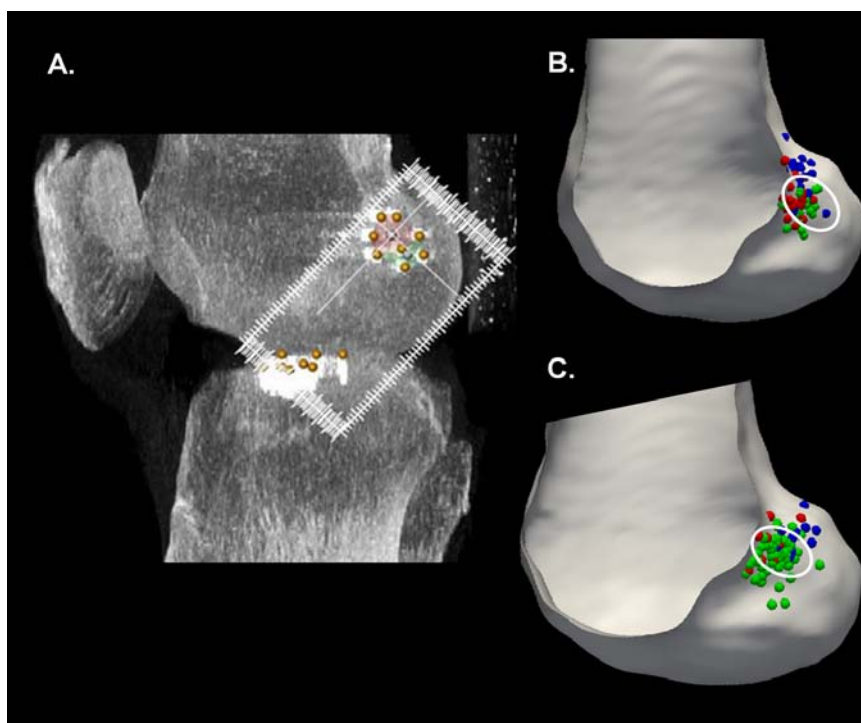


Figure 6.46 The estimated ACL footprint overlapped on the femur. A) An estimation of the ACL footprint on the femur using 3D CT measurements. B) A discrete sphere representation of the femur from the cadaver dataset overlapped with an estimated ACL footprint (white outline); three techniques are demonstrated: medial portal (green), two incision (blue), and transtibial (red). C) A discrete sphere representation of the femur from the patient dataset overlapped with an estimated ACL footprint (white outline); three techniques are demonstrated: medial portal (green), two incision (blue), and transtibial (red).

(Source: A) Lorenz, et al.[212])

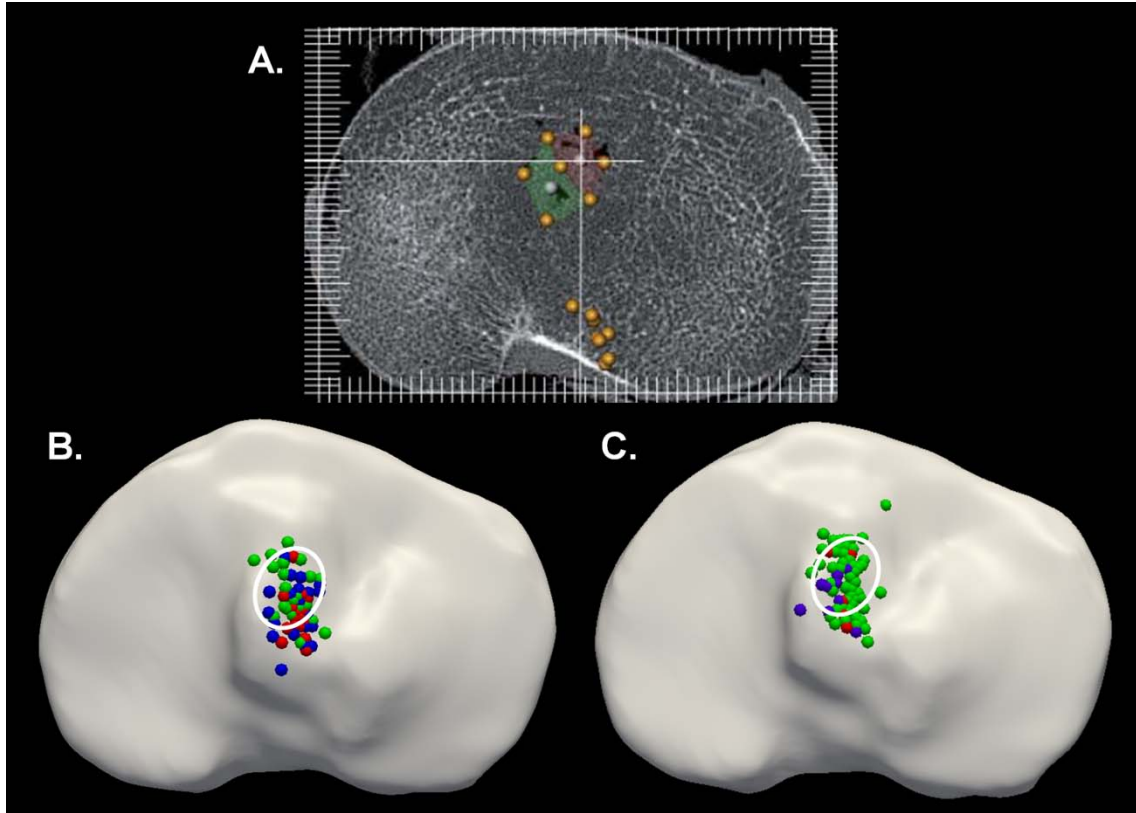


Figure 6.47 The estimated ACL footprint overlapped on the tibial plateau. A) An estimation of the ACL footprint on the tibia using 3D CT measurements. B) A discrete sphere representation of the tibia from the cadaver dataset overlapped with an estimated ACL footprint (white outline); three techniques are demonstrated: medial portal (green), two incision (blue), and transtibial (red). C) A discrete sphere representation of the tibia from the patient dataset overlapped with an estimated ACL footprint (white outline); three techniques are demonstrated: medial portal (green), two incision (blue), and transtibial (red).

(Source: A) Lorenz, et al.[212])

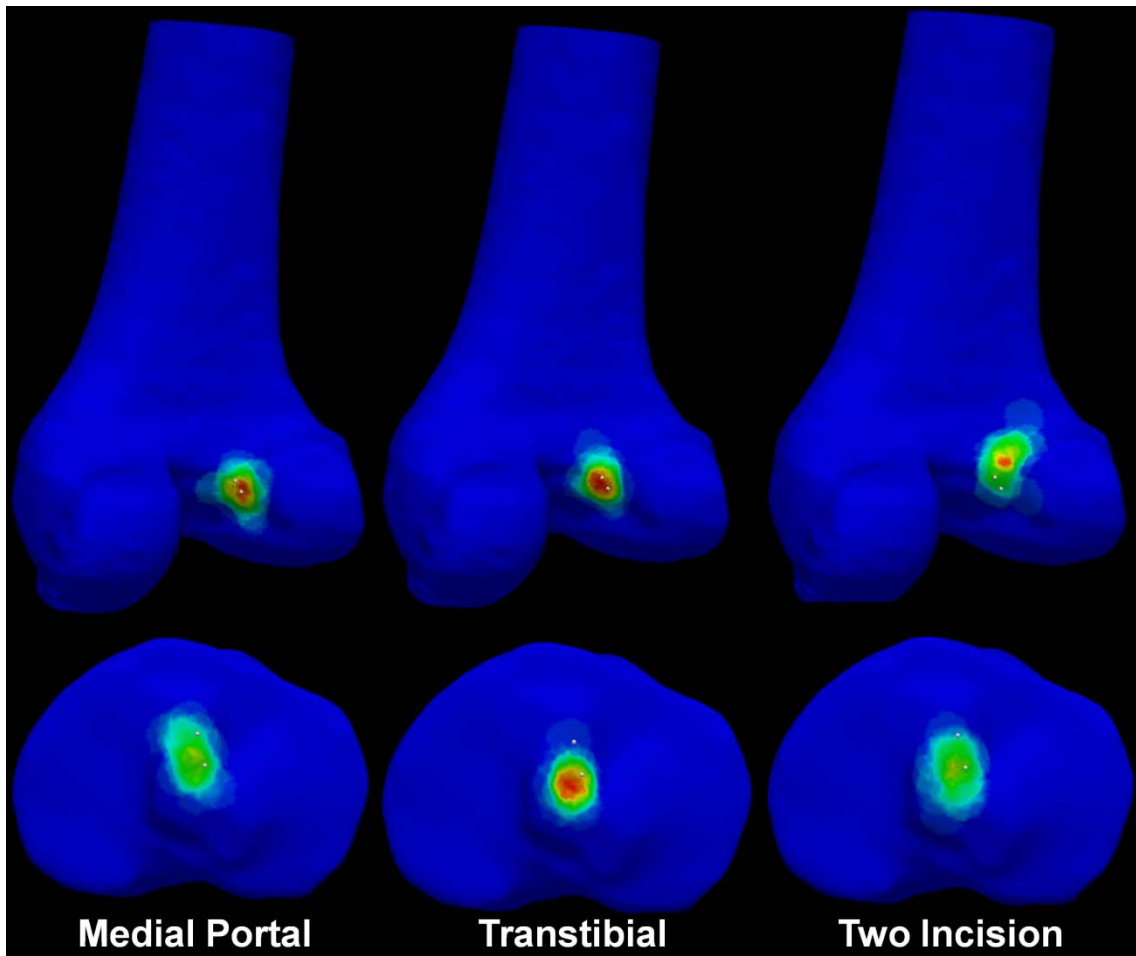


Figure 6.48 Femoral and tibial ACL Tunnel Aperture Overlap Maps for the cadaver dataset representing three ACL reconstruction techniques. Two discrete spheres corresponding to the estimated locations of the AM and PL bundles of the ACL have been placed on both the femur and the tibia.

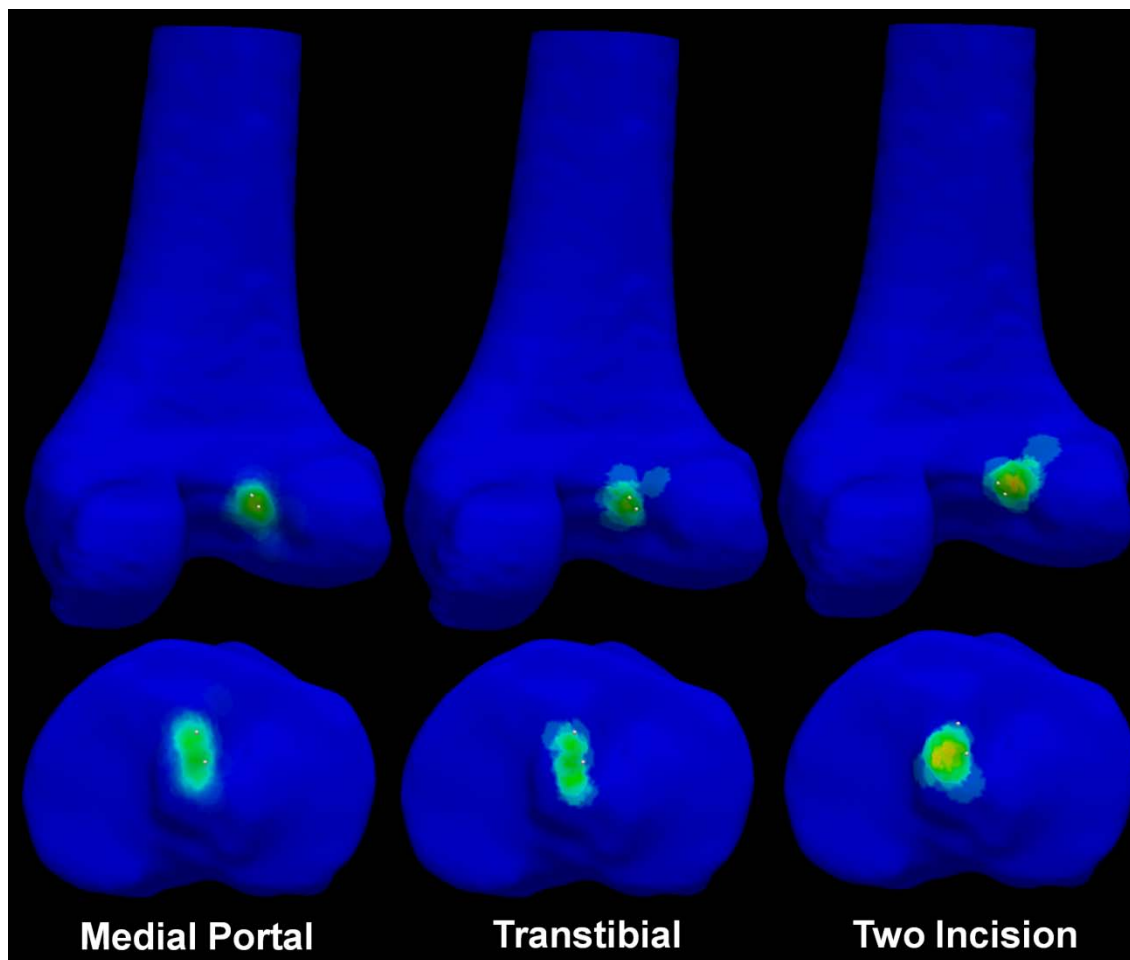


Figure 6.49 Femoral and tibial ACL Tunnel Aperture Overlap Maps for the patient dataset representing three ACL reconstruction techniques. Two discrete spheres corresponding to the estimated locations of the AM and PL bundles of the ACL have been placed on both the femur and the tibia.

Table 6.9 Standard descriptive statistics for the cadaver study describing the distance from the tunnel aperture centroid to the AM bundle center for the tibia and the femur organized by surgical technique.

Bone	Technique	# of Subjects	Average Distance (mm)	Standard Deviation (mm)
Femur	Medial Portal	22	4.35	2.33
	Transtibial	23	3.43	1.83
	Two Incision	22	5.78	3.53
Tibia	Medial Portal	22	6.17	3.04
	Transtibial	23	8.52	2.67
	Two Incision	22	7.84	3.83

Table 6.10 Standard descriptive statistics for the cadaver study describing the distance from the tunnel aperture centroid to the PL bundle center for the tibia and the femur organized by surgical technique.

Bone	Technique	# of Subjects	Average Distance (mm)	Standard Deviation (mm)
Femur	Medial Portal	22	3.51	1.88
	Transtibial	23	3.66	2.29
	Two Incision	22	7.14	3.70
Tibia	Medial Portal	22	4.98	2.63
	Transtibial	23	3.91	1.87
	Two Incision	22	4.62	2.39

Table 6.11 Standard descriptive statistics for the cadaver study describing the distance from the tunnel aperture centroid to the center point between the bundle centers for the tibia and the femur organized by surgical technique.

Bone	Technique	# of Subjects	Average Distance (mm)	Standard Deviation (mm)
Femur	Medial Portal	22	3.69	2.02
	Transtibial	23	3.19	2.09
	Two Incision	22	6.30	3.63
Tibia	Medial Portal	22	4.85	2.06
	Transtibial	23	5.70	2.10
	Two Incision	22	5.42	3.28

Table 6.12 Standard descriptive statistics for the patient study describing the distance from the tunnel aperture centroid to the AM bundle center for the tibia and the femur organized by surgical technique.

Bone	Technique	# of Subjects	Average Distance (mm)	Standard Deviation (mm)
Femur	Medial Portal	58	4.42	2.76
	Transtibial	10	4.07	2.52
	Two Incision	10	5.63	3.45
Tibia	Medial Portal	58	5.98	3.60
	Transtibial	10	6.88	4.05
	Two Incision	10	8.12	3.07

Table 6.13 Standard descriptive statistics for the patient study describing the distance from the tunnel aperture centroid to the PL bundle center for the tibia and the femur organized by surgical technique.

Bone	Technique	# of Subjects	Average Distance (mm)	Standard Deviation (mm)
Femur	Medial Portal	58	3.56	2.28
	Transtibial	10	4.74	2.64
	Two Incision	10	5.62	3.69
Tibia	Medial Portal	58	5.24	2.67
	Transtibial	10	4.78	1.72
	Two Incision	10	5.43	1.85

Table 6.14 Standard descriptive statistics for the patient study describing the distance from the tunnel aperture centroid to the center point between the bundle centers for the tibia and the femur organized by surgical technique.

Bone	Technique	# of Subjects	Average Distance (mm)	Standard Deviation (mm)
Femur	Medial Portal	58	3.78	2.43
	Transtibial	10	4.15	2.58
	Two Incision	10	5.33	3.71
Tibia	Medial Portal	58	4.82	2.62
	Transtibial	10	4.98	2.88
	Two Incision	10	5.91	2.80

6.7.4 Discussion and Conclusions

The qualitative evaluation using the discrete sphere representations demonstrates that the estimated footprint for the femur and tibia aligns well with the regions with the highest frequency of projected drill tunnel centroids. Additionally, the ACL Tunnel Aperture Overlap Maps also show that the estimated locations of the bundle centroids

often lie within the regions that were most frequently hit by a drill bit during the reconstruction.

In the cadaver study with regards to the femur, the transtibial technique on average placed the drill tunnels closest to the AM bundle, the medial portal technique on average placed the drill tunnels closest to the PL bundle, and the transtibial technique on average placed the drill tunnels closest to the midpoint between the AM and PL bundles. With regards to the tibia, the medial portal technique on average placed the drill tunnels closest to the AM bundle, the transtibial technique on average placed the drill tunnels closest to the PL bundle, and the medial portal technique on average placed the drill tunnels closest to the midpoint between the AM and PL bundles.

In the patient study with regards to the femur, the transtibial technique on average placed the drill tunnels closest to the AM bundle, the medial portal technique on average placed the drill tunnels closest to the PL bundle, and the medial portal technique on average placed the drill tunnels closest to the midpoint between the AM and PL bundles. With regards to the tibia, the medial portal technique on average placed the drill tunnels closest to the AM bundle, the transtibial technique on average placed the drill tunnels closest to the PL bundle, and the medial portal technique on average placed the drill tunnels closest to the midpoint between the AM and PL bundles.

These findings suggest that the medial portal and transtibial technique are placing the drill tunnel aperture closest to the ACL footprint. The medial portal technique placed the drill tunnel aperture closest to the midpoint of the bundles on average. This study is very much an estimation, and is a stepping stone for future studies that compare the placement of the reconstruction drill bit with the actual location of the native footprint.

6.8 ACL Revision Cases

A retrospective chart review of the patient dataset at The University of Iowa showed three of the 20 patient's to have required revision surgeries. Figure 6.50

demonstrates the three cases with respect to the estimated AM and PL bundle positions (yellow spheres). One of the three cases showed distances from the midpoint of the estimated femoral bundles to be greater than the average and one standard deviation for the given surgical technique. In two of the cases, two femoral tunnel angles were outside the average and two standard deviations for the given surgical technique. The tibial aperture positions were within the average and standard deviation for the given surgical technique in all cases. In two of the three cases, two tibial tunnel angles were outside the average and two standard deviations for the given surgical technique.

Of the three ACL revisions, two of the three cases were related to a traumatic incident (red and green spheres in Figure 6.50). The other revision case could not be attached to a single traumatic incident (blue sphere in Figure 6.50). This case showed positioning of the tibial aperture and tunnel within the average and standard deviation of the given surgical technique. The femoral aperture positioning as shown in Figure 6.50A was distant from the midpoint of the two ACL bundles, but still within the average and standard deviation for the given technique.

With only a single revision case available for evaluation and with a limitation of an estimated anatomic footprint, drawing any associations between ACL revisions and reasons for failure would be not be prudent. Additional access to the medical records for the remainder of the MOON dataset or establishing a study looking specifically at ACL revisions would be a direction for future research.

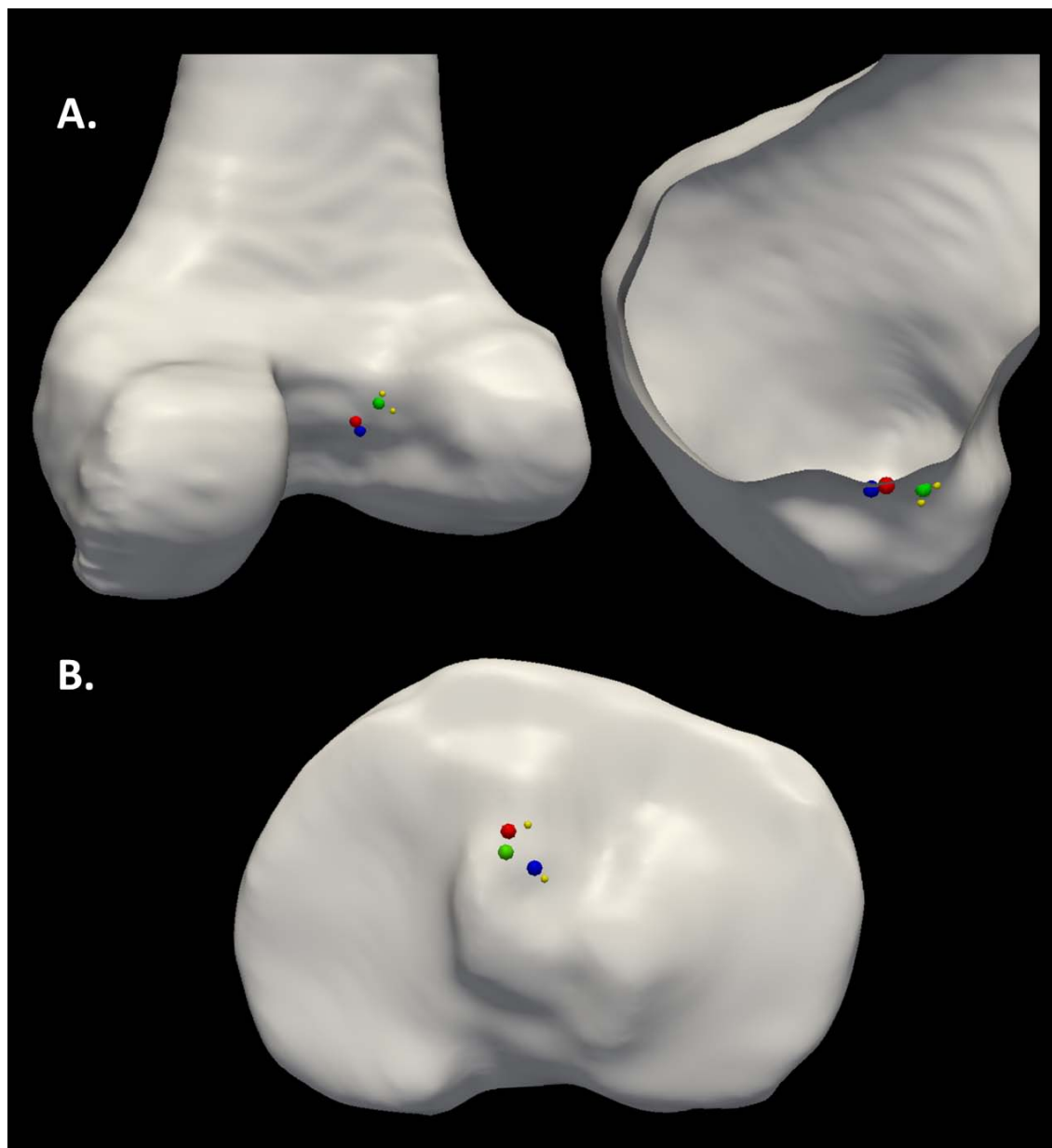


Figure 6.50 Discrete sphere representation of the A) femur (two views) and the B) tibia demonstrating the 3 revisions at The University of Iowa to date from the MOON patient dataset. The red, blue, and green spheres represent the 3 different patients, while the smaller yellow spheres represent the AM and PL bundles of the estimated ACL location.

CHAPTER 7

CONCLUDING REMARKS

7.1 Overview

The potential of improving patient care using patient-specific orthopaedic modeling and analysis is real. We have reviewed the literature regarding patient-specific modeling with special attention given to the anterior cruciate ligament. Our laboratory's software package aims at expediting the patient-specific modeling process. In an effort to automate several manual procedures in the laboratory software, the ABBA and BBGA tools were developed to automate the process of block placement in multiblock hexahedral meshing. We have also shown the EM segmentation method to be applicable to identifying cortical bone from CT images, and we have developed a nearly automated process for generating patient-specific probability maps for the EM algorithm. In addition, we have developed the *IA-Image Processing* toolkit to connect image processing and surface generation operations with the surface modification and meshing tools already contained in our laboratory software package.

We have applied many of the tools that we developed to a study investigating the variability in ACL graft placement. This study also required the development of a consistent 3D measurement system, which was subsequently created. We have shown the measurement system to be consistent across users of varying backgrounds and have developed an automated drill bit alignment method to help automate the manual aspects of the measurement process. After applying the measurement system to 150 CT datasets of the human knee, we compiled, grouped, and analyzed the data. Statistical analysis was performed to investigate statistically significant differences in the surgical technique, level of surgeon experience, and surgeon in the placement of ACL drill tunnels. To help visualize the results for this large-scale study, we have created two methods of visualization: Discrete ACL Aperture Centroid Maps and ACL Tunnel Aperture Overlap

Maps. In addition to visualization, we have compared our results to other studies performed in the past. Figure 7.1 demonstrates a summary of the various items we have addressed in this document.

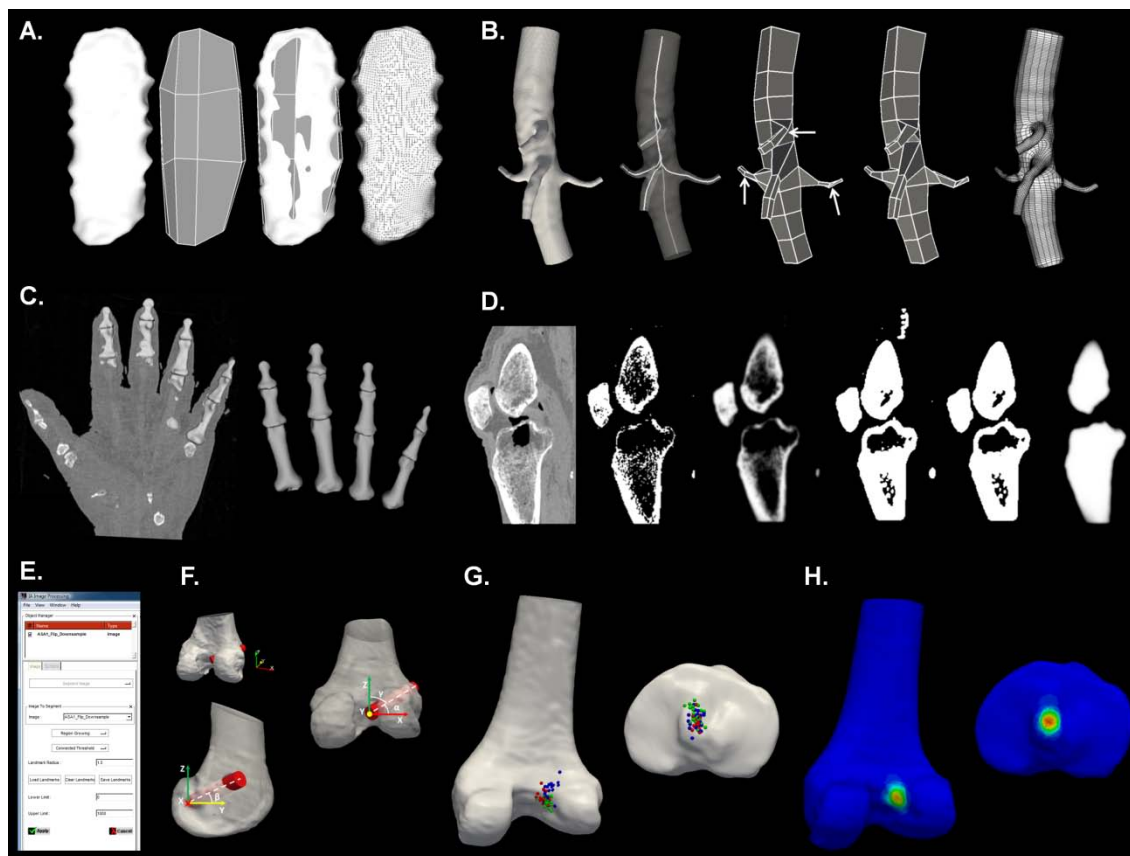


Figure 7.1 Sample results from various sections of this thesis. A) The ABBA applied to the sternum. B) The BBGA applied to a human aorta. C) EM segmentation of the phalanx bones of the hand. D) Patient-specific probability map generation for use with EM segmentation. E) The *IA-Image Processing* toolkit. F) The novel 3D ACL drill tunnel measurement system for the femur. G) Discrete sphere representation from the cadaver study. H) ACL Aperture Overlap Maps from the cadaver study.

7.2 Limitations and Future Work

The ability to analyze patient-specific surgical procedures in a clinically relevant period of time is desirable. Continued development of automated algorithms for high-throughput orthopaedic analysis will be a research priority in the coming years. Thus, future work exists for each research area presented in this document.

With regards to the algorithms for automated multiblock definitions, neither algorithm handled foramina such as that found in the vertebrae. In another effort, our laboratory has developed an independent method to map a template multiblock structure onto a subject multiblock structure. This algorithm has been shown successful on the vertebrae. Additional automated techniques to incorporate bone tunnels into multiblock structures would also be of benefit for mesh development in surgical finite element simulations. Outside orthopaedics, continued application of the BBGA to the vascular system could provide a fast means of hexahedral mesh generation for 3D computational hemodynamic research.

With regards to the Expectation Maximization bone segmentation methods, determining a method to incorporate drill tunnels into bone segmentations would be of future benefit to our work on ACL reconstructions. Additionally, generating a method to automatically determine an image-specific threshold value would help to avoid the current voxel selection procedure used to establish patient-specific probability maps. With these improvements, EM bone segmentation will become more clinically practical.

With regards to the *IA-Image Processing* toolkit, a variety of features could be incorporated. First, the EM segmentation protocol could be incorporated to offer an additional means of automated image segmentation. This additional functionality would add to the image processing, image segmentation, segmentation editing, and surface generation tools already available in the software package. On the programming side, inclusion of `vtkKWImage` would help to cleanly handle the conversion between VTK and ITK images. With regards to the current manual segmentation tools, several

improvements could be implemented including the ability to segment multiple regions of interest simultaneously and the utilization of image data into the contour based tracing methods.

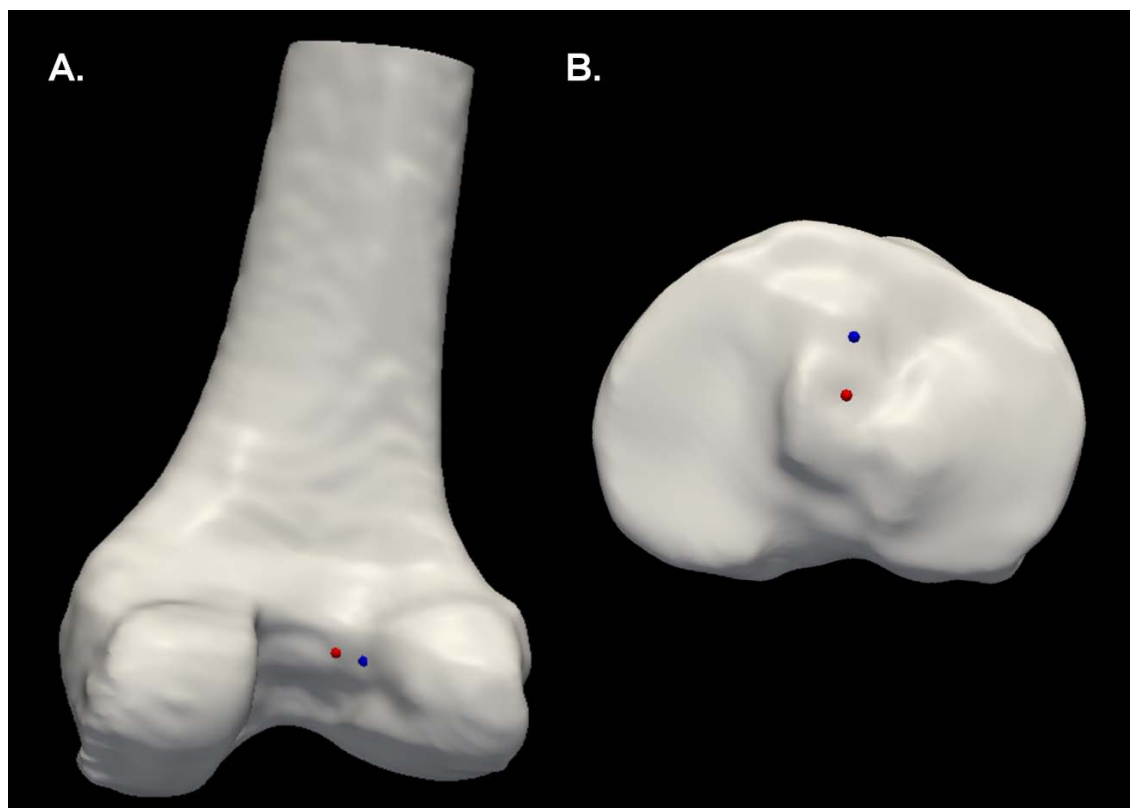


Figure 7.2 A case of bilateral ACL reconstructions performed by the same surgeon on the same day demonstrated on the A) femur and B) tibia. Both left and right ACL tunnel aperture centroids are represented: left (blue) and right (red).

With regards to the ACL tunnel placement variability project, additional studies investigating graft placement with respect to the anatomic footprint are required to establish statistically significant results that can be used to improve patient outcomes. However, a number of research questions have grown from this project. Figure 7.2 demonstrates a case of bilateral ACL reconstructions where both tunnel aperture

centroids are represented on the right femur. Both procedures were performed by the same surgeon, presumably on the same day. Considering that the knees are mirror images of each other, it is surprising to see the difference in graft placement in a single subject performed by a single surgeon. A future study investigating differences between graft placements in bilateral ACL reconstructions would be interesting as it would largely eliminate anatomic variability from confounding measurements across different patients. Additionally, a study comparing the results from a cadaveric versus a patient dataset would help to validate whether cadaveric studies are reasonable representations of in vivo ACL reconstructions.

Due to lack of access to information at other institutions, the number of ACL revisions from the patient dataset was largely unavailable. Thus our analysis was limited to the patients at The University of Iowa. The ability to correlate a larger number of ACL revision cases from other institutions with the established 3D measurements for the patient dataset would be an interesting extension that would allow correlation between clinical outcome and quantitative analysis. The results from this analysis could be used as a starting point for finite element studies investigating the biomechanics of the ACL reconstructed knee on a patient-specific basis. Using the results of this study as baseline values for tunnel angles and aperture positions, finite element studies could provide a computational and biomechanical perspective to the variables investigated in this work.

Additionally, the measurement and visualization methods developed for the single bundle ACL reconstruction study have application to numerous other arthroscopic procedures. Firstly, this method could be easily extended to include double bundle ACL reconstructions and posterior cruciate ligament (PCL) reconstructions using the same surgeon oriented coordinate system we have established. Furthermore, these methods could be extended to evaluate the variability in arthroscopic repairs of the shoulder where drill tunnels are also used.

7.3 Closing

As medicine moves away from the “One-Size-Fits-All” paradigm, patient-specific analysis will become routine. Many of the tools necessary to allow for patient-specific analysis within a clinically practical period of time are still in development. We have developed a number of tools for patient-specific analysis, which will hopefully allow for further investigation of graft placement in ACL reconstruction as well as application to other regions of the human musculoskeletal system. In the future, we hope our tools will be used to improve the surgical outcomes for orthopaedic patients.

APPENDIX A

AUTOMATED MULTIBLOCK DEFINITIONS

Here, we provide two figures relevant to the methods of the automated multiblock hexahedral meshing work. This first image demonstrates a sample loading and constraining condition for a hexahedral mesh. The second image demonstrates the results from a mesh quality check for positive volume elements.

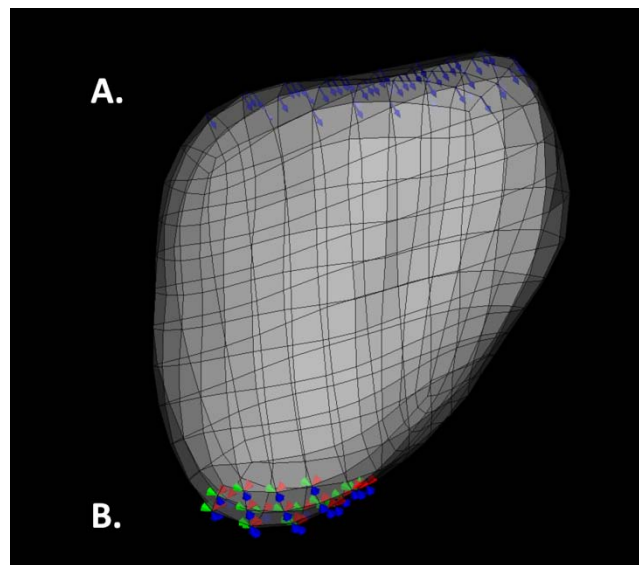


Figure A.1 An example of how loads and boundary conditions were assigned to a hexahedral mesh. A) A load of 30N is distributed to the nodes corresponding to one side of the hexahedral mesh. B) A zero displacement boundary condition for all three primary axes is applied to the nodes opposing the loaded nodes of the hexahedral mesh.

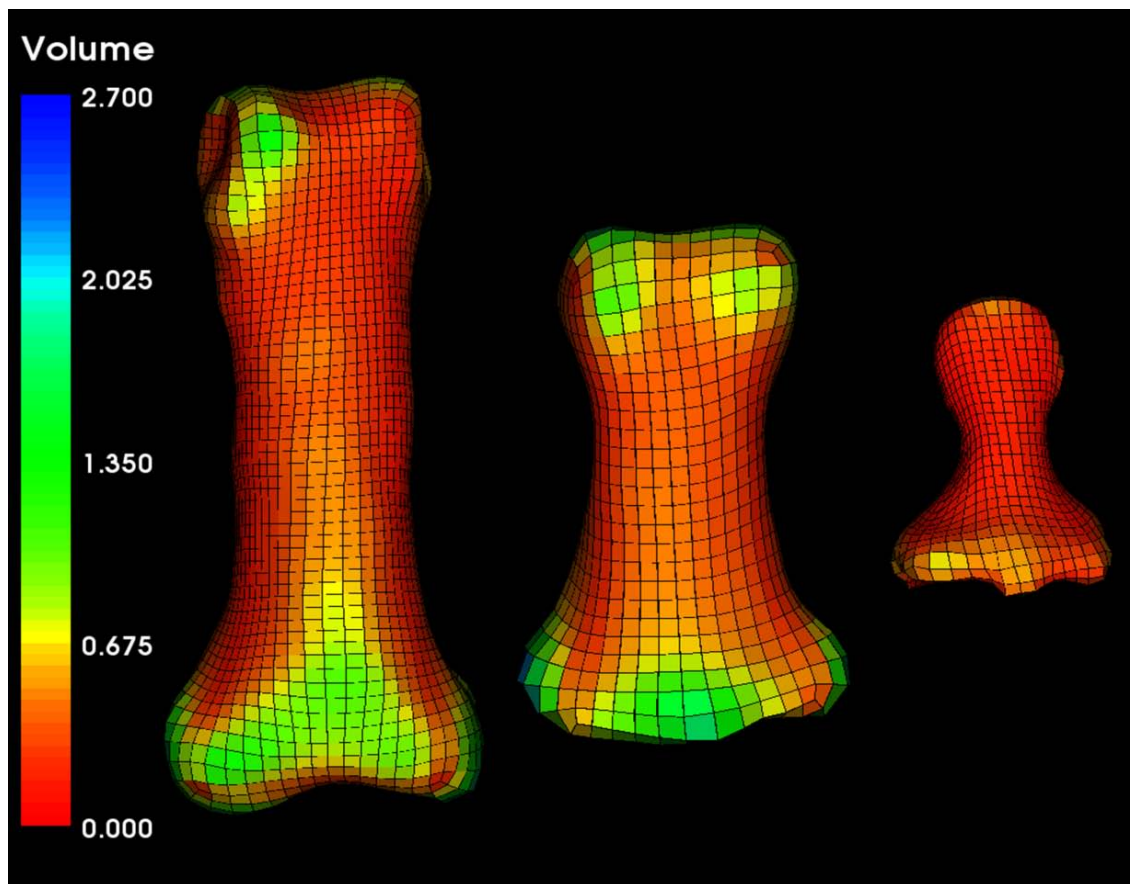


Figure A.2 A volume mesh quality metric for the phalanx bones of the index finger demonstrating positive volume elements.

APPENDIX B

IA-IMAGE PROCESSING TOOLKIT

Here, we describe the tools contained in the *IA-Image Processing* toolkit. This section is broken into five parts: pre-processing tools, orthopaedic segmentation tools, surface tools, graphical user interface, and record keeping.

B.1 Pre-Processing Tools

B.1.1 Resampling Tool

This functionality allows the user to alter the voxel size of a three-dimensional image set as shown in Figure B.2. We have built two programs that allow for user-defined resampling and isotropic resampling. The user-defined resampling functionality allows the user to either downsample or supersample an image set based on specified dimensions for each axis (x, y, and z). Typically, medical images have a slice thickness that is greater than the in-plane resolution. This anisotropy can make it difficult to estimate error when generating anatomic models or when performing measurements on a dataset. The isotropic resampling functionality enables the user to define the desired isotropic voxel dimension for an image set.

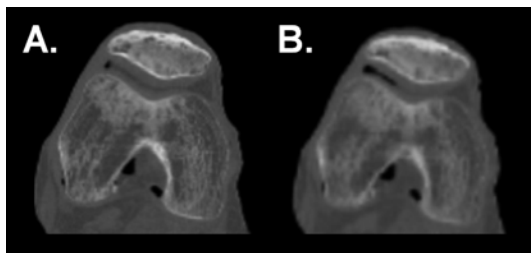


Figure B.1 A resample operation example demonstrated on a human knee CT imaging study. The figure depicts the A) original image and the B) isotropically resampled image. This functionality can be used to reduce the file size of an image to allow for automated segmentation. It can also be used to create an isotropic image to allow for easier error estimation.

B.1.2 Mirror Tool

This functionality allows the user to mirror a three-dimensional image set along any of the three normal axes (x, y, and z). This tool can help to simplify analysis by using the body's symmetry to our advantage. For example, in a study investigating ACL tunnel angles in a knee, mirroring all left knees to be right knees allows for a single measurement system. The mirroring function is also useful in image segmentation by allowing a single atlas to be used as a probability map for the segmentation. An example of the mirror utility is shown in Figure B.3.

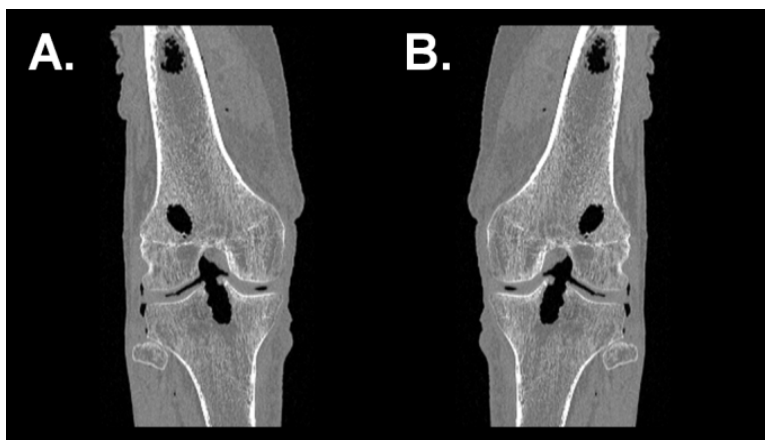


Figure B.2 A mirror operation example demonstrated on a human knee imaging study. This functionality can be used to simplify large-scale studies by transforming all knees to either right or left representations. A) A right knee is transformed to a B) left knee.

B.1.3 Threshold Tool

This functionality provides basic thresholding features for a three-dimensional image. The user can select either a gray-scale or binary output. The user can threshold above, below, or between specified voxel intensity values. This can be useful as a simple method of bone segmentation. It can also be used to remove beam hardening artifacts,

due to implanted hardware, that can obscure images and inhibit other image processing functionalities (Figure B.4).

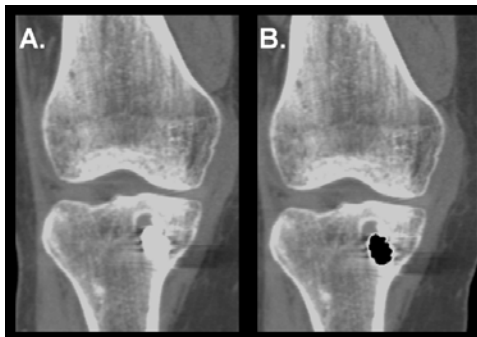


Figure B.3 A thresholding operation used to remove hardware artifacts from an ACL reconstruction CT image. A) The image containing hardware artifact and B) the image after the artifact has been removed.

B.1.4 Cropping Tool

The cropping tool is useful for removing unwanted portions of an image set or for splitting an image into separate image sets. Figure B.5 demonstrates a single CT image containing two separate knees that are transformed into two images, each containing a single knee.

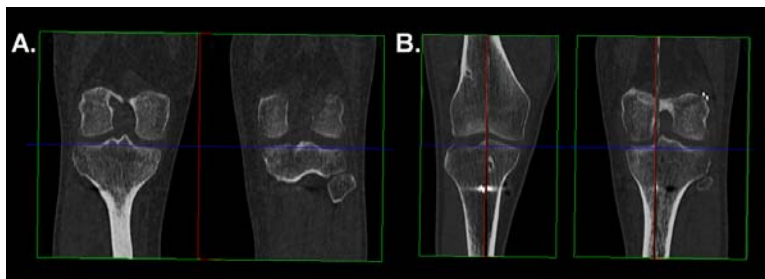


Figure B.4 The cropping tool. A) A CT image containing two knees. B) The cropping tool applied to generate two separate image sets, each containing a single knee.

B.1.5 Image Math Tool

The image math tool is useful for adding and subtracting specific regions from an image set. For example, if two separate mask files were added, a single file containing both mask files could be created as shown in Figure B.6A. Also, consider a mask file for a solid bone and another mask file representing a tunnel through that bone. Image subtraction could be used to generate a mask file of the bone containing the tunnel as shown in Figure B.6B.

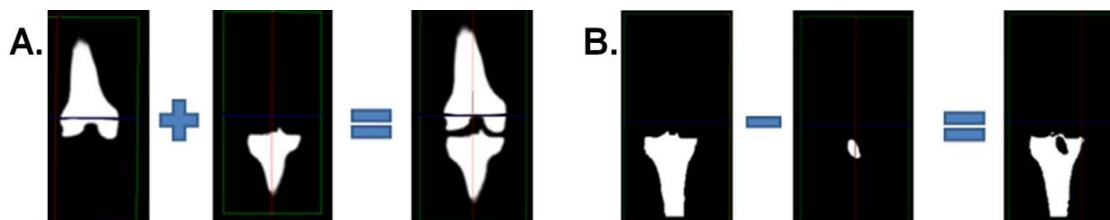


Figure B.5 The image math tool. A) Image addition demonstrated using two mask files: femur and tibia. B) Image subtraction demonstrated using two mask files: tibia and tibial drill tunnel.

B.1.6 Island Removal and Gap Filling Tool

Automated segmentation procedures can result in mask representations of bone such as that seen in Figure B.7A. This mask contains gaps in regions of trabecular bone and islands of incorrectly identified voxels. This tool eliminates the islands and fills gaps in the mask representations as demonstrated in Figure B.7B.

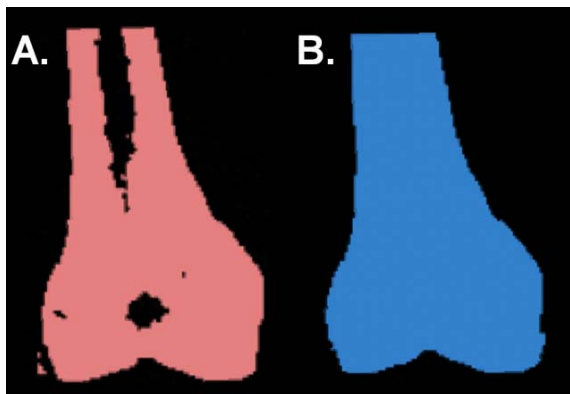


Figure B.6 The island removal and gap filling tool. A) The raw results of automated segmentation can result in mask representations of the region of interest (e.g. distal femur) containing gaps and islands. B) After application of the island removal and gap filling tool, the resulting mask representation contains no islands or gaps.

B.1.7 Gaussian Smoothing Tool

This functionality applies a Gaussian smoothing filter to a three-dimensional image set to reduce noise or to add gray scale levels. In our applications, this can be useful in the generation of probability maps for image segmentation. This functionality is demonstrated in Figure B.8.

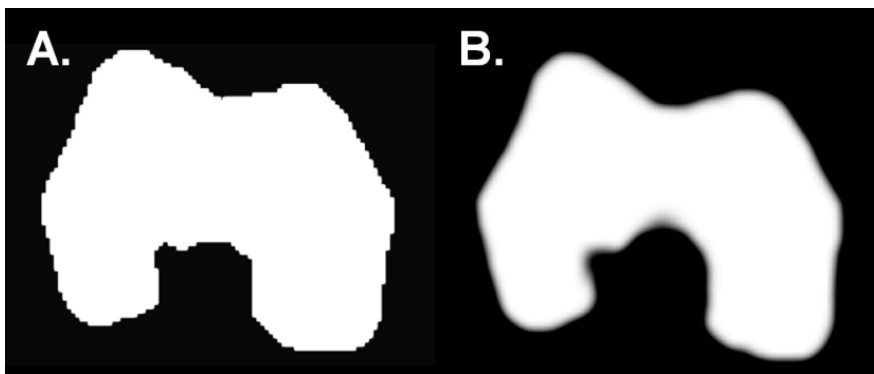


Figure B.7 A Gaussian smoothing operation demonstrated on a A) binary representation of the distal end of a femur and B) the resulting image. This operation is useful in developing probability maps that are required by some statistical image segmentation procedures (e.g. EM segmentation).

B.2 Orthopaedic Segmentation Tools

B.2.1 Simple Thresholding

The thresholding filter that was previously described can also be used as a segmentation tool for regions of interest that have very large differences in voxel intensity. Figure B.9 demonstrates the thresholding tool as a method of cortical bone segmentation.

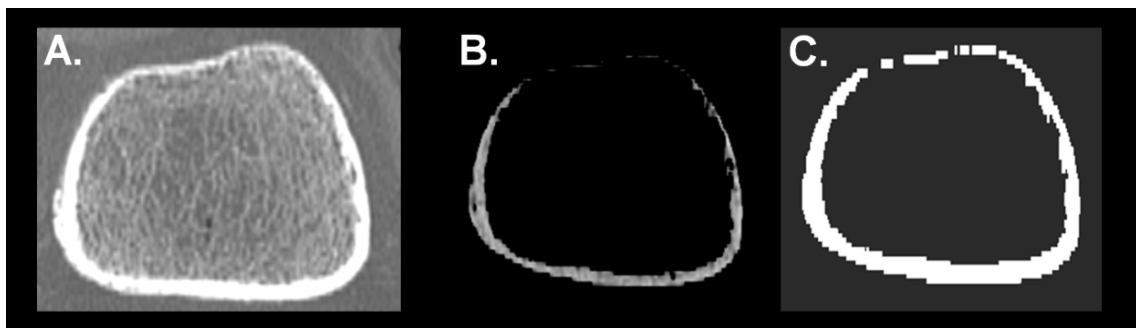


Figure B.8 A thresholding operation demonstrated on A) cortical bone with two possible outputs: B) gray scale or C) binary. This can be useful as a simple method of bone segmentation.

B.2.2 Region Growing

Region growing is a pixel-based means of image segmentation that requires the selection of an initial set of seed points and several user-defined parameters to identify a region of interest from the surrounding tissue structures. Depending on the user-defined criteria and the specific region growing algorithm, neighboring voxels are compared to the seed points to determine whether or not the neighboring voxels should be marked as a part of the region of interest. This process is iterated over until all neighboring voxels are either marked or have been ignored. We include two region growing algorithms in our toolkit that are helpful to orthopaedic segmentation applications: connected threshold and

confidence connected algorithms. An example of the connected threshold algorithm is available in Figure B.10A/B and an example of the confidence connected algorithm is available in Figure B.10C/D.

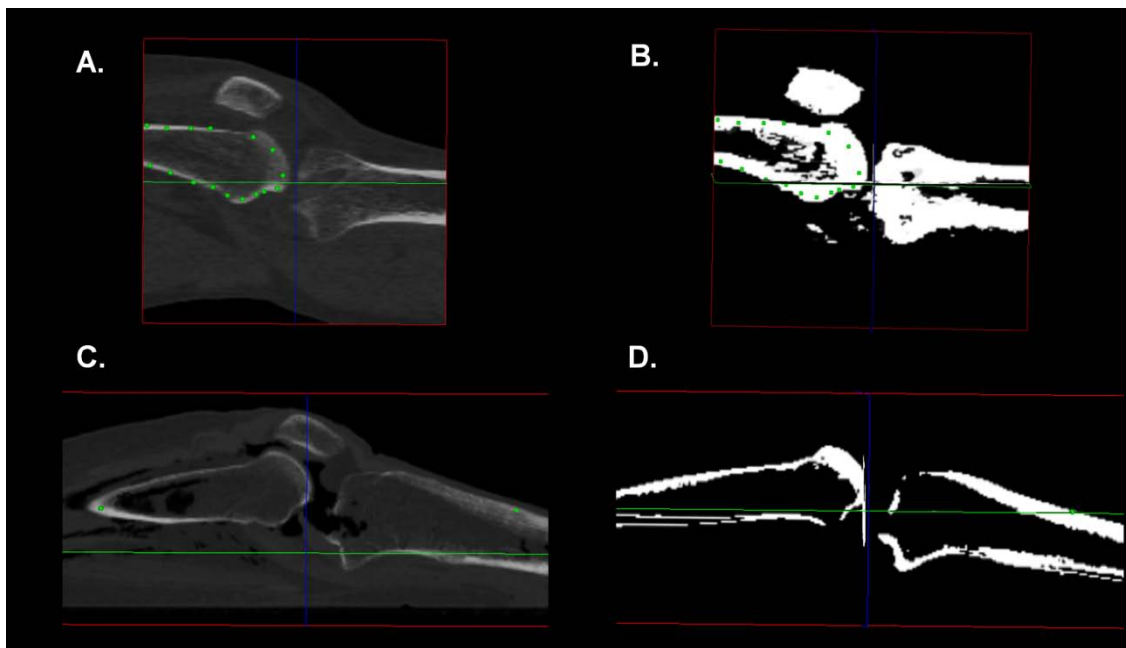


Figure B.9 Region growing segmentation examples. A) Selection of seed points for the connected threshold region growing algorithm. B) An example result from the seed points chosen in (A) for the connected threshold region growing algorithm. C) Selection of seed points for the confidence connected region growing algorithm. D) An example result from the seed points chosen in (C) for the confidence connected region growing algorithm.

The connected threshold algorithm takes a lower and upper threshold value as input; voxels falling within this intensity range are marked as being part of the region of interest during the region growing procedure, while voxels falling outside this range are ignored. The confidence connected algorithm calculates the median intensity value from selected seed points and uses user-defined parameters to automatically calculate the

threshold range to establish which voxels should be accepted as a portion of the region of interest.

B.2.3 Manual Contour-Based Segmentation

Contour-based segmentation is a manual process that allows the user to select points on the outline of a surface. Between the points, an interpolating spline connects the points. Our toolkit allows for placement of contours onto a slice of image data (Figure B.11). It also allows for deletion of a contour from a slice (Figure B.12) and deletion of all contours from a slice (Figure B.13). We have also included the ability to copy contours from one slice to the next or previous slice (Figure B.14). If after a contour is placed modification is necessary, we have included the ability to select and modify a contour. After all contours have been placed, we have included the functionality to convert contours to a binary mask representation (Figure B.15), which can be used for surface generation. After a mask has been generated, we have included a tool to convert the mask back to a contour representation (Figure B.16), which will allow for editing of automatic segmentations. Finally, we have included the ability to load and save contours.

This tool has multiple applications. A user can generate contours for a given bone and subsequently a binary mask representation that can be converted into a surface representation. In addition, a mask representation generated from another segmentation procedure (e.g. region-growing) can be transformed into a set of contours (Figure B.17), which can subsequently be used to edit the segmentation for improved accuracy. The surface functionalities of our toolkit are presented next.

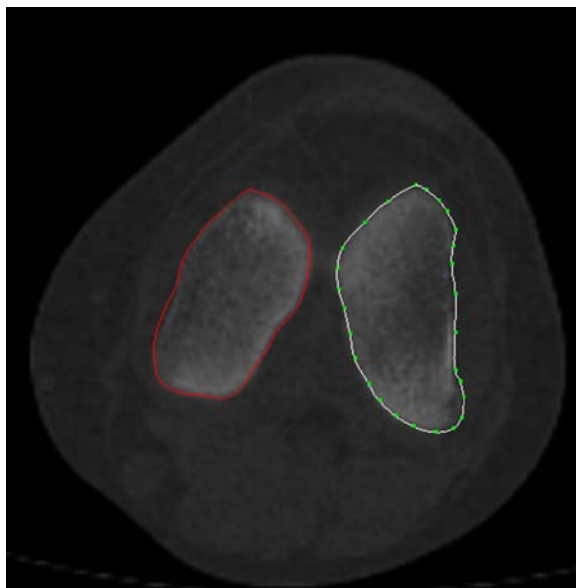


Figure B.10 Addition of a second contour to an axial CT slice.

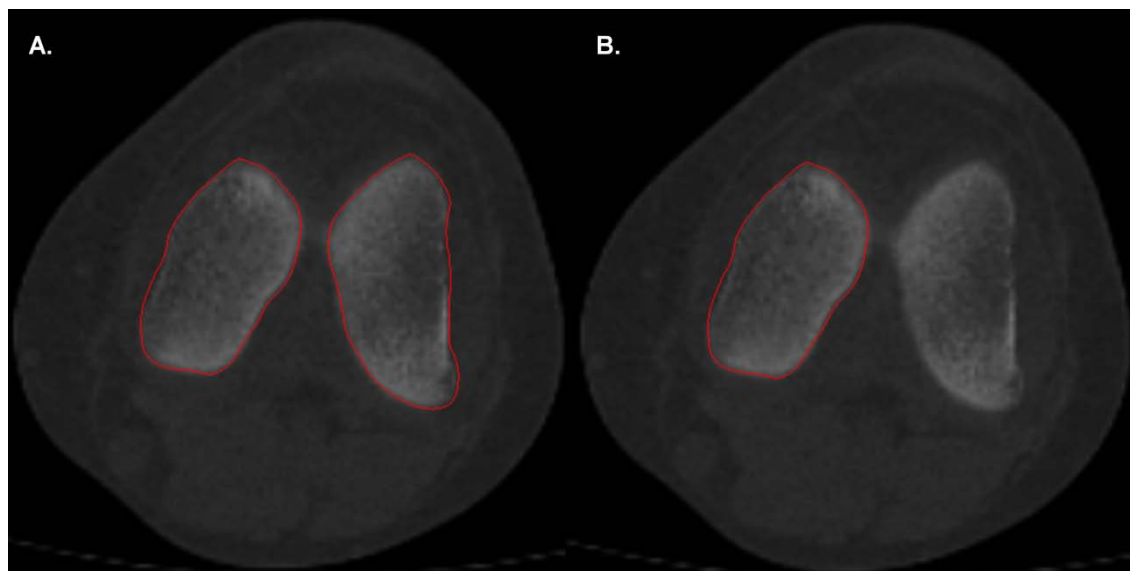


Figure B.11 Contour deletion functionality. A) Two contours for an axial CT slice. B) Deletion of a single contour by a user on an axial CT slice.

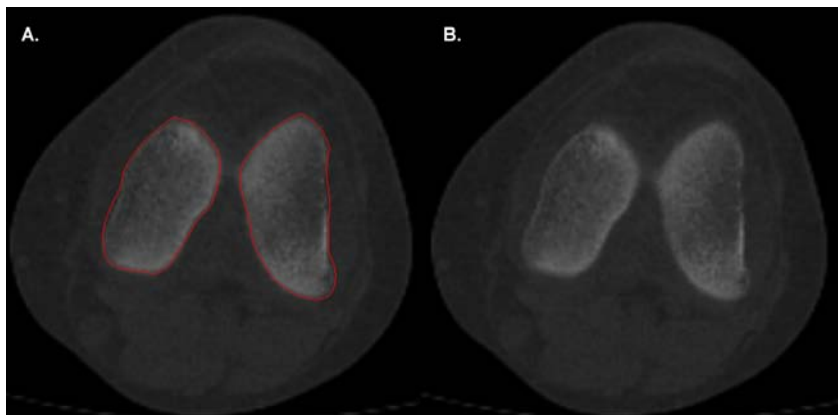


Figure B.12 Contour deletion functionality for all slice contours. A) Two contours assigned to an axial CT slice. B) Deletion of all of a slice's contours from an axial CT slice.

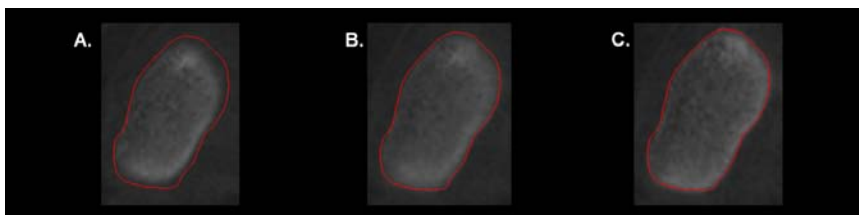


Figure B.13 The copy operation can copy a B) given contour to the A) previous slice and to the C) next slice.

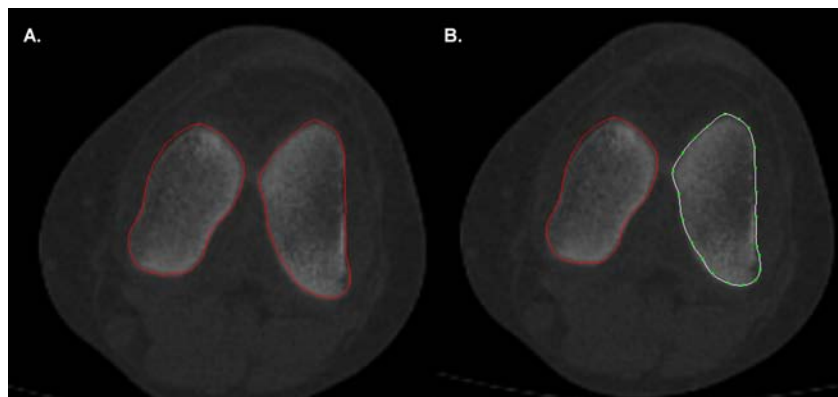


Figure B.14 The contour modification process. A) Two contours for an axial CT slice. B) Modification of a contour after placement.

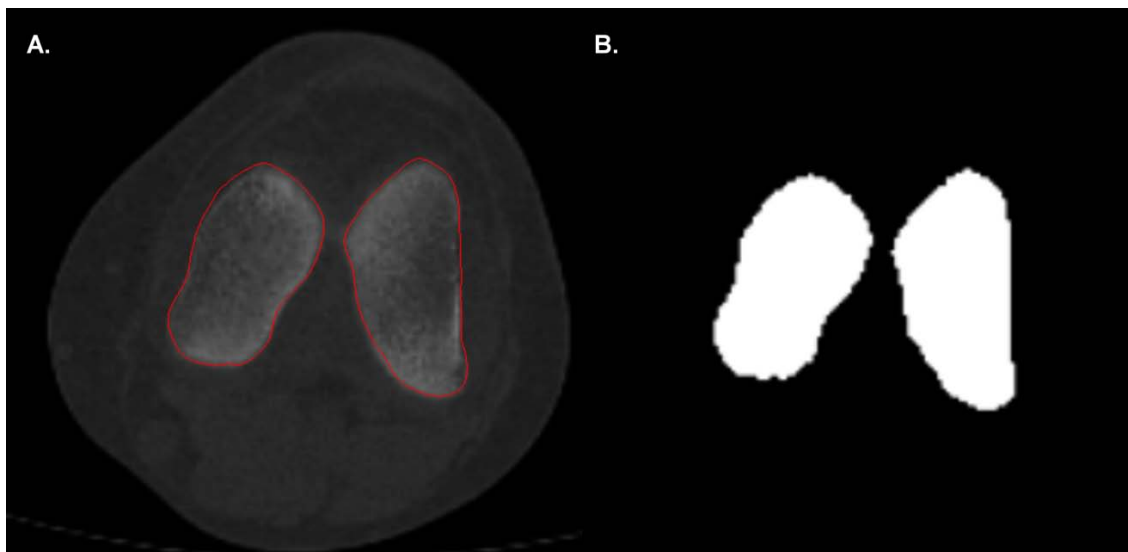


Figure B.15 The contour to mask conversion tool. A) Two contours for an axial CT slice. B) Creation of a binary representation from the contours.

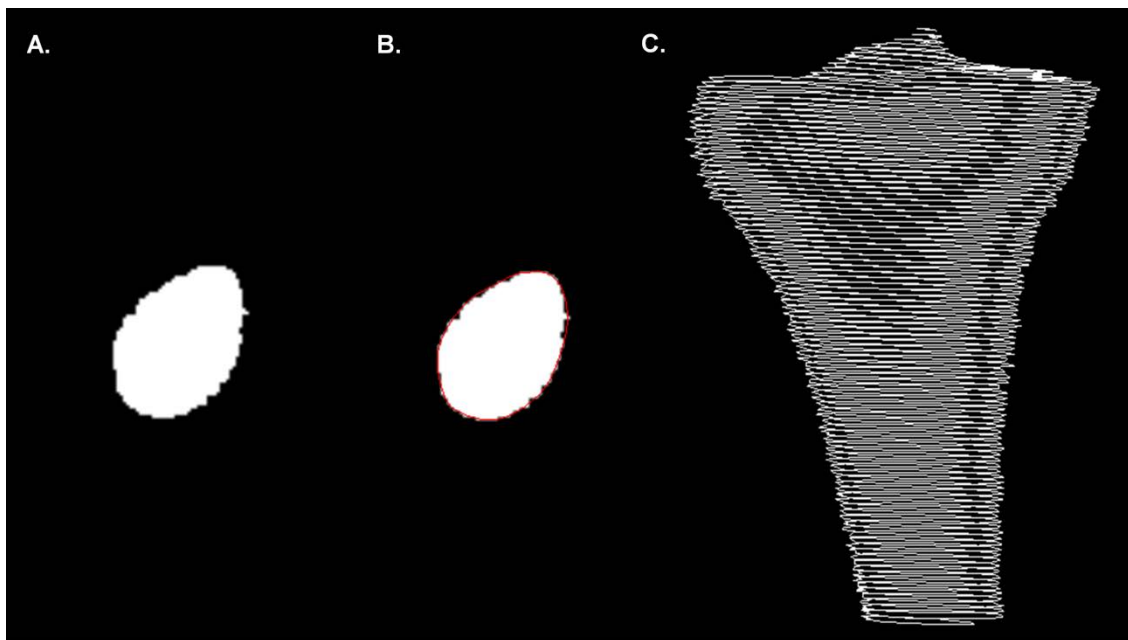


Figure B.16 The mask to contour conversion tool. A) A binary representation of a tibial diaphysis. B) Contour extracted from the binary representation. C) Visualization of all contours that have been extracted from a binary representation of a tibia.

B.3 Surface Tools

B.3.1 Surface Generation, Smoothing, and Decimation

After a binary representation of a region of interest has been generated from a three-dimensional image set, this tool is used to construct a three-dimensional triangulated surface. An example of this procedure can be seen in Figure B.18. This functionality allows for surface generation within the same software as image processing. Triangulated surfaces can be used for a variety of purposes ranging from spatial measurements to generation of hexahedral finite element meshes. Smoothing and decimation parameters have been included to allow for flexibility in the file size and appearance of the generated surface. A surface representation generated from a set of binary representations can result in a stair-step appearance. Surface smoothing can remove this artifact and help to give a more accurate representation of the surface. This tool is incorporated with the surface generation tool. This process can be visualized in Figure B.19. The decimation option allows for a reduction in the number of surface points to reduce file size.

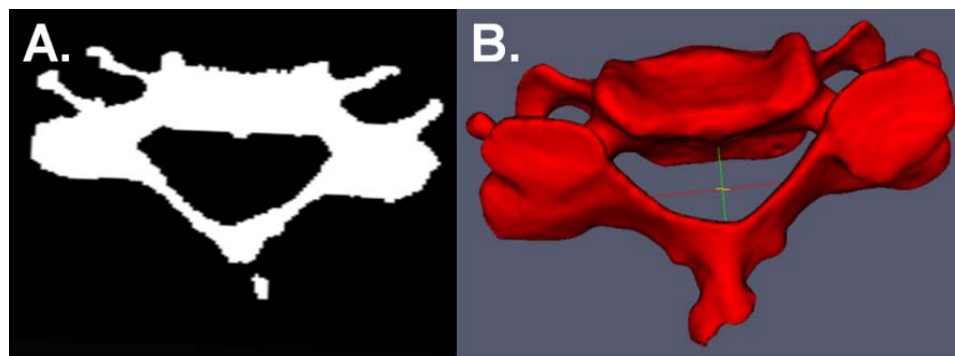


Figure B.17 The surface from mask generation tool. A) One slice from a three-dimensional binary representation of a cervical vertebra. B) A three-dimensional surface generated using the surface generation feature.

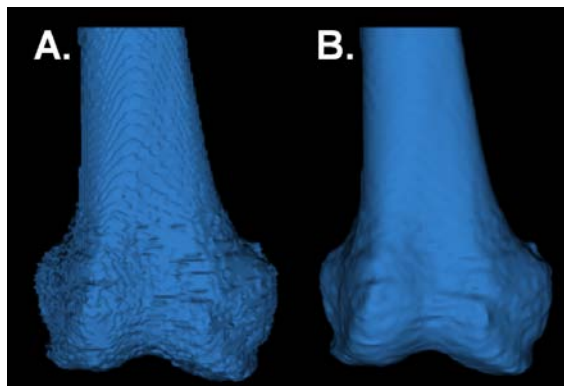


Figure B.18 The surface smoothing tool. A) A three-dimensional surface representation of a femur demonstrating a stair-step appearance artifact. B) A three-dimensional surface of a femur after surface smoothing.

B.3.2 Surface Registration Tool

Three-dimensional surfaces may not be aligned in the correct anatomical position as seen in Figure B.20A. An Iterative Closest Point (ICP) transform is available to orient three-dimensional surface representations of bone by finding the best match of surface points of the surface of interest with an atlas surface. Figure B.20B/C show the alignment of two different distal femur representations in three dimensions.

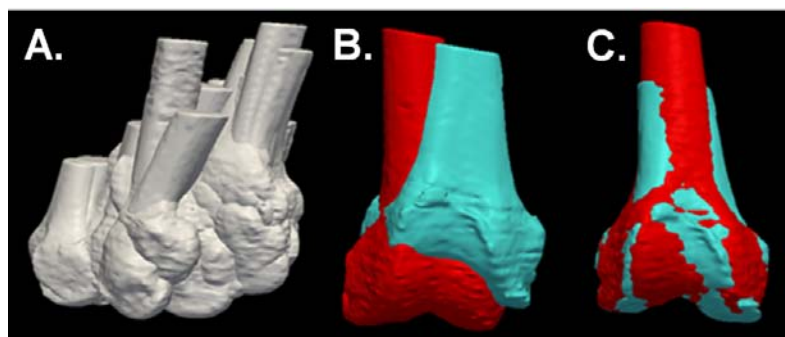


Figure B.19 The surface registration tool. A) Three-dimensional representations of 72 distal femurs demonstrating different positions and orientations of the surfaces. B) An atlas femur (red) and a subject femur (blue) that are not aligned in space. C) The subject femur (blue) aligned with atlas femur (red) using the ICP transform.

B.4 Graphical User Interface

B.4.1 Overview

The image processing tools described above were written using the ITK, VTK, and the C++ programming language. A command line setup was initially developed, which allows for scripting for large-scale studies requiring high throughput. A more user-friendly interface was desired to provide these tools to those with limited programming experience. A graphical user interface (GUI), *IA Image Processing*, was developed to include the described functionalities for orthopaedic image processing and provide a streamlined interface for image processing, segmentation, and surface generation. The GUI is being developed using KWWidgets and a screenshot from the GUI is shown in Figure B.21. This interface will allow those without a background in programming to perform image analysis for orthopaedic investigations.

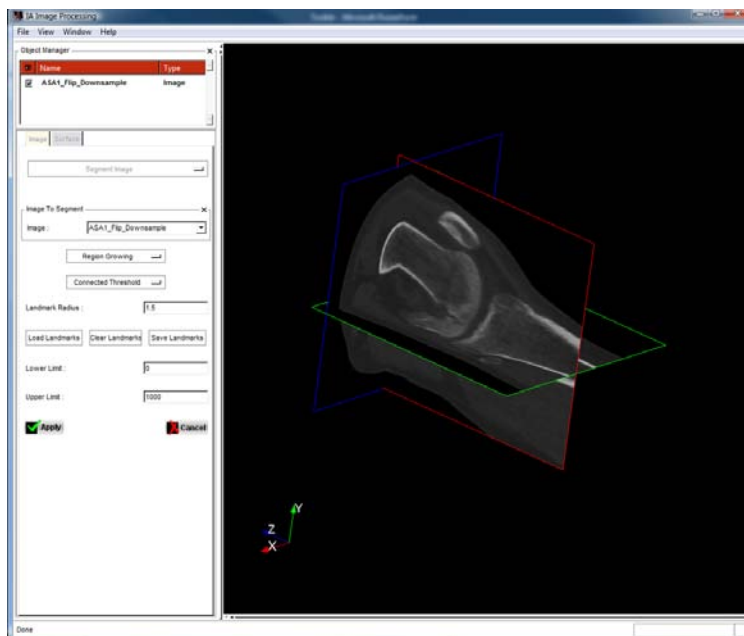


Figure B.20 A screenshot from the *IA-Image Processing* Graphical User Interface. This application allows access to image processing functionalities in a user-friendly interface.

B.4.2 Cropping Widget

Originally, the cropping operation described in Section B.1.4 required the user to manually define the pixel indices desired for the cropping operation from the image; this proved to be cumbersome from a usability standpoint. We have connected slider bars and a box widget in the graphical user interface to allow the user to interactively select the region for cropping as opposed to identifying pixel indices for the cropping procedure. An example of this interactive widget can be seen in Figure B.22.

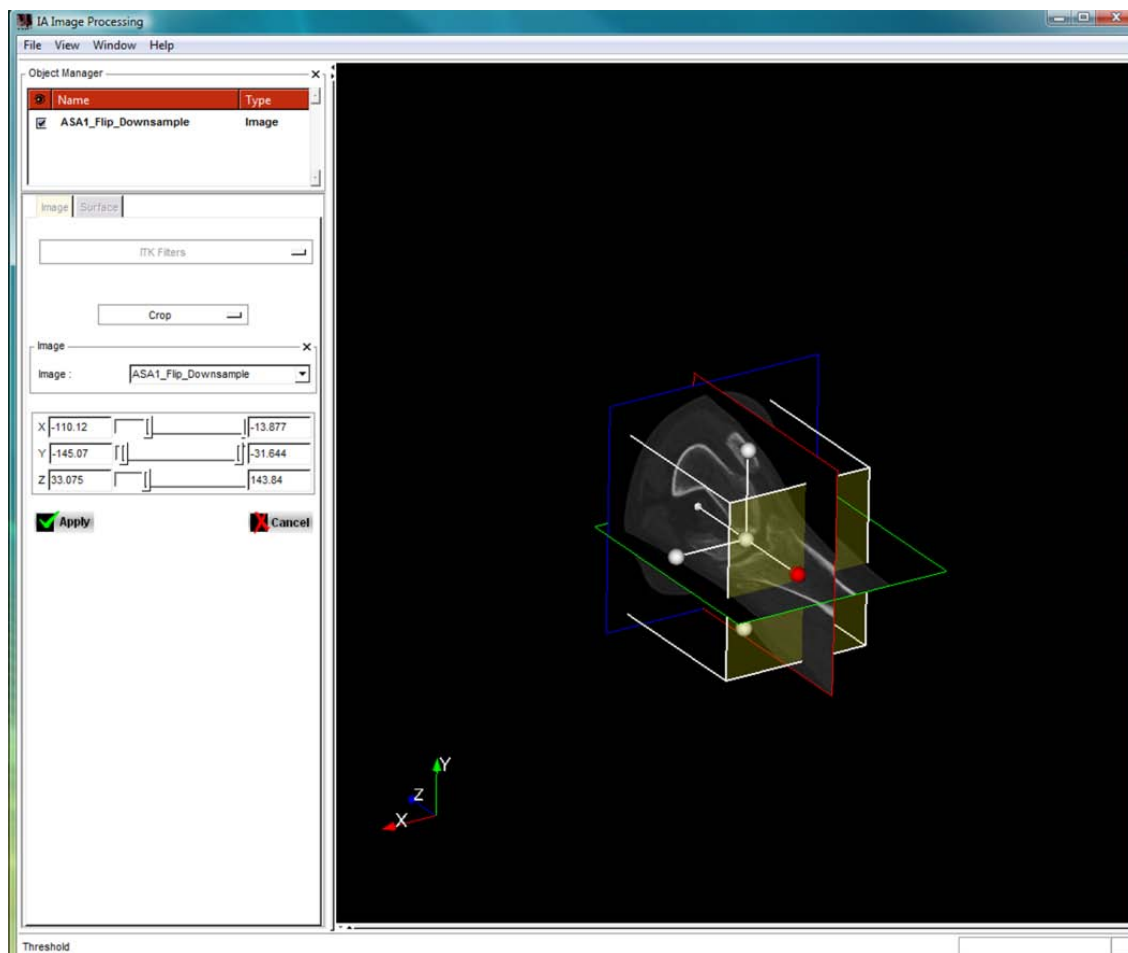


Figure B.21 A screenshot of the interactive cropping widget including a box with moveable faces and slider bars for control over the cropping operations.

B.4.3 Landmark Widget

The ability to select points on an image or surface is required by a number of operations including the Building Block Growing Algorithm (BBGA) and region growing segmentation. We have designed a widget that allows for addition, removal, and modification of landmarks on an image or a surface. By using the mouse and selecting a position, the user can generate a sphere representation of a landmark at the selected point, which is bound to either the surface or an image. The centroid of the sphere representations can be used as seed points for various operations. An example of this procedure is available in Figure B.23.

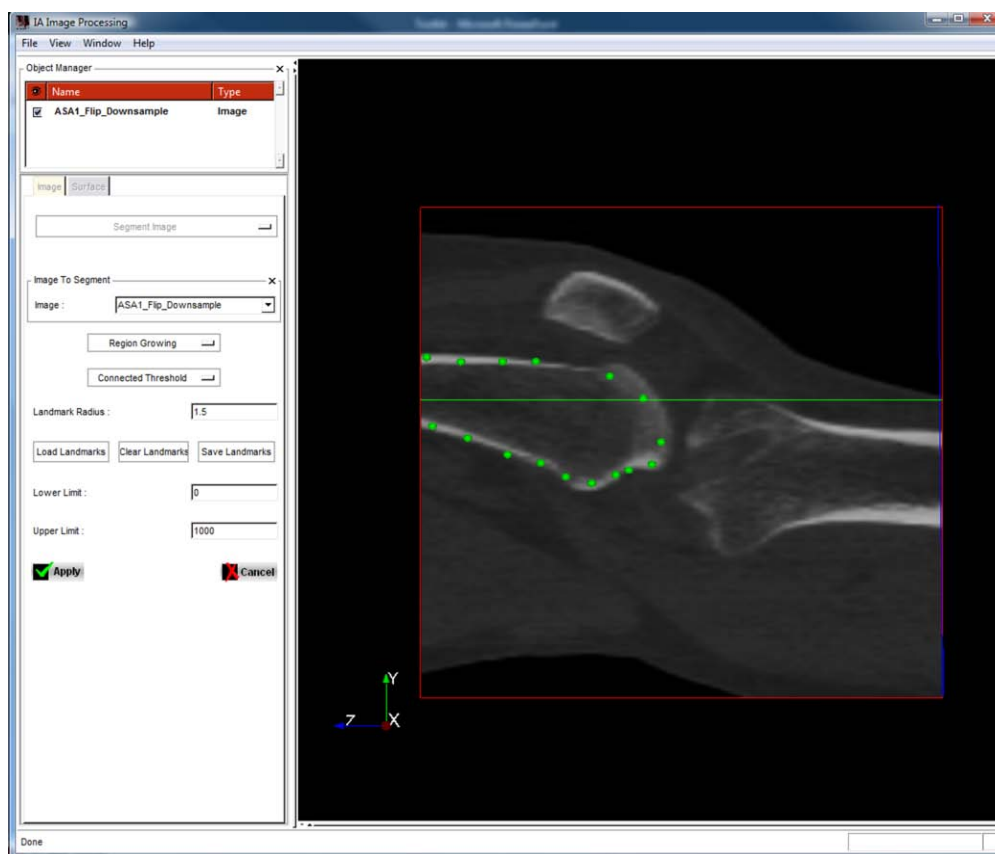


Figure B.22 A screenshot of the landmark widget applied to an image for seed selection used for region growing segmentation. This widget could also be used for landmark selection on a surface for the Building Block Growing Algorithm.

B.4.4 Contour Widget

To allow the ability to perform manual segmentations and edit past manual segmentations, a contour widget has been included into our toolkit. The contour widget allows for selection of points on the image plane viewer which are subsequently connected by a spline representation. We have included the ability to create contours on individual slices from each orthogonal view (Figure B.24A). After a contour is created/closed, it is represented as a red line (Figure B.24B). If the user wishes to edit the contour, they can select a previously created contour and modify the points.

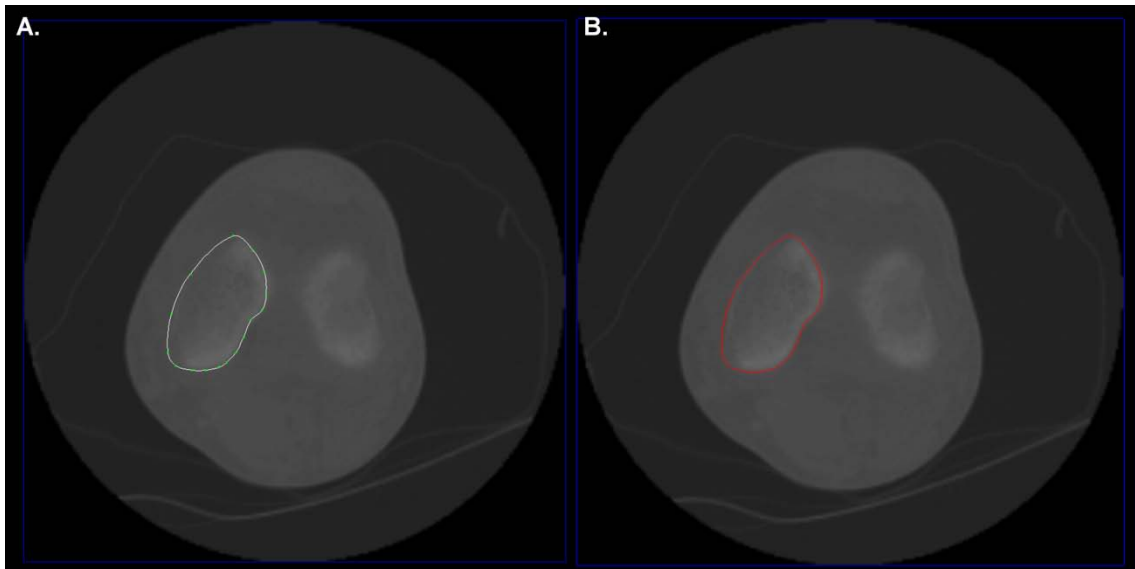
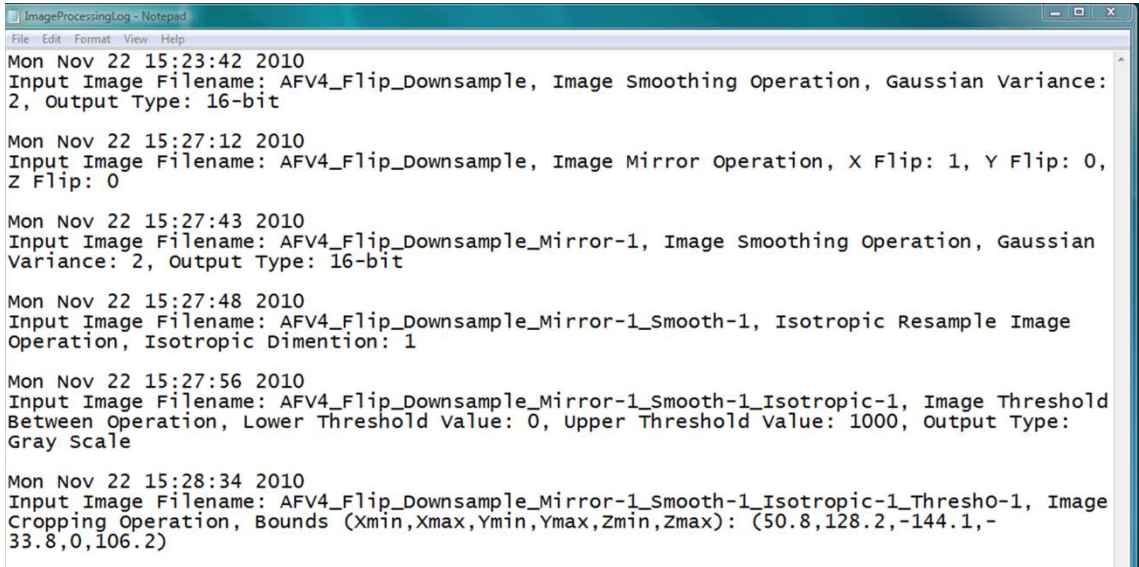


Figure B.23 Demonstration of the contour widget. A) The contour widget allows for point selection (green dots) with interpolated splines between the points. B) After a contour is finalized, it is represented as a red line.

B.5 Record Keeping

In image processing applications, it may be difficult to remember the exact order and parameters used when an image was originally filtered. To supplement this, we have included an automatic step record in the toolkit that records the date and time, filename of the image being processed, the name of the image processing operation, and any parameters that were used in the operation. This information is stored in .txt file and allows the user to trace operations they have used in the past for specific images. Figure B.25 demonstrates a sample step record.



```

ImageProcessingLog - Notepad
File Edit Format View Help
Mon Nov 22 15:23:42 2010
Input Image Filename: AFV4_Flip_Downsampling, Image Smoothing Operation, Gaussian Variance: 2, Output Type: 16-bit

Mon Nov 22 15:27:12 2010
Input Image Filename: AFV4_Flip_Downsampling, Image Mirror Operation, X Flip: 1, Y Flip: 0, Z Flip: 0

Mon Nov 22 15:27:43 2010
Input Image Filename: AFV4_Flip_Downsampling_Mirror-1, Image Smoothing Operation, Gaussian Variance: 2, Output Type: 16-bit

Mon Nov 22 15:27:48 2010
Input Image Filename: AFV4_Flip_Downsampling_Mirror-1_Smooth-1, Isotropic Resample Image Operation, Isotropic Dimension: 1

Mon Nov 22 15:27:56 2010
Input Image Filename: AFV4_Flip_Downsampling_Mirror-1_Smooth-1_Isotropic-1, Image Threshold Between Operation, Lower Threshold Value: 0, Upper Threshold Value: 1000, Output Type: Gray Scale

Mon Nov 22 15:28:34 2010
Input Image Filename: AFV4_Flip_Downsampling_Mirror-1_Smooth-1_Isotropic-1_Thresh0-1, Image Cropping Operation, Bounds (Xmin,Xmax,Ymin,Ymax,Zmin,Zmax): (50.8,128.2,-144.1,-33.8,0,106.2)

```

Figure B.24 A sample step record to allow the user to trace operations they have used in the past.

APPENDIX C

ANTERIOR CRUCIATE LIGAMENT GRAFT PLACEMENT

Here, we provide additional data for the MOON ACL study. This section of the Appendix is split into four components: tables, box and whisker plots, discrete sphere representations, and overlap maps.

C.1 Standard Descriptive Statistics

This section contains standard descriptive statistics in a table format for each of the variables in the MOON ACL study. These tables are meant to complement the box plots presented in the text to numerically characterize the data for future comparisons. The tables from the cadaver dataset are presented first and the patient dataset follows.

Table C.1 Descriptive statistics for the femoral and tibial tunnel angular measurements for the cadaver dataset.

	Femoral Tunnel			Tibial Tunnel		
	α (°)	β (°)	γ (°)	α (°)	β (°)	γ (°)
Average	52.9	55.3	58.0	76.0	58.5	35.0
Standard Deviation	13.4	10.0	14.9	7.3	8.2	8.0

Table C.2 Descriptive statistics for the femoral and tibial tunnel spatial measurements for the cadaver dataset.

	Femoral Tunnel		Tibial Tunnel	
	c/C	n/N	a/A	m/M
Average	0.68	0.47	0.47	0.45
Standard Deviation	0.10	0.08	0.07	0.03

Table C.3 Descriptive statistics for the femoral and tibial tunnel angular measurements for the cadaver dataset organized by surgical technique.

		Femoral Tunnel			Tibial Tunnel		
Technique	Metric	α (°)	β (°)	γ (°)	α (°)	β (°)	γ (°)
Medial Portal	Average	50.0	59.3	55.5	73.0	60.3	34.5
	Standard Deviation	12.3	11.1	8.2	5.6	8.2	7.0
Transtibial	Average	64.3	56.6	44.1	72.8	57.1	37.8
	Standard Deviation	6.9	6.9	5.4	5.1	6.1	5.9
Two Incision	Average	43.8	49.8	75.0	82.3	58.3	32.5
	Standard Deviation	11.2	9.4	8.8	6.6	10.1	10.1

Table C.4 Descriptive statistics for the femoral and tibial tunnel spatial measurements for the cadaver dataset organized by surgical technique.

		Femoral Tunnel		Tibial Tunnel	
Technique	Metric	c/C	n/N	a/A	m/M
Medial Portal	Average	0.62	0.45	0.44	0.45
	Standard Deviation	0.07	0.10	0.06	0.03
Transtibial	Average	0.66	0.49	0.50	0.45
	Standard Deviation	0.08	0.08	0.05	0.02
Two Incision	Average	0.76	0.47	0.48	0.46
	Standard Deviation	0.11	0.07	0.07	0.03

Table C.5 Descriptive statistics for the femoral and tibial tunnel angular measurements for the cadaver dataset organized level of surgeon experience.

		Femur			Tibia		
Experience	Metric	α (°)	β (°)	γ (°)	α (°)	β (°)	γ (°)
Experienced	Average	51.8	55.7	59.4	78.3	58.6	34.0
	Standard Deviation	15.8	11.5	15.4	7.9	8.8	7.7
New	Average	54.1	54.8	56.4	73.4	58.3	36.0
	Standard Deviation	10.4	8.1	14.4	5.7	7.7	8.3

Table C.6 Descriptive statistics for the femoral and tibial tunnel spatial measurements for the cadaver dataset organized by surgical technique and level of surgeon experience.

		Femur		Tibia	
Experience	Metric	c/C	n/N	a/A	m/M
Experienced	Average	0.71	0.48	0.49	0.45
	Standard Deviation	0.10	0.09	0.07	0.03
New	Average	0.65	0.46	0.46	0.46
	Standard Deviation	0.09	0.08	0.07	0.03

Table C.7 Descriptive statistics for the femoral and tibial tunnel angular measurements for the cadaver dataset organized by surgical technique and level of surgeon experience.

			Femur			Tibia		
Technique	Experience	Metric	α (°)	β (°)	γ (°)	α (°)	β (°)	γ (°)
Medial Portal	Experienced	Average	43.3	64.6	57.9	73.6	61.7	33.0
	Experienced	Standard Deviation	12.4	11.5	8.4	6.3	9.7	9.0
	New	Average	56.6	54.0	53.1	72.5	58.9	36.0
	New	Standard Deviation	8.3	8.1	7.7	5.1	6.6	4.29
Transtibial	Experienced	Average	67.5	54.2	43.8	74.5	60.5	33.5
	Experienced	Standard Deviation	5.6	5.0	4.8	5.4	4.8	2.7
	New	Average	60.8	59.3	44.4	70.9	53.2	42.4
	New	Standard Deviation	6.6	8.0	6.3	4.9	4.6	4.5
Two Incision	Experienced	Average	43.8	49.0	76.3	86.5	54.0	35.4
	Experienced	Standard Deviation	13.7	11.7	8.1	4.1	9.7	9.9
	New	Average	43.8	50.7	73.3	77.3	63.4	29.1
	New	Standard Deviation	8.0	6.2	9.7	5.4	8.3	9.73

Table C.8 Descriptive statistics for the femoral and tibial tunnel spatial measurements for the cadaver dataset organized by surgical technique and level of surgeon experience.

			Femur		Tibia	
Technique	Experience	Metric	c/C	n/N	a/A	m/M
Medial Portal	Experienced	Average	0.65	0.41	0.45	0.45
	Experienced	Standard Deviation	0.06	0.09	0.08	0.03
	New	Average	0.61	0.47	0.43	0.45
	New	Standard Deviation	0.07	0.10	0.05	0.02
Transtibial	Experienced	Average	0.67	0.52	0.50	0.45
	Experienced	Standard Deviation	0.08	0.07	0.05	0.02
	New	Average	0.66	0.43	0.50	0.45
	New	Standard Deviation	0.08	0.05	0.08	0.02
Two Incision	Experienced	Average	0.77	0.52	0.46	0.46
	Experienced	Standard Deviation	0.12	0.06	0.03	0.03
	New	Average	0.74	0.44	0.49	0.46
	New	Standard Deviation	0.11	0.07	0.09	0.04

Table C.9 Descriptive statistics for the femoral and tibial tunnel angular measurements for the patient dataset.

	Femoral Tunnel			Tibial Tunnel		
	α (°)	β (°)	γ (°)	α (°)	β (°)	γ (°)
Average	55.6	62.1	48.3	76.7	64.8	28.6
Standard Deviation	10.9	11.3	12.2	6.2	7.5	7.2

Table C.10 Descriptive statistics for the femoral and tibial tunnel spatial measurements for the patient dataset.

	Femoral Tunnel		Tibial Tunnel	
	c/C	n/N	a/A	m/M
Average	0.64	0.46	0.45	0.45
Standard Deviation	0.09	0.07	0.08	0.02

Table C.11 Descriptive statistics for the femoral and tibial tunnel angular measurements for the patient dataset organized by surgeon.

		Femur			Tibia		
Surgeon	Metric	α (°)	β (°)	γ (°)	α (°)	β (°)	γ (°)
1	Average	55.9	59.4	48.1	76.6	66.1	26.7
	Standard Deviation	6.3	3.7	6.3	2.4	5.6	5.4
2	Average	59.0	59.3	48.8	74.9	57.2	36.3
	Standard Deviation	19.9	13.2	18.1	6.1	5.0	4.9
3	Average	53.5	69.4	43.1	76.7	70.2	23.2
	Standard Deviation	6.0	6.2	6.6	3.7	5.5	5.3
4	Average	58.6	57.4	47.8	78.6	65.2	26.7
	Standard Deviation	5.2	8.1	8.2	3.8	4.6	4.5
5	Average	63.1	58.3	42.9	71.4	74.4	23.8
	Standard Deviation	7.2	2.5	6.0	3.2	5.3	3.8
6	Average	49.0	79.5	43.5	71.5	63.0	32.9
	Standard Deviation	10.2	9.5	7.9	4.8	6.7	7.6
7	Average	57.5	61.0	47.1	78.6	58.1	33.5
	Standard Deviation	12.3	6.1	15.9	5.7	5.0	5.7
8	Average	48.8	50.0	65.4	85.9	64.9	24.5
	Standard Deviation	2.0	3.5	4.8	3.9	5.6	6.1

Table C.12 Descriptive statistics for the femoral and tibial tunnel spatial measurements for the patient dataset organized by surgeon.

		Femur		Tibia	
Surgeon	Metric	c/C	n/N	a/A	m/M
1	Average	0.63	0.46	0.45	0.48
	Standard Deviation	0.03	0.05	0.06	0.02
2	Average	0.65	0.54	0.49	0.45
	Standard Deviation	0.06	0.06	0.08	0.03
3	Average	0.51	0.48	0.37	0.45
	Standard Deviation	0.04	0.07	0.03	0.02
4	Average	0.68	0.47	0.53	0.45
	Standard Deviation	0.07	0.04	0.04	0.01
5	Average	0.67	0.44	0.40	0.46
	Standard Deviation	0.05	0.05	0.07	0.03
6	Average	0.58	0.42	0.42	0.46
	Standard Deviation	0.10	0.08	0.07	0.02
7	Average	0.69	0.47	0.47	0.44
	Standard Deviation	0.08	0.08	0.07	0.02
8	Average	0.70	0.38	0.47	0.44
	Standard Deviation	0.08	0.04	0.04	0.02

C.2 Graphical Data Representations

This section contains scatter plots and box plots from the MOON ACL study; the cadaver dataset is presented first and is followed by the patient dataset. The scatter plots summarize the overall cadaver and patient datasets and are meant to complement the tables presented in the previous Appendix section. The box plots included here are comparisons that were described in the text but were not statistically significant.

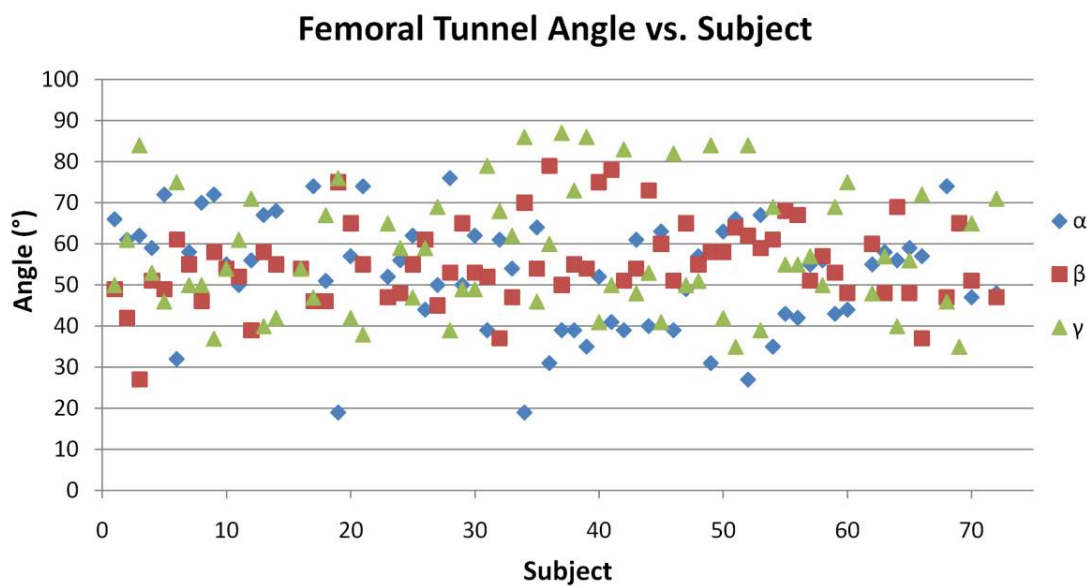


Figure C.1 A scatter plot describing the femoral ACL tunnel angles of the cadaver dataset for the three angular measures (α , β , and γ).

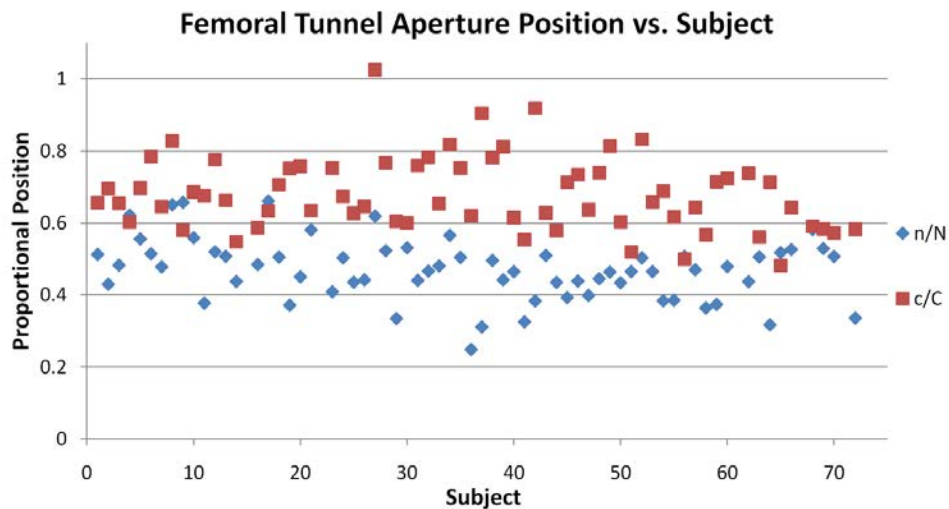


Figure C.2 A scatter plot describing the femoral ACL tunnel aperture's proportional position of the cadaver dataset for the two spatial measures (c/C and n/N).

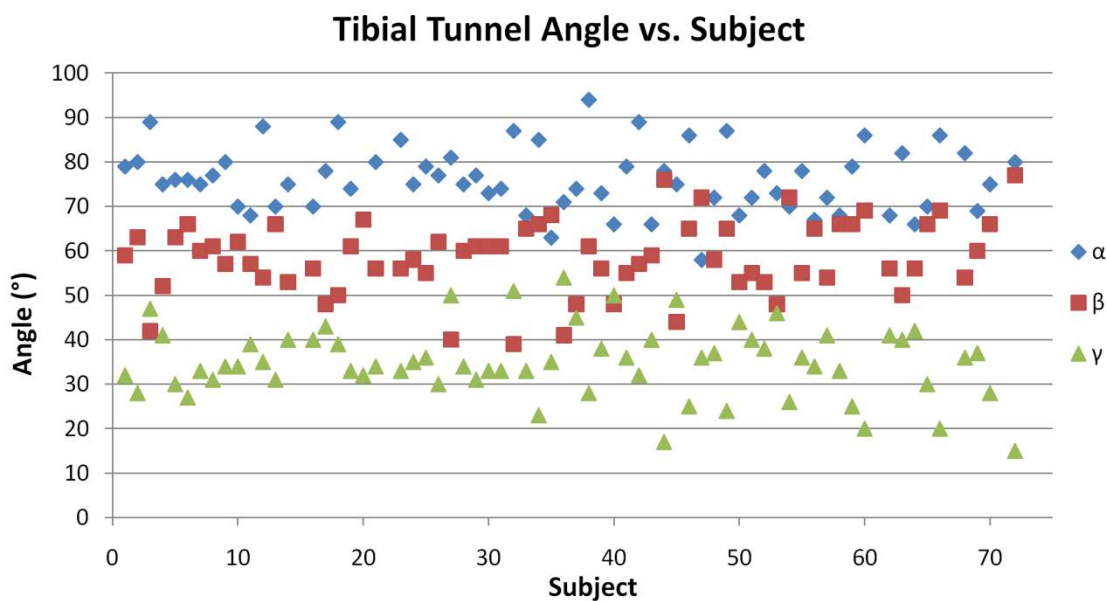


Figure C.3 A scatter plot describing the tibial ACL tunnel angles of the cadaver dataset for the three angular measures (α , β , and γ).

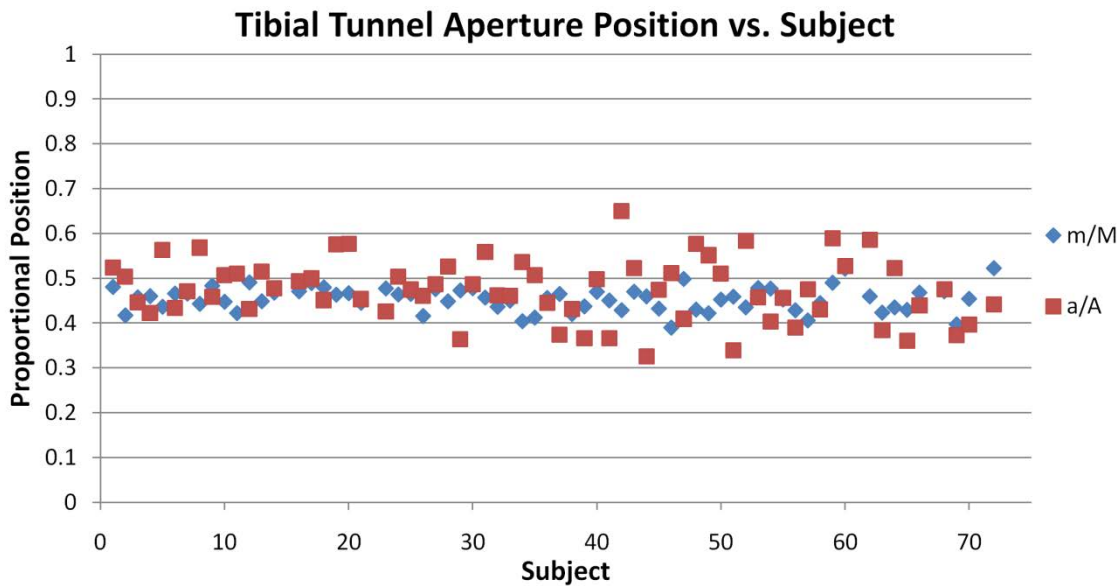


Figure C.4 A scatter plot describing the tibial ACL tunnel aperture's proportional position of the cadaver dataset for the two spatial measures (a/A and m/M).

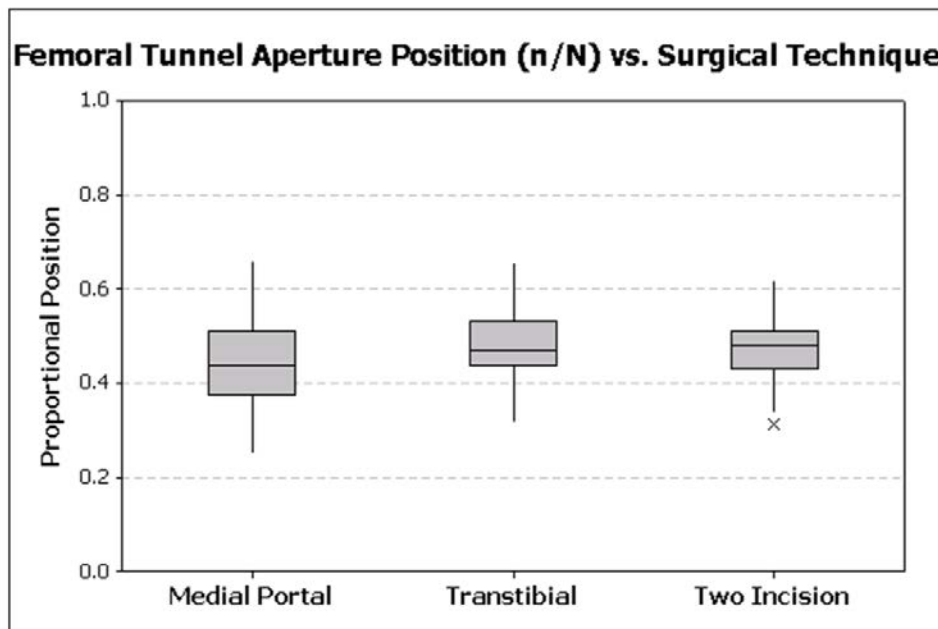


Figure C.5 A box and whisker representation of the cadaver dataset's femoral tunnel aperture position measure n/N organized by ACL reconstruction technique.

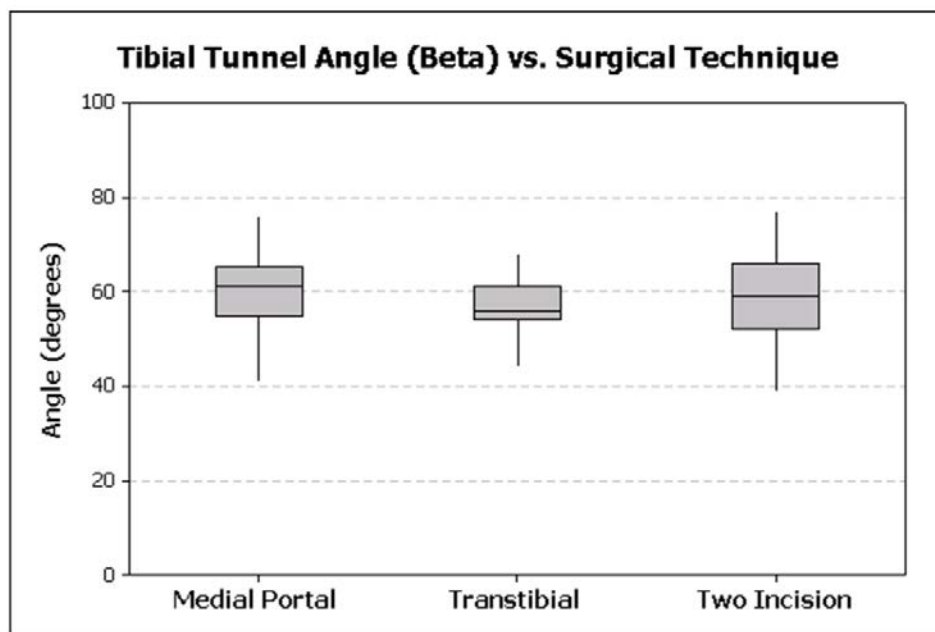


Figure C.6 A box and whisker representation of the cadaver dataset's tibial tunnel angle β organized by ACL reconstruction technique.

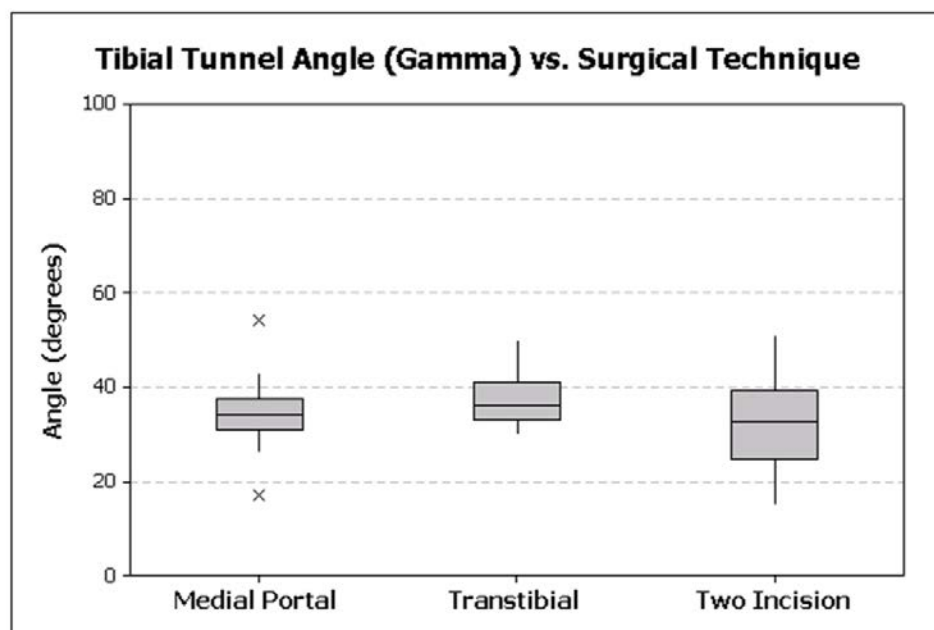


Figure C.7 A box and whisker representation of the cadaver dataset's tibial tunnel angle γ organized by ACL reconstruction technique.

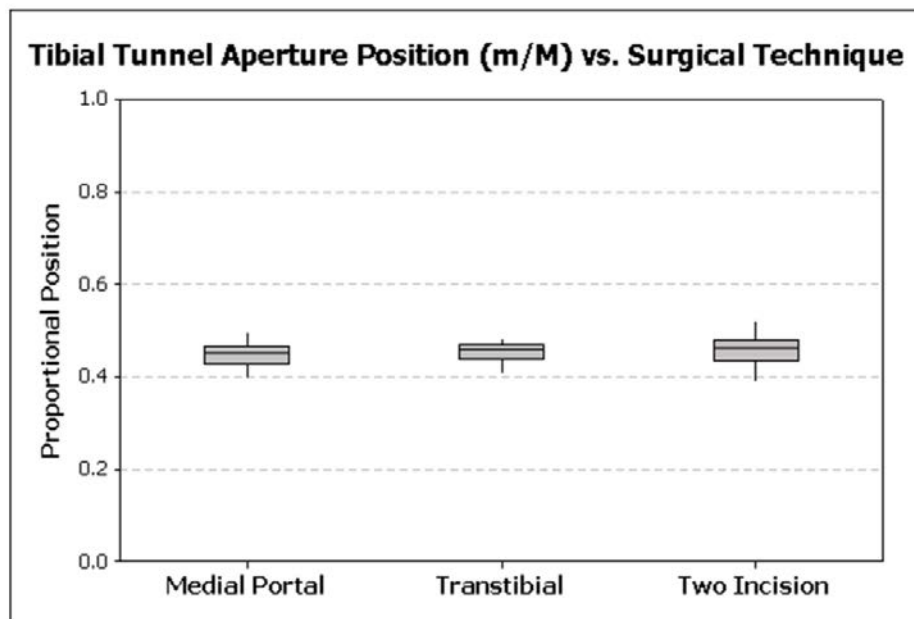


Figure C.8 A box and whisker representation of the cadaver dataset's tibial tunnel aperture position measure m/M organized by ACL reconstruction technique.

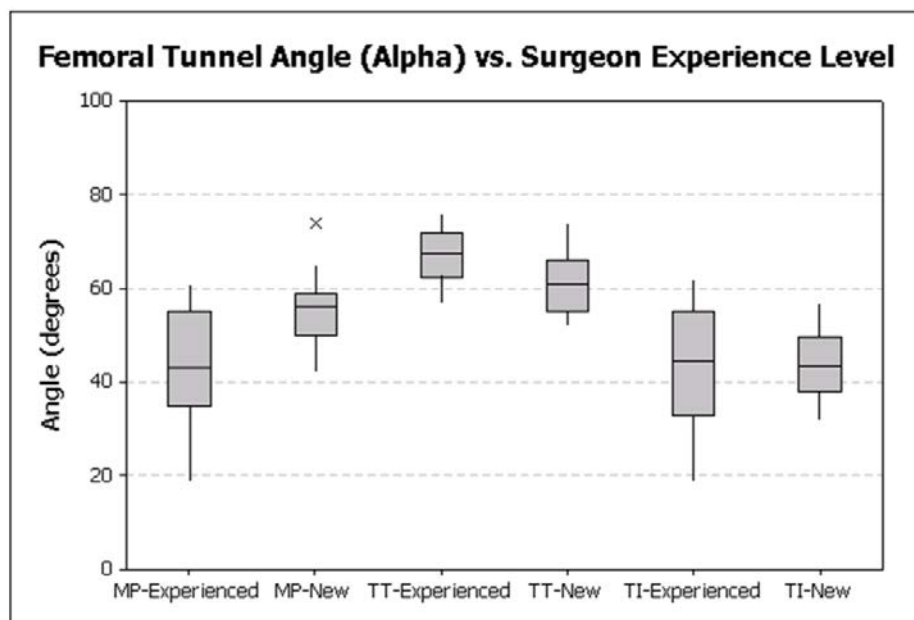


Figure C.9 A box and whisker representation of the cadaver dataset's femoral tunnel angle α organized by level of surgeon experience and ACL reconstruction surgical technique (MP = medial portal, TT = transtibial, TI = two incision).

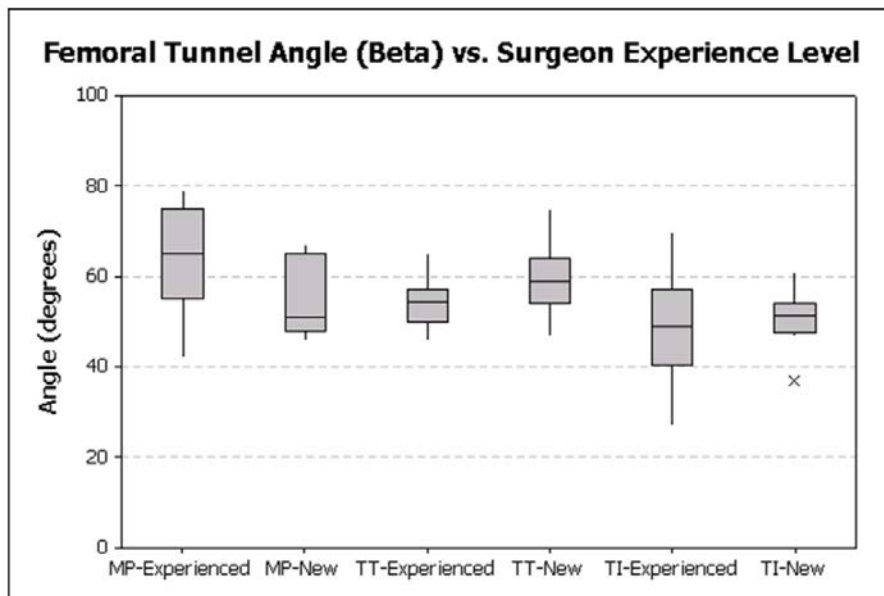


Figure C.10 A box and whisker representation of the cadaver dataset's femoral tunnel angle β organized by level of surgeon experience and ACL reconstruction surgical technique (MP = medial portal, TT = transtibial, TI = two incision).

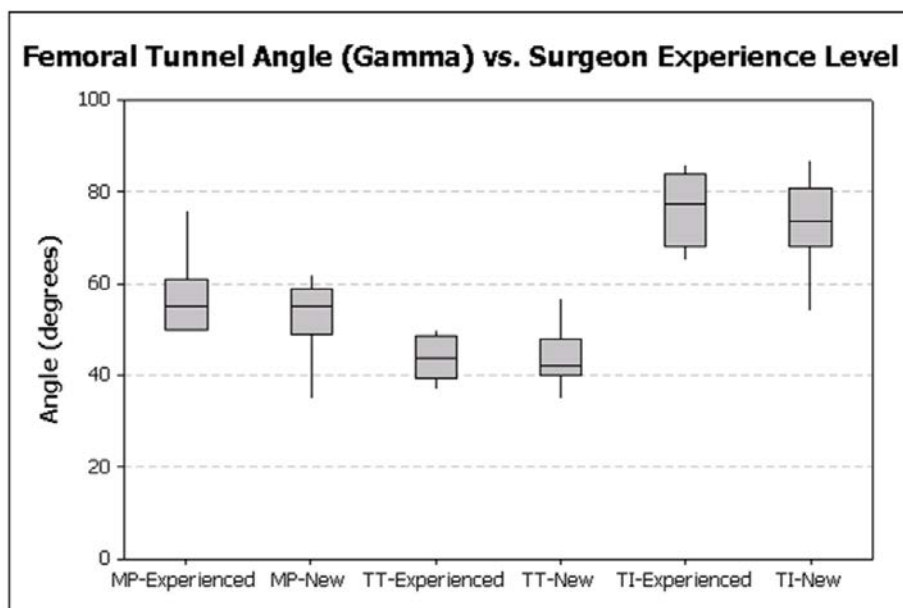


Figure C.11 A box and whisker representation of the cadaver dataset's femoral tunnel angle γ organized by level of surgeon experience and ACL reconstruction surgical technique (MP = medial portal, TT = transtibial, TI = two incision).

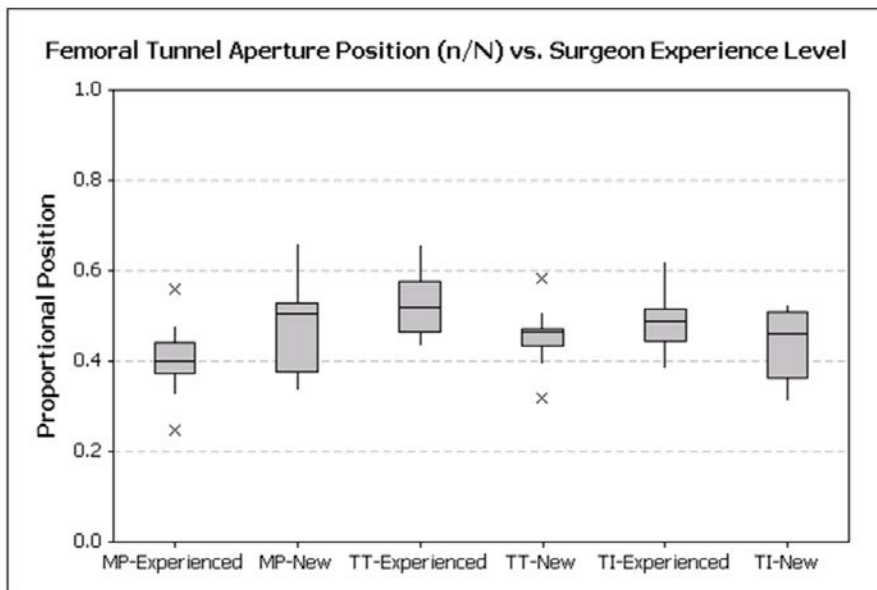


Figure C.12 A box and whisker representation of the cadaver dataset's femoral tunnel aperture position measure n/N organized by level of surgeon experience and ACL reconstruction surgical technique (MP = medial portal, TT = transtibial, TI = two incision).

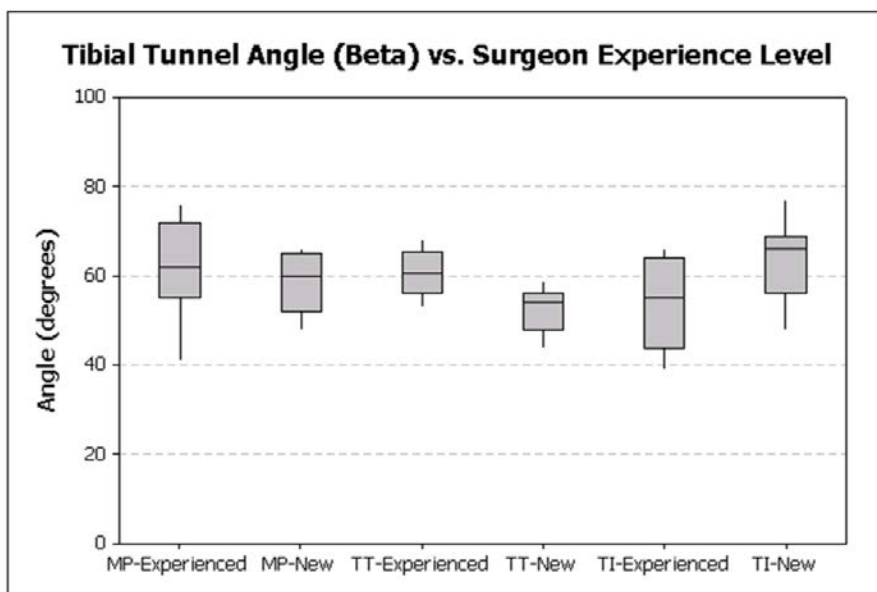


Figure C.13 A box and whisker representation of the cadaver dataset's tibial tunnel angle β organized by level of surgeon experience and ACL reconstruction surgical technique (MP = medial portal, TT = transtibial, TI = two incision).

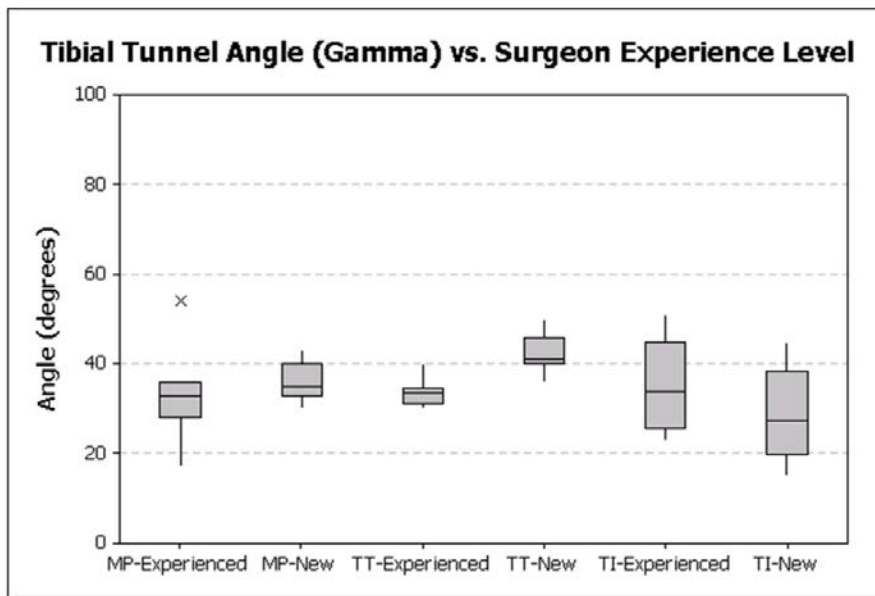


Figure C.14 A box and whisker representation of the cadaver dataset's tibial tunnel angle γ organized by level of surgeon experience and ACL reconstruction surgical technique (MP = medial portal, TT = transtibial, TI = two incision).

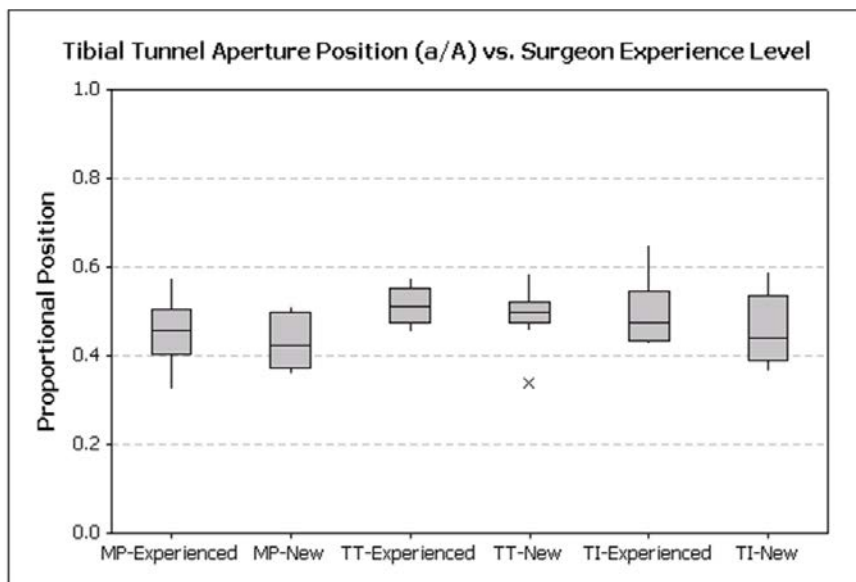


Figure C.15 A box and whisker representation of the cadaver dataset's tibial tunnel aperture position measure a/A organized by level of surgeon experience and ACL reconstruction surgical technique (MP = medial portal, TT = transtibial, TI = two incision).

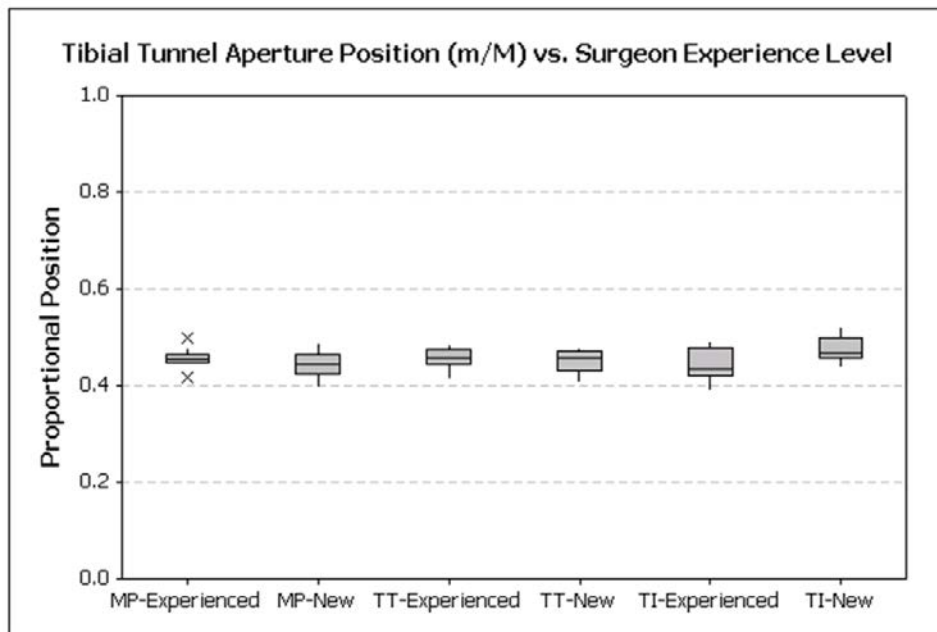


Figure C.16 A box and whisker representation of the cadaver dataset's tibial tunnel aperture position measure m/M organized by level of surgeon experience and ACL reconstruction surgical technique (MP = medial portal, TT = transtibial, TI = two incision).

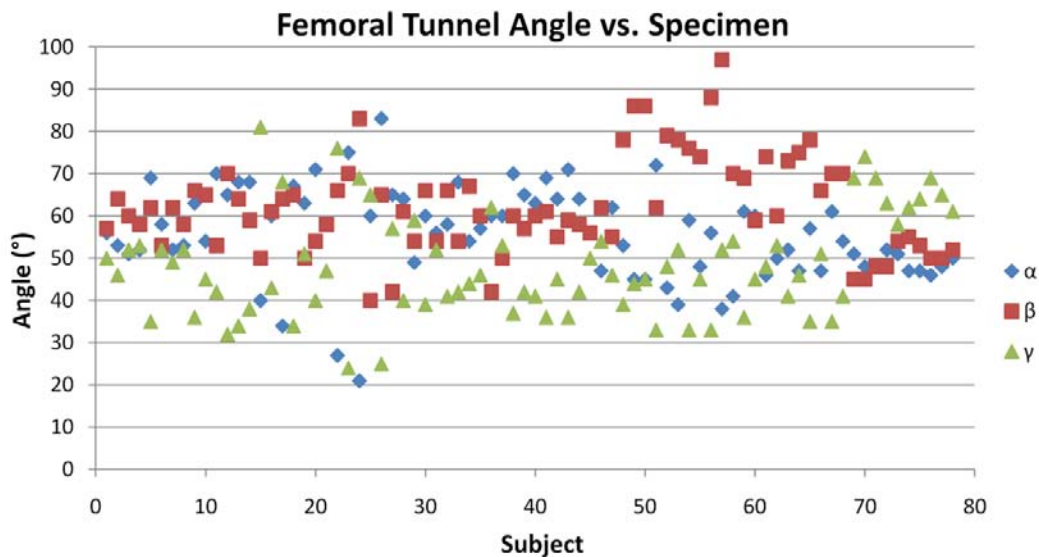


Figure C.17 A scatter plot describing the femoral ACL tunnel angles of the patient dataset for the three angular measures (α , β , and γ).

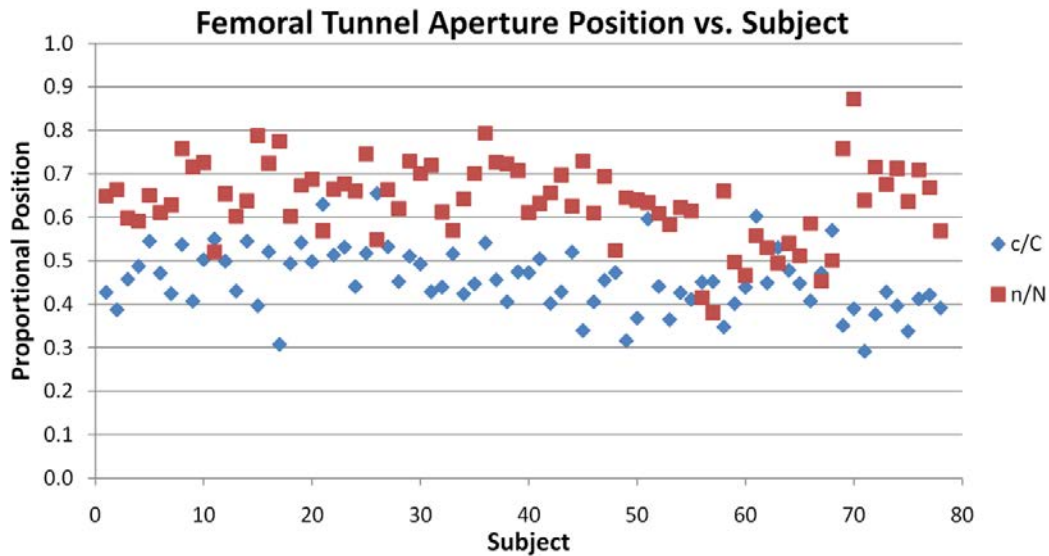


Figure C.18 A scatter plot describing the femoral ACL tunnel aperture's proportional position of the patient dataset for the two spatial measures (c/C and n/N).

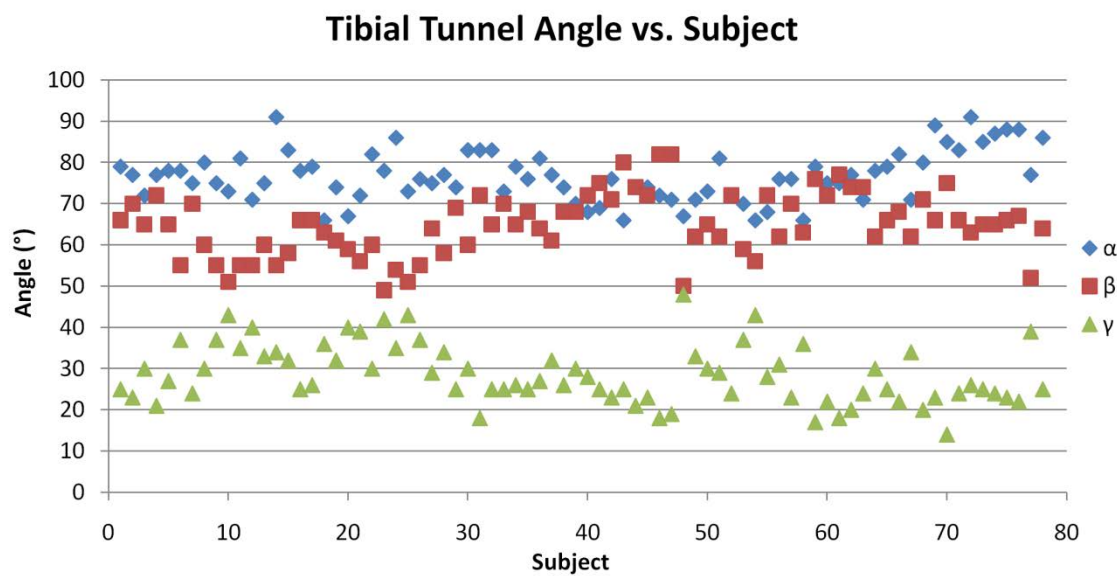


Figure C.19 A scatter plot describing the tibial ACL tunnel angles of the patient dataset for the three angular measures (α , β , and γ).

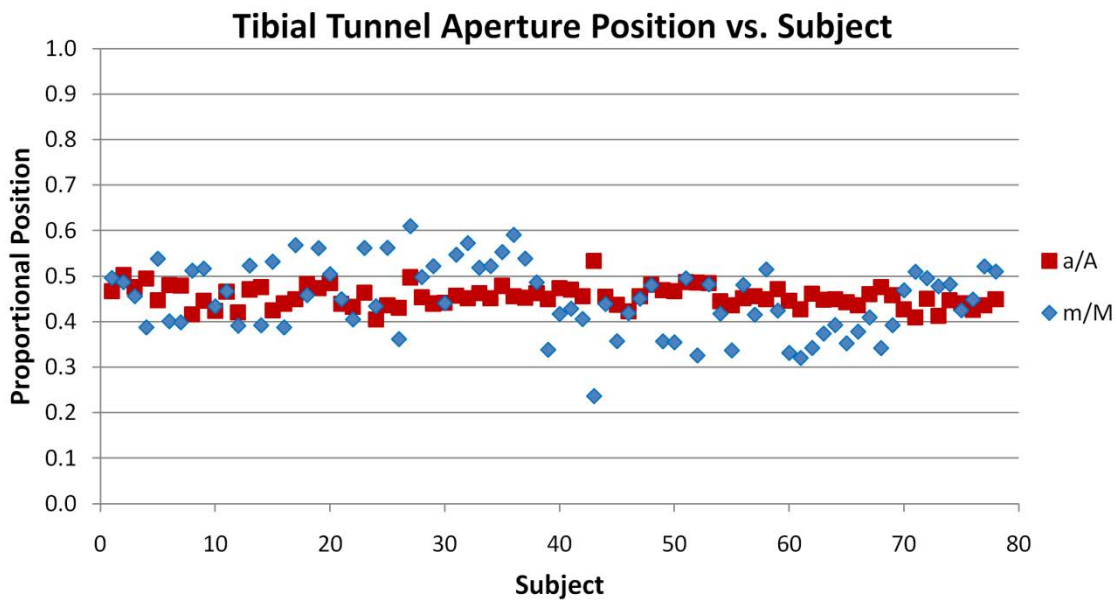


Figure C.20 A scatter plot describing the tibial ACL tunnel aperture's proportional position of the patient dataset for the two spatial measures (a/A and m/M).

C.3 Discrete ACL Aperture Centroid Maps

This section contains additional discrete sphere representations from the MOON ACL study; the cadaver dataset is presented first and is followed by the patient dataset. Overall representations of the cadaver and patient datasets are presented, and additional detail regarding level of surgeon experience is presented for easier visualization.

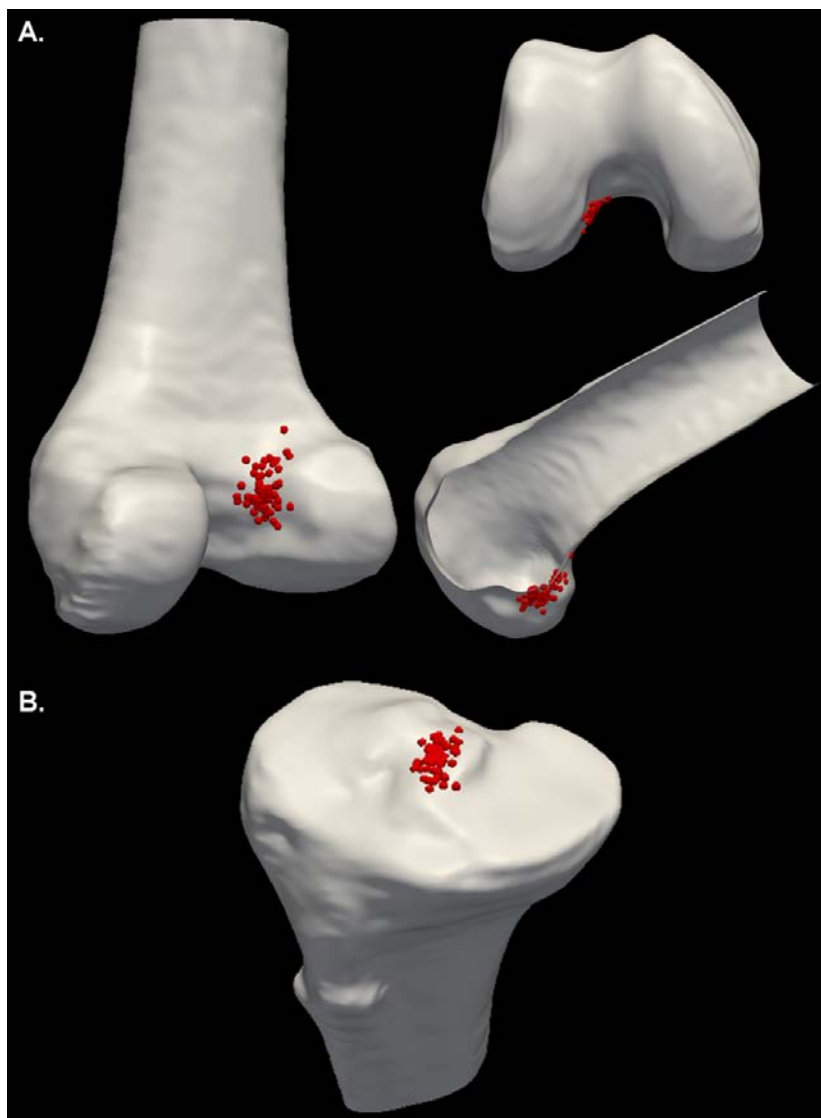


Figure C.21 The MOON cadaver dataset. A) Three views of the native femur with sphere representations of the tunnel aperture centroids. B) A view of the tibia with sphere representations of the tunnel aperture centroids.

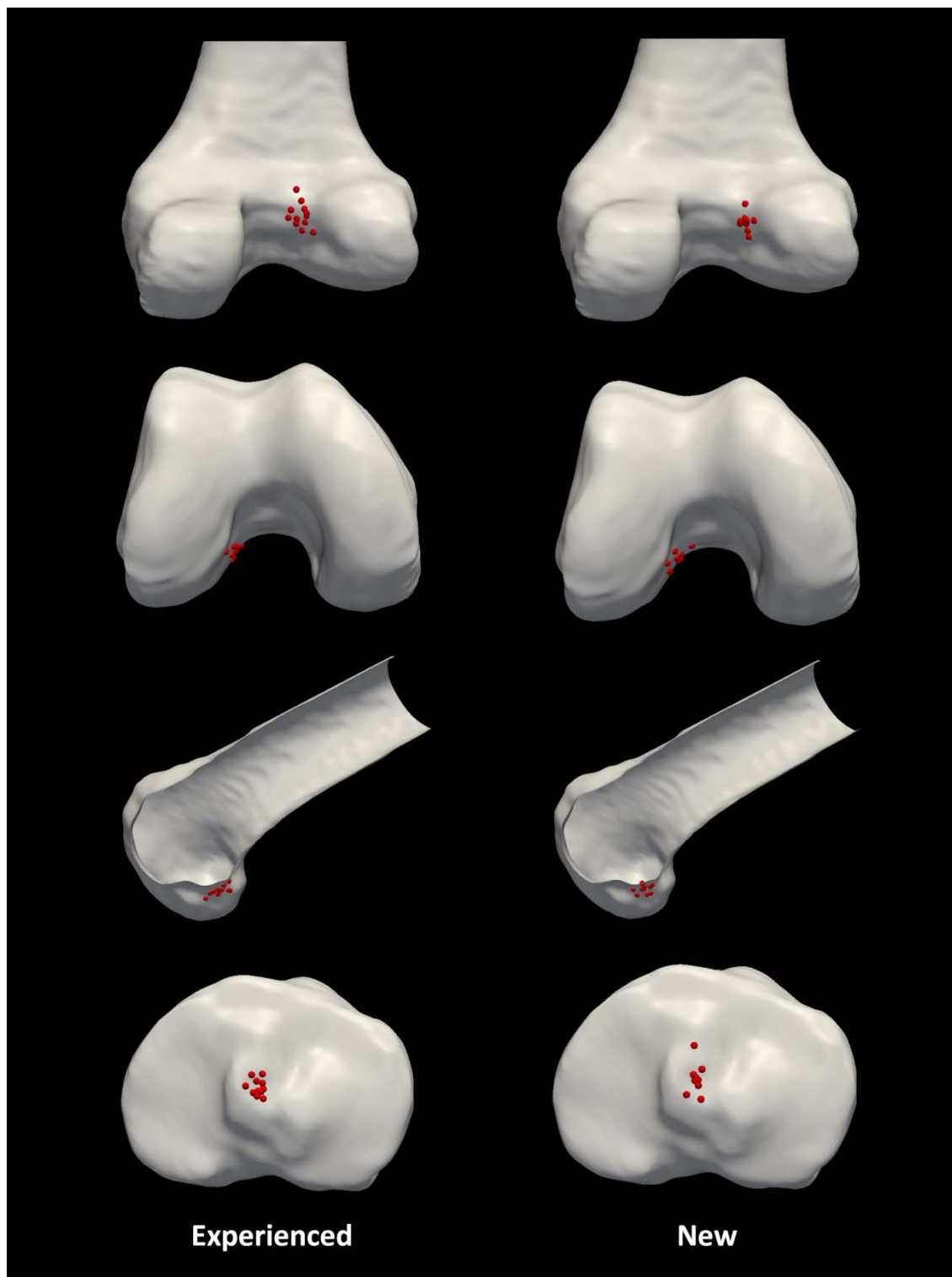


Figure C.22 Discrete sphere representations of the femur (3 views) and the tibia for the cadaver dataset organized by the level of surgeon experience for the transtibial technique for ACL reconstruction.

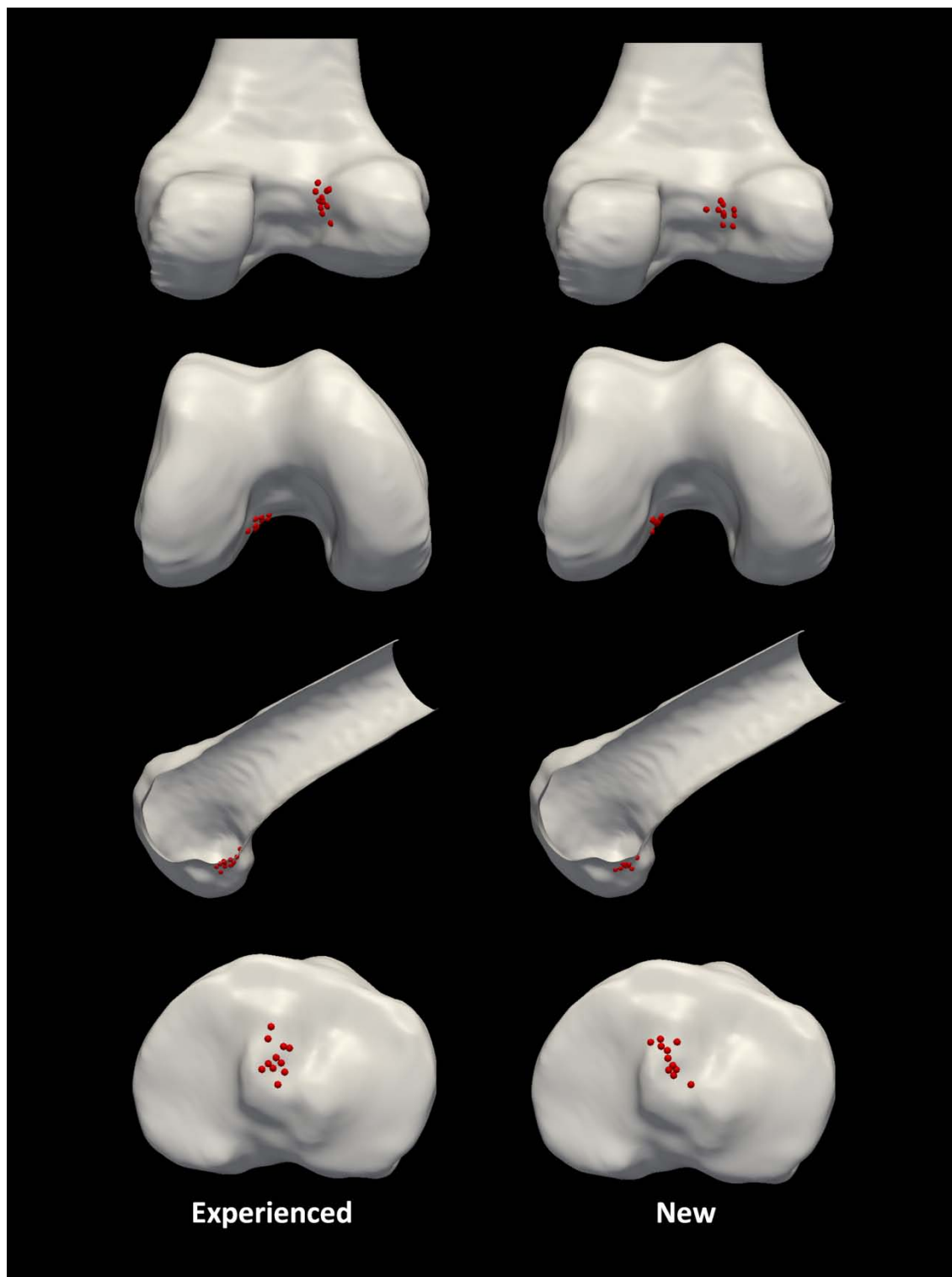


Figure C.23 Discrete sphere representations of the femur (3 views) and the tibia for the cadaver dataset organized by the level of surgeon experience for the medial portal technique for ACL reconstruction.

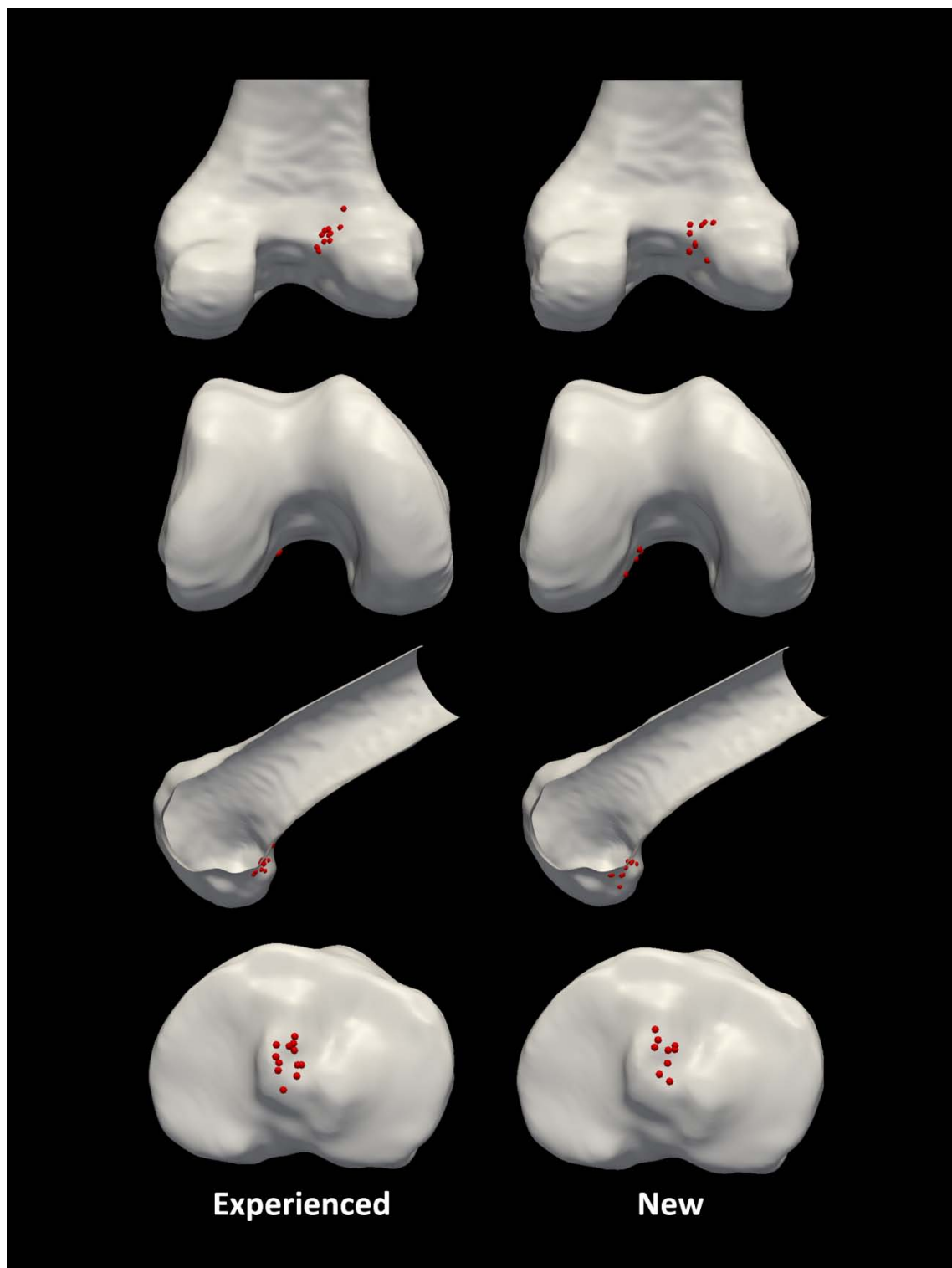


Figure C.24 Discrete sphere representations of the femur (3 views) and the tibia for the cadaver dataset organized by the level of surgeon experience for the two incision technique for ACL reconstruction.

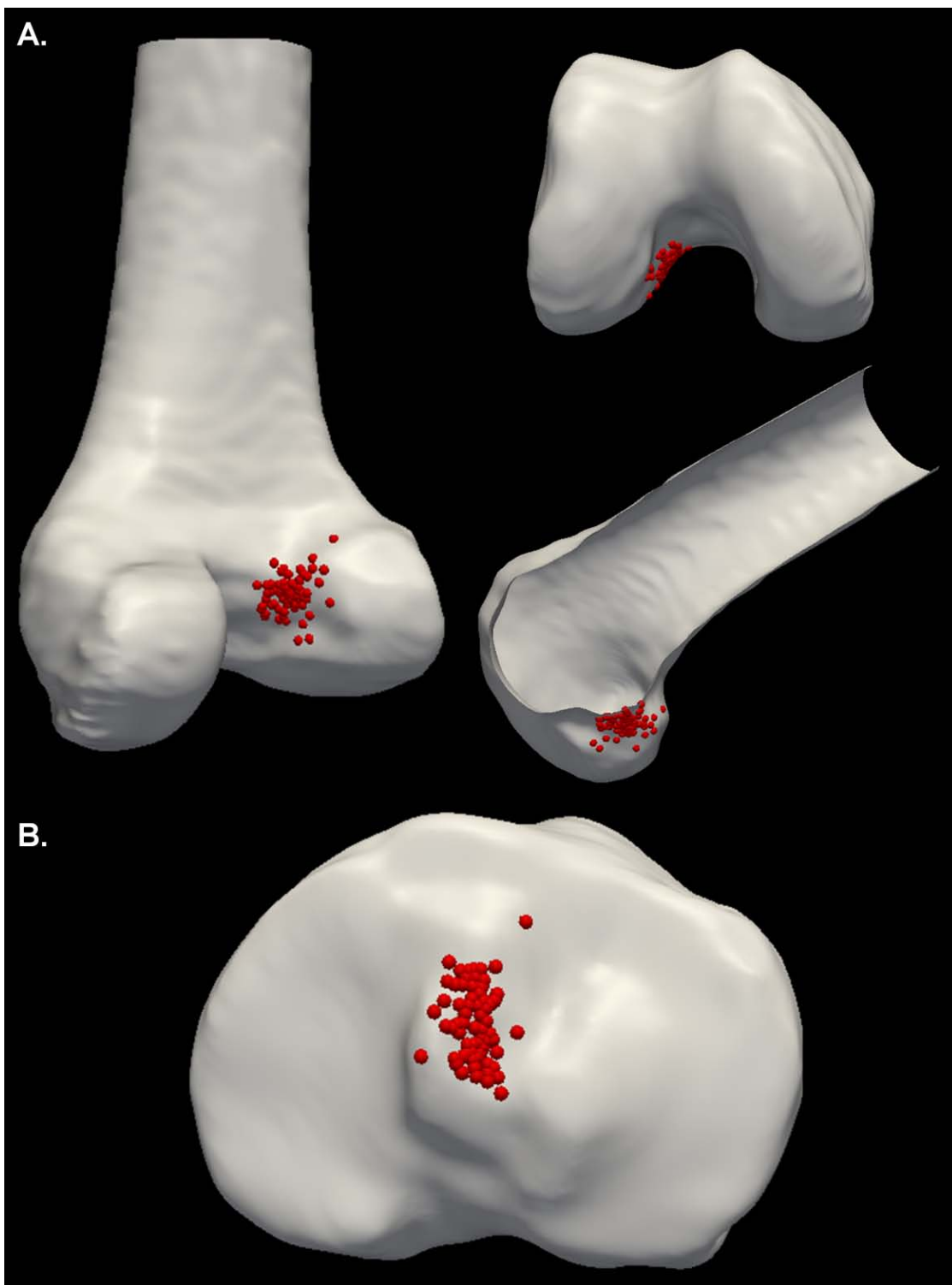


Figure C.25 The MOON patient dataset. A) Three views of the native femur with sphere representations of the tunnel aperture centroids for the patient dataset. B) A view of the tibia with sphere representations of the tunnel aperture centroids for the patient dataset.

C.4 ACL Tunnel Aperture Overlap Maps

This section contains additional tunnel aperture overlap maps from the MOON ACL study; the cadaver dataset is presented first and is followed by the patient dataset. Overall representations of the cadaver and patient datasets are presented. In addition, overlap maps with respect to technique, level of experience, and operating surgeon are presented to complement the figures in the text.

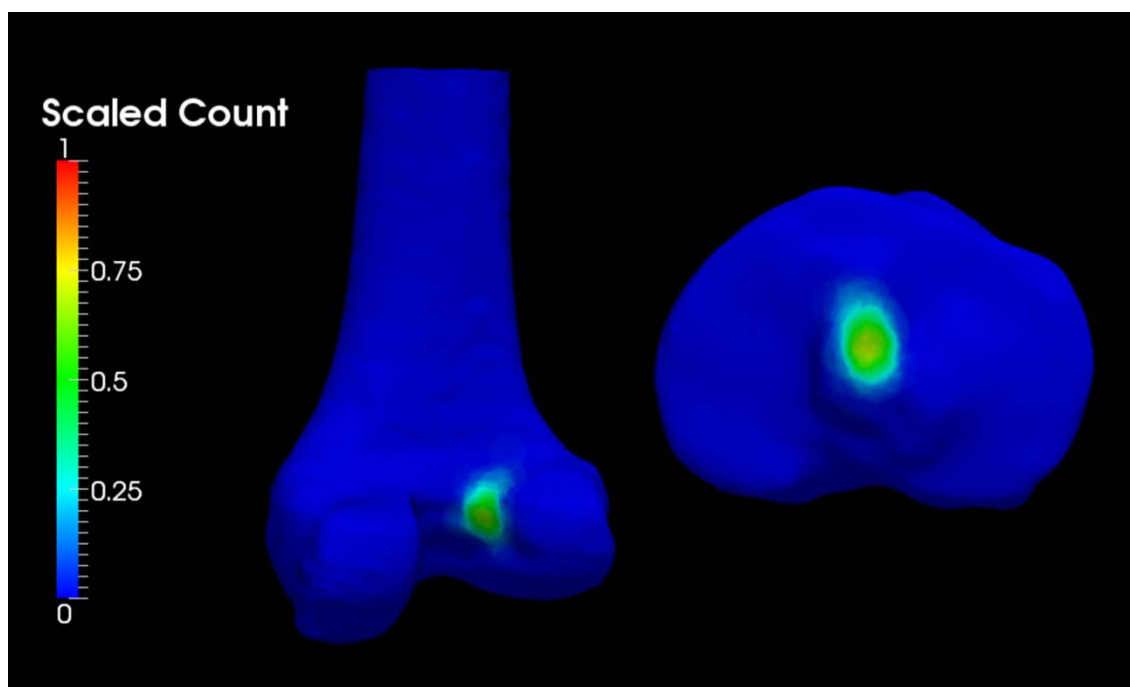


Figure C.26 ACL Tunnel Aperture Overlap Maps for the femur (left) and tibia (right) for the cadaver dataset depicting the likelihood of ACL tunnel placement on a native bone surface.

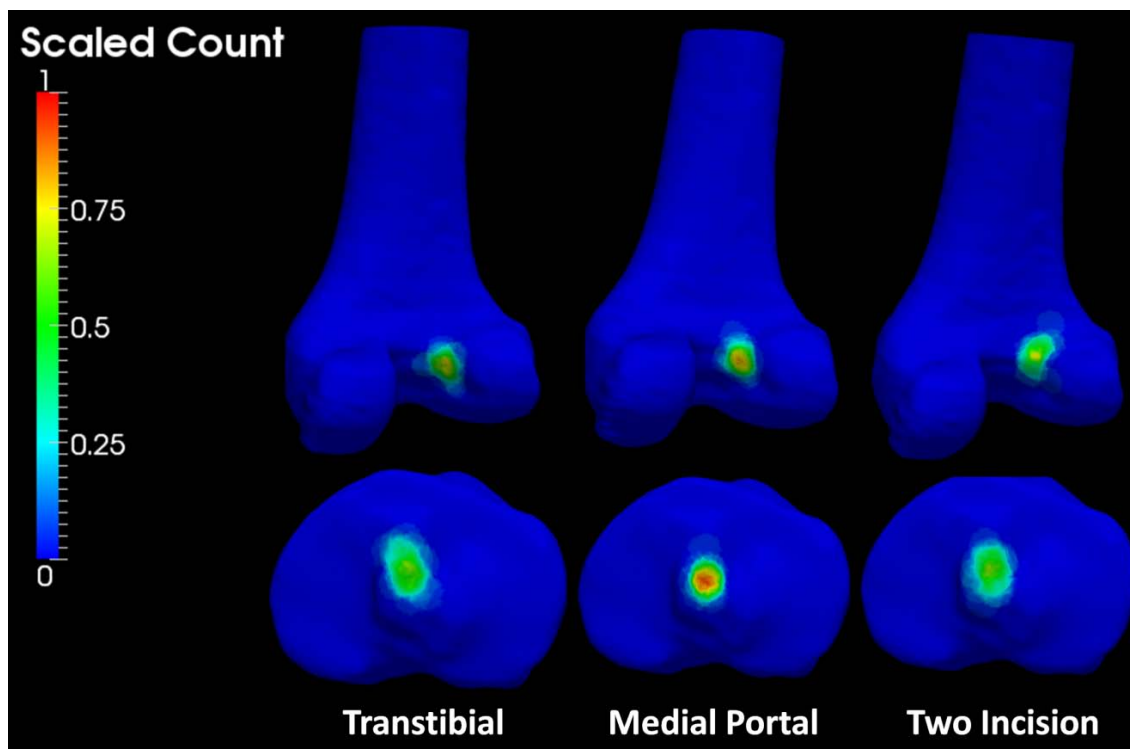


Figure C.27 ACL Tunnel Aperture Overlap Maps for the femur (left) and tibia (right) for the cadaver dataset depicting the likelihood of ACL tunnel placement on a native bone surface organized by surgical technique.

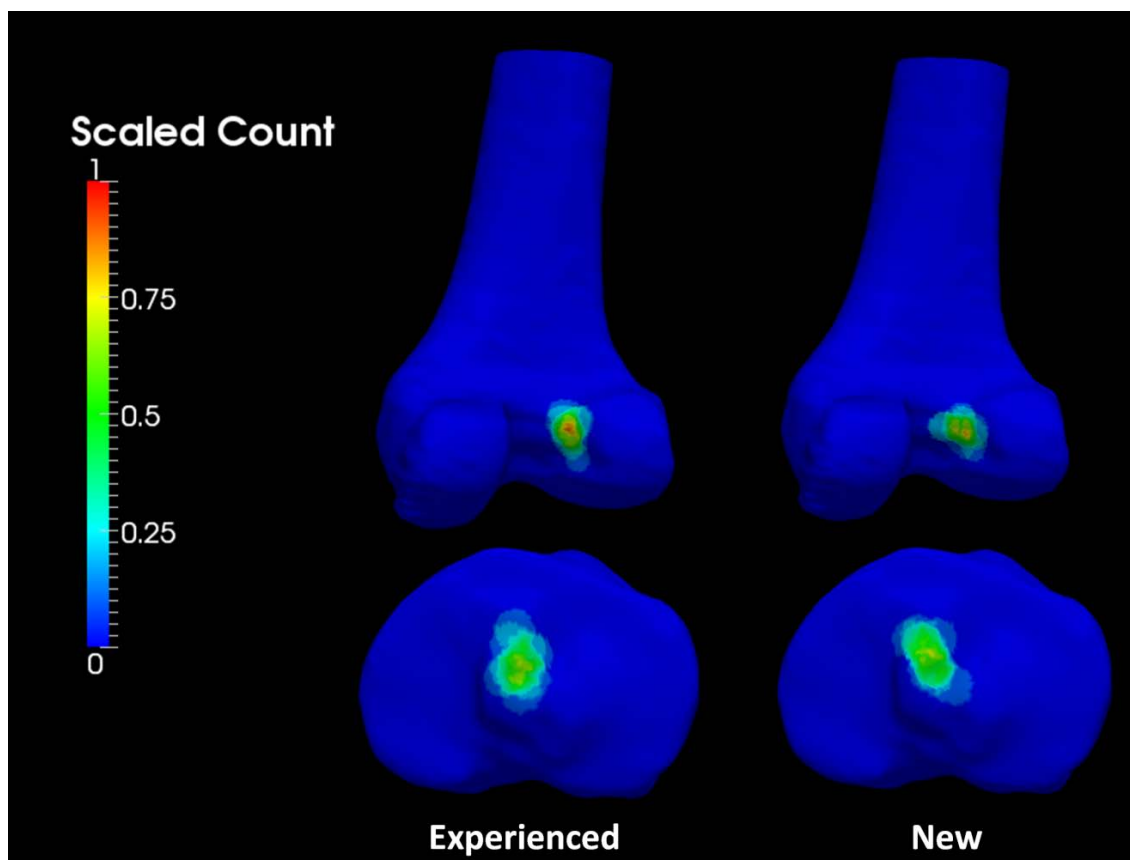


Figure C.28 ACL Tunnel Aperture Overlap Maps for the femur (left) and tibia (right) for the cadaver dataset depicting the likelihood of ACL tunnel placement on a native bone surface for the medial portal technique organized by level of surgeon experience.

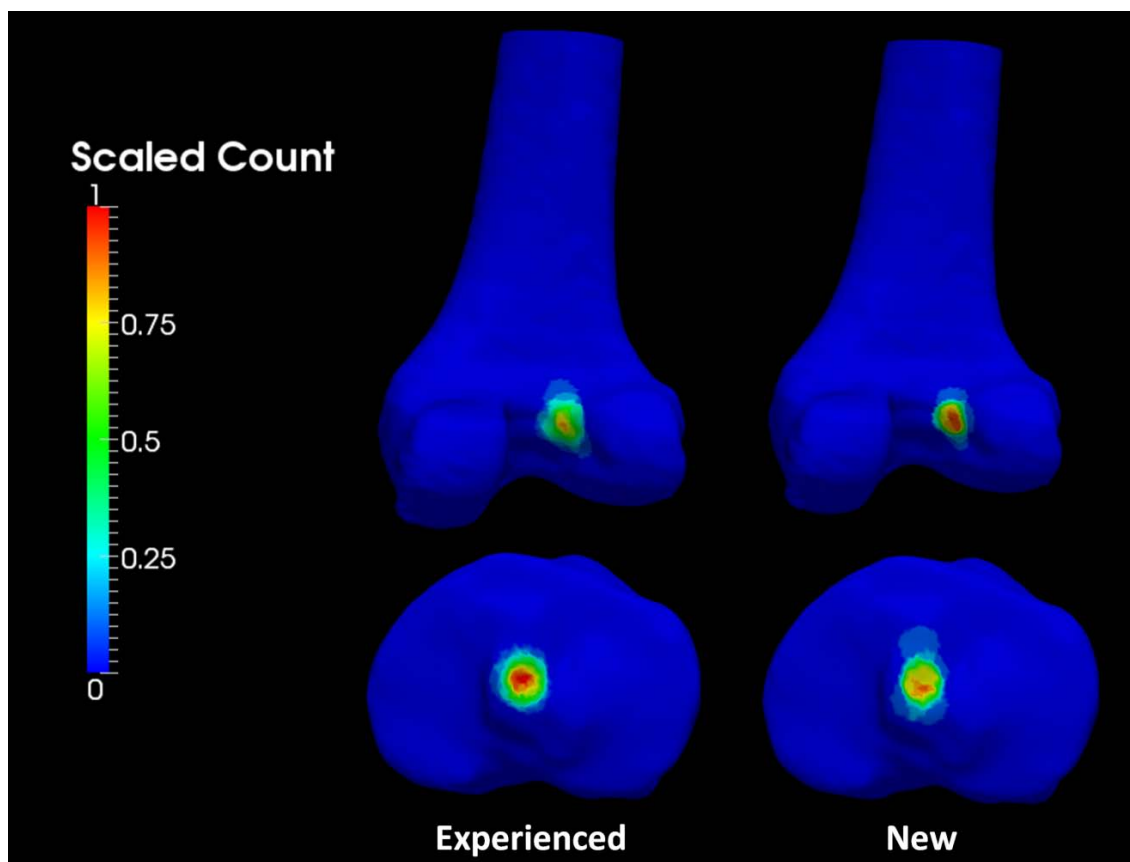


Figure C.29 ACL Tunnel Aperture Overlap Maps for the femur (left) and tibia (right) for the cadaver dataset depicting the likelihood of ACL tunnel placement on a native bone surface for the transtibial technique organized by level of surgeon experience.

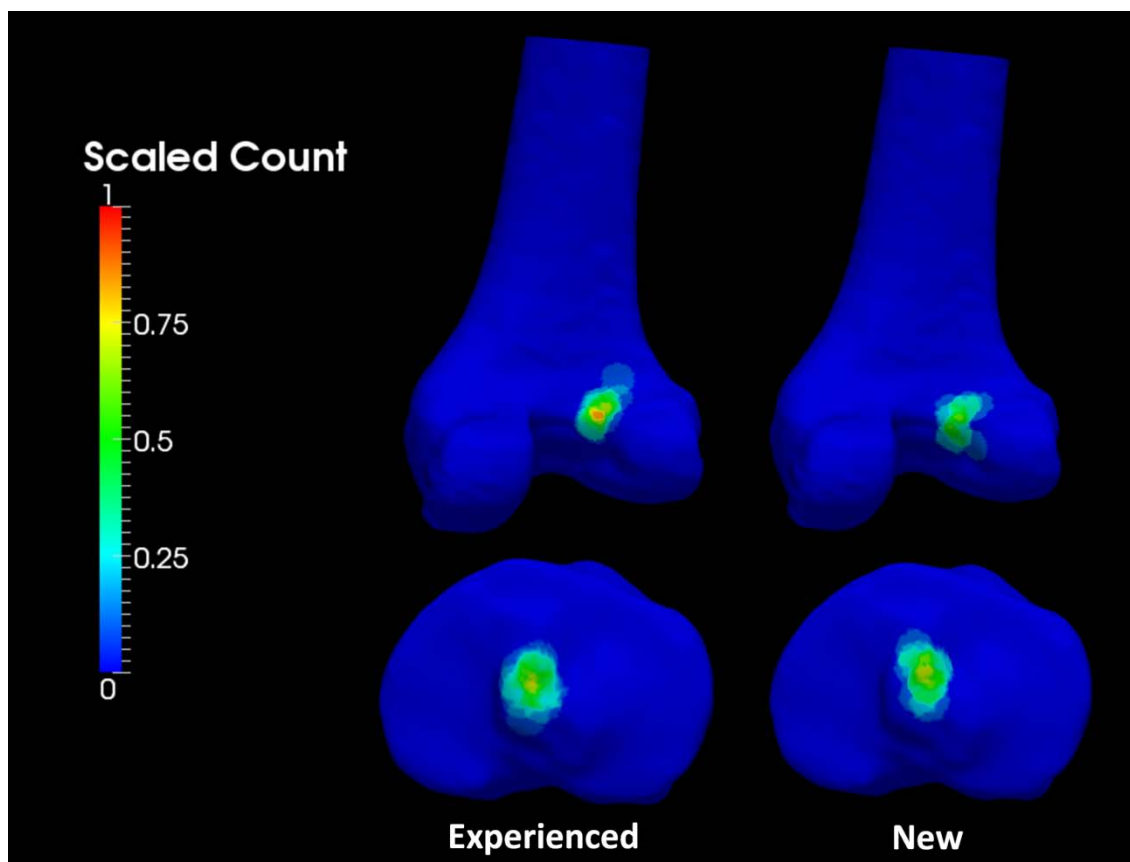


Figure C.30 ACL Tunnel Aperture Overlap Maps for the femur (left) and tibia (right) for the cadaver dataset depicting the likelihood of ACL tunnel placement on a native bone surface for the two incision technique organized by level of surgeon experience.

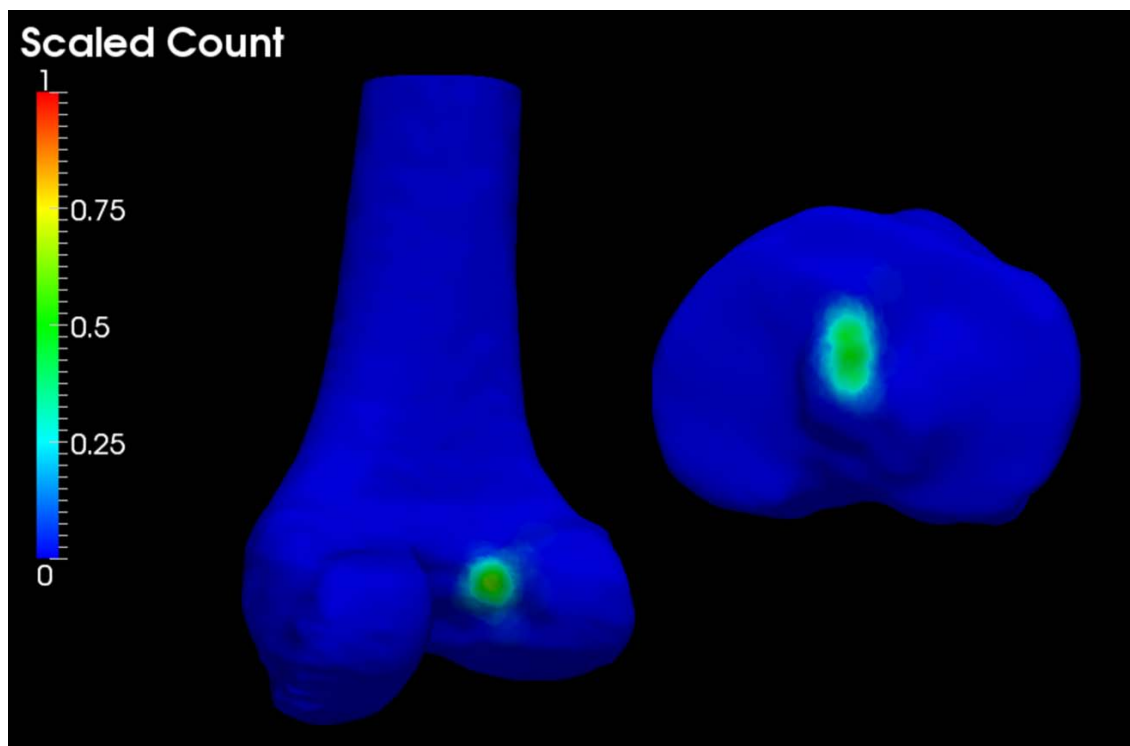


Figure C.31 ACL Tunnel Aperture Overlap Maps for the femur (left) and tibia (right) for the patient dataset depicting the likelihood of ACL tunnel placement on a native bone surface.

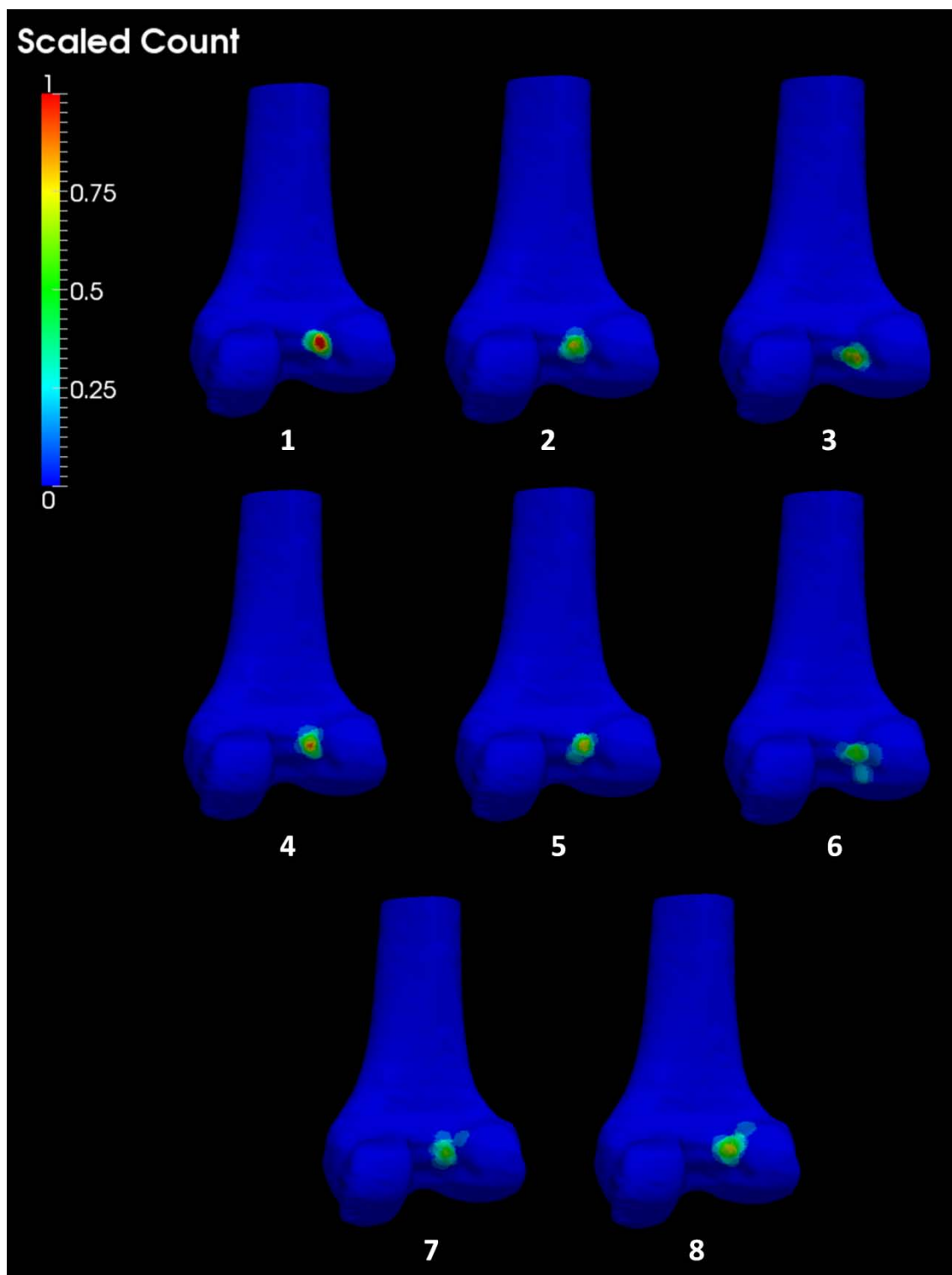


Figure C.32 ACL Tunnel Aperture Overlap Maps for the patient dataset depicting the likelihood of ACL tunnel placement on a native femur bone surface organized by surgeon. Eight surgeons are depicted.

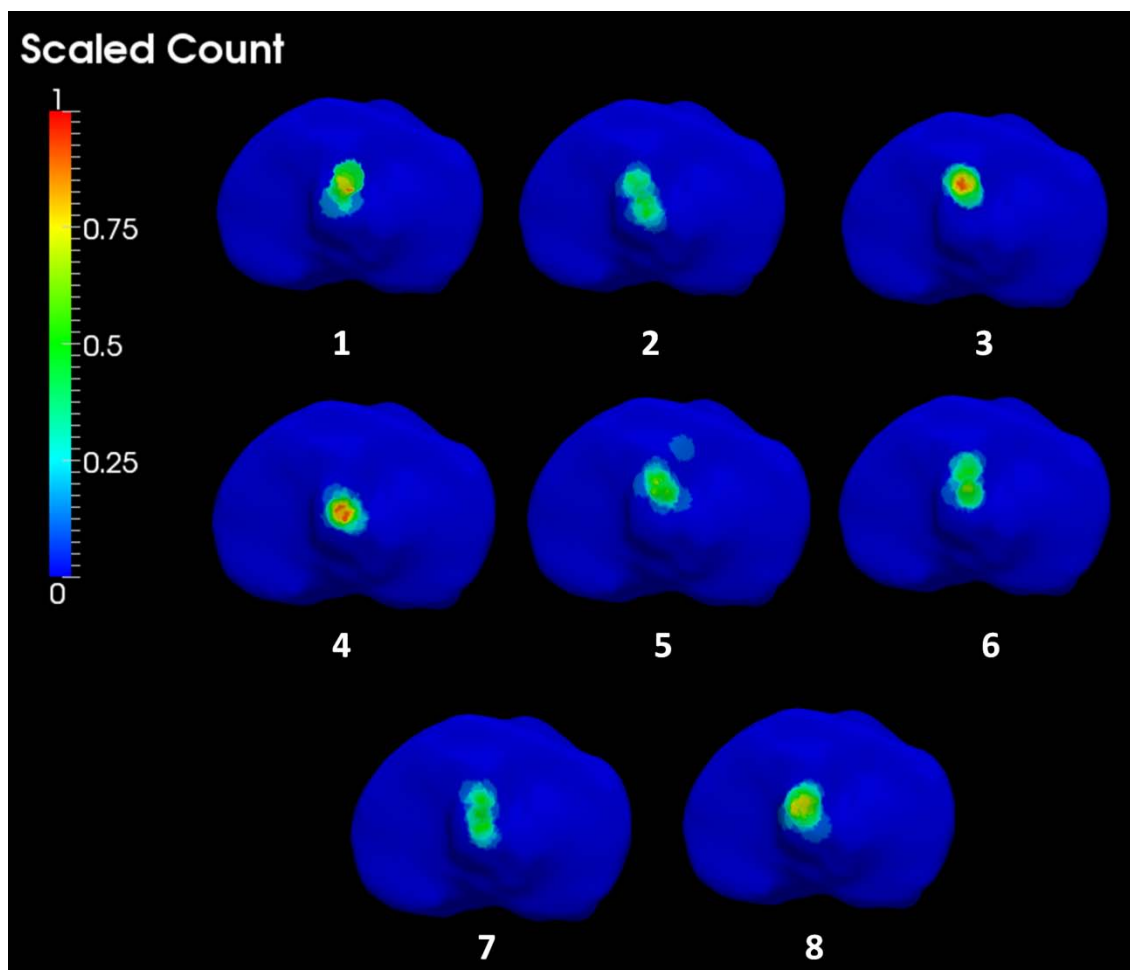


Figure C.33 ACL Tunnel Aperture Overlap Maps for the patient dataset depicting the likelihood of ACL tunnel placement on a native tibia bone surface organized by surgeon. Eight surgeons are depicted.

REFERENCES

- [1] W. Silvert, "Modelling As A Discipline," *Int. J. General Systems*, vol. 0, pp. 1-22, 2000.
- [2] D. L. Bartel, D. T. Davy and T. M. Keaveny, *Orthopaedic Biomechanics: Mechanics and Design in Musculoskeletal Systems*. New Jersey: Pearson Prentice Hall, 2006.
- [3] R. Bibb, *Medical Modelling: The Application of Advanced Design and Development Techniques in Medicine*. Florida: CRC Press LLC, 2006.
- [4] L. Capitanu, I. Iliuc, A. Iarovici, J. Onisoru and C. Tiganesteanu, "Solid 3D model realization of anatomical structures using computed tomography (CT scan) and magnetic rezonance imaging (MRI scan) data," in *Proceedings of the 3rd International Conference on Manufacturing Engineering*, Chalkidiki, Greece, 2008, .
- [5] I. Iliuc, L. Capitanu, M. Baubec and C. Tiganesteanu, "About some aspects of solid 3d models manufacturig of homan bone stuctures," in Bucharest, 2008, .
- [6] L. Scheys, I. Jonkers, F. Schutyser, S. Pans, A. Spaepen and P. Suetens, "Image based methods to generate subject-specific musculoskeletal models for gait analysis," *Int. Congr. Ser.*, vol. 1281, pp. 62-67, 5, 2005.
- [7] *Physics and Psychophysics*. Washington: SPIE Press, 2000.
- [8] *Medical Image Processing and Analysis*. Washington: SPIE Press, 2004.
- [9] Guoyan Zheng, "Reconstruction of Patient-Specific 3D Bone Model from Biplanar X-Ray Images and Point Distribution Models," *Image Processing, 2006 IEEE International Conference on*, pp. 1197-1200, 2006.
- [10] X. Dong and G. Zheng, "Automatic extraction of proximal femur contours from calibrated X-ray images using 3D statistical models: an in vitro study," *Int. J. Med. Robot.*, vol. 5, pp. 213-222, Jun, 2009.
- [11] F. Matthews, P. Messmer, V. Raikov, G. A. Wanner, A. L. Jacob, P. Regazzoni and A. Egli, "Patient-Specific Three-Dimensional Composite Bone Models for Teaching and Operation Planning," *J. Digit. Imaging*, Sep 21, 2007.
- [12] Joshua L. Simon, E. Dianne Rekow, Van P. Thompson, Heather Beam, John L. Ricci and J. Russell Parsons, "MicroCT analysis of hydroxyapatite bone repair scaffolds created via three-dimensional printing for evaluating the effects of scaffold architecture on bone ingrowth," *Journal of Biomedical Materials Research Part A*, vol. 85A, pp. 371-377, 2008.

- [13] C. Westin, S. Warfield, A. Bhalerao, L. Mui, J. Richolt and R. Kikinis, "Tensor controlled local structure enhancement of CT images for bone segmentation," *Medical Image Computing and Computer-Assisted Intervention — MICCAI'98*, pp. 1205-1212, 1998.
- [14] B. Gilles, L. Moccozet and N. Magnenat-Thalmann, "Anatomical modelling of the musculoskeletal system from MRI," *Med. Image Comput. Comput. Assist. Interv. Int. Conf. Med. Image Comput. Comput. Assist. Interv.*, vol. 9, pp. 289-296, 2006.
- [15] A. J. Ramme, N. DeVries, N. A. Kallemyn, V. A. Magnotta and N. M. Grosland, "Semi-automated phalanx bone segmentation using the expectation maximization algorithm," *J. Digit. Imaging*, vol. 22, pp. 483-491, Oct, 2009.
- [16] B. Potocnik, H. Dusan, Z. Damjan, B. Cigale and D. Bernad, "Construction of Patient Specific Virtual Models of Medical Phenomena," *Informatica*, vol. 29, pp. 209, 2005.
- [17] L. I. Wang, M. Greenspan and R. Ellis, "Validation of bone segmentation and improved 3-D registration using contour coherency in CT data," *IEEE Trans. Med. Imaging*, vol. 25, pp. 324-334, Mar, 2006.
- [18] *Display and PACS*. Washington: SPIE Press, 2000.
- [19] F. M. Vos, P. W. de Bruin, J. G. M. Aubel, G. J. Streekstra, M. Maas, L. J. van Vliet and A. M. Vossepoel, "A statistical shape model without using landmarks," *Pattern Recognition, 2004. ICPR 2004. Proceedings of the 17th International Conference on*, vol. 3, pp. 714-717 Vol.3, 2004.
- [20] L. H., S. M., H. H.-C. and D. P., "A 3D statistical shape model of the pelvic bone for segmentation," in *Society of Photo-Optical Instrumentation Engineers (SPIE) Conference Series; Society of Photo-Optical Instrumentation Engineers (SPIE) Conference Series*, 2004, pp. 1341-1351.
- [21] J. Fripp, S. Ourselin, S. Warfield, A. Mewes and S. Crozier, "Automatic Generation of 3D Statistical Shape Models of the Knee Bones," *Digital Image Computing*, 02, 2005.
- [22] J. Ehrhardt, H. Handels, W. Plotz and S. J. Poppl, "Atlas-based recognition of anatomical structures and landmarks and the automatic computation of orthopedic parameters," *Methods Inf. Med.*, vol. 43, pp. 391-397, 2004.
- [23] M. Egmont-Petersen, D. de Ridder and H. Handels, "Image processing with neural networks—a review," *Pattern Recognit*, vol. 35, pp. 2279-2301, 10, 2002.
- [24] J. Lotjonen, "Construction of patient-specific surface models from MR images: application to bioelectromagnetism," *Comput. Methods Programs Biomed.*, vol. 72, pp. 167-178, Oct, 2003.

- [25] T. S., P. G., B. D., D. P. and H. D., "Use of a CT statistical deformation model for multi-modal pelvic bone segmentation," in *Society of Photo-Optical Instrumentation Engineers (SPIE) Conference Series; Society of Photo-Optical Instrumentation Engineers (SPIE) Conference Series*, 2008, .
- [26] C. Lorenz and N. Krahnstover, "3D statistical shape models for medical image segmentation," *3-D Digital Imaging and Modeling, 1999. Proceedings. Second International Conference on*, pp. 414-423, 1999.
- [27] I. Diamant, R. Shahar, Y. Masharawi and A. Gefen, "A method for patient-specific evaluation of vertebral cancellous bone strength: in vitro validation," *Clin. Biomech. (Bristol, Avon)*, vol. 22, pp. 282-291, Mar, 2007.
- [28] C. M. Les, J. H. Keyak, S. M. Stover, K. T. Taylor and A. J. Kaneps, "Estimation of material properties in the equine metacarpus with use of quantitative computed tomography," *Journal of Orthopaedic Research*, vol. 12, pp. 822-833, 1994.
- [29] *Encyclopedia of Computational Mechanics: Fundamentals*. England: John Wiley & Sons, 2004.
- [30] A. A. Becker, *An Introductory Guide to Finite Element Analysis*. New York: ASME Press, 2004.
- [31] J. H. Kane, *Boundary Element Analysis: In Engineering Continuum Mechanics*. New Jersey: Prentice-Hall, 1994.
- [32] M. Viceconti, M. Davinelli, F. Taddei and A. Cappello, "Automatic generation of accurate subject-specific bone finite element models to be used in clinical studies," *J. Biomech.*, vol. 37, pp. 1597-1605, Oct, 2004.
- [33] J. Gao, W. Xu and Z. Ding, "3D finite element mesh generation of complicated tooth model based on CT slices," *Comput. Methods Programs Biomed.*, vol. 82, pp. 97-105, May, 2006.
- [34] S. Lu, Y. Q. Xu, Y. Z. Zhang, L. Xie, H. Guo and D. P. Li, "A novel computer-assisted drill guide template for placement of C2 laminar screws," *Eur. Spine J.*, Jun 11, 2009.
- [35] B. Schlatterer, I. Suedhoff, X. Bonnet, Y. Catonne, M. Maestro and W. Skalli, "Skeletal landmarks for TKR implantations: evaluation of their accuracy using EOS imaging acquisition system," *Orthop. Traumatol. Surg. Res.*, vol. 95, pp. 2-11, Feb, 2009.
- [36] S. H. Pettersen, T. S. Wik and B. Skallerud, "Subject specific finite element analysis of stress shielding around a cementless femoral stem," *Clin. Biomech. (Bristol, Avon)*, vol. 24, pp. 196-202, Feb, 2009.

- [37] R. P. Crawford, C. E. Cann and T. M. Keaveny, "Finite element models predict in vitro vertebral body compressive strength better than quantitative computed tomography," *Bone*, vol. 33, pp. 744-750, Oct, 2003.
- [38] J. R. Cebal, M. A. Castro, J. E. Burgess, R. S. Pergolizzi, M. J. Sheridan and C. M. Putman, "Characterization of cerebral aneurysms for assessing risk of rupture by using patient-specific computational hemodynamics models," *AJNR Am. J. Neuroradiol.*, vol. 26, pp. 2550-2559, Nov-Dec, 2005.
- [39] E. L. Leventhal, S. W. Wolfe, E. F. Walsh and J. J. Crisco, "A computational approach to the "optimal" screw axis location and orientation in the scaphoid bone," *J. Hand Surg. Am.*, vol. 34, pp. 677-684, Apr, 2009.
- [40] R. Wicker and B. Tedla, "Automatic determination of pedicle screw size, length, and trajectory from patient data," *Conf. Proc. IEEE Eng. Med. Biol. Soc.*, vol. 2, pp. 1487-1490, 2004.
- [41] M. Chabanas, V. Luboz and Y. Payan, "Patient specific finite element model of the face soft tissues for computer-assisted maxillofacial surgery," *Med. Image Anal.*, vol. 7, pp. 131-151, Jun, 2003.
- [42] D. Blana, J. G. Hincapie, E. K. Chadwick and R. F. Kirsch, "A musculoskeletal model of the upper extremity for use in the development of neuroprosthetic systems," *J. Biomech.*, vol. 41, pp. 1714-1721, 2008.
- [43] L. Antiga, M. Piccinelli, L. Botti, B. Ene-Iordache, A. Remuzzi and D. A. Steinman, "An image-based modeling framework for patient-specific computational hemodynamics," *Med. Biol. Eng. Comput.*, vol. 46, pp. 1097-1112, Nov, 2008.
- [44] J. Lin, S. J. Lin, P. Q. Chen and S. H. Yang, "Stress analysis of the distal locking screws for femoral interlocking nailing," *J. Orthop. Res.*, vol. 19, pp. 57-63, Jan, 2001.
- [45] M. Barink, W. M. De, P. Celada, P. Vena, A. Van Kampen and N. Verdonschot, "A mechanical comparison of high-flexion and conventional total knee arthroplasty," *Proc. Inst. Mech. Eng. Part H J. Eng. Med.*, vol. 222, pp. 297-307, 03/01, 2008.
- [46] V. A. Magnotta, G. Harris, N. C. Andreasen, D. S. O'Leary, W. T. Yuh and D. Heckel, "Structural MR image processing using the BRAINS2 toolbox," *Comput. Med. Imaging Graph.*, vol. 26, pp. 251-264, Jul-Aug, 2002.
- [47] R. Huiskes and S. J. Hollister, "From structure to process, from organ to cell: recent developments of FE-analysis in orthopaedic biomechanics," *J. Biomech. Eng.*, vol. 115, pp. 520-527, Nov, 1993.

- [48] J. Vander Sloten, M. C. Hobatho and P. Verdonck, "Applications of computer modelling for the design of orthopaedic, dental and cardiovascular biomaterials," *Proc. Inst. Mech. Eng. H.*, vol. 212, pp. 489-500, 1998.
- [49] Q. H. Zhang and E. C. Teo, "Finite element application in implant research for treatment of lumbar degenerative disc disease," *Med. Eng. Phys.*, vol. 30, pp. 1246-1256, Dec, 2008.
- [50] A. Mellal, H. W. Wiskott, J. Botsis, S. S. Scherrer and U. C. Belser, "Stimulating effect of implant loading on surrounding bone. Comparison of three numerical models and validation by in vivo data," *Clin. Oral Implants Res.*, vol. 15, pp. 239-248, Apr, 2004.
- [51] R. A. Brand, C. M. Stanford and C. C. Swan, "How do tissues respond and adapt to stresses around a prosthesis? A primer on finite element stress analysis for orthopaedic surgeons," *Iowa Orthop. J.*, vol. 23, pp. 13-22, 2003.
- [52] T. D. Brown, M. J. Rudert and N. M. Grosland, "New methods for assessing cartilage contact stress after articular fracture," *Clin. Orthop. Relat. Res.*, vol. 423, pp. 52-58, Jun, 2004.
- [53] S. Portnoy, I. Siev-Ner, N. Shabshin, A. Kristal, Z. Yizhar and A. Gefen, "Patient-specific analyses of deep tissue loads post transtibial amputation in residual limbs of multiple prosthetic users," *J. Biomech.*, Sep 17, 2009.
- [54] J. M. Fritz, Y. Guan, M. Wang, P. A. Smith and G. F. Harris, "A fracture risk assessment model of the femur in children with osteogenesis imperfecta (OI) during gait," *Med. Eng. Phys.*, Aug 14, 2009.
- [55] N. Wakao, A. Harada, Y. Matsui, M. Takemura, H. Shimokata, M. Mizuno, M. Ito, Y. Matsuyama and N. Ishiguro, "The effect of impact direction on the fracture load of osteoporotic proximal femurs," *Med. Eng. Phys.*, Aug 6, 2009.
- [56] B. Helgason, H. Palsson, T. P. Runarsson, L. Frossard and M. Viceconti, "Risk of failure during gait for direct skeletal attachment of a femoral prosthesis: a finite element study," *Med. Eng. Phys.*, vol. 31, pp. 595-600, Jun, 2009.
- [57] O. L. Harrysson, Y. A. Hosni and J. F. Nayfeh, "Custom-designed orthopedic implants evaluated using finite element analysis of patient-specific computed tomography data: femoral-component case study," *BMC Musculoskelet. Disord.*, vol. 8, pp. 91, Sep 13, 2007.
- [58] J. Furmanski, M. Anderson, S. Bal, A. S. Greenwald, D. Halley, B. Penenberg, M. Ries and L. Pruitt, "Clinical fracture of cross-linked UHMWPE acetabular liners," *Biomaterials*, vol. 30, pp. 5572-5582, Oct, 2009.

- [59] R. Shirazi and A. Shirazi-Adl, "Computational biomechanics of articular cartilage of human knee joint: Effect of osteochondral defects," *J. Biomech.*, Aug 4, 2009.
- [60] P. Varga, S. Baumbach, D. Pahr and P. K. Zysset, "Validation of an anatomy specific finite element model of Colles' fracture," *J. Biomech.*, vol. 42, pp. 1726-1731, Aug 7, 2009.
- [61] A. Zeinali, B. Hashemi and S. Akhlaghpour, "Noninvasive prediction of vertebral body compressive strength using nonlinear finite element method and an image based technique," *Phys. Med.*, Sep 23, 2009.
- [62] T. B. Sebastian, H. Tek, J. J. Crisco and B. B. Kimia, "Segmentation of carpal bones from CT images using skeletally coupled deformable models," *Med. Image Anal.*, vol. 7, pp. 21-45, Mar, 2003.
- [63] P. Sapiro, J. S. Thomsen, J. Kurths, G. Beller and W. Gowin, "Segmentation of bone CT images and assessment of bone structure using measures of complexity," *Med. Phys.*, vol. 33, pp. 3857-3873, Oct, 2006.
- [64] N. M. Grosland, K. H. Shivanna, V. A. Magnotta, N. A. Kallemeyn, N. A. DeVries, S. C. Tadepalli and C. Lisle, "IA-FEMesh: an open-source, interactive, multiblock approach to anatomic finite element model development," *Comput. Methods Programs Biomed.*, vol. 94, pp. 96-107, Apr, 2009.
- [65] F. Gelaude, J. Vander Sloten and B. Lauwers, "Semi-automated segmentation and visualisation of outer bone cortex from medical images," *Comput. Methods Biomech. Biomed. Engin.*, vol. 9, pp. 65-77, Feb, 2006.
- [66] J. Ehrhardt, H. Handels, T. Malina, B. Strathmann, W. Plotz and S. J. Poppl, "Atlas-based segmentation of bone structures to support the virtual planning of hip operations," *Int. J. Med. Inform.*, vol. 64, pp. 439-447, Dec, 2001.
- [67] A. O. Cifuentes and A. Kalbag, "A performance study of tetrahedral and hexahedral elements in 3-D finite element structural analysis," *Finite Elements Anal. Des.*, vol. 12, pp. 313-318, 12, 1992.
- [68] M. L. Staten, R. A. Kerr, S. J. Owen and T. D. Blacker, "Unconstrained paving and plastering: Progress update," in *15th International Meshing Roundtable*, Birmingham, Alabama, 2006, .
- [69] R. W. Leland, D. J. Melander, R. J. Meyers, S. A. Mitchell and T. J. Tautges, "The geode algorithm: Combining Hex/Tet plastering, dicing and transition elements for automatic, all-hex mesh generation," in *7th International Meshing Roundtable*, Dearborn, Michigan, 1998, pp. 515-521.

- [70] A. Sheffer, M. Etzion, A. Rappoport and M. Bercovier, "Hexahedral Mesh Generation using the Embedded Voronoi Graph," *Eng.Comput.(Lond.)*, vol. 15, pp. 248-262, 1999.
- [71] M. Muller-Hannemann, "Shelling Hexahedral Complexes for Mesh Generation," *J.Graph Algorithms Appl.*, vol. 5, pp. 59-91, 2001.
- [72] T. J. Tautges, T. Blacker and S. A. Mitchell, "The Whisker Weaving Algorithm: A Connectivity-Based Method for Constructing All-Hexahedral Finite Element Meshes," *Int J Numer Methods Eng*, vol. 39, pp. 3327-3349, 1996.
- [73] S. J. Owen, "A survey of unstructured mesh generation technology," in *7th International Meshing Roundtable*, Dearborn, Michigan, 1998, pp. 239-267.
- [74] P. Sampl, "Semi-structured mesh generation based on medial axis," in *9th International Meshing Roundtable*, New Orleans, Louisiana, 2000, .
- [75] D. Guoy and J. Erickson, "Automatic blocking scheme for structured meshing in 2d multiphase flow simulation," in *13th International Meshing Roundtable*, Williamsburg, Virginia, 2004, pp. 121-132.
- [76] T. Blacker, "The cooper tool," in *5th International Meshing Roundtable*, Pittsburgh, Pennsylvania, 1996, pp. 13-29.
- [77] A. Gaither, "An efficient block detection algorithm for structured grid generation," in *5th International Conference on Numerical Grid Generation in Computational Field Simulations*, 1996, pp. 443-451.
- [78] J. F. Dannenhoffer III, "Automatic block-structured grid generation - progress and challenges," Tech. Rep. FS-92-01, 1992.
- [79] N. A. Artyomova and O. B. Khairullina, "Generation of Three-Dimensional Block-Structured Grids Based on Rotation of Two-Dimensional Multiply Connected Cross Sections," *Computational Methods and Mathematical Physics*, vol. 48, pp. 2093, 2007.
- [80] S. Ng, C. C. Weng, L. W. Ming, L. C. Ling and T. H. Mann, "SMESH3D: An interactive structured mesh generation system," in *High-Performance Computing on the Information Superhighway*, 1997, pp. 728.
- [81] A. Aksenova and V. Chudanov, "A multi-block orthogonal grid generation using CAD system," in *8th International Meshing Roundtable*, South Lake Tahoe, CA, 1999, pp. 179.
- [82] J. P. Steinbrenner and J. R. Chawner, "Gridgen's implementation of partial differential equation based structured grid generation methods," in *8th International Meshing Roundtable*, South Lake Tahoe, CA, 1999, pp. 143-152.

- [83] K. Subburaj, B. Ravi and M. G. Agarwal, "3D Shape Reasoning for Identifying Anatomical Landmarks," *Computer-Aided Design and Applications*, vol. 5, pp. 153-160, 2008.
- [84] K. Subburaj, B. Ravi and M. Agarwal, "Automated identification of anatomical landmarks on 3D bone models reconstructed from CT scan images," *Comput. Med. Imaging Graph.*, vol. 33, pp. 359-368, Jul, 2009.
- [85] W. Yi and S. Marshall, "Principal Component Analysis In Application To Object Orientation," *Geo-Spatial Information Science*, vol. 3, pp. 76-78, 2000.
- [86] H. Fu, D. Cohen-Or, G. Dror and A. Sheffer, "Upright orientation of man-made objects," *ACM Trans.Graph.*, vol. 27, pp. 1-7, 2008.
- [87] M. Chaouch and A. Verroust-Blondet, "A novel method for alignment of 3D models," in *IEEE International Conference on Shape Modeling and Applications*, 2008, pp. 187-195.
- [88] A. J. Ramme, K. H. Shivanna, V. A. Magnotta and N. M. Grosland, "Gaussian curvature analysis allows for automatic block placement in multi-block hexahedral meshing," *Comput. Methods Biomech. Biomed. Engin.*, pp. 1, Oct 1, 2010.
- [89] B. K. P. Horn, "Closed-form solution of absolute orientation using unit quaternions," *Journal of the Optical Society of America A*, vol. 4, pp. 629-642, 1987.
- [90] R. A. Zoroofi, Y. Sato, T. Sasama, T. Nishii, N. Sugano, K. Yonenobu, H. Yoshikawa, T. Ochi and S. Tamura, "Automated segmentation of acetabulum and femoral head from 3-D CT images," *IEEE Trans. Inf. Technol. Biomed.*, vol. 7, pp. 329-343, Dec, 2003.
- [91] A. Mastmeyer, K. Engelke, C. Fuchs and W. A. Kalender, "A hierarchical 3D segmentation method and the definition of vertebral body coordinate systems for QCT of the lumbar spine," *Med. Image Anal.*, vol. 10, pp. 560-577, Aug, 2006.
- [92] J. Staal, B. van Ginneken and M. A. Viergever, "Automatic rib segmentation and labeling in computed tomography scans using a general framework for detection, recognition and segmentation of objects in volumetric data," *Med. Image Anal.*, vol. 11, pp. 35-46, Feb, 2007.
- [93] T. Dufresne, "Segmentation techniques for analysis of bone by three-dimensional computed tomographic imaging," *Technol. Health Care*, vol. 6, pp. 351-359, Dec, 1998.
- [94] S. S. Burnett, G. Starkschalla, C. W. Stevens and Z. Liao, "A deformable-model approach to semi-automatic segmentation of CT images demonstrated by application to the spinal canal," *Med. Phys.*, vol. 31, pp. 251-263, Feb, 2004.

- [95] Y. Li, B. Hong, S. Gao and K. Liu, "Bone segmentation in human CT images," *Sheng Wu Yi Xue Gong Cheng Xue Za Zhi*, vol. 21, pp. 169-173, Apr, 2004.
- [96] S. Rueda, J. A. Gil, R. Pichery and M. Alcaniz, "Automatic segmentation of jaw tissues in CT using active appearance models and semi-automatic landmarking," *Med. Image Comput. Comput. Assist. Interv. Int. Conf. Med. Image Comput. Comput. Assist. Interv.*, vol. 9, pp. 167-174, 2006.
- [97] E. E. Gassman, S. M. Powell, N. A. Kallemeyn, N. A. Devries, K. H. Shivanna, V. A. Magnotta, A. J. Ramme, B. D. Adams and N. M. Grosland, "Automated bony region identification using artificial neural networks: reliability and validation measurements," *Skeletal Radiol.*, Jan 3, 2008.
- [98] K. M. Pohl, J. Fisher, J. J. Levitt, M. E. Shenton, R. Kikinis, W. E. Grimson and W. M. Wells, "A unifying approach to registration, segmentation, and intensity correction," *Med. Image Comput. Comput. Assist. Interv. Int. Conf. Med. Image Comput. Comput. Assist. Interv.*, vol. 8, pp. 310-318, 2005.
- [99] K. M. Pohl, J. Fisher, W. E. Grimson and W. M. Wells, "An Expectation Maximization Approach for Integrated Registration, Segmentation, and Intensity Correction," *AI Memo*, vol. 2005-010, pp. 1-13, 2005.
- [100] K. M. Pohl, J. Fisher, W. E. Grimson, R. Kikinis and W. M. Wells, "A Bayesian model for joint segmentation and registration," *Neuroimage*, vol. 31, pp. 228-239, May 15, 2006.
- [101] N. Rannou, S. Jaume, S. Pieper and R. Kikinis, "New Expectation Maximization Segmentation Pipeline in Slicer3," *The Insight Journal*, 2009.
- [102] K. M. Pohl, J. Fisher, R. Kikinis, W. E. Grimson and W. M. and Wells, "Shape Based Segmentation of Anatomical Structures in Magnetic Resonance Images," *Lecture Notes in Computer Science*, vol. 3765, pp. 489-498, 2005.
- [103] N. A. DeVries, E. E. Gassman, N. A. Kallemeyn, K. H. Shivanna, V. A. Magnotta and N. M. Grosland, "Validation of phalanx bone three-dimensional surface segmentation from computed tomography images using laser scanning," *Skeletal Radiol.*, vol. 37, pp. 35-42, Jan, 2008.
- [104] M. H. Davis, A. Khotanzad, D. P. Flamig and S. E. Harms, "A physics-based coordinate transformation for 3-D image matching," *IEEE Trans. Med. Imaging*, vol. 16, pp. 317-328, Jun, 1997.
- [105] J. P. Thirion, "Image matching as a diffusion process: an analogy with Maxwell's demons," *Med. Image Anal.*, vol. 2, pp. 243-260, Sep, 1998.

- [106] T. L. Donahue, M. L. Hull, M. M. Rashid and C. R. Jacobs, "A finite element model of the human knee joint for the study of tibio-femoral contact," *J. Biomech. Eng.*, vol. 124, pp. 273-280, Jun, 2002.
- [107] S. Powell, V. A. Magnotta, H. Johnson, V. K. Jammalamadaka, R. Pierson and N. C. Andreasen, "Registration and machine learning-based automated segmentation of subcortical and cerebellar brain structures," *Neuroimage*, vol. 39, pp. 238-247, Jan 1, 2008.
- [108] G. C. Sharp, S. W. Lee and D. K. Wehe, "Invariant features and the registration of rigid bodies." *In: Proc. IEEE Int. Conf. on Robotics and Autom.*, vol. 1999, pp. 932-937, 1999.
- [109] O. Museyko, F. Eisa, A. Hess, G. Schett, W. A. Kalender and K. Engelke, "Binary Segmentation Masks Can Improve Intrasubject Registration Accuracy of Bone Structures in CT Images," *Ann. Biomed. Eng.*, vol. 38, pp. 2464-2472, Jul, 2010.
- [110] Y. Kang, K. Engelke and W. A. Kalender, "A new accurate and precise 3-D segmentation method for skeletal structures in volumetric CT data," *IEEE Trans. Med. Imaging*, vol. 22, pp. 586-598, May, 2003.
- [111] X. M. Pardo, M. J. Carreira, A. Mosquera and D. Cabello, "A snake for CT image segmentation integrating region and edge information," *Image Vision Comput.*, vol. 19, pp. 461-475, 5/1, 2001.
- [112] J. Liu, J. K. Udupa, P. K. Saha, D. Odhner, B. E. Hirsch, S. Siegler, S. Simon and B. A. Winkelstein, "Rigid model-based 3D segmentation of the bones of joints in MR and CT images for motion analysis," *Med. Phys.*, vol. 35, pp. 3637-3649, Aug, 2008.
- [113] P. Dodin, J. Pelletier, J. Martel-Pelletier and F. Abram, "Automatic Human Knee Cartilage Segmentation From 3-D Magnetic Resonance Images," *Biomedical Engineering, IEEE Transactions on*, vol. 57, pp. 2699-2711, 2010.
- [114] C. B. Do and S. Batzoglou, "What is the expectation maximization algorithm?" *Nat. Biotechnol.*, vol. 26, pp. 897-899, Aug, 2008.
- [115] N. J. Tustison and J. C. Gee, "Introducing Dice, Jaccard, and Other Label Overlap Measures to ITK," *The Insight Journal*, 2009.
- [116] A. Klein, J. Andersson, B. A. Ardekani, J. Ashburner, B. Avants, M. C. Chiang, G. E. Christensen, D. L. Collins, J. Gee, P. Hellier, J. H. Song, M. Jenkinson, C. Lepage, D. Rueckert, P. Thompson, T. Vercauteren, R. P. Woods, J. J. Mann and R. V. Parsey, "Evaluation of 14 nonlinear deformation algorithms applied to human brain MRI registration," *Neuroimage*, vol. 46, pp. 786-802, Jul 1, 2009.

- [117] F. Cimino, B. S. Volk and D. Setter, "Anterior cruciate ligament injury: diagnosis, management, and prevention," *Am. Fam. Physician*, vol. 82, pp. 917-922, Oct 15, 2010.
- [118] T. Zantop, W. Petersen, J. K. Sekiya, V. Musahl and F. H. Fu, "Anterior cruciate ligament anatomy and function relating to anatomical reconstruction," *Knee Surg. Sports Traumatol. Arthrosc.*, vol. 14, pp. 982-992, Oct, 2006.
- [119] B. D. Beynnon, R. J. Johnson, J. A. Abate, B. C. Fleming and C. E. Nichols, "Treatment of anterior cruciate ligament injuries, part I," *Am. J. Sports Med.*, vol. 33, pp. 1579-1602, Oct, 2005.
- [120] R. V. West and C. D. Harner, "Graft selection in anterior cruciate ligament reconstruction," *J. Am. Acad. Orthop. Surg.*, vol. 13, pp. 197-207, May-Jun, 2005.
- [121] F. Giron, P. Cuomo, P. Aglietti, A. M. Bull and A. A. Amis, "Femoral attachment of the anterior cruciate ligament," *Knee Surg. Sports Traumatol. Arthrosc.*, vol. 14, pp. 250-256, Mar, 2006.
- [122] E. K. Bicer, S. Lustig, E. Servien, T. A. Selmi and P. Neyret, "Current knowledge in the anatomy of the human anterior cruciate ligament," *Knee Surg. Sports Traumatol. Arthrosc.*, vol. 18, pp. 1075-1084, Aug, 2010.
- [123] A. A. Amis, B. Beynnon, L. Blankevoort, P. Chambat, P. Christel, L. Durselen, N. Friederich, E. Grood, P. Hertel and R. Jakob, "Proceedings of the ESSKA Scientific Workshop on Reconstruction of the Anterior and Posterior Cruciate Ligaments," *Knee Surg. Sports Traumatol. Arthrosc.*, vol. 2, pp. 124-132, 1994.
- [124] D. Endeke, C. Jung, U. Becker, G. Bauer and F. Mauch, "Anterior cruciate ligament reconstruction with and without computer navigation: a clinical and magnetic resonance imaging evaluation 2 years after surgery," *Arthroscopy*, vol. 25, pp. 1067-1074, Oct, 2009.
- [125] D. Kendoff, M. Citak, J. Voos and A. D. Pearle, "Surgical navigation in knee ligament reconstruction," *Clin. Sports Med.*, vol. 28, pp. 41-50, Jan, 2009.
- [126] K. P. Spindler and R. W. Wright, "Clinical practice. Anterior cruciate ligament tear," *N. Engl. J. Med.*, vol. 359, pp. 2135-2142, Nov 13, 2008.
- [127] R. B. Frobell, E. M. Roos, H. P. Roos, J. Ranstam and L. S. Lohmander, "A randomized trial of treatment for acute anterior cruciate ligament tears," *N. Engl. J. Med.*, vol. 363, pp. 331-342, Jul 22, 2010.
- [128] J. Goldstein and J. A. Bosco 3rd, "The ACL-deficient knee: natural history and treatment options," *Bull. Hosp. Jt. Dis.*, vol. 60, pp. 173-178, -2002, 2001.

- [129] C. C. Prodromos, F. H. Fu, S. M. Howell, D. H. Johnson and K. Lawhorn, "Controversies in soft-tissue anterior cruciate ligament reconstruction: grafts, bundles, tunnels, fixation, and harvest," *J. Am. Acad. Orthop. Surg.*, vol. 16, pp. 376-384, Jul, 2008.
- [130] B. P. Boden, F. T. Sheehan, J. S. Torg and T. E. Hewett, "Noncontact anterior cruciate ligament injuries: mechanisms and risk factors," *J. Am. Acad. Orthop. Surg.*, vol. 18, pp. 520-527, Sep, 2010.
- [131] R. H. Brophy, H. J. Silvers and B. R. Mandelbaum, "Anterior cruciate ligament injuries: etiology and prevention," *Sports Med. Arthrosc.*, vol. 18, pp. 2-11, Mar, 2010.
- [132] B. P. Boden, G. S. Dean, J. A. Feagin Jr and W. E. Garrett Jr, "Mechanisms of anterior cruciate ligament injury," *Orthopedics*, vol. 23, pp. 573-578, Jun, 2000.
- [133] C. E. Quatman, C. C. Quatman-Yates and T. E. Hewett, "A 'plane' explanation of anterior cruciate ligament injury mechanisms: a systematic review," *Sports Med.*, vol. 40, pp. 729-746, Sep 1, 2010.
- [134] B. E. Oiestad, L. Engebretsen, K. Storheim and M. A. Risberg, "Knee osteoarthritis after anterior cruciate ligament injury: a systematic review," *Am. J. Sports Med.*, vol. 37, pp. 1434-1443, Jul, 2009.
- [135] A. Papadonikolakis, L. Cooper, N. Stergiou, A. D. Georgoulis and P. N. Soucacos, "Compensatory mechanisms in anterior cruciate ligament deficiency," *Knee Surg. Sports Traumatol. Arthrosc.*, vol. 11, pp. 235-243, Jul, 2003.
- [136] V. B. Duthon, C. Barea, S. Abrassart, J. H. Fasel, D. Fritschy and J. Menetrey, "Anatomy of the anterior cruciate ligament," *Knee Surg. Sports Traumatol. Arthrosc.*, vol. 14, pp. 204-213, Mar, 2006.
- [137] M. J. DeFranco and B. R. Bach Jr, "A comprehensive review of partial anterior cruciate ligament tears," *J. Bone Joint Surg. Am.*, vol. 91, pp. 198-208, Jan, 2009.
- [138] W. R. Dunn, K. P. Spindler, A. Amendola, J. T. Andrish, C. C. Kaeding, R. G. Marx, E. C. McCarty, R. D. Parker, F. E. Harrell Jr, A. Q. An, R. W. Wright, R. H. Brophy, M. J. Matava, D. C. Flanigan, L. J. Huston, M. H. Jones, M. L. Wolcott, A. F. Vidal, B. R. Wolf and MOON ACL Investigation, "Which preoperative factors, including bone bruise, are associated with knee pain/symptoms at index anterior cruciate ligament reconstruction (ACLR)? A Multicenter Orthopaedic Outcomes Network (MOON) ACLR Cohort Study," *Am. J. Sports Med.*, vol. 38, pp. 1778-1787, Sep, 2010.
- [139] J. C. Thompson, *Netter's Concise Orthopaedic Anatomy*. 2010.

- [140] P. Aglietti, G. Zaccherotti, P. P. Menchetti and P. De Biase, "A comparison of clinical and radiological parameters with two arthroscopic techniques for anterior cruciate ligament reconstruction," *Knee Surg. Sports Traumatol. Arthrosc.*, vol. 3, pp. 2-8, 1995.
- [141] S. Arneja and J. Leith, "Review article: Validity of the KT-1000 knee ligament arthrometer," *J. Orthop. Surg. (Hong Kong)*, vol. 17, pp. 77-79, Apr, 2009.
- [142] K. L. Markolf, S. R. Jackson and D. R. McAllister, "A Comparison of 11 O'clock Versus Oblique Femoral Tunnels in the Anterior Cruciate Ligament-Reconstructed Knee: Knee Kinematics During a Simulated Pivot Test," *Am. J. Sports Med.*, Mar 22, 2010.
- [143] E. Lopez-Vidriero and D. Hugh Johnson, "Evolving concepts in tunnel placement," *Sports Med. Arthrosc.*, vol. 17, pp. 210-216, Dec, 2009.
- [144] K. W. Lawhorn and S. M. Howell, "Principles for using hamstring tendons for anterior cruciate ligament reconstruction," *Clin. Sports Med.*, vol. 26, pp. 567-585, Oct, 2007.
- [145] L. A. Pinczewski, L. J. Salmon, W. F. Jackson, R. B. von Bormann, P. G. Haslam and S. Tashiro, "Radiological landmarks for placement of the tunnels in single-bundle reconstruction of the anterior cruciate ligament," *J. Bone Joint Surg. Br.*, vol. 90, pp. 172-179, Feb, 2008.
- [146] T. J. Gill and J. R. Steadman, "Anterior cruciate ligament reconstruction the two-incision technique," *Orthop. Clin. North Am.*, vol. 33, pp. 727-35, vii, Oct, 2002.
- [147] E. S. Abebe, C. T. Moorman 3rd, T. S. Dziedzic, C. E. Spritzer, R. L. Cothran, D. C. Taylor, W. E. Garrett Jr and L. E. DeFrate, "Femoral tunnel placement during anterior cruciate ligament reconstruction: an in vivo imaging analysis comparing transtibial and 2-incision tibial tunnel-independent techniques," *Am. J. Sports Med.*, vol. 37, pp. 1904-1911, Oct, 2009.
- [148] A. Bedi, B. Raphael, A. Maderazo, H. Pavlov and R. J. Williams 3rd, "Transtibial versus anteromedial portal drilling for anterior cruciate ligament reconstruction: a cadaveric study of femoral tunnel length and obliquity," *Arthroscopy*, vol. 26, pp. 342-350, Mar, 2010.
- [149] P. Yerys, "Anterior cruciate ligament reconstruction using allograft: single tunnel technique," *Sports Med. Arthrosc.*, vol. 15, pp. 191-198, Dec, 2007.
- [150] J. H. Lubowitz, "Anteromedial portal technique for the anterior cruciate ligament femoral socket: pitfalls and solutions," *Arthroscopy*, vol. 25, pp. 95-101, Jan, 2009.
- [151] M. Nakamura, M. Deie, H. Shibuya, A. Nakamae, N. Adachi, H. Aoyama and M. Ochi, "Potential risks of femoral tunnel drilling through the far anteromedial portal: a cadaveric study," *Arthroscopy*, vol. 25, pp. 481-487, May, 2009.

- [152] P. Kasten, M. Szczodry, J. Irrgang, E. Kropf, J. Costello and F. H. Fu, "What is the role of intra-operative fluoroscopic measurements to determine tibial tunnel placement in anatomical anterior cruciate ligament reconstruction?" *Knee Surg. Sports Traumatol. Arthrosc.*, Mar 9, 2010.
- [153] K. R. Flik and B. R. Bach, "Anterior Cruciate Ligament Reconstruction Using a Two-Incision Arthroscopy-Assisted Technique With Patellar Tendon Autograft," *Techniques in Orthopaedics*, vol. 20, pp. 372-376, 2005.
- [154] J. Michaelson, "ACL Reconstruction - Medial Portal," *Biomet Sports Medicine*, 2009.
- [155] H. Steckel, F. H. Fu, M. H. Baums and H. M. Klinger, "Arthroscopic evaluation of the ACL double bundle structure," *Knee Surg. Sports Traumatol. Arthrosc.*, vol. 17, pp. 782-785, Jul, 2009.
- [156] P. Aglietti, F. Giron, M. Losco, P. Cuomo, A. Ciardullo and N. Mondanelli, "Comparison between single-and double-bundle anterior cruciate ligament reconstruction: a prospective, randomized, single-blinded clinical trial," *Am. J. Sports Med.*, vol. 38, pp. 25-34, Jan, 2010.
- [157] A. C. Colvin, W. Shen, V. Musahl and F. H. Fu, "Avoiding pitfalls in anatomic ACL reconstruction," *Knee Surg. Sports Traumatol. Arthrosc.*, vol. 17, pp. 956-963, Aug, 2009.
- [158] M. P. Walsh, C. A. Wijdicks, B. M. Armitage, B. D. Westerhaus, J. B. Parker and R. F. LaPrade, "The 1:1 versus the 2:2 tunnel-drilling technique: optimization of fixation strength and stiffness in an all-inside double-bundle anterior cruciate ligament reconstruction--a biomechanical study," *Am. J. Sports Med.*, vol. 37, pp. 1539-1547, Aug, 2009.
- [159] B. Forsythe, S. Kopf, A. K. Wong, C. A. Martins, W. Anderst, S. Tashman and F. H. Fu, "The location of femoral and tibial tunnels in anatomic double-bundle anterior cruciate ligament reconstruction analyzed by three-dimensional computed tomography models," *J. Bone Joint Surg. Am.*, vol. 92, pp. 1418-1426, Jun, 2010.
- [160] J. Y. Ho, A. Gardiner, V. Shah and M. E. Steiner, "Equal kinematics between central anatomic single-bundle and double-bundle anterior cruciate ligament reconstructions," *Arthroscopy*, vol. 25, pp. 464-472, May, 2009.
- [161] Y. Kato, S. J. Ingham, S. Kramer, P. Smolinski, A. Saito and F. H. Fu, "Effect of tunnel position for anatomic single-bundle ACL reconstruction on knee biomechanics in a porcine model," *Knee Surg. Sports Traumatol. Arthrosc.*, vol. 18, pp. 2-10, Jan, 2010.
- [162] J. L. Koh, "The future of computer-assisted surgery (CAS) in sports medicine," *Sports Med. Arthrosc.*, vol. 16, pp. 108-110, Jun, 2008.

- [163] U. W. Muller-Alsbach and A. E. Staubli, "Computer aided ACL reconstruction," *Injury*, vol. 35 Suppl 1, pp. S-A65-7, Jun, 2004.
- [164] J. K. Sekiya, B. C. Ong and J. P. Bradley, "Complications in anterior cruciate ligament surgery," *Orthop. Clin. North Am.*, vol. 34, pp. 99-105, Jan, 2003.
- [165] B. D. Beynnon, R. J. Johnson, J. A. Abate, B. C. Fleming and C. E. Nichols, "Treatment of anterior cruciate ligament injuries, part 2," *Am. J. Sports Med.*, vol. 33, pp. 1751-1767, Nov, 2005.
- [166] D. J. Deehan and T. E. Cawston, "The biology of integration of the anterior cruciate ligament," *J. Bone Joint Surg. Br.*, vol. 87, pp. 889-895, Jul, 2005.
- [167] M. Ekdahl, J. H. Wang, M. Ronga and F. H. Fu, "Graft healing in anterior cruciate ligament reconstruction," *Knee Surg. Sports Traumatol. Arthrosc.*, vol. 16, pp. 935-947, Oct, 2008.
- [168] S. L. Woo, S. D. Abramowitch, R. Kilger and R. Liang, "Biomechanics of knee ligaments: injury, healing, and repair," *J. Biomech.*, vol. 39, pp. 1-20, 2006.
- [169] D. J. Pezzullo and P. Fadale, "Current controversies in rehabilitation after anterior cruciate ligament reconstruction," *Sports Med. Arthrosc.*, vol. 18, pp. 43-47, Mar, 2010.
- [170] D. S. Johnson and R. B. Smith, "Outcome measurement in the ACL deficient knee-what's the score?" *Knee*, vol. 8, pp. 51-57, Mar, 2001.
- [171] E. M. Roos and L. S. Lohmander, "The Knee injury and Osteoarthritis Outcome Score (KOOS): from joint injury to osteoarthritis," *Health. Qual. Life. Outcomes*, vol. 1, pp. 64, Nov 3, 2003.
- [172] A. Heijne, B. O. Ang and S. Werner, "Predictive factors for 12-month outcome after anterior cruciate ligament reconstruction," *Scand. J. Med. Sci. Sports*, vol. 19, pp. 842-849, Dec, 2009.
- [173] E. Laboute, L. Savalli, P. L. Puig, P. Trouve, M. Larbaigt and M. Raffestin, "Validity and reproducibility of the PPLP scoring scale in the follow-up of athletes after anterior cruciate ligament reconstruction," *Ann. Phys. Rehabil. Med.*, vol. 53, pp. 162-179, Apr, 2010.
- [174] J. T. Bencardino, J. Beltran, M. I. Feldman and D. J. Rose, "MR imaging of complications of anterior cruciate ligament graft reconstruction," *Radiographics*, vol. 29, pp. 2115-2126, Nov, 2009.
- [175] R. Allum, "Complications of arthroscopic reconstruction of the anterior cruciate ligament," *J. Bone Joint Surg. Br.*, vol. 85, pp. 12-16, Jan, 2003.

- [176] O. Papakonstantinou, C. B. Chung, K. Chanchairujira and D. L. Resnick, "Complications of anterior cruciate ligament reconstruction: MR imaging," *Eur. Radiol.*, vol. 13, pp. 1106-1117, May, 2003.
- [177] T. C. Wilson, A. Kantaras, A. Atay and D. L. Johnson, "Tunnel enlargement after anterior cruciate ligament surgery," *Am. J. Sports Med.*, vol. 32, pp. 543-549, Mar, 2004.
- [178] S. Ristanis, N. Stergiou, E. Siarava, A. Ntoulia, G. Mitsionis and A. D. Georgoulis, "Effect of femoral tunnel placement for reconstruction of the anterior cruciate ligament on tibial rotation," *J. Bone Joint Surg. Am.*, vol. 91, pp. 2151-2158, Sep, 2009.
- [179] M. D. Miller, A. C. Gerdeman, C. D. Miller, J. M. Hart, C. M. Gaskin, S. R. Golish and W. G. Clancy Jr, "The effects of extra-articular starting point and transtibial femoral drilling on the intra-articular aperture of the tibial tunnel in ACL reconstruction," *Am. J. Sports Med.*, vol. 38, pp. 707-712, Apr, 2010.
- [180] E. Tsuda, Y. Ishibashi, A. Fukuda, Y. Yamamoto, H. Tsukada and S. Ono, "Tunnel position and relationship to postoperative knee laxity after double-bundle anterior cruciate ligament reconstruction with a transtibial technique," *Am. J. Sports Med.*, vol. 38, pp. 698-706, Apr, 2010.
- [181] J. Dargel, R. Schmidt-Wiethoff, S. Fischer, K. Mader, J. Koebke and T. Schneider, "Femoral bone tunnel placement using the transtibial tunnel or the anteromedial portal in ACL reconstruction: a radiographic evaluation," *Knee Surg. Sports Traumatol. Arthrosc.*, vol. 17, pp. 220-227, Mar, 2009.
- [182] O. Uzumcugil, A. Dogan, M. Yalcinkaya, Y. E. Akman, E. Mumcuoglu and N. Azar, "Clinical importance of femoral and tibial tunnel localizations in arthroscopic anterior cruciate ligament reconstruction," *Eklem Hastalik Cerrahisi*, vol. 20, pp. 25-31, 2009.
- [183] A. Burkart, R. E. Debski, P. J. McMahon, T. Rudy, F. H. Fu, V. Musahl, A. van Scyoc and S. L. Woo, "Precision of ACL tunnel placement using traditional and robotic techniques," *Comput. Aided Surg.*, vol. 6, pp. 270-278, 2001.
- [184] S. M. Howell, M. E. Gittins, J. E. Gottlieb, S. M. Traina and T. M. Zoellner, "The relationship between the angle of the tibial tunnel in the coronal plane and loss of flexion and anterior laxity after anterior cruciate ligament reconstruction," *Am. J. Sports Med.*, vol. 29, pp. 567-574, Sep-Oct, 2001.
- [185] Y. S. Chan, Y. P. Lo, L. C. Lien, C. J. Fu, Y. L. Wan, K. Y. Hsu, C. J. Wang and W. J. Chen, "Improved divergence angles with femoral interference screw placement through the tibial tunnel as measured by multiplanar reconstruction computed tomography," *Arthroscopy*, vol. 25, pp. 54-61, Jan, 2009.

- [186] G. Basdekis, P. Christel and F. Anne, "Validation of the position of the femoral tunnels in anatomic double-bundle ACL reconstruction with 3-D CT scan," *Knee Surg. Sports Traumatol. Arthrosc.*, vol. 17, pp. 1089-1094, Sep, 2009.
- [187] C. Hoser, K. Tecklenburg, K. H. Kuenzel and C. Fink, "Postoperative evaluation of femoral tunnel position in ACL reconstruction: plain radiography versus computed tomography," *Knee Surg. Sports Traumatol. Arthrosc.*, vol. 13, pp. 256-262, May, 2005.
- [188] M. Inoue, S. Tokuyasu, S. Kuwahara, N. Yasojima, Y. Kasahara, E. Kondo, S. Onodere and K. Yasuda, "Tunnel location in transparent 3-dimensional CT in anatomic double-bundle anterior cruciate ligament reconstruction with the trans-tibial tunnel technique," *Knee Surg. Sports Traumatol. Arthrosc.*, Dec 10, 2009.
- [189] H. Tsukada, Y. Ishibashi, E. Tsuda, A. Fukuda and S. Toh, "Anatomical analysis of the anterior cruciate ligament femoral and tibial footprints," *J. Orthop. Sci.*, vol. 13, pp. 122-129, Mar, 2008.
- [190] G. Papaioannou, G. Nianios, C. Mitrogiannis, D. Fyhrie, S. Tashman and K. H. Yang, "Patient-specific knee joint finite element model validation with high-accuracy kinematics from biplane dynamic Roentgen stereogrammetric analysis," *J. Biomech.*, vol. 41, pp. 2633-2638, Aug 28, 2008.
- [191] E. Pena, B. Calvo, M. A. Martinez and M. Doblare, "A three-dimensional finite element analysis of the combined behavior of ligaments and menisci in the healthy human knee joint," *J. Biomech.*, vol. 39, pp. 1686-1701, 2006.
- [192] G. Limbert, M. Taylor and J. Middleton, "Three-dimensional finite element modelling of the human ACL: simulation of passive knee flexion with a stressed and stress-free ACL," *J. Biomech.*, vol. 37, pp. 1723-1731, Nov, 2004.
- [193] X. Zhang, G. Jiang, C. Wu and S. L. Woo, "A subject-specific finite element model of the anterior cruciate ligament," *Conf. Proc. IEEE Eng. Med. Biol. Soc.*, vol. 2008, pp. 891-894, 2008.
- [194] J. Yao, J. Snibbe, M. Maloney and A. L. Lerner, "Stresses and strains in the medial meniscus of an ACL deficient knee under anterior loading: a finite element analysis with image-based experimental validation," *J. Biomech. Eng.*, vol. 128, pp. 135-141, Feb, 2006.
- [195] J. J. Elias and A. J. Cosgarea, "Computational modeling: an alternative approach for investigating patellofemoral mechanics," *Sports Med. Arthrosc.*, vol. 15, pp. 89-94, Jun, 2007.
- [196] J. L. Lanovaz and R. E. Ellis, "A cadaverically evaluated dynamic FEM model of closed-chain TKR mechanics," *J. Biomech. Eng.*, vol. 131, pp. 051002, May, 2009.

- [197] W. Mesfar and A. Shirazi-Adl, "Knee joint biomechanics in open-kinetic-chain flexion exercises," *Clin. Biomech. (Bristol, Avon)*, vol. 23, pp. 477-482, May, 2008.
- [198] E. Pena, B. Calvo, M. A. Martinez, D. Palanca and M. Doblare, "Influence of the tunnel angle in ACL reconstructions on the biomechanics of the knee joint," *Clin. Biomech. (Bristol, Avon)*, vol. 21, pp. 508-516, Jun, 2006.
- [199] E. Pena, M. A. Martinez, B. Calvo, D. Palanca and M. Doblare, "A finite element simulation of the effect of graft stiffness and graft tensioning in ACL reconstruction," *Clin. Biomech. (Bristol, Avon)*, vol. 20, pp. 636-644, Jul, 2005.
- [200] R. Shirazi and A. Shirazi-Adl, "Analysis of partial meniscectomy and ACL reconstruction in knee joint biomechanics under a combined loading," *Clin. Biomech. (Bristol, Avon)*, vol. 24, pp. 755-761, Nov, 2009.
- [201] S. Lyman, P. Koulouvaris, S. Sherman, H. Do, L. A. Mandl and R. G. Marx, "Epidemiology of anterior cruciate ligament reconstruction: trends, readmissions, and subsequent knee surgery," *J. Bone Joint Surg. Am.*, vol. 91, pp. 2321-2328, Oct, 2009.
- [202] S. Kopf, B. Forsythe, A. K. Wong, S. Tashman, W. Anderst, J. J. Irrgang and F. H. Fu, "Nonanatomic tunnel position in traditional transtibial single-bundle anterior cruciate ligament reconstruction evaluated by three-dimensional computed tomography," *J. Bone Joint Surg. Am.*, vol. 92, pp. 1427-1431, Jun, 2010.
- [203] S. C. Tadepalli, K. H. Shivanna, V. A. Magnotta, N. A. Kallemeyn and N. M. Grosland, "Toward the development of virtual surgical tools to aid orthopaedic FE analyses," *EURASIP J. Adv. Signal. Process.*, vol. 2010, pp. 1902931-1902937, Jan 1, 2010.
- [204] G. C. Sharp, S. W. Lee and D. K. Wehe, "ICP Registration Using Invariant Features," *IEEE Trans. Pattern Anal. Mach. Intell.*, vol. 24, pp. 90-102, 2002.
- [205] A. J. Ramme, A. J. Criswell, B. R. Wolf, V. A. Magnotta and N. M. Grosland, "EM Segmentation of the Distal Femur and Proximal Tibia: A High Throughput Approach to Anatomic Surface Generation," *Ann. Biomed. Eng.*, [Submitted].
- [206] E. S. Grood and W. J. Suntay, "A joint coordinate system for the clinical description of three-dimensional motions: application to the knee," *J. Biomech. Eng.*, vol. 105, pp. 136-144, May, 1983.
- [207] M. Kazhdan, "An Approximate and Efficient Method for Optimal Rotation Alignment of 3D Models," *IEEE Trans. Pattern Anal. Mach. Intell.*, vol. 29, pp. 1221-1229, 2007.

- [208] J. Tedjokusumo and W. Leow, "Normalization and alignment of 3D objects based on bilateral symmetry planes," in *Advances in Multimedia Modeling* Anonymous 2006, pp. 74-85.
- [209] G. Barequet and S. Har-Peled, "Efficiently approximating the minimum-volume bounding box of a point set in three dimensions," pp. 82-91, 1999.
- [210] S. Gottschalk, M. C. Lin and D. Manocha, "OBBTree: A hierarchical structure for rapid interference detection," pp. 171-180, 1996.
- [211] F. Giron, R. Buzzi and P. Aglietti, "Femoral tunnel position in anterior cruciate ligament reconstruction using three techniques. A cadaver study," *Arthroscopy*, vol. 15, pp. 750-756, Oct, 1999.
- [212] S. Lorenz, F. Elser, M. Mitterer, T. Obst and A. B. Imhoff, "Radiologic evaluation of the insertion sites of the 2 functional bundles of the anterior cruciate ligament using 3-dimensional computed tomography," *Am. J. Sports Med.*, vol. 37, pp. 2368-2376, Dec, 2009.
- [213] T. Zantop, M. Wellmann, F. H. Fu and W. Petersen, "Tunnel positioning of anteromedial and posterolateral bundles in anatomic anterior cruciate ligament reconstruction: anatomic and radiographic findings," *Am. J. Sports Med.*, vol. 36, pp. 65-72, Jan, 2008.
- [214] M. Doi, M. Takahashi, M. Abe, D. Suzuki and A. Nagano, "Lateral radiographic study of the tibial sagittal insertions of the anteromedial and posterolateral bundles of human anterior cruciate ligament," *Knee Surg. Sports Traumatol. Arthrosc.*, vol. 17, pp. 347-351, Apr, 2009.
- [215] D. M. Lintner, S. E. Dewitt and J. B. Moseley, "Radiographic evaluation of native anterior cruciate ligament attachments and graft placement for reconstruction. A cadaveric study," *Am. J. Sports Med.*, vol. 24, pp. 72-78, Jan-Feb, 1996.
- [216] R. Siebold, T. Ellert, S. Metz and J. Metz, "Femoral insertions of the anteromedial and posterolateral bundles of the anterior cruciate ligament: morphometry and arthroscopic orientation models for double-bundle bone tunnel placement--a cadaver study," *Arthroscopy*, vol. 24, pp. 585-592, May, 2008.
- [217] R. Siebold, T. Ellert, S. Metz and J. Metz, "Tibial insertions of the anteromedial and posterolateral bundles of the anterior cruciate ligament: morphometry, arthroscopic landmarks, and orientation model for bone tunnel placement," *Arthroscopy*, vol. 24, pp. 154-161, Feb, 2008.

[218] P. Colombet, J. Robinson, P. Christel, J. P. Franceschi, P. Djian, G. Bellier and A. Sbihi, "Morphology of anterior cruciate ligament attachments for anatomic reconstruction: a cadaveric dissection and radiographic study," *Arthroscopy*, vol. 22, pp. 984-992, Sep, 2006.

[219] S. Kopf, V. Musahl, S. Tashman, M. Szczodry, W. Shen and F. H. Fu, "A systematic review of the femoral origin and tibial insertion morphology of the ACL," *Knee Surg. Sports Traumatol. Arthrosc.*, vol. 17, pp. 213-219, Mar, 2009.

[220] M. L. Purnell, A. I. Larson and W. Clancy, "Anterior cruciate ligament insertions on the tibia and femur and their relationships to critical bony landmarks using high-resolution volume-rendering computed tomography," *Am. J. Sports Med.*, vol. 36, pp. 2083-2090, Nov, 2008.